The Development of a Novel Multi-Scale Modelling Framework to Predict the Effect of Porosity on the Transverse Strength of Fibre Reinforced Polymer Composites

Benjamin Leigh Fisher

Cardiff University

A thesis submitted in partial fulfilment for the degree of
Doctor of Philosophy

School of Engineering
January 2024

Abstract

The use of composites in automotive applications is fast becoming prevalent due to increasing requirements for low-emission vehicles and the extension of the electric vehicle range. A main obstacle in the wide application of composites is a plethora of manufacturing-induced defects. Currently, more work is still required to accurately predict the exact material response for different defects.

One of the most significant manufacturing defects is the inclusion of porosity, it is almost impossible to completely mitigate and if not controlled or accounted for properly, can have a catastrophic impact on structural composites. Previous work has attempted to address this issue; however, for the most part, it has only focused on the void content as the main contributing factor in degrading the material properties. Recent studies have since found that the shape and size of the porosity also have an important role in determining the response.

This thesis focuses on developing a design tool to predict the effect of porosity in unidirectional carbon fibre reinforced polymer composites. The main output from this project is a modelling framework which can account for accurate porosity parameters, including void content, shape, and size. The modelling framework achieves this by splitting the procedure into two distinct stages; first, studying how voids knock down the strength of neat matrix and second, the '*knocked-down*' matrix strength is used in a Representative Unit Cell to predict ply properties.

The modelling process was conceptualised and used to study the correlation between the void parameters and the matrix strength. Observations were established on how voids act as stress raisers on the surrounding material and comparisons were investigated using a representative analytical model. An experimental campaign was undertaken whereby laminates were manufactured through prepreg/autoclave procedures as well as through resin infusion, using various methods to vary the porosity. The laminates were mechanically tested, and the porosity parameters were characterised. The porosity characterisation data was subsequently used to build representative models which were correlated to the empirical testing.

This thesis is dedicated to everyone who has supported, encouraged and believed in me.

Acknowledgements

I would like to express my immense gratitude to my two supervisors Professor Rhys Pullin and Dr Mark Eaton for their continuous support, guidance, and encouragement. Without their help, I would not have been able to achieve what I have done, and I will always acknowledge how fortunate I have been for their supervision. Although, I am sure we are all glad to not have any more lock-down 'perplexing' Zoom meetings! Thank you, both.

I would also like to thank the technicians in the civil basement for their help with all of the testing I have done. Their unwavering support, no matter whether the task was difficult or last minute, is greatly appreciated. I am sure they are very happy that one less person is using the Z050 testing machine! Furthermore, I would like to thank Garry for all his help in assisting me with the composite manufacture I have done throughout my PhD. I will always remember the many fruitful discussions we had in the composites lab.

In addition, I would like to thank all of the CUSP lab members whom I have had the opportunity to meet and work with throughout my time in the group. It was a pleasure to collaborate with many of the group members on various projects and I don't think I will ever forget the 'tea-call' each day.

Thank you to all of Cardiff Racing, it has been a pleasure to be a part of the team throughout my whole time at Cardiff University. There have been many highs in the past 9 years, but I have always been grateful to be able to take a break and come down to the Paddock to escape the PhD stresses. A special thank you goes to Lee, to whom I am forever indebted, for being there for me many times over the years. I am sure I will see you at FSUK in the years to come!

I would like to thank Mum and Dad, Cameron and Matthew for the encouragement and support throughout not just my PhD, but in everything that I have done. And yes Mum, those extra GCSE Maths lessons paid off! I would finally like to thank my biggest supporter, Sophie, who has been there for me through the thick and thin of it. Whenever I have had any doubts, you have always offered reassurance and encouragement. You are an inspiration.

Table of Contents

List of Figures

List of Tables

Glossary

Term	Description
	Materials and Manufacturing
Autoclave	Machines used to apply heat and pressure, can used to cure composites.
Composite	A material that is formed of two distinct constituents, clearly identifiable.
Degassing	The process used to remove gas from resin before combining it with the preform.
Fibre tow	Discrete bundles of fibres that can be intertwined to form a fabric.
Fibre reinforced composite	A composite where the main load bearing comes from thin strands of a high-performance material.
Fibre volume fraction	The percentage of a composite that is made up of fibre reinforcement.
Glass transition temperature	The transition temperature that results in a polymer's 'glassy' state becoming 'rubbery', due to the carbon chains that form the polymer beginning to move.
Laminate	A flat plate made from fibre reinforced composite, typically used for testing purposes.
Layup	Multiple plies which are placed on top of one another to form a laminate.
Matrix	The material that holds the reinforcement form in a composite.
Major axis	The axis along the longest length of a void, that is assumed to take the shape of an ellipsoid.
Minor axis	The two axes along the shortest lengths of a void that is assumed to take the shape of an ellipsoid. Often these two axes are assumed to be of the same length.
Out-of-Autoclave	A composite manufacturing process that does not make use of an autoclave.
Ply	A single layer of a fibre reinforced composite.

Preform	The name given to the reinforcement before being combined with the matrix.
Pre-preg	A type of fibre reinforced composite where the matrix is already combined with the reinforcement from the supplier.
Racetracking	Found in Out-of-Autoclave manufacturing processes where the introduction of matrix spreads quickly around the outside of the mould.
Reinforcement	The main load-bearing constituent in a composite
Resin infusion (VARTM)	Type of Out-of-Autoclave manufacturing process where the matrix is drawn through the preform. Also known as Vacuum Assisted Resin Transfer Moulding.
Uniaxial layup	A layup where all plies have the reinforcement co-aligned in the same direction.
Unidirectional	Type of fibre architecture where all fibres in a single ply are orientated in the same direction.
Void Content	The volume fraction of empty regions within a material.
Woven	Type of fibre architecture where fibre tows are intertwined into a fabric.
Inspection	
Micro-computed tomography	3-dimensional X-ray imaging technique used to build representative computational/graphical models.
Optical microscopy	Use of microscopy to inspect materials at the micron scale.
Phase contrast edge enhancement	The phenomenon in μ-CT scans where the border between two materials, which differ in densities, is observed.
Testing	
Combined Loading Compression	A test fixture designed to induce both end loading and shear loading into compression specimens.
Crosshead displacement	The method used to induce load into specimens through a combination of gripping and extension/compression
Failure	When specimens lose all load-bearing ability.
Platen	Flat metallic plates which are used as an interface between specimen surfaces and the test machine. Used in compression testing.
Preload	A small amount of load that is induced into a specimen prior to starting the test.
Modelling	
Integration points	Specific locations used to map how a structure performs under load.
Knocked-down property	A material property that has lower performance due to a defect

Linear elastic	Type of modelling process where only linear material properties are included.
Mesh	The global arrangement of divisions used to create elements.
Mesh elements	Sub-divisions of a structure used to define where calculations take place.
Modelling framework	A high-level overview of how a modelling procedure works, various procedures can follow it.
Molecular Dynamics	Computational simulation approach to model the behaviour of materials at the atomic/molecular scale.
Mesh generation	Creation of the mesh which is first defined based on the mesh seed.
Mesh seed	The points at which the initial mesh is defined and grows from.
Micromechanical model	The material model with a working scale at the micrometre.
Modelling approach	This is the exact procedure that is being followed in the modelling framework.
Model series	These are several simulations that can be analysed together.
Nodes	These are the vertices of the mesh elements.
Periodic Boundary Conditions	A type of boundary condition that allows for periodicity to be included in the model. Often used in micromechanical models.
Pristine matrix	Term given to the matrix region of the void module where it is assumed that there are no defects (such as voids).
Representative Unit Cell	A micromechanical model that is representative of the whole structure.
Void module	A model of a composite that only includes voids in the matrix.
Extended Finite Element Method	A numerical modelling procedure used to predict crack propagation in materials, without requiring remeshing newly formed surfaces.

Acronyms

AFP	Automated Fibre Placement
ATL	Automated Tape Laying
CLC	Combined Load Compression
CSA	Cross-Sectional Area
DMA	Dynamic Mechanical Analysis
FEA	Finite Element Analysis
FEM	Finite Element Method
GRP	Glass Reinforced Polymer
ICE	Internal Combustion Engine
IDE	Integrated Development Platform
AC	In-Autoclave
MD	Molecular Dynamics
OoA	Out-of-Autoclave
PBC	Periodic Boundary Conditions
RUC	Representative Unit Cell
RI	Resin Infusion
US	Ultrasonic
XFEM	Extended Finite Element Method
µ-CT	Micro-Computed Tomography

Nomenclature

Symbol	Description	SI Units
	Constituent Calculations	
v_c	Void content	%
ρ_c	Density, composite	$Kg \cdot m^{-3}$
ρ_m	Density, matrix	$Kg \cdot m^{-3}$
ρ_r	Density, reinforcement	$Kg \cdot m^{-3}$
W_m	Weight percentage, matrix	%
W_r	Weight percentage, reinforcement	%
M_i	Initial constituent mass	Kg
M_f	Final constituent mass	Kg
V_m	Volume, matrix	m^3
V_r	Volume, fibre	m^3
T_g	Glass Transition Temperature	K
	Resin Flow	
Ca^*	Modified capillary number	$N \cdot m^{-1}$
μ	Resin viscosity	$Pa \cdot s$
v	Global resin velocity	$m \cdot s^{-1}$
γ	Resin surface tension	$N \cdot m^{-1}$
θ	Resin-fibre contact angle	°
$K(\emptyset)$	Macroscopic preform permeability	m^2
V_{meso}	Void content of meso voids	%
V_{micro}	Void content of microvoids	%
	Void Modelling	
a	Major void radii	μm
b	Minor void radii (axis 1)	μm
c	Minor void radii (axis 2)	μm
V_v	Void volume	μm^3
V_t	Stage 1 model, total volume	μm^3
	Calculations	
F_{max}	Ultimate strength	N
P_{max}	Maximum load	Pa
A	Cross-sectional area	m^2
E	Young's modulus	Pa
ΔS_{le}	Change in stress	Pa
$S_{max,le}$	Max stress	Pa
$S_{min,le}$	Min stress	Pa
$\Delta \in_{le}$	Change in strain	$-$
$\in_{max,le}$	Max strain	$-$
$\in_{min,le}$	Min strain	$-$

Symbol	Description	SI Units
	Stress Concentrations	
σ_m	Maximum stress	Pa
σ_0	Applied stress	Pa
a	Halve defect length	m
ρ_t	Defect tip radius	m

1. Introduction

1.1. Background

Composites, particularly Carbon Fibre Reinforced Plastics (CFRP), are synonymous with motorsports and high-performance vehicles. For instance, the pioneering work of the McLaren F1 team involved building and successfully competing with the first-ever full composite monocoque race car in the Formula 1 race series. This led to a great surge in the development of composites in motorsport.[1] Likewise, the first fully composite monocoque of a production car was achieved by Lamborghini when they introduced the Aventador sports car, as shown in **Figure 1-1**.[2]

Figure 1-1 *Lamborghini's Aventador composite monocoque*[2]

The possibility to achieve composites with a high strength-to-mass ratio is what makes them extremely attractive to high-performance environments, alongside their increased efficiency for the same input. For instance, BMW used composites extensively in the i3 range of electric city cars as this was a way of improving mileage from a single charge. This is becoming increasingly important as there is an extremely high focus on the emissions of greenhouse gases and their link to global warming and climate change. The increase in global temperature can be seen in **Figure 1-2** where a rate of approximately 0.08 °C per decade has been reported.[3]

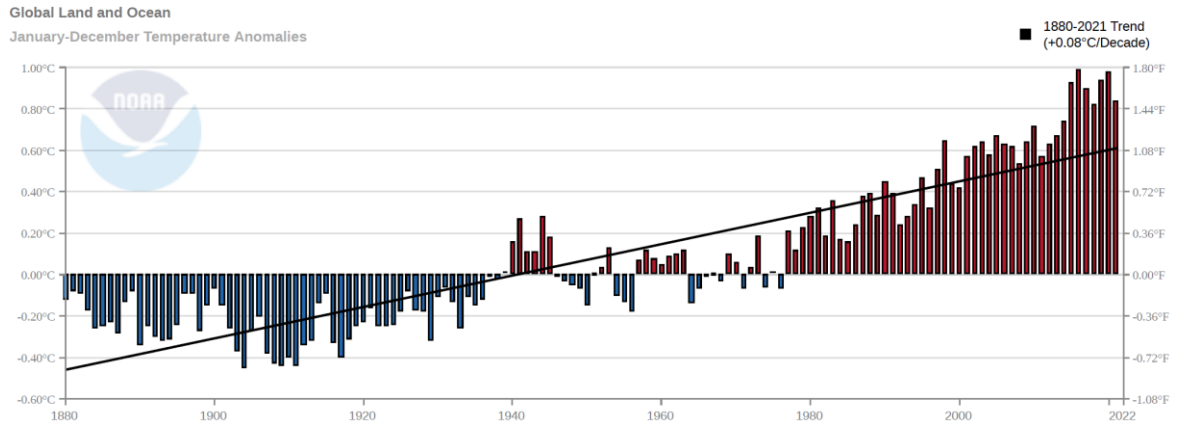

Figure 1-2 *Global increase in temperature, compared to 1990. National Centers for Environmental Information.* [3]

To tackle this phenomenon, organisations around the world are setting policies to reduce greenhouse gas emissions. For instance, in 2008 the UK set the Climate Change Act[4] with the goal of being 'Net Zero', i.e., the net carbon account being at least 100 % lower than that of the 1990 baseline by 2050. The EU has also followed a similar trend, where in 2019 the European Green Deal[5] was presented which was set to reduce emissions by 55 % of the 1990 baseline by the year 2030 and 100 % by 2050.[6] On a global scale, the Paris Agreement[7] is an international legal treaty to reduce greenhouse gas emissions to limit global warming to 1.5 °C when compared to pre-industrial temperatures.

Meeting these targets is extremely important and many organisations have introduced policies to tackle climate change. For instance, in 2020, the UK government published a white paper report[8] identifying how they were addressing the issue and the plans being put in place. The report documented a ten-point plan intending to kickstart a 'Green Industrial Revolution'. The plan includes increased use of offshore wind farms, implementation of carbon capture usage and storage, as well as transitioning to zero-emission vehicles.

Nevertheless, for zero-emission vehicles, the biggest relevant change is a transition from Internal Combustion Engines (ICE) to electric drivetrains, due to their low operational emissions.[9] However, regardless of the drivetrain format, the heavier the vehicle is, the more energy is required for the same journey. This means that by lowering the vehicle's overall mass better mileage can be achieved. In a Plenary lecture at the Composites 2021 conference[10] a presentation discussing the use of composites in automotive applications explained that metallic structures are very well optimised,

meaning that there is very little scope to reduce mass any further without the transition to composite materials. Nonetheless, the plenary lecture went on to further explain that the design knowledge regarding composites is still in its infancy and so, whilst the designs of metallic and composite structures are currently of similar mass, there is a great potential for improvement.

The reason that composite design processes are still in the early development stage, even after several decades of research, is due to the high number of defects that can arise during manufacture and understanding how these affect the performance during the structure's lifecycle. For many years high safety factors have been applied in structural design, which has resulted in over-engineered designs. To both fully optimise a composite structure and minimise energy usage, a full understanding of the exact composite structure's behaviour is required. This means being able to predict how certain defects arise and their effect on the design integrity.

1.2. Thesis Aims and Objectives

There is a fine balance between not accounting for manufacturing defects and over-engineering a composite design, and in either case, the outcome is less than desirable. The governing factor is accurately understanding the relevant mechanical properties of the defects. Although empirically testing a design for a given manufacturing process provides exact data, this is far from ideal; tooling and moulds must be manufactured, materials must be purchased (which may not be decided upon yet) and most importantly, testing would be required throughout design iterations. This provides reason to develop prediction tools on how defects affect mechanical properties.

The most prevalent defect in composite manufacture is porosity. This is an extremely difficult defect to prevent, predict the formation of and understand the resulting impact. Current modelling techniques are still simplistic, they either assume that voids are infinitely long in a planar model, or the properties of 3D elements are degraded to simulate a void. In either case, there is a poor geometrical representation of voids, which is problematic as recent studies have begun to identify that it is not just the volume fraction of voids that is important, but also the shape.[11,12]

The overall aim of this work is:

"To develop and validate a multiscale modelling framework that can be used to predict the strength degradation of carbon fibre reinforced polymer materials due to the inclusion of voids during manufacture."

To achieve this aim, the following objectives were set:

- To conceptualise a multiscale modelling framework that accounts for both the void content as well as geometrical parameters used to characterise porosity. This modelling framework will be the main Finite Element Method (FEM) approach used in this thesis.
- To investigate, using the multiscale modelling framework, how geometrical parameters affect the strength of a composite. This is to assess if firstly, the modelling approach can determine a change in strength due to various porosity parameters and secondly, to what extent a change in the relevant parameter affects the reduction in strength.
- To experimentally test the mechanical performance of composite laminates containing porosity that have been generated to varying degrees, using samples manufactured through both autoclave and Out-of-Autoclave (OoA) processing techniques. This information is to be used to determine what properties are affected by porosity and test data can be used to validate the modelling approach against.
- To characterise the porosity generated in the laminates that are tested. Firstly, this allows for an understanding of how a change in the porosity affects the mechanical properties and secondly, the data can be used to build representative models using the developed modelling framework.
- To validate the modelling framework through a correlation campaign where representative models are built, and the predicted FEM results are compared to the experimental results. This will determine how successful the modelling approach is at addressing the main aim.

1.3. Novelty Statement

The research presented in this thesis focuses on developing a novel modelling framework accounting for accurate void representation. The novel aspects of this research are summarised as follows:

- Development of a dual stage modelling framework that can predict the reduction in transverse strength of a composite for a given set of porosity parameters. The effect of voids on neat matrix is first studied and the homogenised/degraded matrix is then used in a representative unit cell, all whilst focusing on the effect on transverse strength. There are very few approaches which have split the modelling process in this way and those that have, were focused on the change in stiffness and did not consider the reduction in strength.
- Varying autoclave cure pressures to change the void content between laminates has been implemented on numerous occasions. However, the resulting size and shape of the voids has only been the focus of a few studies. The porosity produced through autoclave processing was measured using optical microscopy, allowing for the shape and size of microvoids (voids with lengths of approximately 10μm) to be studied.
- A case study was conducted investigating the influence of porosity in resin-infused laminates on transverse mechanical properties. To the author's best knowledge, this is the first time that a highly detailed analysis of the variation of void content across a resin-infused laminate has been undertaken in combination with empirical testing. The experimental data was also used as inputs and validation criteria for the developed model.

1.4. Thesis Structure

The current chapter gives a broad introduction to the thesis focus, including the thesis's overall aim and corresponding objectives. Chapter 2 reviews the current literature in the area of this thesis. Porosity is defined, including characterisation processes, which is followed by studies into the impact it has on mechanical properties. The chapter finishes by reviewing the current modelling approaches and states the gap in knowledge that this thesis aims to address. Chapter 3 gives an overview of the common techniques that have been used in this thesis. This includes composite manufacturing and testing, void characterisation and modelling techniques. Chapter 4 defines the modelling framework that has been conceptualised and how it can be implemented. Chapter 5 details the experimental campaign including laminate manufacture, mechanical testing and microstructure characterisation. Chapter 6

utilises the data gathered from Chapter 5 to build representative models of the laminates that were tested and correlate to the experimental results. Chapter 7 provides an overall discussion of the results and Chapter 8 draws conclusions together for this thesis highlighting the outcomes, limitations, and potential future work. Any additional information and supplementary material are included in the appendices.

1.5. Published Outputs

Work Published:

Fisher, B. L., Eaton, M. J. & Pullin, R. A novel multi-scale modelling approach to predict the reduction of transverse strength due to porosity in composite materials. *Composite Structures (2023). Doi: 10.1016/j.compstruct.2023.116861*

Fisher, B. L., Eaton, M. J. & Pullin, R. A multi-scale modelling approach to predict the effect of porosity on transverse strength. in *8th ECCOMAS Thematic Conference on the Mechanical Response of Composites* 12 (2021). doi:10.23967/composites.2021.093.

2. Literature Review

2.1. Chapter Overview

This chapter highlights the relevant research applicable to this thesis. An initial definition of what composites are in terms of this work and the types of associated defects is first given. Attention is then focused on porosity, where it is defined, and characterisation techniques are addressed. Subsequently, studies into the effect porosity has on mechanical performance and current modelling approaches are detailed. The chapter concludes by drawing together the current state of the art, gaps and shortcomings in the research and presents key points for the thesis to address.

2.2. Manufacturing Variability Overview

2.2.1. Composite definition

To understand the different types of defects and how they arise, it is first important to address what a composite is and what they are made from. A composite is a material that contains two or more different constituents. In the context of this work, this refers to fibre reinforced polymers where the fibres are used as the main load bearing[13–27] constituent which are held together using a polymer-based matrix. There are a variety of different types of constituents which are selected based on their properties and user case. The most common types are summarised in **Table 2-1**.

Table 2-1 *Types of fibres used in fibrous composites.*[28]

Constituent	Constituent type	Density / Kgm^{-3}	Modulus[a] / GPa	Poisson Ratio	Strength[a] / GPa
Fibre	Glass	2600	76	0.22	3-4
	Kevlar	1470	150	0.35	2-3
	Carbon (high strength)	1750	250-300	0.20	3-6
	Carbon (high modulus)	1940	400-800	0.20	2-4
	Flax	1500	80	0.30	2
Matrix	Epoxy	1250	3.5	0.38	0.04
	Polyester	1380	3.0	0.37	0.04
	Polyether ether ketone (PEEK)	1300	4.0	0.37	0.07

[a]For fibre constituents the property is taken in the axial direction.

There are several different forms that the reinforcement can take, known as fibre architecture, illustrated in **Figure 2-1**. The most common is unidirectional, which is where all the fibres are orientated in the same direction and arranged into a flat layer called a 'ply.' Multiple plies are laminated together to form a 'stack-up/laminate' where the fibre orientation is rotated to suit the structural loading. A woven fibre architecture is where each ply is made up of 'tows' which are bundles of between 1000-15,000 fibres. Each tow is then woven into a fabric following a weave type, as shown in **Figure 2-2**. The third general fibre architecture is short-strand composites, where the fibres are chopped into short lengths and are dispersed randomly throughout the matrix.

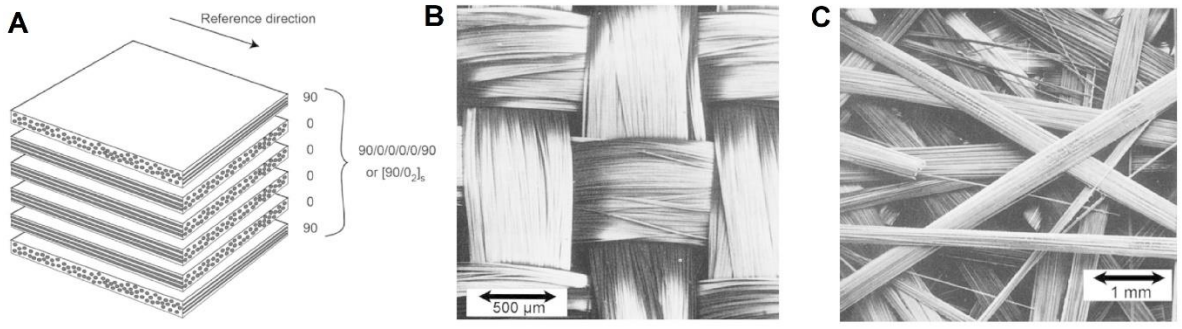

Figure 2-1 *Different fibre architectures. (A) Unidirectional, (B) woven and (C) random chopped strand.*[28]

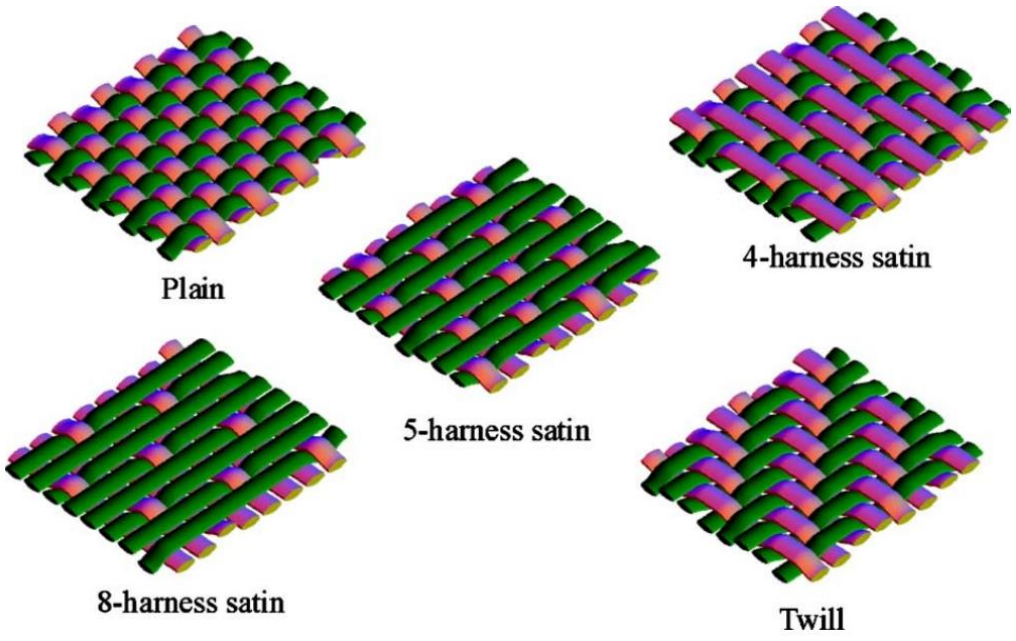

Figure 2-2 *Examples of the different types of woven fabrics.*[29]

2.2.2. Types of manufacturing induced defects

In composites, many different types of defects can be induced during the manufacturing stage. These defects can be extremely problematic if the tolerances are not correctly set or not controlled stringently during manufacture. The types of defects broadly fall into categories that are based on either the constituent material or the macro (part) scale. Examples of the most common types of defects can be seen in **Figure 2-3**.

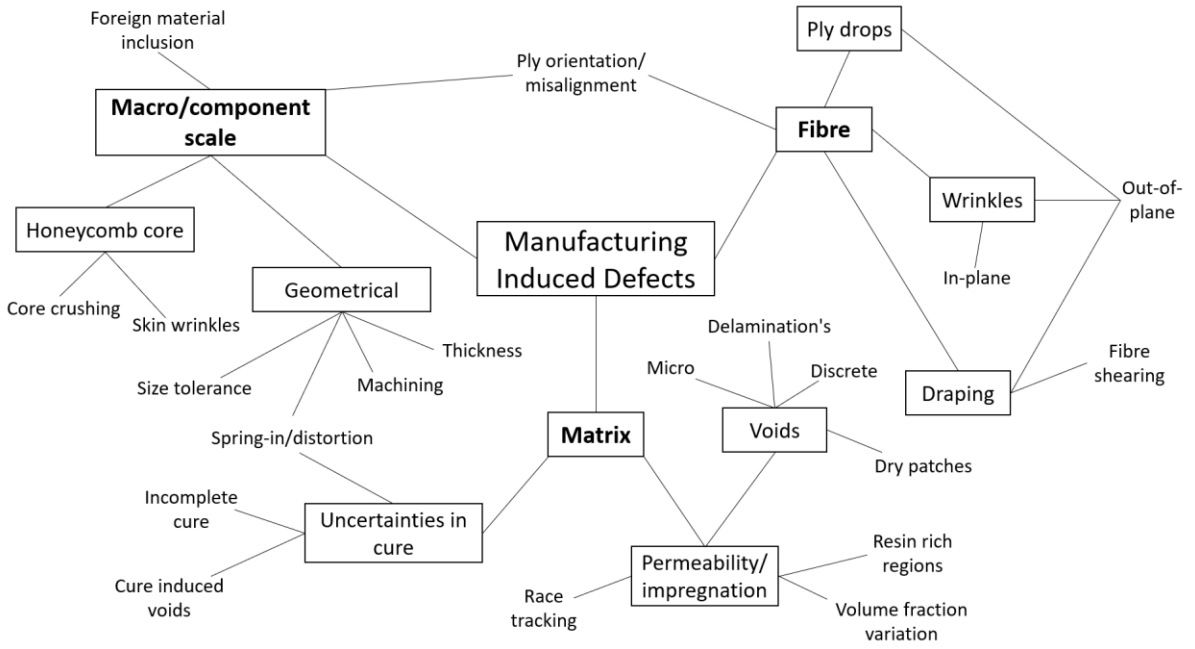

Figure 2-3 *Schematic of the types of defects showing that they are typically either matrix, fibre or macroscale based.*

It is clear from **Figure 2-3** that there is a plethora of different defects that can occur during manufacture and gives reason why significant safety factors have been used as a way of addressing the uncertainty. However, to maximise the design efficiency an understanding of how each of the defects affects the integrity of a structure is needed. Macro and fibre-based defects are certainly important and can be extremely detrimental, however, they can be evaluated generally through inspection techniques and measurements. On the contrary, matrix defects are a lot more difficult to account for since, firstly, it is difficult to control them consistently (i.e., two laminates following an identical manufacturing process may have different void content or dry patches). Secondly, matrix defects such as voids and incomplete cure are difficult to measure, which results in significant investment into process characterisation and control.

2.2.3. Porosity Overview/Definition

When it comes to matrix-based defects, one of the most well-known and significant imperfections are voids. These are regions of the composite that do not contain either the matrix or reinforcement and instead are unfilled gap(s).[30] Several types of voids can be found in composites with the most common being 'discrete voids'. These are large voids in the order of millimetres and can individually affect the mechanical

properties of a composite. Porosity on the other hand is a collection of much smaller voids on the scale of micrometres and whilst the individual voids are unlikely to affect the mechanical properties, often they generate throughout the material in which case, collectively, they can be cause for concern.[31]

Voids have been a subject of research for several decades, because of their significance in reducing mechanical properties.[31] A literature search through 'Google Scholar' between the years 1950-1979 using keywords such as 'composite', 'void', 'porosity' and 'defect' (date searched 14th April 2022) shows that research into how voids affect fibrous composites started in the late 1960s and early 1970s. Examples of this research include a study by Bascom and Romans[32] in 1968 where they investigated how microvoids in glass reinforced resin form during filament winding processes. They found that the nonuniformity of fibre distribution inhibited full wet through as the fibres were drawn through the resin bath. In 1974, Cilley et al[33] presented work at Composite Materials: Testing and Design conference where they showed different approaches to determine the void content of laminate. They showed that resin-removal techniques are more precise, however do not offer spatial distribution analysis that optical methods can.

When the search is changed to include research between 1980 and 2000 it is clear that in the mid 1990's the field became a lot more active. For instance, in 1996 Patel and Lee[34,35] published a two-part study investigating void formation and reduction. The first part focused on tow permeability through wicking tests and capillary pressure-saturation measurement where this information is subsequently used in the second part to develop a model of the formation of voids. The model can be used to investigate how different process parameters affect the generation of voids. Thomas et al.[36] carried out an extensive investigation into understanding how parameters of autoclave curing affect the final part including the void content. These parameters include pressure, temperature, ramp and dwell times as well as prepreg age. The results showed that whilst the pressure influenced the void content the most, the other parameters also influenced the resulting porosity levels.

Whilst historically porosity has been investigated, it is still an active research field. In recent years there has been a consistent number of papers published related to porosity, notably an extensive review paper by Mehdikhani et al.[30] which covers all aspects of porosity from formation and characterisation to the impact on mechanical

properties. Tretiak et al.[37] recently published work describing a model which can account for accurate 3D void geometry to be used when investigating the impact of porosity on short beam shear strength. Another recent publication by Machado et al.[38] uses machine learning to improve the efficiency of optical microscopy techniques. Typically to use optical microscopy for void content analysis, thresholds have to be set manually for image processing, however, the model can automatically segment porous regions from the image and calculate the void content.

The significant ongoing research into porosity shows the implication that is poses if not properly accounted for. This is due to the complexity of the microstructure of composites causing the formation of voids to be a complex phenomenon as well as the large impact that voids have on the structural performance. This means that a full understanding and ability to predict not only the impact porosity has, but also the formation during manufacture since the final porosity features (e.g. void content, geometry etc.) can influence how the mechanical properties are affected.

2.3. Porosity Features

Porosity is extremely important from the magnitude of related research both historically (i.e., since the 1970's) and from the number of papers that are published currently. It is also very well accepted that porosity is a major defect in composites[30,31,39] and so it is important to evaluate the porosity found in structural parts to determine if they pose a risk of premature failure or not. Whilst the definition of porosity can simply be described as regions that are unfilled by either fibres or polymer[30], accurately describing porosity within a laminate/component is much more difficult. Several factors contribute to the overall makeup of porosity including the void content, shape, size, distribution and location[30,40]. These factors are defined as follows:

Void Content: This is the overall volume fraction of porosity that a given laminate/component has within it and is typically given as a percentage of the overall structure/region in question[30]. Void content is a very common factor when describing the porosity within a laminate and is often the only measured porosity-based tolerance when determining acceptable void characteristics[40].

Shape: Since there are no specific controlling measures that influence the exact shape of voids (i.e. ensuring voids take a precise shape), in practise voids take an

arbitrary/irregular shape[30]. However, it is a common simplification to assume that, whilst they are not perfect, they are roughly ellipsoidal and so the shape is defined by the three axes of an ellipsoid. Whilst different researchers may use different notations, the principle remains the same whereby the void can be measured by its length (l_v), width(w_v) and height(h_v)[40]. The shape of the void is an important parametric since voids act as stress concentrations and therefore the radius of the void correlates to the level of local stress around the void when subjected to a load. It is possible to change the shape of a void whilst retaining the same void content and subsequently affecting the knockdown factor that the void contributes.[40]

Size: Size is directly related to the shape of a void since it is the three axes that define the shape which are measured to determine the size of a void. Whilst it is possible to fully define a void based on these three measurements, it is often useful to express the size of a void in terms of its 'roundness' and 'elongation' factor as a ratio. This allows an evaluation of the severity of the stress concentration, i.e., a high ratio would mean that there is a sharp geometrical feature that may be cause for concern.

Location and Distribution: To fully characterize porosity within a structure the location of voids and how they are dispersed must also be reported. Porosity location refers to the region of a structure that is being defined. This is important as porosity may vary across a structure, such as at a geometrical feature (e.g., internal radius or thickness change), and therefore it is important to specifically define the region the characterisation is taking place for[30]. As well as reporting global location, intra-laminate location (i.e., within the thickness of a composite) is also another void positioning parameter that can be reported. Voids will either be found between plies where there are high local matrix volume fractions or intra-ply[30] where fibres are displaced to make room for the void.[40] Linked to the location, the distribution is another parameter used to describe porosity. Whilst location refers to the region at which certain porosity is found, distribution can be described as how the voids are spread out at a given location. This includes the distance between voids, how porosity varies through the laminate thickness and whether the distribution is uniform or not.[12,30,39,40]

2.4. Characterisation Techniques

There are several porosity characterisation and measurement techniques commonly used which range from simplistic density tests and calculations through to highly specialised μ-CT scanning. Each approach has its advantages and disadvantages some of which include what characteristics the technique can pick up, cost of setup and running as well as skill and training required. To understand which approach is most appropriate to use, it is important to understand not only the benefits but also the drawbacks. For instance, only being able to measure the void volume fraction may not be enough information for further evaluation. This section details each of the most common techniques used to evaluate porosity including a description of how the technique works, what it can determine as well as the benefits and drawbacks.

2.4.1. Density calculations

This is an approach which follows the ASTM Standard D2734[41] whereby the void content of a composite is calculated based on determining the density of both the defective composite as well as the density and mass fractions of its constituents. Once these values are either known or calculated, Equation (2-1) can be used to predict the void content, where v_c is the void content, W and ρ are the weight percentage and density of the constituents and the subscripts m, r and c represent the matrix, reinforcement, and composite respectively.

$$v_c = 100 - \rho_c \left(\frac{W_m}{\rho_m} + \frac{W_r}{\rho_r} \right) \tag{2-1}$$

Whilst it is straightforward to calculate the void content using Equation (2-1), determining each of the parameters is more involved. First, to calculate the required densities of all three materials the standard recommends using the test methods outlined in ASTM standard D792[42]. This test method uses the water displacement technique to determine the specific gravity of the material and subsequently the density. It is not the only technique that can be used to determine the density. If the mass and volume for the matrix and/or composite can be measured accurately, then the density can be calculated directly. The final measurement that is required is to determine the resin content of the composite, in terms of its mass, using the ASTM standard D2584. This test method uses the ignition method to combust the matrix; taking mass measurements before and after combustion allows for the resin content

to be calculated. The main benefit of this technique is that once the constituent properties have been determined only the density and resin content of the composite are required making the evaluation fast.[30] However, porosity characterisation is limited to only evaluating the void content and no other features can be determined. It must also be noted that the accuracy of this approach is also limited where error is up to ±0.5 %[30].

2.4.2. Constituent Contents

This approach follows the ASTM standard D3171[43], which calculates the constituent content based on the removal of the matrix via several optional approaches. The test method requires the matrix to be removed such that the mass of the fibres can be measured. This allows for the mass percentage of both the fibres and matrix to be calculated using equations (2-2) and (2-3) respectively, where M is the mass and the subscripts f and i represent the final mass after matrix removal and initial mass before matrix removal.

$$W_r = \left(\frac{M_f}{M_i}\right) \times 100 \tag{2-2}$$

$$W_m = \frac{\left(M_i - M_f\right)}{M_i} \times 100 \tag{2-3}$$

Using the density of both the reinforcement and matrix the respective volume percentages can also be calculated using equations (2-4) and (2-5) where V is the volume percentage and ρ is the density.

$$V_r = \left(\frac{M_f}{M_i}\right) \times \frac{\rho_c}{\rho_r} \times 100 \tag{2-4}$$

$$V_m = \frac{\left(M_i - M_f\right)}{M_i} \times \frac{\rho_c}{\rho_m} \times 100 \tag{2-5}$$

Once the volume of the respective constituent is known, the void content can be calculated using equation (2-6).

$$v_c = 100 - (V_r - V_m) \tag{2-6}$$

As mentioned, this method requires the mass of both the composite specimen and the reinforcement to be known. This means the matrix must be removed to isolate the reinforcement for measurement. The ASTM standard for this approach recommends using one of three ways, either through matrix digestion, ignition or carbonisation. These approaches are described as follows:

Matrix digestion: Several different processes can be used for matrix digestion which depend on what acid is used to break down the matrix. The acids that can be used include nitric acid, sulfuric acid, hydrogen peroxide, ethylene glycol, potassium hydroxide, sodium hydroxide and hydrochloric acid. Whilst numerous processes are possible to use, the general approach is similar across all of them. First, the sample is prepared, weighed and density measured. It is then placed in a flask with the corresponding acid and heat is applied in a controlled manner. Once the acid has broken down the matrix, often identified by the reinforcement floating, the acid is drained through a filter under a vacuum. The fibres are washed and filtered three times using distilled water. Optionally acetone can be used as the final wash as the next step is drying the fibres and the acetone reduces the drying time. To dry the reinforcement the sample is placed in an oven and heated until fully dry (approximately an hour) at which point the fibres can now be weighed.

Ignition: Specimens are suitably prepared by machining and grinding such that their density can be measured. The specimens are then placed into a cleaned crucible and placed into a preheated oven up to 500°C. The heat is then increased to 565±30°C (depending on the composite) and left for 6 hours such that the matrix is burnt off leaving the reinforcement behind.

Carbonisation: This approach is similar to the ignition method whereby an oven is used to burn off the matrix, however, in this approach not only is the composite specimen placed into the oven, but also a neat resin specimen (same as what is used in the composite). The oven is purged with nitrogen and heated to 560±40°C, however, for a minimum of 1 hour. After which the specimens are cooled and weighed. The neat resin specimen is used as a control to measure the percentage of how much matrix was removed and this percentage is used when calculating the volume fractions.

Similar to the density calculations, the constituent contents approach is a destructive technique which will only calculate the void content and does not provide any

information regarding geometry or location/dispersion etc. Another significant drawback to this approach is the magnitude of error that can occur. For instance, high-accuracy analytical balances are required (±1mg), however, it is still possible to calculate a negative void content, particularly at low porosity levels. Also, there is the possibility that not all of the matrix is removed, therefore the mass of the residual matrix is attributed to the mass of the reinforcement leading to further error.

2.4.3. Ultrasonic testing

The change in attenuation (and less commonly measured, velocity) of an ultrasonic (US) wave can be used to measure the magnitude of porosity of a composite.[31] This is achieved through US waves being transmitted and received through the use of transducers containing piezoelectric crystals. The piezoelectric crystals convert electrical energy into US waves to transmit or receive sound waves and convert them back to electrical energy. The change in electrical energy can then be calibrated to the change in velocity or attenuation.[44] There are two types of setup, either using a single transducer which transmits and receives an echo (pulse-echo) or using two transducers positioned on either side of the test sample (through-transmission) which transmit and receive respectively.[30] The benefit of through-transmission measurements is the excellence at detecting porosity, as well as other defects such as delamination. However, it cannot determine the location/depth of the defect, whereas the pulse-echo technique can account for this based on the time delay of the echo. Pulse-echo measurements are not as accurate at measuring the magnitude of the defect therefore, if possible, the use of both techniques is recommended.[44] A couplant, typically water, between the transducers and sample must be required to ensure that US waves are efficiently transmitted. For smaller test samples a submerged/water bath system can be used with a reflector plate at the bottom for pulse-echo techniques. For larger samples, typically full-size components, a squirter system is used often through full 3D computer control for non-flat surfaces. In this case, the US waves pass through a jet of water between the sensor and panel. Schematics of these two processes can be seen in **Figure 2-4**[45]

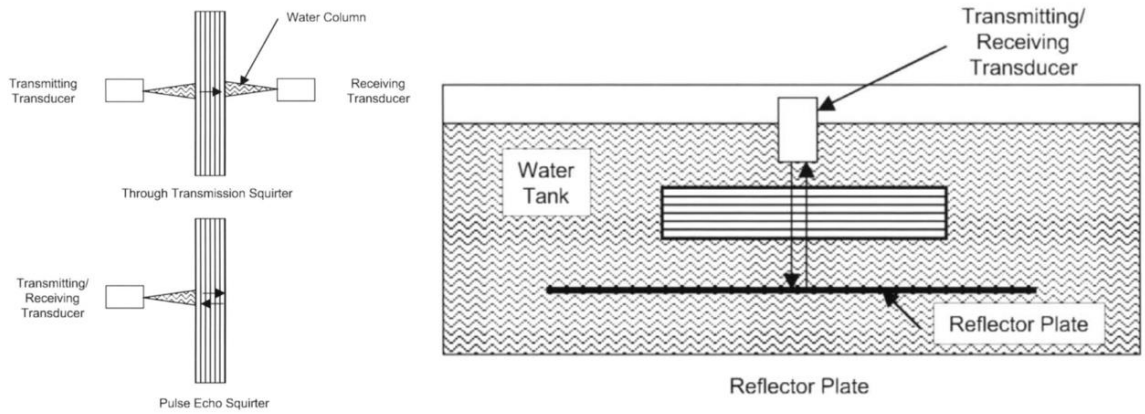

Figure 2-4 *Through-transmission and pulse-echo setups for US measurement using (**A**) squirter or (**B**) submerged systems.*[45]

Stone and Clarke[46] present a good investigation into how both velocity and attenuation are affected by porosity. The results for the velocity testing, using a pulse-echo setup, showed that for a void content of 5 %, the velocity of the US wave was reduced by approximately 6 %. However, the measurements were done in a water bath and they found that a change in water temperature, even as little as 1°, will result in inaccurate measurements. For this reason, they recommend that attenuation measurements are used instead for any practical use case. For the attenuation measurements, three different frequencies were used, 2.5, 5 and 7 MHz in a through-transmission setup. The results, as seen in **Figure 2-5** show that a bi-linear trend is present, such that the rate of increase in attenuation increases after a void content of approximately 1.5 %. This was explained by evaluating the microstructure of each laminate. The porosity in the laminates with a void content of 1.5 % or less were typically spherical voids between 5 to 20μm. Whereas above the 1.5 % void content mark, there was a change in the shape of the voids where they were instead much larger and elongated.

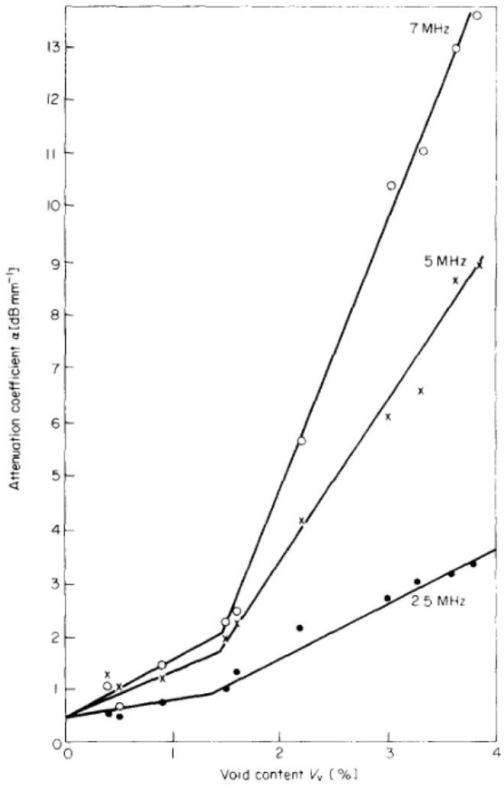

Figure 2-5 *Bi-linear trend of attenuation coefficient as void content increases with the knee occurring at approximately 1.5 %.*[46]

2.4.4. Microscopy

The techniques described so far can only measure the void content, however, as shown in Section 2.2 there are other parameters (mostly geometrical) that need to be accounted for to fully characterise the porosity. Optical microscopy is a very common approach utilised for void characterisation as it not only provides accurate void content measurements but also the size, shape and location can directly be analysed.[47,48] To analyse the microstructure the samples must first be sectioned perpendicular to the fibre direction, mounted in resin (optional) and polished to a high finish. [49,50] The samples are then placed on the bed of an optical microscope with the capacity to take digital images. Voids are identified as dark regions allowing measurement and analysis of the shape/size/location etc. Various image processing techniques can be used to isolate the voids by thresholding the dark regions and the void content is calculated based on the ratio between the area of collective voids to image size. The process of identifying and thresholding voids to calculate the void content can be seen in **Figure 2-6** where a void content of 2.7 % was measured by Saenz-Castillo et al. [51] Due to the non-periodic generation of porosity, care must be

given to ensure that a representative is captured. A statistical study by Bodaghi et al.[52] showed that analysing between 20-25 images provides a void content with an acceptable degree of accuracy.

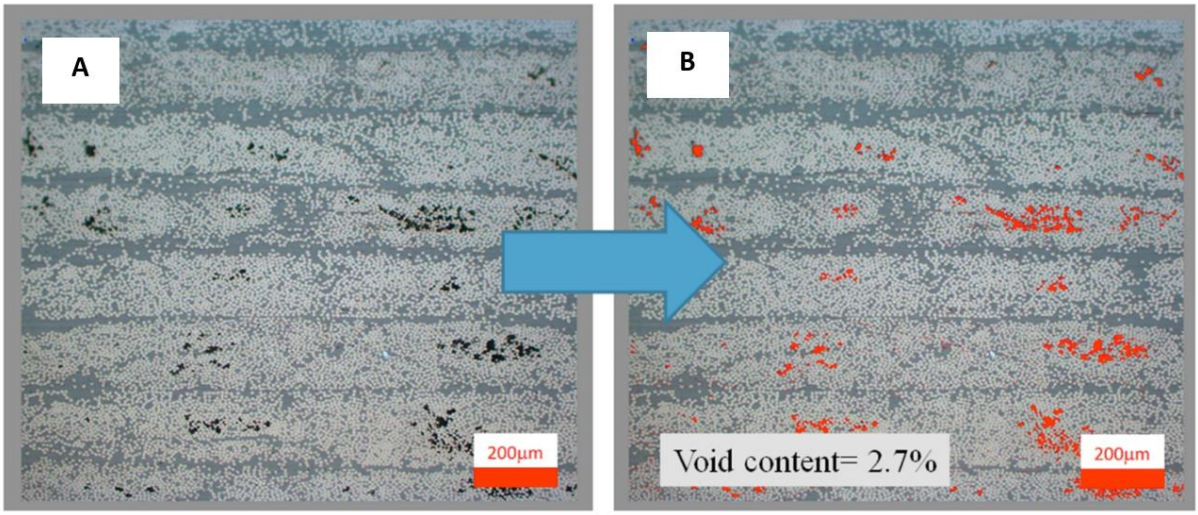

Figure 2-6 *Process to calculate void content where (**A**) shows the contrast between voids and surrounding material, and (**B**) shows the voids identified by software.*[51]

2.4.5. X-Ray µ-Computed Tomography

X-ray µ-Computed Tomography (µ-CT) is a process which can accurately and non-destructively image the microstructure of a composite with high spatial resolution.[53–55] This is achieved through scanning samples using X-ray imaging from multiple angles about a central axis. The composite constituents have different X-ray attenuation properties, therefore, when scanned from multiple angles, the difference in attenuation can be used to reconstruct the microstructure. This allows voids to be identified as they will have a different level of attenuation than the surrounding material. This can be seen in **Figure 2-7**[56] where voids have been successfully identified and coloured red.

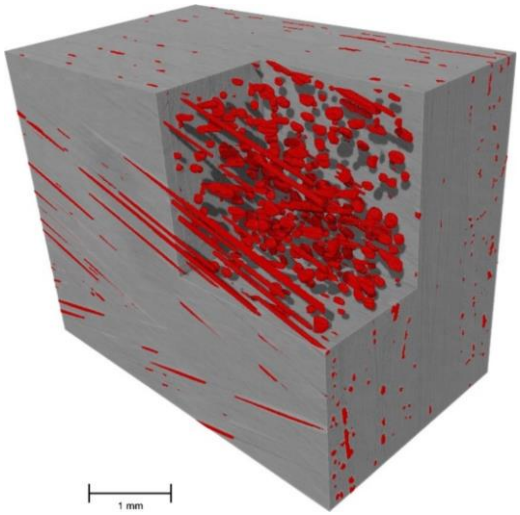

Figure 2-7 *μ-CT scan reconstruction of a CFRP containing voids which have been identified and coloured for inspection.*[56]

The major benefit of μ-CT scanning is that an accurate full 3D representation of the porosity can be characterised. Meaningful data including the number of voids, dimensions, area, and volume of each void can be obtained.[39,56] As the number of voids that can be measured is very large, for instance, Elkolali et al.[56] counted between 2000 to 6500 voids across 6 samples (with sample volumes of 60mm^3), an in-depth statistical study must be undertaken. Mehdikhani et al.[57] investigated the size, shape and orientation distribution of discrete voids with the results seen in **Figure 2-8**.

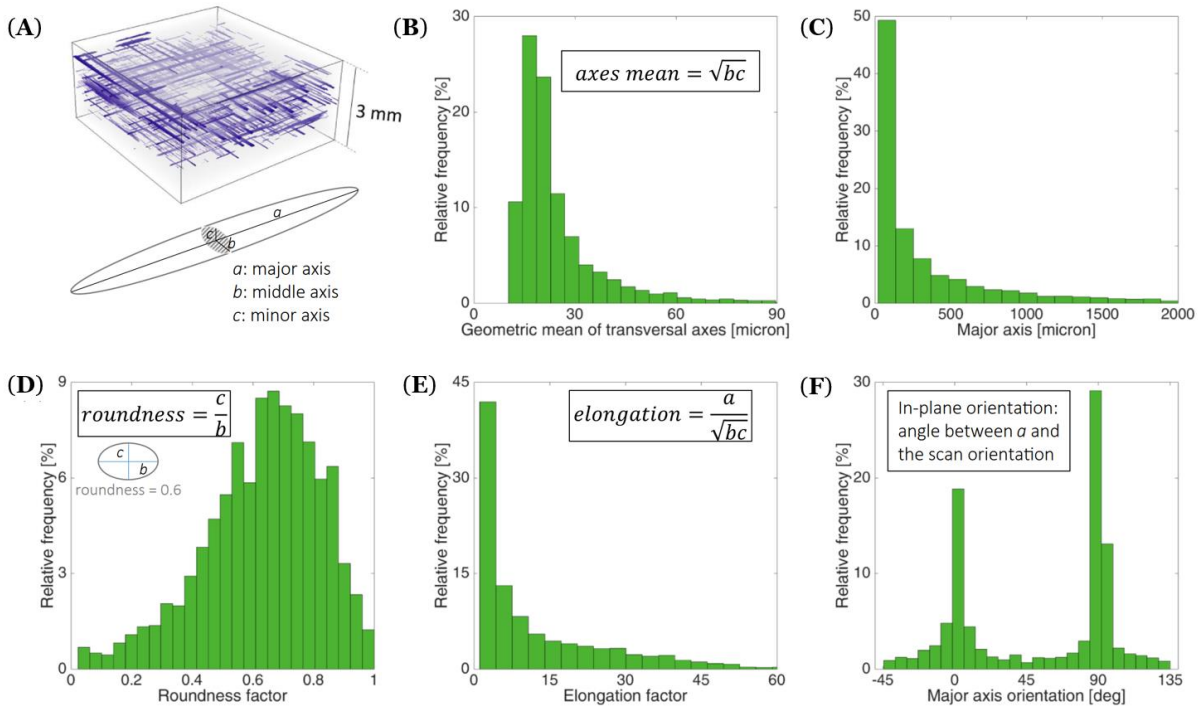

Figure 2-8 *Statistical study of void dimensions; (**A**) 3D representation of voids within the composite, (**B**) mean of the transverse axis, (**C**) longitudinal axis, (**D**) void cross-sectional roundness, (**E**) elongation between the longitudinal and transverse axes and (**F**) orientation of voids.*[57]

Whilst μ-CT can accurately identify and characterise the porosity there are a few drawbacks. The use is highly specialised and, in most cases, will need to be outsourced. This may be sufficient for validation and research purposes, however, for general usage, this then becomes impractical due to financial and time constraints. Also, depending on the constituent materials and scan setup there may be difficulty in identifying certain features due to similar x-ray attenuation between the differing materials.[55] For instance, the scanning completed by Elkolali et al.[56] could not differentiate between the matrix and fibres meaning that the fibre volume fraction could not be calculated. The scan resolution is also another factor which will dictate what can be identified; to capture larger areas containing discrete voids a lower resolution is required due to the scanning length of time, which means that microvoids cannot be detected. Instead, a high-resolution scan is required, however, the trade-off is a reduction in sample size.[55]

2.4.6. Concluding remarks on void characterisation

There are several techniques which can be used to characterise the porosity. The techniques are either destructive (such as density calculation) or non-destructive (such as ultrasonic) and the parameters that can be measured range from just the void content to full 3D reconstruction with detailed geometrical analysis. Whilst μ-CT scanning will provide the most detailed characterisation, this may not be required when simply the void content is sufficient. For instance, the aerospace industry is required to follow the standard ASTM D3171-15 to measure just the void content through acid digestion.[54] However, to fully understand and predict how porosity affects the mechanical properties all parameters must be considered, not just the void content.[39,56–60] To decide as to what technique is to be used, the following factors must first be considered: the parameter required for characterisation, accuracy, number of samples, recurrence of test, cost, time, and access to equipment.

2.5. Porosity Generation

The method by which porosity is generated in a composite structure is dependent on the overall composite manufacturing technique, however, it can be summarised into two categories: Liquid Composite Moulding (LCM) or prepreg techniques.[13,30,40] The void generation for these two categories of composite manufacture are discussed here.

2.5.1. Liquid composite moulding

Composite manufacture through LCM techniques starts with the placement of the reinforcement into a mould and subsequently adding the matrix. Techniques include Resin Transfer Moulding (RTM) and Vacuum Assist Resin Transfer Moulding (VARTM) also known as Resin Infusion (RI).[13] There are numerous ways that voids can be generated in LCM, resulting in increased difficulty in limiting the void fraction. This is likely why these processes are generally assumed to produce lower quality parts than through prepreg processes. Possible void formation mechanisms include gases released during the curing process, air dissolved within the resin prior to infusion and through part shrinkage during cure.[14,15,61] However, the most widely cited mechanism for porosity generation is due to mechanical entrapment during infusion.[13–16,61] This occurs when air is still present in the mould after a vacuum has been drawn, which is then absorbed by the resin during infusion. It is also well documented that the speed

at which the resin is drawn through the reinforcement dictates the void formation.[13,23,62,63] As the vacuum pulls the resin through the reinforcement, capillary action draws the resin within the tows. If the resin flow is too high, then the capillary action is not strong enough to fully wet out the tows. However, if the resin flow is too slow, whilst full wet through of the tows is achieved, voids form between adjacent tows. This trade-off is illustrated in **Figure 2-9**. The result of the competition between resin flow and capillary action can be determined based on the modified capillary number, Ca*, as shown in equation (2-7)[64], where μ, v, γ and $Cos\theta$ are the resin velocity, global resin velocity, resin surface tension and resin-fibre contact angle.

$$Ca^* = \frac{\mu v}{\gamma Cos\theta} \tag{2-7}$$

When the modified capillary number is small, the result is that the capillary action is dominant and voids between fibres, named 'meso-voids' form, whereas, for larger modified capillary numbers the global resin flow is dominant and 'micro-voids' within the fibre tows form.[30] These types of voids are illustrated in **Figure 2-9**.

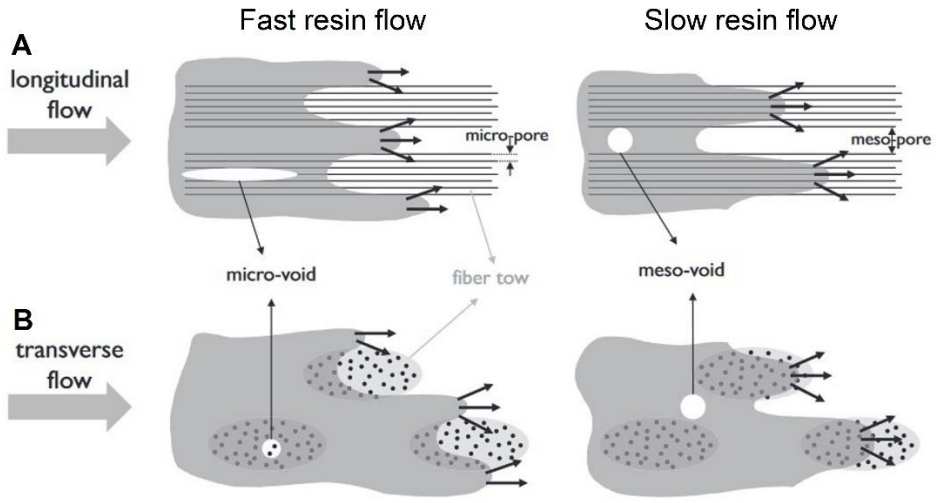

Figure 2-9 *Schematic of the difference between fast and slow resin injection speed resulting in micro and meso size voids.*[30]

It has been reported that the percentage of micro and meso voids follows a near logarithmic function on flow velocity.[65] The result of extensive testing by LaBat et al.[66] was able to derive the following relationships shown in Equations (2-8) and (2-9):

$$V_{meso} = -32.28 - 11.8log(v) \tag{2-8}$$

$$V_{micro} = 6.35 + 2.35log(v) \tag{2-9}$$

Where V_{meso} and V_{micro} are the percentage void content for meso and microvoids respectively. Ruiz et al.[65] reordered equation (2-7) substituted into equations (2-8) and (2-9) to give the following relationships (Equations (2-10) and (2-11)):

$$V_{meso} = -32.28 - 11.8log(\frac{Ca^*\gamma Cos\theta}{\mu}) \quad (2\text{-}10)$$

$$V_{micro} = 6.35 + 2.35log(\frac{Ca^*\gamma Cos\theta}{\mu}) \quad (2\text{-}11)$$

Patel and Lee[34] characterised the modified capillary action parameters for a polyester resin, finding that $\mu = 0.05462\ Pa \cdot s$, $\gamma = 0.0345\ Nm^{-1}$ and $\theta = 34°$. Substituting these values into equations (2-10) and (2-11) shows how the percentage of micro and meso voids varies as a function of global resin velocity[65] and is illustrated in **Figure 2-10**.

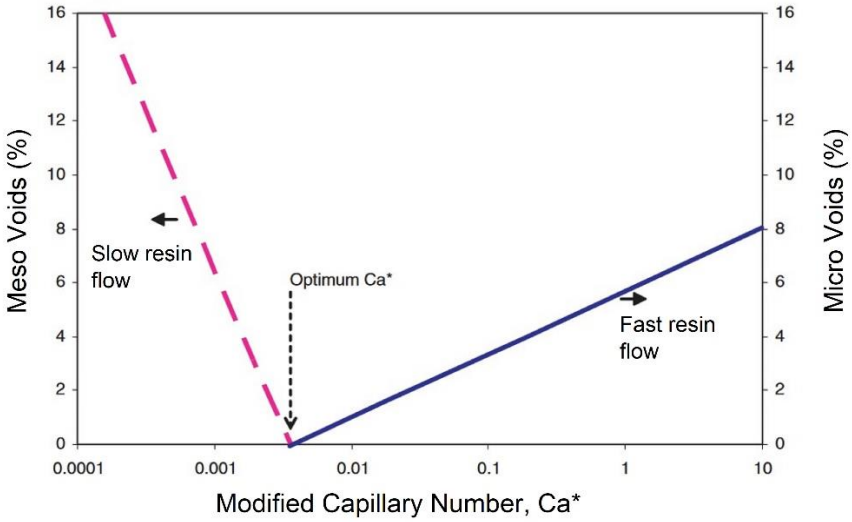

Figure 2-10 *Logarithmic function of how the percentage of micro and meso voids change as the modified capillary number is varied.*[65]

It should also be noted that one of the major porosity defects that can arise in LCM, which when present will result in part scrappage, are macro voids otherwise known as dry patches. This is where the global resin flow front reaches the outlets before full wet-through has been achieved, leaving regions that have not yet been impregnated.[30,67] Several factors can cause dry patches such as incorrect positing of inlets and outlets[67–69], variation in the permeability across the structure (such as on the edge causing 'race tracking')[68] and the addition of substrates such as ribs, inserts and core material causing a change in flow form.[69] It is clear that this type of defect

occurs due to improper design of resin introduction and changes must be made before committing to a manufacturing process, otherwise high part scrappage will occur.

2.5.2. Prepreg methods

Whereas in LCM techniques porosity generation is mainly studied during the introduction of the matrix, for prepreg techniques research efforts have been predominately focused on how layup and curing affect porosity.[30] Within prepreg manufacturing methods, porosity formation can be broken down into curing using '*in-autoclave*' (AC) methods, or '*Out-of-Autoclave*' (OoA) methods.

In-autoclave methods: For high-performance structural composites AC manufacturing is often used as the additional consolidation pressures, as well as the applied temperature, results in a high quality of standard that can be achieved. The additional pressure produces high fibre volume fractions as well as reducing the void content by compressing and removing air bubbles that would have otherwise been a void in the final part.[70] Voids form in prepreg AC manufacturing by several methods, the most common is through mechanical entrapment as air is trapped between plies during layup.[15,71,72] This is why AC processes are effective at producing low porosity laminates as the high pressures drive out the trapped air. Liu et al.[71] showed that there is a strong correlation between the autoclave cure pressure and resultant void content within the laminate, as illustrated in **Figure 2-11**. However, whilst it is generally accepted that a high cure pressure will result in a laminate containing low porosity, how the autoclave cure parameters are specified will also have an effect. These include when the temperature and pressures are initialised and at what ramps they are increased and decreased. For instance, void removal through applied pressure is dependent on resin viscosity which is dependent on the applied temperature.[71,72] The other consideration that affects the void content is moisture/humidity. Water vapour in the surrounding air can become dissolved within the resin, when the resin is subjected to heat this results in the dissolved water boiling off leaving voids.[73–76] Netzel et al.[73] conducted an extensive study into the effect of humidity on uncured prepreg properties (prepreg tack, compaction behaviour and interply friction) as well as the overall void content. Their results showed that humidity significantly affected the consolidation of complex geometries, such as internal radii, and the increase in tackiness of the prepreg plies resulted in a higher risk of entrapped air.

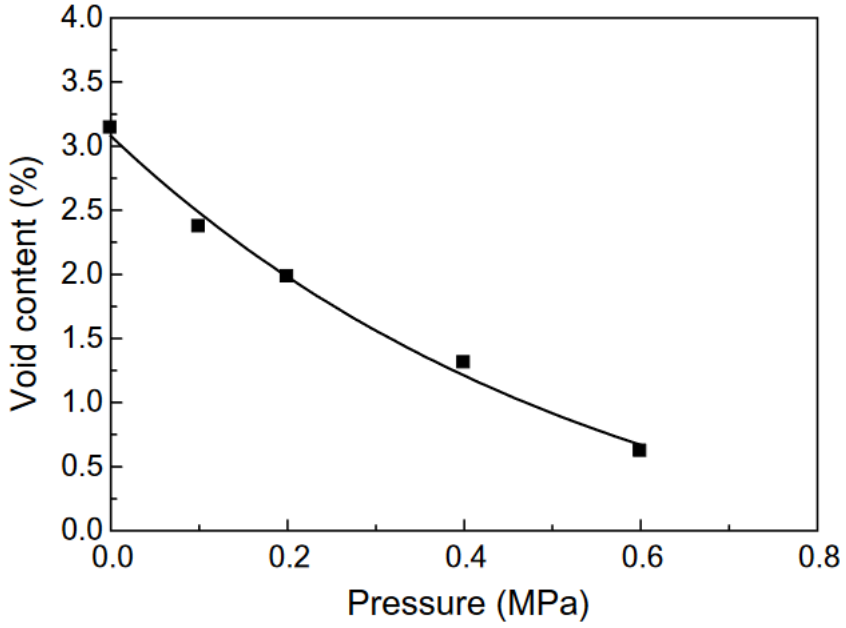

Figure 2-11 *Correlation between autoclave cure pressure and resultant void content.*[71]

Out-of-Autoclave methods: In recent years there has been a strong drive towards OoA manufacturing methods for increased production rates and reduced capital investment.[77] Whilst OoA techniques are synonymous with LCM, there are also approaches using prepreg materials such as Vacuum Bag Only (VBO) and hot press curing.[30] VBO processes rely only on the atmospheric pressure for consolidation and applied temperature for resin flow and cure. As the high pressures provided by an autoclave are not present, which are required for the removal of voids, a change to the material pre-pregnation state is required. As supplied, the resin only surrounds the tows rather than fully saturating the fibres meaning that there is an escape path for the air to be removed as the vacuum is applied. As the temperature is increased the resin becomes less viscous and is drawn into the tows to, ideally, fully saturate the fibres.[17,18,70] This process is illustrated in **Figure 2-12**.[70] Whilst a great deal of research has gone into developing this approach, in practice it is not possible to completely remove all voids. This method is susceptible to the same '*gas-induced*' void generation as AC methods such as mechanical entrapment and moisture absorption, but also through a '*flow-induced*' mechanism. Flow-induced voids occur when the resin has not completely wetted out the dry tows before curing and can be a result of several factors such as a high initial cured state, dense fibre packing[70] or exceeding the out-time limit before curing.[18] It is clear that to ensure low porosity parts are manufactured through VBO, extensive process evaluation is required.

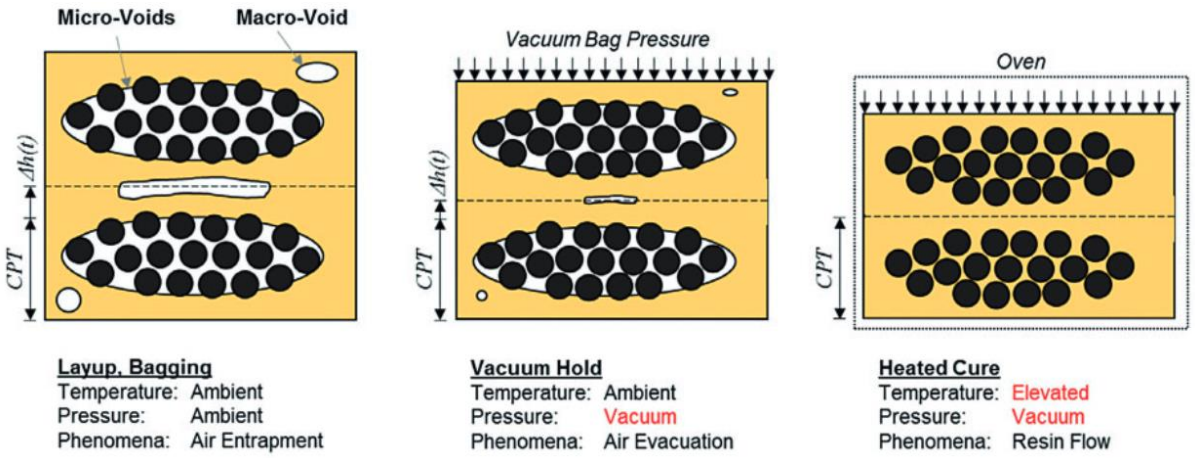

Figure 2-12 *Schematic of the VBO process using unsaturated tows for air removal.*[70]

Hot press curing is an OoA prepreg technique that works by placing the prepreg material within two matching solid moulds which are pressed together and heated according to the cure cycle. As with other processes, the increase in temperature allows the resin to become less viscous to promote coalescence and cross-linking reactions. The applied pressure advances the mixing of resin between plies and evacuation of voids as well as reduces laminate thickness and increases fibre volume fraction.[19] The main mechanisms for void generation through hot press curing is via entrapped air and moisture[74] and most research efforts have been focused on how the processing parameters affect the void content. For instance, Agius et al.[77] investigated how void development was affected by the rate at which temperature was applied and found higher gelation temperatures resulted in higher void contents. Anderson and Atlan[19] increased the moisture content of the resin from 'as-supplied', to pre-conditioning the prepreg at 25% and 100% relative humidity increased the void content. Their results showed that at a low cure pressure of 1.7 bar, the relative humidity has a high influence (with results ranging from 2.79 % to 4.94 % void content) however when the cure pressure was increased to 5.8 bar the void content stabilised at 1.6 %.

The final prepreg manufacturing technique is Automated Tape Laying (ATL) and Automated Fibre Placement (AFP) which can be cured either through AC or OoA. These two approaches employ the use of a robot to automatically place down lines of prepreg over a mould and the difference between these two approaches is the width of the tape. The benefit of AFP is that where a single tape of widths up to 300 mm is used

for ATL, AFP processes place multiple smaller tapes instead typically up to 32 tapes that are between 3-6mm wide.[78] By having multiple narrower tapes means that AFP can make use of more complex geometrical moulds including double curvature and making tight 90° radii turns.[79] The main defect associated with automated layup is any inaccuracy in the placement of the tapes/tows where there is the possibility for there to be gaps and overlaps of the plies.[30] Air entrapment is a common issue with automated layup which is typically addressed through the first ramp-up of the cure cycle,[20] however, the work of Lukaszewicz et al. showed that consolidation through heat during the layup reduces the surface roughness of the plies which directly reduces the entrapped air.[78]

2.5.3. Concluding remarks on void generation

The mechanism for void generation is dependent on the manufacturing process; for LCM there is a strong link between how the resin is injected into the preform whereas for prepreg materials void generation is closely linked with the layup and curing processes. In any case, it is clear manufacturing a 'void-free' part is not possible and the current drive towards OoA processes (LCM or prepreg) for lower costs and higher production rates brings with it added difficulty. It should also be noted that the majority of the published literature was focused on the void content and does not include how void morphology is affected through the different manufacturing techniques.

2.6. Epoxy Resin Curing Process

The current literature survey has shown that porosity is closely linked to the matrix of a composite, rather than the reinforcement. When investigating the effect of porosity, other parameters such as the matrix should be kept constant. It is important to understand the curing process, including the cure mechanics and factors that affect the resultant cure, to ensure that the matrix properties (such as the Young's modulus) are constant throughout various experimental studies. This subsection investigates these areas.

2.6.1. Curing mechanics

Epoxy resins are a type of thermoset resin which require an irreversible chemical reaction in order to cure. The chemical reaction is initiated via a curing agent, of which there are several types that result in different cure behaviour, such as the cure time or temperature. When the curing agent is added to the epoxy resin, the result is that a highly cross-linked network of polymer chains are formed.[80,81] There are three main processes that the curing reaction can be categorised into: room temperature curing, elevated temperature curing or photo-curing. Epoxy resins can be cured using infrared or ultraviolet light, and high exposure results in reduced cure time.[80] Depending on the epoxy resin system being used will dictate which procedure is followed, which can then lead to different properties. For instance, a room temperature cure results in higher flexibility and impact resistance, whereas an elevated temperature cure produces an epoxy resin with greater tensile strength and a higher glass transition temperature.[80]

2.6.2. Cross-link density

Depending on the processing conditions the number of cross-links that are established can vary. This leads to the term 'cross-link density', which is defined as the number of cross-links per unit volume.[82] Factors that affect the cross-link density include varying the cure time and temperature[83] or varying the epoxy-to-hardener ratio.[84] Previously, experimental test programs studied the effect of process conditions on cross-link density; however, due to the significant time and cost investment there has been a transition towards computation simulations using Molecular Dynamics (MD).[81] MD is a computational tool to simulate the atomic and molecular behaviour of materials.[81,85] MD simulations were set up and performed by Shokuhfar and Arab[86] to investigate how the material properties of epoxy resin are affected by the cross-link density. Their results showed that by increasing the cross-link density, the elastic modulus can increase by 1.04 GPa, the results of which can be seen in **Figure 2-13**. It should be noted that their results have not been validated experimentally.

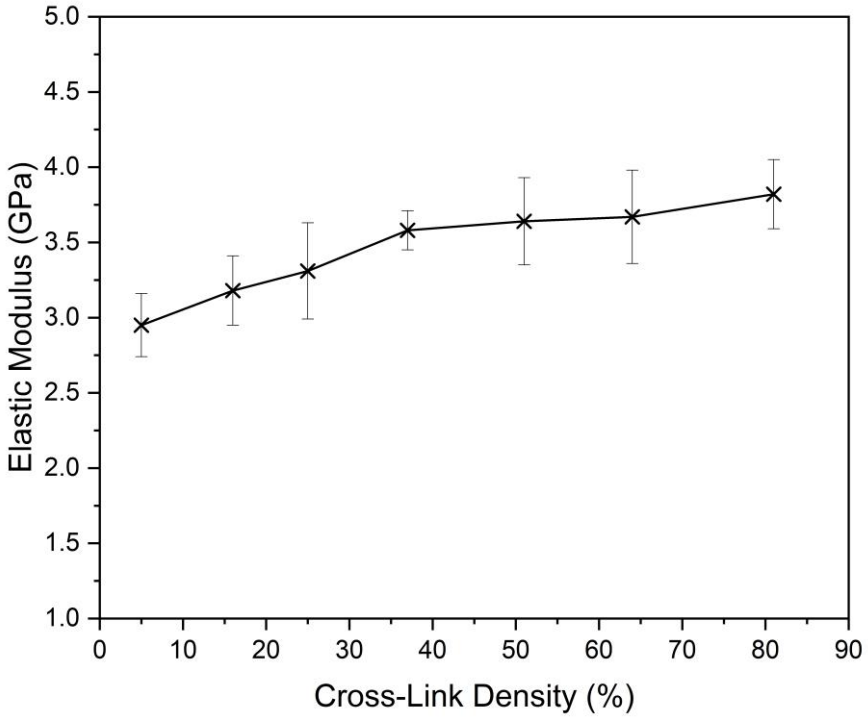

Figure 2-13 *Influence of cross-link density on the elastic modulus.*[86]

2.6.3. Pressure influence on cross-link density and mechanical properties

As evidenced above, it is clear that processing conditions can affect the cross-link density of epoxy resin, which in turn impacts the material properties. A processing condition associated with epoxy resin curing is the applied pressure (commonly used with autoclave-manufactured composites). One hypothesis could be that the applied pressure may consolidate the polymer during cure, resulting in a higher cross-link density with greater material properties.

A study was performed by Nakamae et al.[87] where the influence of pressure on the mechanical properties was studied. Their results showed a change in material properties; however, they found that as pressure was increased, the Young's modulus, tensile strength and elongation at break all reduced. Their results are detailed in **Table 2-2.** The reasoning that the authors gave for the reduction in material properties was that the high cure pressures resulted in insufficient curing. It should also be noted that the pressures used in this study are not representative of typical composite curing pressures, where a maximum of 0.6 MPa is usually applied.[88,89] Although it would be possible to interpolate to 0.6 MPa, a negligible change would be expected. As explained

by Loos and Springer[90], and Li et al.[69], the applied temperature is responsible for the curing process, whereas the role of the applied pressure is to squeeze out excess resin.

Table 2-2 *Influence of cure pressure on material properties.*[87]

Cure Pressure / MPa	Young's modulus / GPa	Tensile Strength / MPa	Elongation at break / %
0.1	2.23	98.4	13.8
500	1.98	40.8	1.97
1000	1.39	18.5	1.45

In another study, Liang et al.[91] investigated the effect of cure pressure on the curing reaction through differential scanning calorimetry, a process which measures the thermal energy absorption of a sample during heating over a temperature range.[92] The study involved analysing epoxy resin cured at 0.1 MPa, 1 MPa and 2 MPa, where the cure kinetics were used in a forming simulation to determine at what laminate thickness the degree of cure is affected by cure pressure. Their results showed that it is only when the laminate is at least 18 mm thick that there is any variation in the time taken to achieve full cure due to variation in cure pressure.

Zapico et al.[93] investigated the application of high cure pressure on the toughness of epoxy resin, as well as other mechanical properties. The samples produced were cured between 0.0 – 1500 MPa, showing no substantial change up to 200 MPa; as described before, this is beyond the typical pressures applied during conventional autoclave processing. Gushurst et al.[94] also investigated the influence of high pressures on the curing behaviour of composite structures, concluding that most composite manufacturing processes involve low pressures (less than 1 MPa) and this has a negligible effect on the composite. However, the authors acknowledge that with recent developments in high pressure resin transfer moulding, pressures can reach up to 12 MPa which will have an influence on the curing reaction. Their results show that by increasing the cure pressure from 0.8 MPa to 8 MPa, the degree of cure increases from 97.4 % to 98.5 %. Their results also showed a similar trend for the glass-transition temperature, which correlates with the degree of cure. Cruz et al.[95] investigated the change in mechanical performance of epoxy resin as the cure pressure was increased from 0.0 MPa to 13.8 MPa. Their results showed no difference in Modulus as the pressure increased.

2.7. Effect on Mechanical Performance

The current literature review so far has shown that porosity is a major manufacturing defect in composites, and this has led to a huge research effort to understand the effect on mechanical properties. As porosity is a matrix-based defect, it has been commonly observed that matrix-dominate properties, such as transverse tensile strength, longitudinal compressive strength, and Interlaminar Shear Strength (ILSS), are predominately affected. This section aims to review the literature surrounding how porosity affects specific properties addressing both unidirectional and woven fibre architectures.

2.7.1. Tensile modulus

It is accepted that porosity has little effect on the longitudinal modulus of unidirectional composites[96] which has been demonstrated experimentally[15,97] and recently through finite element and analytical modelling by Chu et al.[98]. The reason that porosity has little to no effect on the longitudinal modulus is the fibres play a dominant role in the amount of strain due to their high stiffness. Therefore, the reduction in matrix, due to voids, has a minimal effect. On the other hand, in the transverse direction fibre stiffness plays a minor role in the strain response to load, therefore, some researchers claim that voids do affect the transverse modulus. A reduction in transverse modulus has been experimentally shown by numerous researchers[15,97,99] as well as through finite element and analytical modelling.[22,96,98] Conversely, not all researchers agree that porosity affects the transverse modulus.[21,71,100,101] For instance, Liu et al.[71] found for a void content range between 0.5 -3.0 % there was only a minor difference in modulus and Stamopoulos et al.[100] finding no difference between laminates with a similar void content range. This disagreement shows the difficulty in understanding how changes to the microstructure affect the global material properties and why porosity is still subjected to research efforts.

The influence of porosity on the stiffness of woven composites has been investigated mostly through modelling, however, there is a small number of publications that have investigated this topic experimentally. Zhu et al.[102] studied the tensile response to porosity in two differing layups containing woven fabrics. Whilst the porosity ranged from 0.4 % to 8.0 and 9.0 % in the two laminates it was found that only one laminate was sensitive to the increase in porosity. It was determined that it was not due to the

specific layup that caused the sensitivity to porosity but rather the void morphology and that the laminate that was affected by the increase in void content had much larger voids. Similarly, Naganuma et al.[103] found that void morphology played a role in how much the laminate stiffness was affected by porosity. Their results agreed with Zhu et al.[102] such that the modulus was more affected when the voids were larger and irregular shaped, rather than smaller voids. Due to the geometrical complexity of woven structures analytical models are considered difficult to generate[104], therefore, most recent models use FEA and often use third-party software such as '*WiseTex*'[105] or '*TexGen*'[106] to generate the geometry, where examples can be seen in **Figure 2-14**. With this approach, often voids are modelled as elements, such as the work done by Van Den Broucke et al.[107] where WiseTex was used to create the geometry and the voids were modelled as tetrahedral elements. Whilst the void morphology was simplified, their results showed a decrease in modulus as the void volume fraction increased. An 8-harness satin weave was modelled by Choudhry et al.[104] however, instead of explicitly modelling the void geometry the matrix properties were reduced by the percentage of the void fraction to give a set of 'effective' matrix properties and their results were within 1% of experimental data.

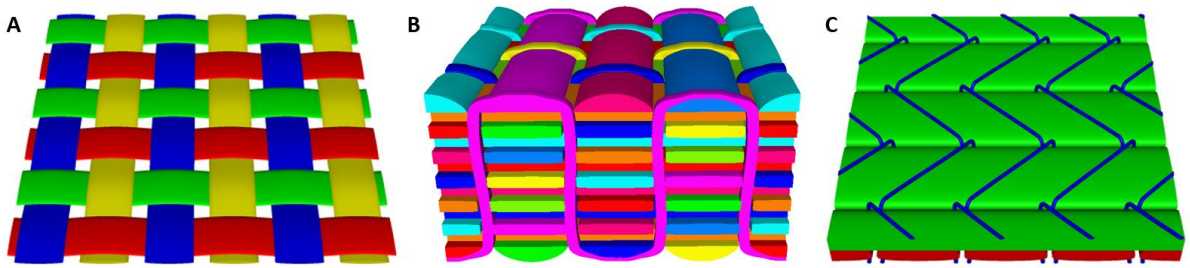

Figure 2-14 *Woven geometry created using TexGen, (**A**) 2D weave, (**B**) 3D weave and (**C**) non-crimp fabric.*[108]

2.7.2. Tensile strength

For unidirectional composites, the tensile strength in the fibre direction is known to not be affected by porosity due to the load being taken up by the fibres, which are particularly strong in tensile loading. As the matrix does not play a load-bearing role, any porosity present has no effect. In contrast, however, in the transverse direction, where the matrix does have a load-bearing role, porosity has often been shown to affect the transverse strength. An early experimental study by Olivier et al.[15] showed that transverse strength is very sensitive to porosity, where the strength can be reduced by

up to 30 % for a 10 % increase in void content. A more recent study by Tserpes et al.[109] utilises μ-CT scan data to characterise how differences in porosity such as pore volume, shape, and overall void content affect the transverse strength. The μ-CT scan data was used to build representative FE models of each of the laminates. Their results found that as the void content increased from 1.56 % to 3.43 % the transverse strength reduced by approximately 15 % as illustrated in **Figure 2-15**. In a similar study, Stamopoulos et al.[100] used μ-CT to measure the porosity of four composite laminates with void contents ranging from 0.82 % to 3.43 % and found that the transverse strength reduced by a maximum of 14.7 %. They found that there is a non-linear trend between the overall void content and strength of the laminate which they determined was indicative of the morphology of the voids. By studying the pore volumes of each laminate, it was found that for the laminates with lower overall porosity, there is a higher count of smaller-sized voids that are spherical/elliptical. This is in contrast to the higher void content laminates, where the voids are much more elongated. A histogram showing the variation in pore volume is illustrated in **Figure 2-16**

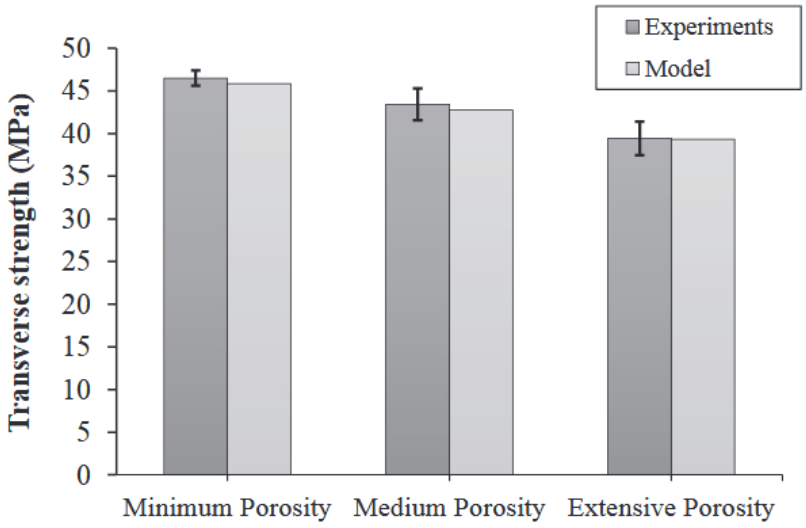

Figure 2-15 *Influence of void content on the transverse strength for laminates with three different porosity values, including model correlation.*[109]

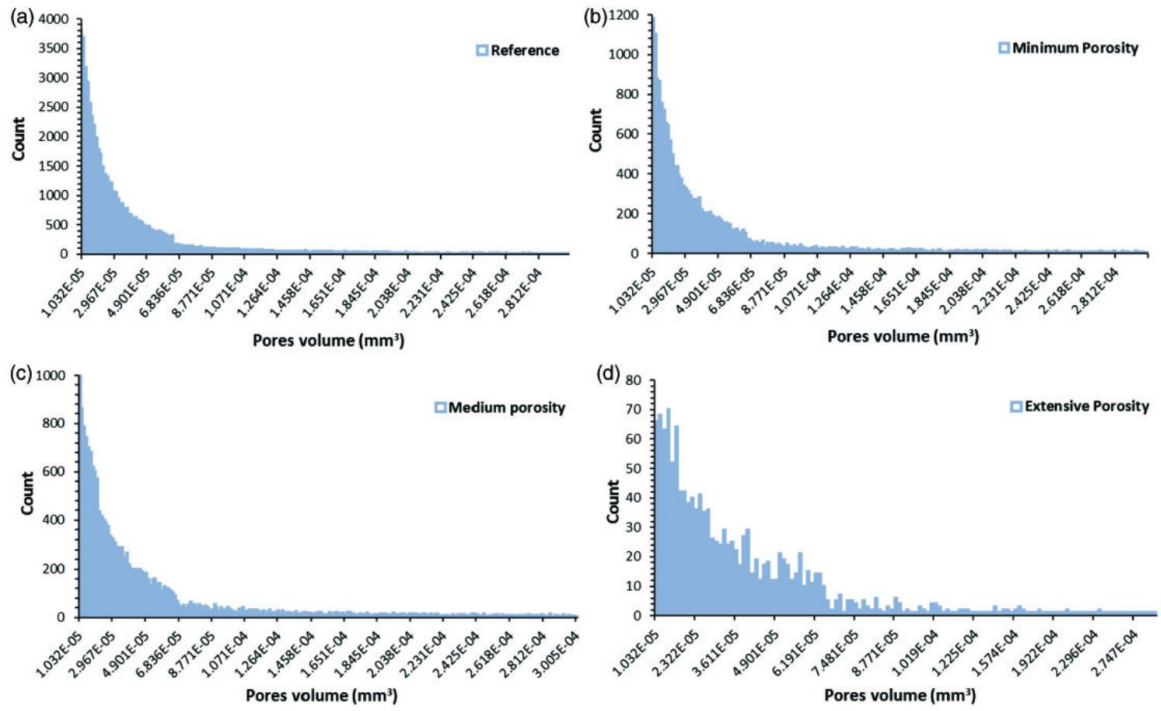

Figure 2-16 *pore volume histogram, revealed through μ-scanning, for (a) reference, (b) minimum porosity, (c) medium porosity and (D) extensive porosity.*[100]

Voids also affect the tensile strength of woven composites, as demonstrated by Zhu et al.[102] where they found a 2 – 2.5 % reduction in tensile strength for an increase in void content from 0.4 % to 8.0 – 9.0 % respectively (based on two different laminates). Likewise, Zhang et al.[110] found a 2.36 % reduction in tensile strength for an increase in void content from 0.33 % to 1.50 %. As was the case for unidirectional composites, the void morphology has also been shown to be important for woven fibre architectures. Naganuma et al.[103] showed that specific 'finite' voids had little effect on the tensile strength, however, larger irregular voids that spanned across fibre tows did affect the tensile strength. Whilst voids have a clear effect on the tensile strength of woven composites their impact is not as great as that seen in transverse unidirectional composites. This is most likely due to the natural architecture of woven fabrics; fibres travel in both the warp and weft directions (analogous to longitudinal and transverse directions). As found from the published information on unidirectional composites, the effect that porosity has on the tensile strength is highly linked to the fibre direction. Therefore, as the fibres travel in both directions in woven fabrics the effect of voids, whilst present, is minimised. In a recent study, Pineda et al.[111] conducted a numerical multiscale failure analysis of a woven fabric containing voids. The model is separated into two levels; first, there are two models which analyse the individual tows and voids separately. This information is then used in the top-level which is a Representative

Unit Cell (RUC) comprising of a '*block*' based system to identify warp, weft and binder tows as shown in **Figure 2-17**. The model predicted that when the void content is increased (from 0.4 % to 4.0 %) the yield point and ultimate strength of the RUC reduced by 10 and 11 %, respectively.

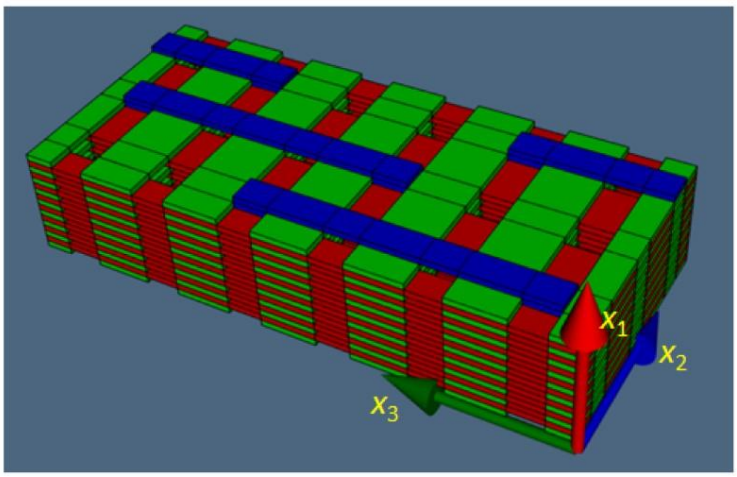

Figure 2-17 *Geometry used to create the RUC where the warp (red, x3), weft (green, x2) and binder (blue, x1 through thickness) tows are shown.*[111]

2.7.3. Compressive modulus

The effect that voids have on the compressive modulus is not an area that has been widely published and of the related articles available there is not a consensus. For instance, Hernández et al.[112] reported that the compressive modulus, for a quasi-isotropic laminate, was unaffected as porosity increased. However, a study by Cinquin et al.[24] used additives placed between specific plies in a quasi-isotropic laminate to artificially create porosity. They successfully demonstrated a linear reduction in modulus such that for every percent increase in void content the stiffness reduced by 0.56 GPa. Kosmann et al.[25] were also able to demonstrate that by increasing porosity the modulus reduces, however, their explanation was not due to a reduction in area due to voids, but due to early micro-cracks forming and local fibre kinking at void locations as illustrated in **Figure 2-18**.

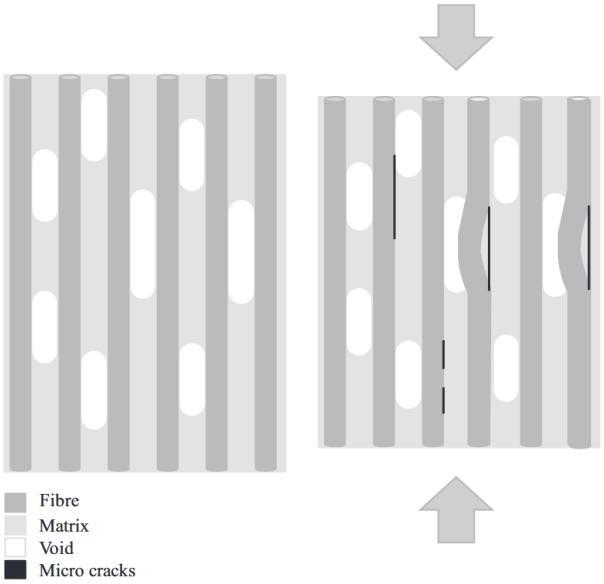

Figure 2-18 *Schematic of the formation of micro cracks and local fibre kinking in the vicinity of voids.*[25]

2.7.4. Compressive strength

The compressive strength, in the longitudinal direction, of a composite is affected by porosity only once the void volume fraction is above a certain amount.[113] For instance, in the compression testing that Kosmann et al.[25] conducted they found that the compressive strength was unaffected in their testing, which included samples up to 4.5 %. Springer et al.[113] found that samples containing a void content past 5.0 % were subsequently affected. In-situ SEM analysis during longitudinal compression testing by Hapke et al.[26] found that specimens, with a notch for controlling damage location, failed through kink-bands and that depending on the location of large discrete voids determined if there was a subsequent effect. For instance, if the kink band occurred at the tip of a void, this acts as a stress concentration magnifying the effect, however, if the kink band path is located at the centre of a void, the void stops further propagation occurring. This happens due to the fibres bending into the void and the other side then supports the failure, as shown in **Figure 2-19**. This helps explain why the longitudinal compressive strength is only affected at very high void contents as it is only when large voids are present. The role of the matrix in longitudinal compression is to support fibres and voids would only be a cause for concern if they were sufficiently large enough to not support the fibres causing local bending and kinking.

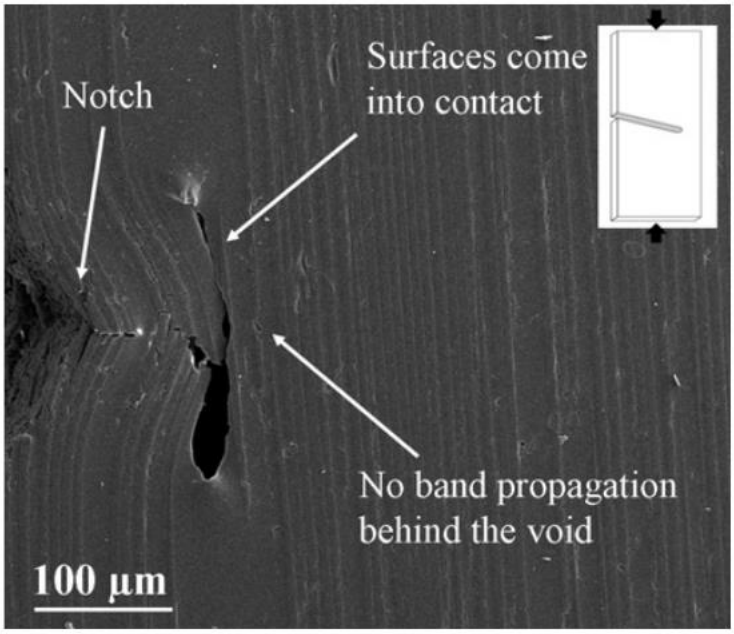

Figure 2-19 *Kink band propagation hindered by a void.*[26]

The transverse compressive strength is sensitive to voids due to the matrix taking a load-bearing role.[114,115] For this reason, the majority of research efforts have gone into developing models to predict their effect, rather than conducting experimental studies.[30,114] One such numerical study was performed by Li et al.[116] who developed a 2D microscale model which demonstrated a reduction of 12.1 % in the transverse compressive strength for a 2.0 % void content, compared to a void-free unit cell. Using a similar model, Vajari et al.[114] found that there is a rapid decrease in transverse compressive strength when the void content is increased from 0 – 5 %. The compressive load response in that study can be seen in **Figure 2-20**.

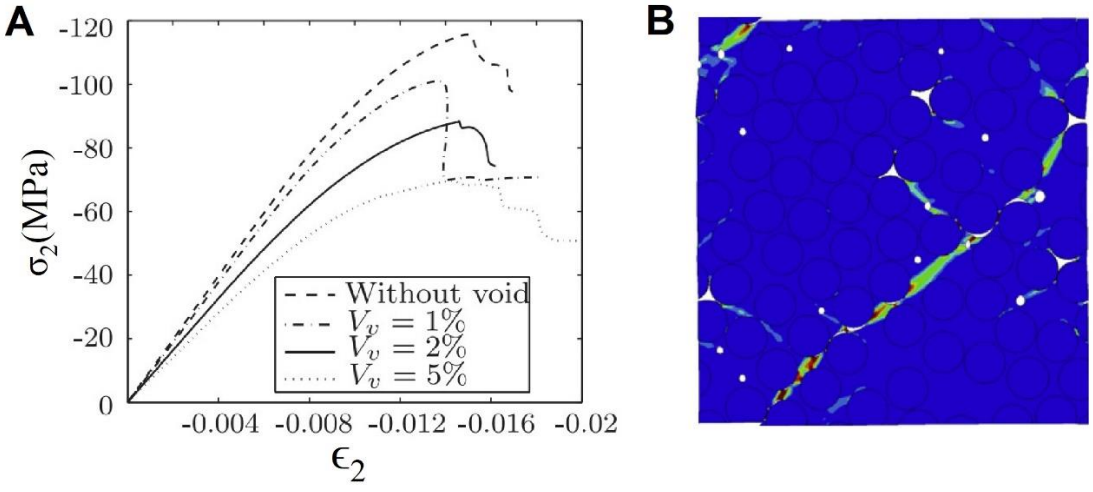

Figure 2-20 *Transverse compressive load response to porosity. (A) shows the stress-strain graph and (B) shows a colour map of the load response.*[114]

2.7.5. Flexural properties

The flexural modulus is calculated using a 3-point bend, following a standard such as ASTM D790[117], test using specimens with a high span-to-depth ratio (typically 16:1) and not to be confused with the short beam test to calculate interlaminar properties. Published literature has shown that the flexural modulus is negatively affected, to various degrees, by an increase in void content.[71,100,118,119] For instance, Hagstrand et al.[118] found that for a 1 % increase in void content, the flexural modulus reduces by 1.4 %, however, Liu et al.[71] found in their testing the flexural modulus is a lot more sensitive (approximately 6.7 % reduction in flexural modulus per 1.0 % increase in void content). The difference in magnitude is explained by Olivier et al.[15] who suggest that the void morphology has a significant influence on results and that if for the same void content there are fewer voids but larger, then this will have a bigger impact on reducing the flexural modulus.

The flexural strength is also calculated from the same test method and the published literature agrees that the strength is sensitive to increasing porosity. For instance, Liu et al.[71] found a linear trend where when the void content increased by 2.5 % the flexural strength decreased by approximately 22.5 %. Similarly, Stamopoulos et al.[100] found a 17.38 % reduction in flexural strength for an increase in void content from 1.56 % to 3.43 %. Chambers et al.[120] also found that the flexural strength reduced by 22 % for every 1 % increase in void content. Interestingly, Hagstrand et al.[118] found that the flexural strength in their testing only reduced by 1.5 % for every 1 % increase in void content. They considered that this was lower than other reported literature, however, suggested that as the load was predominately taken by the fibres then the increase in void content would only have a small effect on the overall reduction in strength. Hayashi et al.[119] conducted an interesting study testing cross-ply layups and chopped fibre tapes. In both cases the flexural strength was notably affected by the increase in porosity, however, the chopped fibre tapes were found to be more sensitive. This was explained by the cross-ply layup, again, having more fibres in the loading direction which are typically less affected by voids.

2.7.6. Short beam strength

The short beam strength, otherwise known as Interlaminar Shear Strength (ILSS), is a measure of the inter-ply bond/adhesion strength (assuming failure occurs through

interlaminar shear) and is tested following a test standard such as ASTM D2344.[121] The adhesion between plies is a matrix dominate property and therefore is likely to be susceptible to voids. For this reason, there have been many studies investigating how porosity affects the short beam strength in unidirectional composites.[30,72,101,122–125] For instance, Olivier et al. studied the ILSS for laminates with porosity ranging up to 6.8 % and found a reduction in the ILSS of up to 35 %. Liu et al.[71] studied how porosity affects many mechanical properties and found that the ILSS was the most affected, where it had reduced by over 25 % for a 2.5 % increase in void content. Stamopoulos et al.[100] also found that the ILSS was the most affected property due to an increase in void content when compared to tensile and 3-point bend tests.

Similar to unidirectional composites, the ILSS of woven laminates are very sensitive to voids and have been subjected to many studies. For instance, Di Landro et al.[126] found that the ILSS reduced by approximately 25 % for an increase in 6.6 % void content. Similarly, Bureau and Denault[127] found a linear relationship between increasing void content and a reduction in ILSS. They found that for an 8.5 % increase in void content, the ILSS reduced by 20 MPa, equating to a 48 % reduction. Costa et al.[128] correlated void content between 0.0 – 6.0 % with ultrasonic attenuation and subsequently showed that as the ultrasonic attenuation increased the ILSS reduced. The influence of void morphology on ILSS has also been studied, where Zhu et al.[102] found that for a void content range of 0.0 – 8.0 % when voids have a larger aspect ratio the ILSS of the laminates are more sensitive. Goodwin et al.[129] compared a plain weave to a 5-harness satin weave and found that the laminate manufactured using a 5-harness weave pattern was more susceptible to increasing void content. However, the reason was explained by the void morphology; as illustrated in **Figure 2-21** whilst the plain weave laminate had symmetrical and elliptical shaped voids the 5-harness weave had more asymmetric voids with sharper stress concentrations.

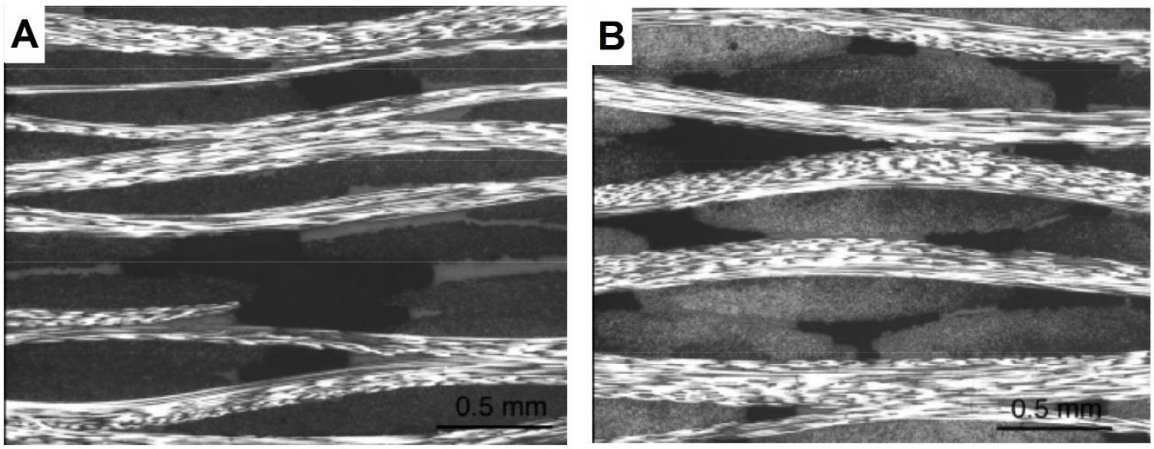

Figure 2-21 *Difference in void morphology between the (A) plain weave and (B) 5-harness weave laminates.*[129]

2.7.7. Fatigue life

The fatigue life of a composite structure is extremely important for real-world applications and understanding how a change in porosity (whether its void content or void morphology) affects the fatigue life is crucial.[30] In published literature at first it appears that there are conflicting arguments as to whether porosity affects the fatigue life of a composite. For instance, Lambert et al.[60] conducted an extensive study investigating various porosity parameters and claimed that the overall void content did not affect the fatigue life. Similarly, Protz et al.[130] found that there was almost no implications on the fatigue life when the void content is increased. However, a study from Maragoni et al.[131] showed that when microvoids were present in a composite, they had no impact on the damage initiation or evolution. They subsequently studied how both the void content and average void diameter affect fatigue life. Their results showed that the life to first crack initialisation can be substantially reduced as both the void content and void size are increased as well as a reduction in life to 5 % stiffness drop. Another study by Chambers et al.[120] found that when the void content is below 2 % then the fatigue life is not affected, however, over 2 % there is a negative effect on the fatigue performance. This explains why the studies by Lambert et al.[60] and Protz et al.[130] found no correlation between void content and fatigue life because, as illustrated in **Figure 2-22** from the figures in the respective publications, the voids in their studies are microvoids rather than larger discrete voids.

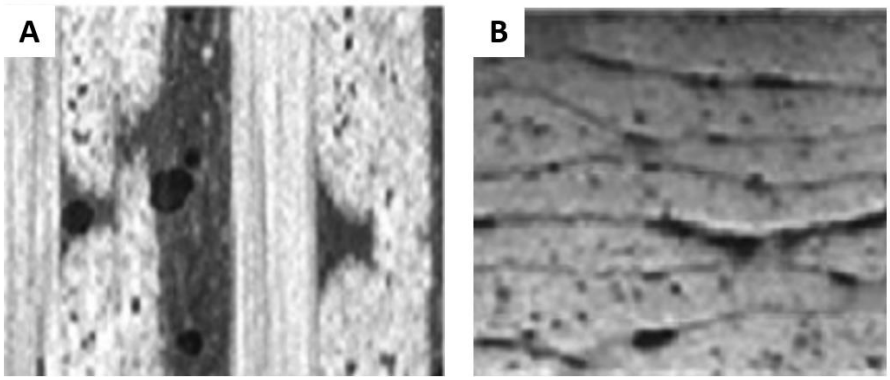

Figure 2-22 *Microscopy of samples from both Lambert et al.[60] (**A**) and Protz et al.[130] (**B**) studies showing that the porosity is made up of microvoids.*

Other fatigue-related studies have included the works of Gehrig et al.[132] who showed that the fatigue life of both tension-tension and compression-compression are affected by voids and Schmidt et al.[133] showed that voids result in early initiation of delamination which results in catastrophic failure. Sisodia et al.[115] compared two laminates which had 0.8 % and 3.0 % void content respectively and found that there was a significantly larger crack density in the higher void content laminate which subsequently resulted in earlier failure. Depending on the porosity that is generated within the composite, the fatigue life can be significantly affected.

2.7.8. Concluding remarks on the implication of porosity on mechanical properties

Porosity is a major defect that can significantly affect the mechanical properties of a laminate.[30,116,128,134] If the effect on mechanical properties due to porosity in a structure is not understood, then serious implications can occur. The general trend is that there is a negative impact across all mechanical properties when the overall void content is increased. However, exceptions to this are for when the load is predominately taken up by the fibres, particularly in tension. Another key observation is that the most common porosity characteristic to evaluate the effect on structural performance is void content, however, it is becoming increasingly observed that this is only one parameter and other parameters, such as the shape and size or spatial distribution, must also be accounted for. There is a negative impact that voids have on the mechanical performance of a composite. Seeing that it is nearly impossible to produce a void-free composite, there must be an understanding of how the generated porosity affects relevant material properties for a given design.

2.8. Modelling Porosity

Porosity is a major defect that can arise during the manufacturing process. Two factors must be considered to ensure that the generated porosity does not cause unexpected behaviour. First, the generation of porosity must be characterised for a given manufacturing process and second understanding how that specific porosity affects the behaviour of a structure. Porosity has been studied experimentally for many years and whilst general trends and rules of thumb can be used (such as adequate degassing of resin, high cure pressures and void content thresholds), it is still difficult to accurately predict the effect of porosity without testing. Whilst physical testing gives empirical data that can be used to evaluate various parameters, it is often time-consuming and expensive. Physical testing is also often limited to flat coupon specimens which may or may not be representative of the final structure. With the recent advances in computational power and the ability to carry out extensive simulations in relatively quick time frames, there has been a large push towards developing computational simulations.[135] The simulations that have been developed so far not only investigate the effect of porosity but also study the generation. This section highlights the computational simulation processes that have been developed which relate to porosity.

2.8.1. Void formation

Modelling the formation of voids is closely linked with how the resin flows during cure. For this reason, many of the simulations are based on Darcy's Law, Equation (2-12)[63], where v is the global resin velocity, $K(\emptyset)$ is the macroscopic permeability of the preform, μ is the resin viscosity and $\frac{dP}{dn}$ is the pressure gradient at the flow front.

$$v = -\frac{K(\emptyset)}{\mu}\frac{dP}{dn} \tag{2-12}$$

For liquid composite moulding, as described in Section 2.4.1, the type of void generated is determined by the velocity of the flow front. This is due to the difference in the permeability within the tows and the channels between them. In a study which set the foundation for void process modelling using Darcy's Law, Kang et al.[63] proposed two analytical models dependent on the flow characteristic to determine the void content. These models were a function of tow and channel geometry, resin viscosity, capillary pressure and global pressure gradient. These analytical models

were developed by Park et al.[13] to also account for complex fibre architecture, such as woven fabrics by incorporating them into FEM code. Void compression as the resin pressure changes was also accounted for using the ideal gas law with the void fraction being updated as the resin pressure changed. For efficiency reasons, the model was first used to calculate the void content fractions within the tows and channels for a simple rectilinear mould for constant injection and air vent pressures. This information was then used to predict the total void content (summation of both types of voids) of an automotive front panel manufactured through RTM. The resin flow and consequent void content can be seen in **Figure 2-23**.

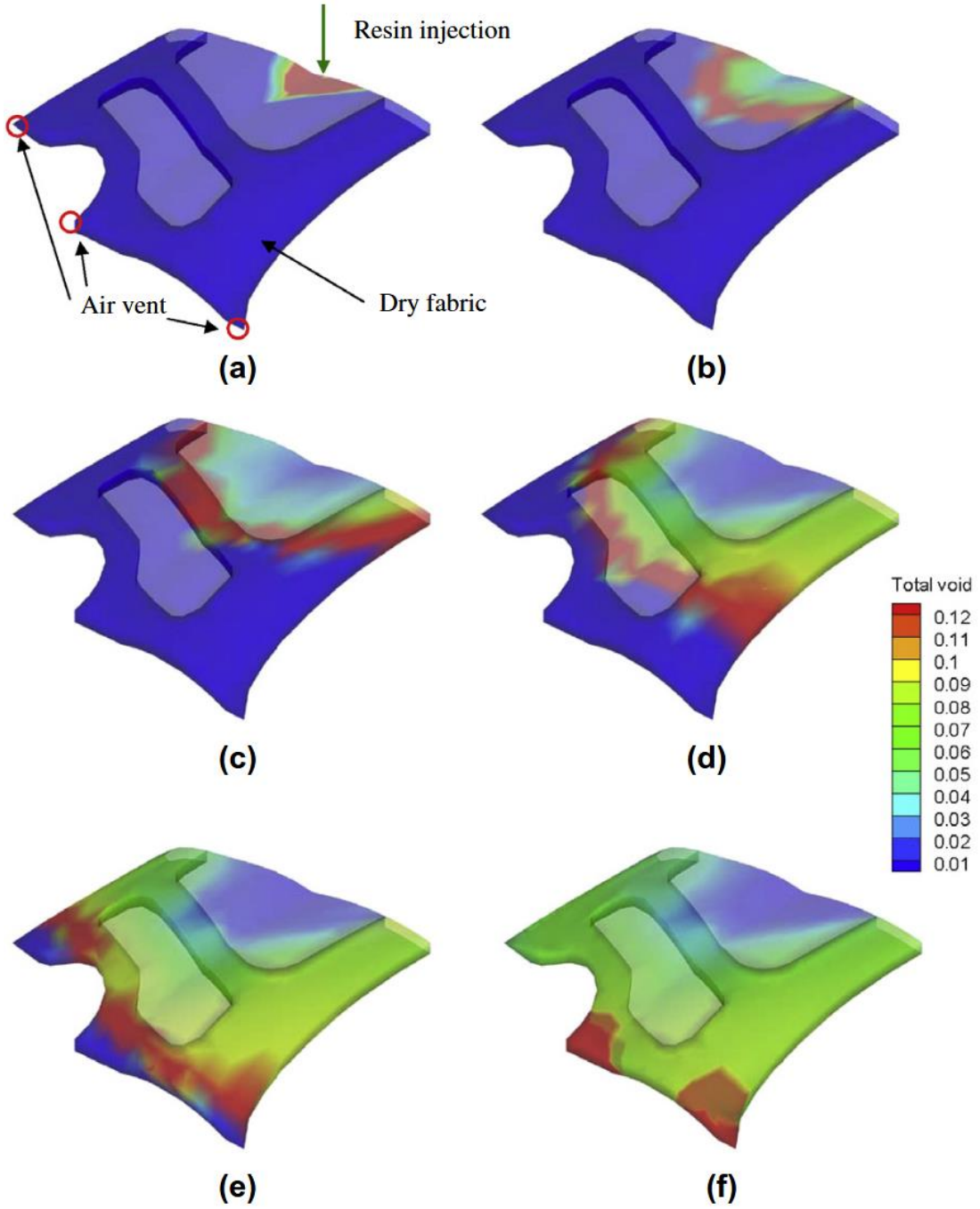

Figure 2-23 *Void content at percentage time to complete infusion (**a**) 0.003, (**b**) 0.032, (**c**) 0.163, (**d**) 0.476, (**e**) 0.849 and (**f**) 0.999.*[13]

For prepreg materials, fewer publications predict the void generation and evolution. This is likely due to voids being more prevalent in LCM than in prepreg materials. However, in the available published works, there is agreement that the voids in the final structure are present at the start as microcavities, most likely due to mechanical entrapment of air or gasses resulting from moisture or volatile reactions. For this reason, void generation models for prepreg materials work based on a single bubble

surrounded by liquid.[136,137] Ledru et al.[138] uses this assumption, as shown in **Figure 2-24**, to derive a nonlinear differential equation, which considers the pressure difference between the autoclave and within the void, the temperature of the gas within the void and the surrounding resin viscosity. The analysis is solved using Matlabs RK4 implicit solver to find how the void radius changes during the cure.

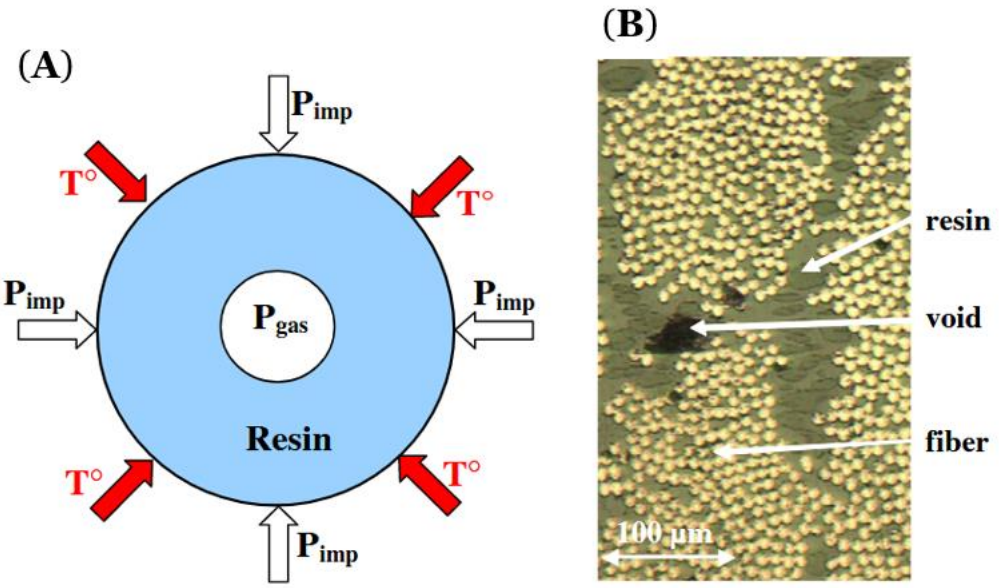

Figure 2-24 *The modelling approach uses the assumption of a void surrounded by matrix. (**A**) Schematic of this assumption and (**B**) micrograph of a typical void being represented.*[138]

2.8.2. Impact on mechanical properties

2.8.2.1. Elastic modelling

Before discussing the methods of modelling how voids affect the stiffness of a composite, it should be considered how the modulus of void-free composites are modelled. This is typically achieved using analytical models, for instance, possibly the most well-known and often used approach is the Rule of Mixtures (RoM), which is a simplified approach which 'stacks' the constituents in the loading direction and assumes that there is equal strain in both the fibres and matrix. This is a two-part model which determines either the longitudinal (Voigt model) or transverse (Reuss model) modulus, using equations (2-13) and (2-14). Where E_{11} and E_{22} are the elastic moduli for the longitudinal and transverse direction of the composite, E_{11f} and E_{22f}, are longitudinal and transverse elastic modulus of the fibre, E_m is the elastic modulus of the matrix, V_f is the fibre volume fraction. The shear modulus can also be calculated

using equation (2-15) where G_{12}, G_{12f} and G_m are the shear modulus for the composite, fibre and matrix respectively.[139]

$$E_{11} = E_{11f}V_f + E_mV_m = E_{11f}V_f + E_m(1 - V_f) \tag{2-13}$$

$$\frac{1}{E_{22}} = \frac{V_f}{E_{22f}} + \frac{1 - V_f}{E_m} \tag{2-14}$$

$$\frac{1}{G_{12}} = \frac{V_f}{G_{12f}} + \frac{1 - V_f}{G_m} \tag{2-15}$$

It was found that the equations for transverse and shear moduli were inaccurate, which was determined to be due to the geometry of fibre packing. The model assumes that there is uniform stress, however, due to the distribution of discrete fibres there are stress gradients resulting in a deviation from the model's assumption. This led to a refined model based on splitting the RUC into subsections forming a square fibre-matrix arrangement, as shown in **Figure 2-25**. The developed the transverse and shear modulus equations as presented in equations (2-16) and (2-17).[140]

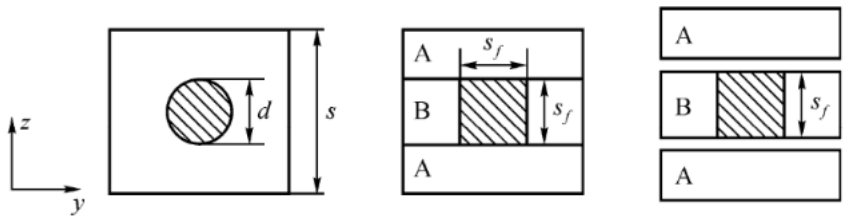

Figure 2-25 *Subsection arrangement which forms the basis of the developed model.*[140]

$$E_{22} = \frac{E_m}{1 - \sqrt{V_f\left(1 - \frac{E_m}{E_{22f}}\right)}} \tag{2-16}$$

$$G_{ij} = \frac{G_m}{1 - \sqrt{V_f\left(1 - \frac{G_m}{G_{ijf}}\right)}}, i, j = 1, 2 \; or \; 2, 3 \tag{2-17}$$

From reviewing the analytical works, an observation can be made that the models are based on the geometry of the RUC. For an analytical model, this limits the geometry to being simplistic, i.e. a single fibre surrounded by matrix. Moving to computational models solved using FEA means that more complex geometry can be generated, as well as accounting for voids. An example of this is the work published by Nikopour[22] whereby a 2D planar model was generated with a uniform array of fibres surrounded by matrix. To simulate voids, circular sections of the matrix between the fibres at uniform distances were removed, as shown in **Figure 2-26** (**A**) and (**B**). For each model, a finite amount of strain is applied to the unit cell in the transverse and shear directions to measure the respective modulus. The transverse and shear stress distribution for models with and without voids can be seen in **Figure 2-26** (**C**) – (**F**). The results of the simulations showed that whilst all models were degraded when voids were introduced, the bulk modulus was most affected. The results were compared to analytical models proposed by Hashin and Rosen[141] with very good correlation.

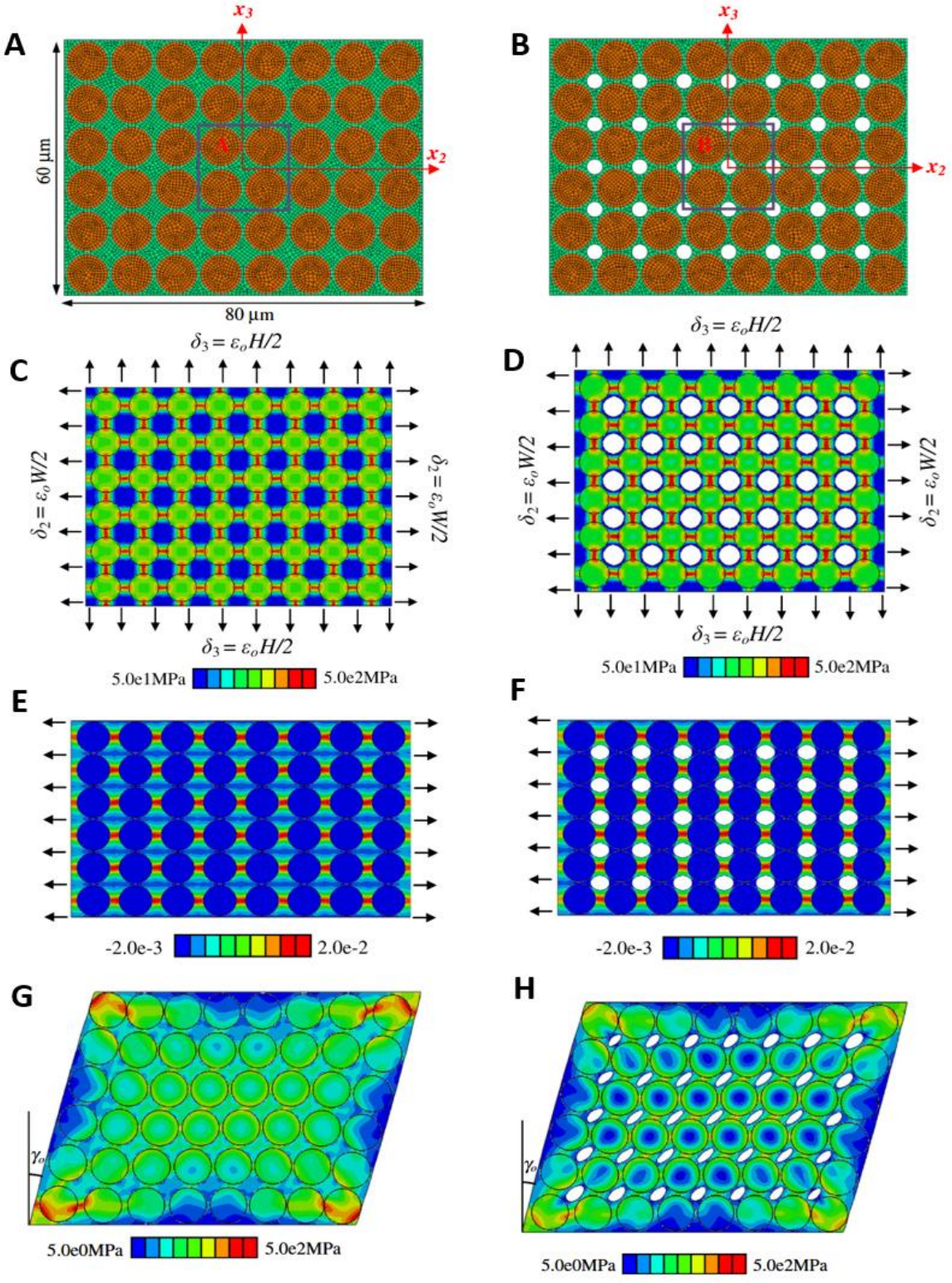

Figure 2-26 *Representation of a Planar model with (**A**) uniform fibre surrounded by matrix and (**B**) void array surrounded by matrix. (**C**) and (**D**) show the stress distributions for a bulk modulus analysis with and without voids. (**E**) and (**F**) show the respective stress distribution under transverse load without and with voids, and (**G**) and (**H**) show the respective stress distribution under shear load without and with voids.*[22]

To account for a non-uniform array of fibres and voids, Dong[96] also modelled a 2D RUC and randomly distributed both the fibres and voids throughout it, as illustrated in **Figure 2-27** (**A**). A load of 1 MPa was introduced on one side of the RUC and the resultant displacements were used to measure the modulus. The stress distribution is illustrated in **Figure 2-27** (**B**). The modelling approach was used to compare how various fibre volume fractions at different void contents affected the modulus. Their results showed that higher fibre volume fractions resulted in stiffer models and in all cases every 1.0 % increase in void content the transverse modulus reduced by approximately 1.5 %. The results also showed that a 2.0 % void content is the critical value after which the transverse strength is then degraded. In this case, however, the results showed that the lower the fibre volume fraction the more affected the strength was for a given void content.

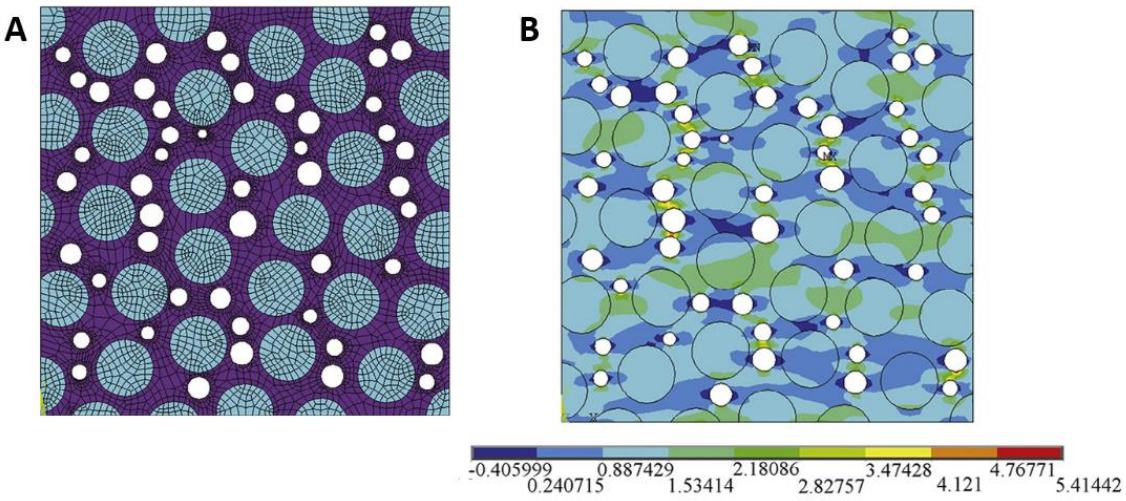

Figure 2-27 *RUC using randomly distributed fibres and voids, (**A**) shows the distribution and (**B**) shows the stress distribution after induced loading.*[96]

A different approach is to use a 'short length' 3D model which essentially gives the planer model a finite thickness in the fibre direction. This approach was utilized by Carrera et al.[27] who modelled voids by randomly selecting a specific percentage of integration points which relate to the void content and degrading the stiffness to near zero. This has the effect of reducing the stiffness of the domains that each of the integration points refers to. The short-length RUC and simulated voids can be seen in **Figure 2-28**. An initial model containing no voids is first used to generate a baseline to reference against, and then a second model containing the required voids is used. As the location of the voids was randomly selected, the second model was repeated 100 times with different void distributions for statistical evaluation. The results of the

models showed whilst void content affected transverse modulus, a minimal effect on stiffness was found when void distributions were varied.

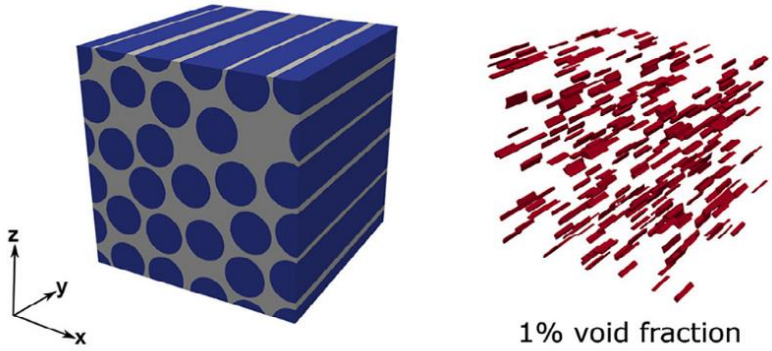

Figure 2-28 *Illustration of the randomly inserted voids into a 3D model.*[27]

A similar short-length model was implemented by Chu et al.[98], however, with the distinct difference that instead of selecting voids using a randomiser, the voids are explicitly modelled through geometry, as illustrated in **Figure 2-29**, with the results shown in **Figure 2-30**. This has the benefit that there is complete freedom in how the geometry of the voids are modelled including the location and distributions. However, such a defined model brings several disadvantages. Firstly, the model setup and ability to adapt and adjust various parameters (such as void content and void dispersion) is extremely limited and would require extensive user processing to make various changes. Secondly, due to the size of the voids, the element count will be significantly high, with the paper recognising that some of the models have over 3 million elements. Whilst this is a high-fidelity modelling approach, the setup and computational time are expensive and are not practical. This modelling approach was used to study the effect of increasing both the void content and fibre volume fraction on the stiffness. The results showed that whilst increasing the void content reduced the transverse modulus, increasing the fibre volume fraction did not affect the results. This is interesting as whilst the reduction of the modulus due to increasing void content is in line with previous studies, the results of varying the fibre volume fraction are not.

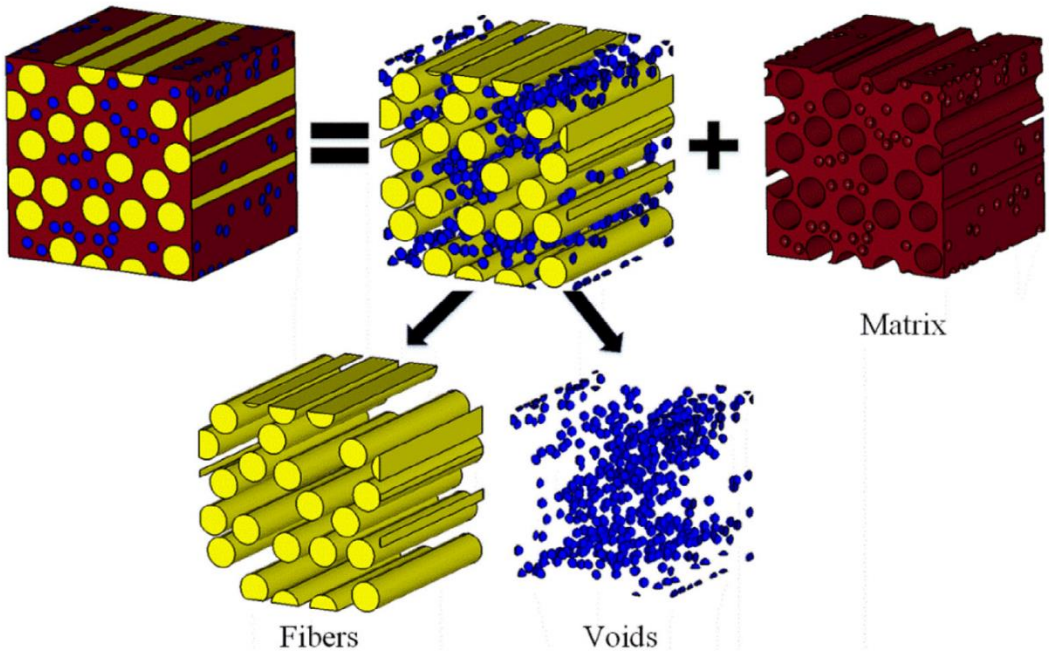

Figure 2-29 *Geometry used to create the RUC containing voids.*[98]

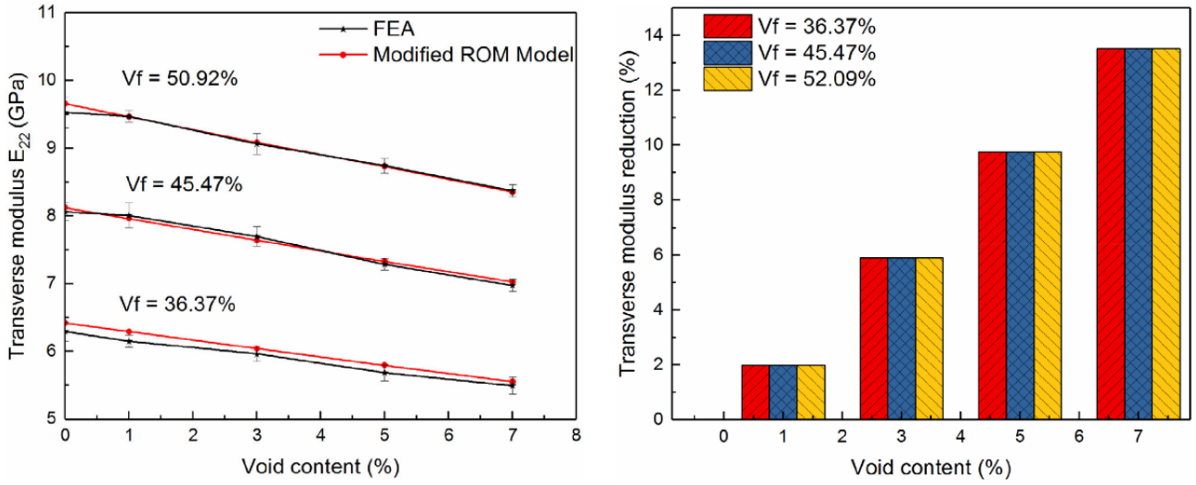

Figure 2-30 *Result of increasing the void content at three different fibre volume fraction.*[98]

The final modelling approach to predict the elastic properties of unidirectional composites is segregating the model into two distinct stages. The first stage predicts the effective/reduced stiffness of the matrix with voids in and the second stage uses the calculated effective stiffness in a typical RUC, i.e. one without voids. One of the most widely cited papers is the work of Huang and Talrega[40] who used this approach by modelling a single void surrounded by matrix using FEA. The model was used to predict how the stiffness of the matrix degraded with different void geometry and fraction. The effective matrix stiffness was subsequently used in an analytical RUC to

show that as porosity increases the composite stiffness significantly reduces in the transverse direction and less so in the longitudinal.

Selmi[142] also followed a two-stage approach to understand how voids affect the stiffness of a composite. In their work, rather than using FEA to calculate the effective stiffness of the matrix containing voids, the Mori-Tanaka homogenization[143] process was used. This process calculates the average stress state of a material containing inclusions (i.e., voids). This approach functions by placing the inclusion in a stress field and considers the contributions of both the far-field stress state of the material and the local stress fluctuations around the inclusion. The effective stiffness was subsequently used in a RUC through modelling using FEA was able to be used to predict the transverse and shear moduli.

Currently, only elastic modelling approaches for unidirectional fibre architecture have been discussed. The modelling perspective on more complex composites, such as woven or braided, is that the geometry is often split into intra-tow and inter-tow. This means that there are typically two distinct models used, first for the intra-tow geometry a simple continuous fibre unit cell, similar to that of the RUC of unidirectional composites, is used to provide tow properties. Secondly, a geometrically accurate unit cell for the given fibre architecture is then modelled. A schematic of this approach is illustrated in **Figure 2-31**[144] where, for three different fibre architectures, the geometry is shown how it can be split into the two distinct models.

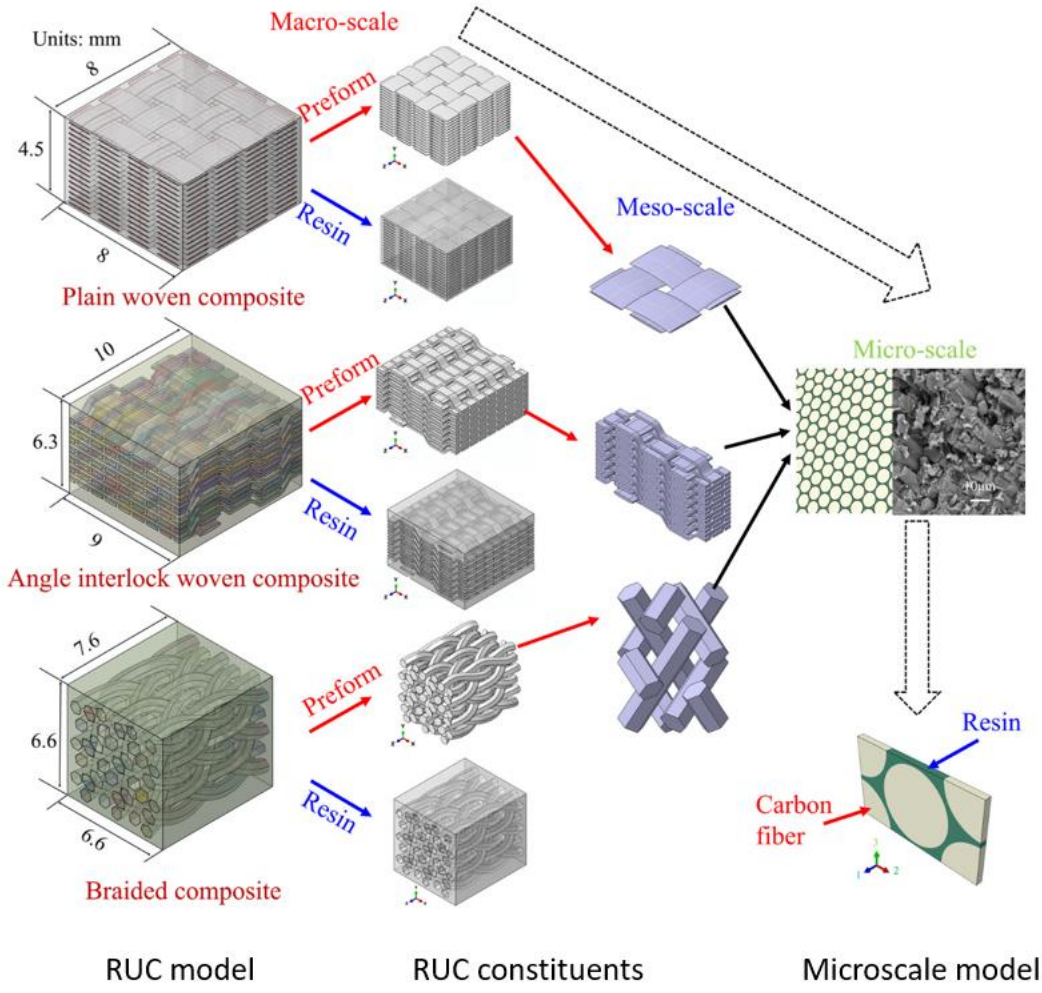

Figure 2-31 *Schematic of how complex fibre architecture is separated into distinct stages for modelling purposes.*[144]

This approach was implemented by Huang and Gong[145] by using a simple uniform fibre array for the microscale model and modelled a woven composite by simplifying the warp, weft and binder tows to rectangular sections. Voids were modelled by randomly selecting matrix elements within both models, as illustrated in **Figure 2-32**, and degrading the stiffness to near zero.

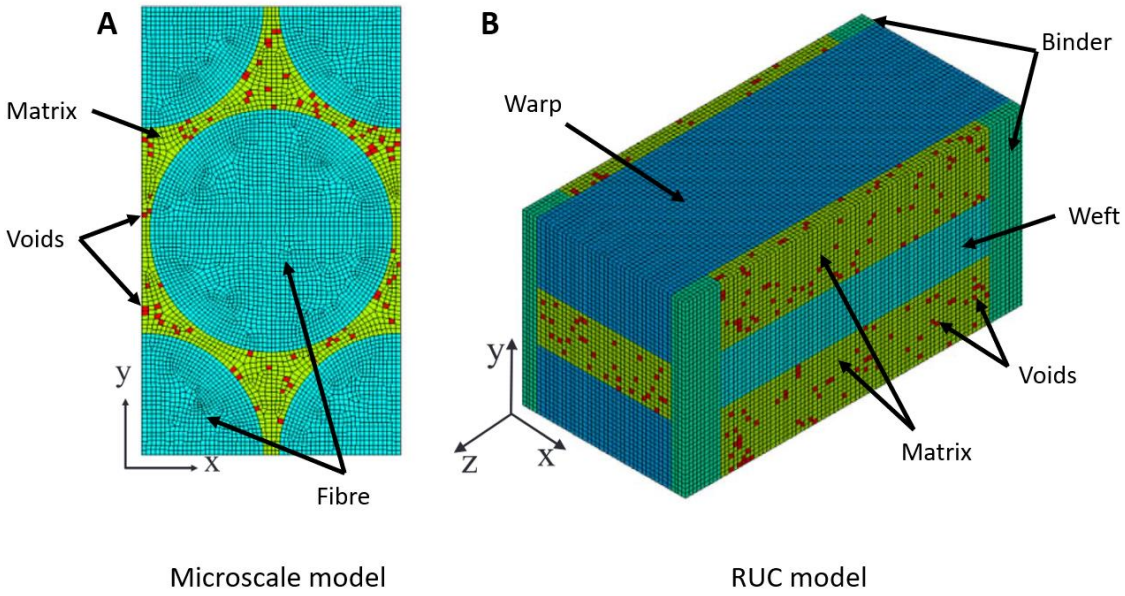

Figure 2-32 *Example of the defined regions of the microscale model and RUC model proposed by Huang and Gong.*[145]

To account for more accurate geometry, there have been releases of specialist software for complex fibre architecture to be modelled in more detail. For instance, Gong et al.[146] used TexGen[106] to accurately generate the woven geometry which was subsequently discretised into a voxel mesh, as illustrated in **Figure 2-33**. Voids were generated in the same approach whereby matrix elements were randomly selected. Similar approaches have also been carried out by Van Den Brouckle et al.[107], Liu et al.[144] and Wang[147] for woven composites, and by Xu and Qian[148] and Liu et al.[144] for braided composites where in all cases the results showed a reduction in mechanical performance.

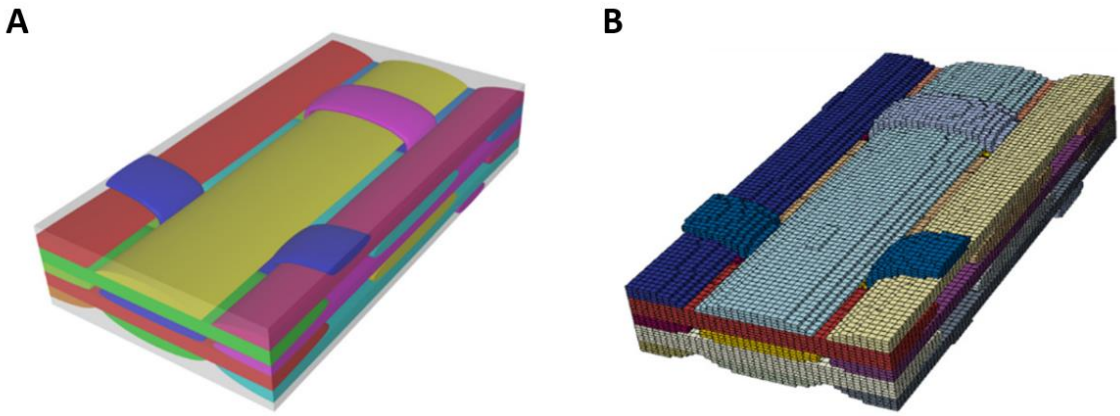

Figure 2-33 *Accurate woven geometry created using TexGen (A) and discretised into a voxel mesh for modelling (B).*[146]

2.8.2.2. Strength modelling

Aside from simulating the change in stiffness response as porosity is varied in a composite structure, another key area is being able to predict the knockdown in strength. One such approach is to study how the matrix is affected by the introduction of voids, which can then subsequently be used in a model containing the appropriate fibre architecture. For instance, McMillan[149] investigated the effect of voids on a planar model subjected to shear loading. To predict the knockdown in strength a nominal stress value, representative of the strength of the matrix, was selected. The load was induced into a void-free model until the nominal was met, the load at this point was chosen as the application load. Voids were then introduced into the model and after applying application load the maximum stress within the model was measured. The percentage reduction in matrix strength was subsequently calculated using Equation (2-18).

$$Percentage\ strength\ knockdown = \frac{\sigma_{max} - \sigma_{nom}}{\sigma_{nom}} \times 100 \qquad (2\text{-}18)$$

The limitation of McMillan's approach is that it only considers a planar model and does not go further than analysing the effect voids have on the matrix. In contrast, Tserpes et al.[109], use μ-CT analysis to characterise the porosity which is used to build 3D representations. Their results found two types of voids present in the composite, small microvoids and elongate voids longer than 1mm. The approach taken was to simulate the two types of voids separately; first modelling how neat matrix is degraded through microvoids and subsequently the same process was followed for the elongated voids but instead using the properties calculated from the microvoid model instead of neat matrix. Finally, a micromechanical analytical model was used to calculate the ply strength based on using the matrix properties of the second model with the associated fibre properties.

Similar to modelling the elasticity, there are several different approaches to determining the strength of a unidirectional composite containing voids. A geometrically simplistic approach was proposed by Chowdhury et al.[150] who modelled a single void in the centre of a planar model which contained two halves of a fibre on the sides of the model, as illustrated in **Figure 2-34**. The model does account for matrix plasticity and fibre-matrix debonding and due to the simplistic geometry has a low element count, in the order of 5,000 elements. However, this approach is not

realistic as it assumes the same void volume fraction as the fibre volume fraction. Strength is measured based on the stress-strain curve generated from the model.

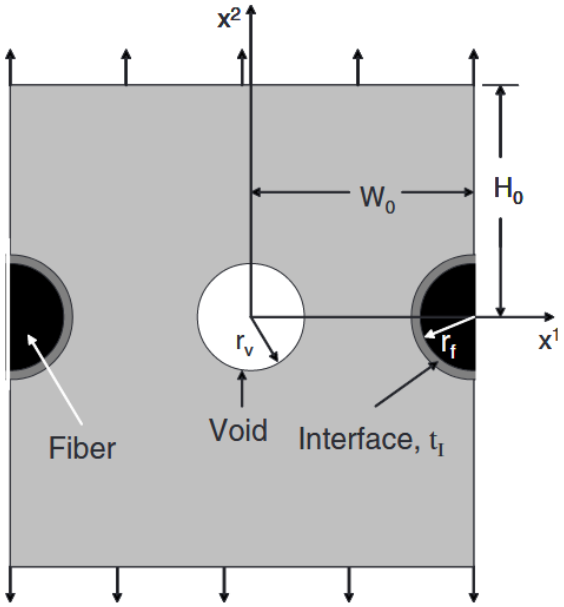

Figure 2-34 *Modelling a single void loaded in transverse tension.*[150]

Another 2D analysis was conducted by Wang et al.[151] using realistic fibre volume and void content values. Their study investigated the differences in the way that voids were geometrically modelled, as illustrated in **Figure 2-35**. Their results found that degrading elements only had a minimal effect on the strength, however when modelling the voids explicitly as a circular shape had a more significant effect. When varying the shape of the voids, the location and void content were kept constant, and their results found that the inclusion of arbitrarily shaped voids resulted in a lower strength.

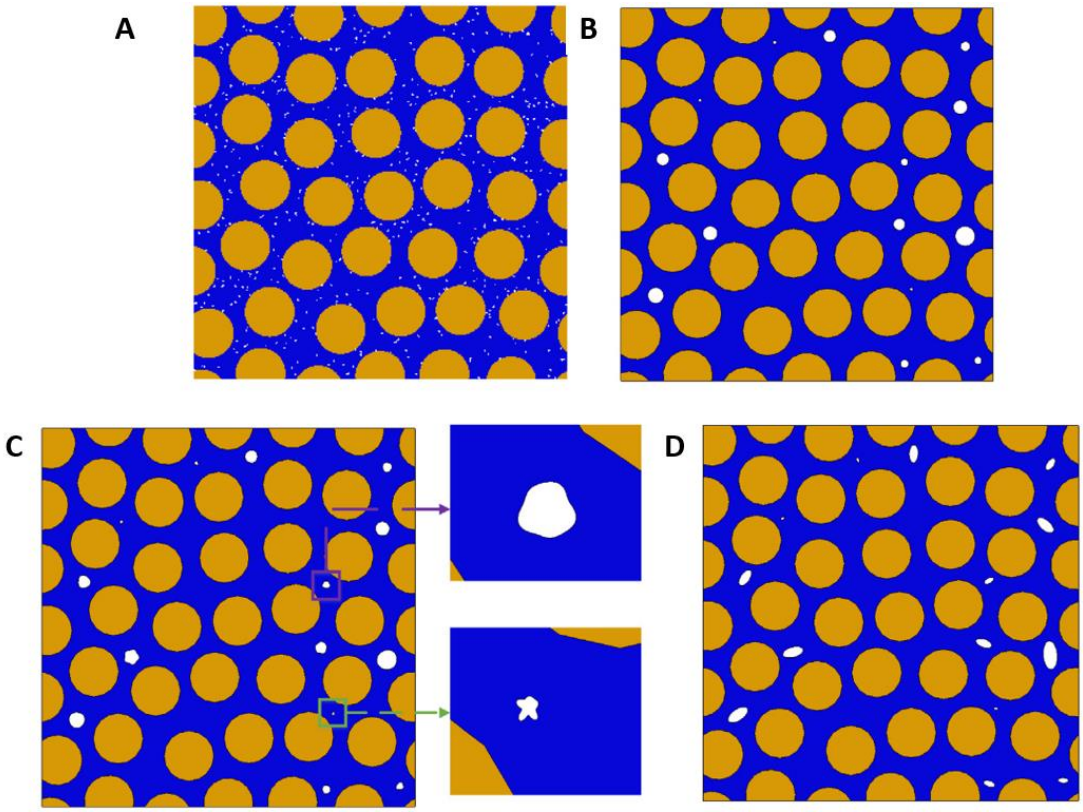

Figure 2-35 *Varying the approach to model void geometry. (**A**) Voids as elements, (**B**) explicitly - circular, (**C**) explicitly - arbitrary and (**D**) explicitly elliptical.*[151]

A similar study which investigated the effect of various void shapes was published by Vajari et al.[114] Through a microscopy study they found that there were two types of void present in their composite, microvoids between the fibres and larger arbitrarily shaped voids surrounding multiple fibres. These two types of voids were modelled explicitly in FEA, as shown in **Figure 2-36**. Their results found that the maximum strength was determined by the fibre-matrix decohesion at void locations. The damage propagated along the interfaces as well as being influenced by the location of the microvoids. The final failure occurred when multiple interface cracks linked up.

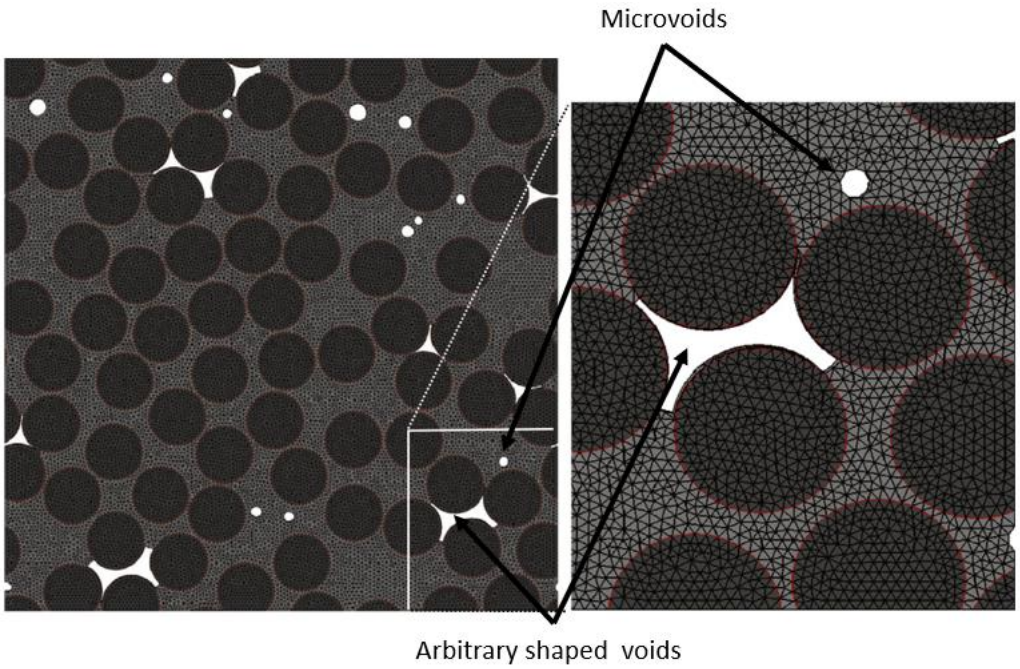

Figure 2-36 *Two types of void shape, micro and arbitrarily shaped, represented in the FEA model.*[114]

A multiscale modelling approach to account for the transverse cracking due to voids was proposed by Mehdikhani et al.[57] Their model comprised of three separate steps, as illustrated in **Figure 2-37**. First, two RUCs were generated with and with a void present, **Figure 2-38** (**A**) and (**B**). Step 2 involved calculating the stiffness matrix, transverse tensile strength and Mode I fracture toughness for these two models. These properties were then used in the third step where the Extended Finite Element Method (XFEM),[152] a numerical modelling technique to predict crack propagation, was utilized to predict the cracking in a transverse ply block containing both pristine and defected regions, which is designed to be representative of a laminate containing both pristine and defective regions. The model was used to investigate how two different void contents, 1.6 % and 5.0 % made up of voids with diameter 30μm and 60μm affect cracking onset and development. Their results found that the maximum effect of porosity was for the 5.0 % with a diameter of 30μm where crack onset beings earlier, however, crack development was consistent across all models.

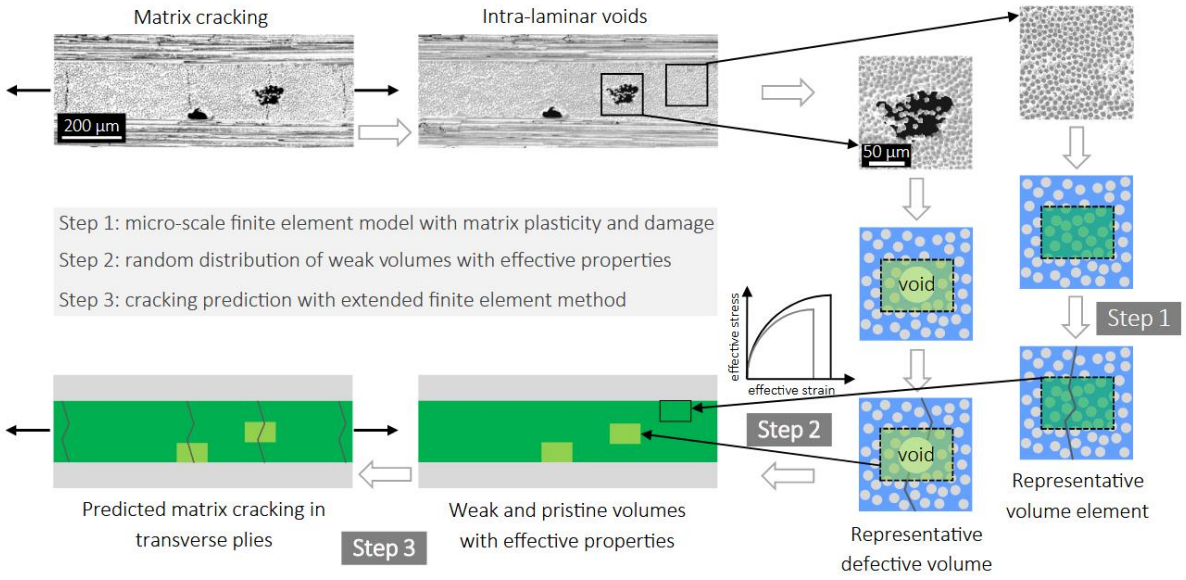

Figure 2-37 *Three-stage modelling approach to account for the effect of voids in transverse cracking.*[57]

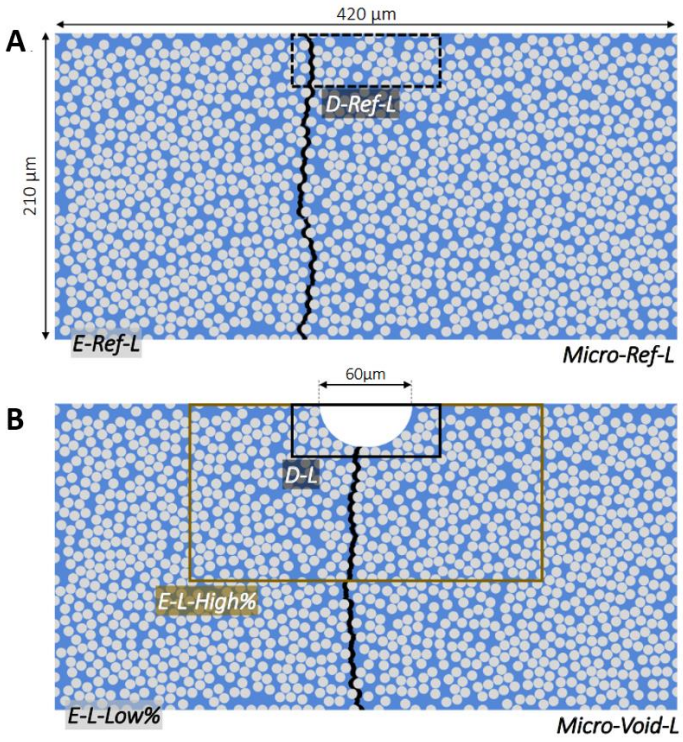

Figure 2-38 *Difference in step 1 model, (**A**) pristine and (**B**) defective.*[57]

Another approach to modelling the strength of unidirectional composites is randomly selecting matrix elements in an RUC and degrading their properties to near zero. Plasticity can be incorporated into the model by degrading subsequent elements as they meet a failure criterion. This approach was utilized by Jiang et al.[153] who modelled a three-fibre RUC with voids represented as randomly selected matrix elements, as illustrated in **Figure 2-39**. They developed an ABAQUS user subroutine, UMAT, to

determine if an element has failed and subsequently degraded it. They were successfully able to demonstrate that as the void content increased the strength reduced in the transverse direction, however, there was no change in the longitudinal direction.

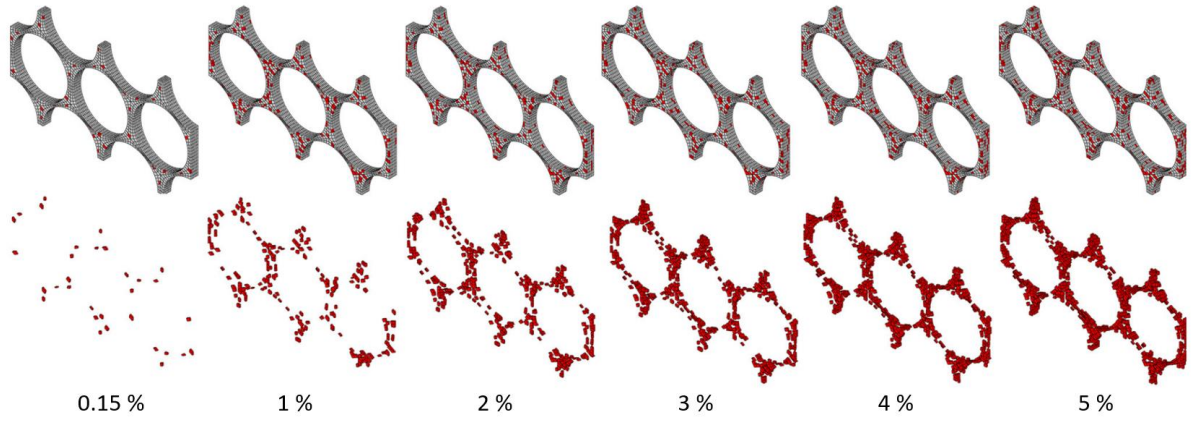

Figure 2-39 *Representation of voids through randomly selecting elements from 0.15 % to 5 %. The top row shows matrix and void elements and the bottom row shows the voids in isolation.*[153]

There are a limited number of studies published that have investigated how the strength of a woven composite containing voids can be modelled. This is likely due to the complexity of the combined intra- and inter-tow geometry, as well as the complex failure mechanics that would need to be captured. From the studies that have been published, there is a general two-stage approach that is taken, whereby the intra-tow is modelled first, and then these properties are used in a mesoscale inter-tow model. For both models, some form of failure criteria is required so that the strength of each model can be determined. For instance, this approach was utilised by Gong et al.[146] who assumed the intra-tow model to be simplified to a planar unidirectional model containing voids. Fibre failure is assumed to be brittle and the matrix damage is incorporated using a modified Drucker–Prager yield model presented by Lubliner et al.[154] This model is described by Equation (2-19), where f_m is the matrix failure; α is the pressure-sensitivity (set to 0.13); J_2 is the second invariant of the deviatoric stress tensor; I_1 is the first invariant of the stress tensor; β is the function of the tensile (σ_{xt}) and compressive yield stress(σ_{xt}), as defined by Equation (2-20). Equation (2-20) is applied to each of the matrix elements to determine if they have failed. For the inter-tow model, a 3D woven unit cell was generated using TexGen with voids modelled as randomly selected elements. Damage in the matrix surrounding the tows was modelled using the same modified Drucker-Prager[154] yield model (Equation (2-20), as described previously). For the tows, however, they were again assumed to be

unidirectional and Puck's failure criterion was used. The models showed that both the intra and inter-modulus were affected by voids. However, in contrast, the results showed that whilst the tensile and shear strengths were sensitive to voids within the fibre tows, the compressive strength was found to be sensitive when voids were between the voids.

$$f_m = \frac{1}{1-\alpha}\left(\sqrt{3J_2} + \alpha I_1 + \beta\langle\sigma_1\rangle\right) - \sigma_{xc} \tag{2-19}$$

$$\beta = \frac{\sigma_{xc}}{\sigma_{xt}}(1-\alpha) - (1+\alpha) \tag{2-20}$$

This approach has also been applied to braided material by Ge et al.[155] where the tows of the braided preform are first modelled as unidirectional unit cells with elements randomly selected to simulate voids. Matrix damage is modelled using the maximum principal stress criterion and fibre damage is modelled using Hashin's criterion.[156] Hashin's criterion are a set of failure criteria that determine if failure occurs in either the fibres or matrix under tension or compression, which are defined through equations (2-21) to (2-24):

Tensile Fibre Mode: $\sigma_1 > 0$

$$\left(\frac{\sigma_1}{X^t}\right)^2 + \left(\frac{\tau_{12}}{S}\right)^2 = 1 \tag{2-21}$$

Compressive Fibre Mode: $\sigma_1 < 0$

$$\sigma_1 = X^c \tag{2-22}$$

Tensile Matrix Mode: $\sigma_2 > 0$

$$\left(\frac{\sigma_2}{Y^t}\right)^2 + \left(\frac{\tau_{12}}{S}\right)^2 = 1 \tag{2-23}$$

Compressive Matrix Mode: $\sigma_2 < 0$

$$\left(\frac{\sigma_2}{2S^T}\right)^2 + \left[\left(\frac{Y^t}{2S^T}\right) - 1\right]\frac{\sigma_2}{Y^c} + \left(\frac{\tau_{12}}{S}\right)^2 = 1 \tag{2-24}$$

A RUC of the braided geometry is modelled with inter-tow voids modelled again as randomly selected elements. Matrix damage is modelled using the same criterion as was used in the intra-tow model and the maximum stress criterion was used to model

damage in the tows. The strength of the models was determined by plotting the stress-strain response.

2.9. Conclusion

This subsection summarises the following: key findings of the literature review, the present knowledge gap in evaluating the porosity in CFRP, and how this defines the research that was undertaken in this PhD thesis.

2.9.1. Key Findings

One of the main reasons for using composite materials in engineering structures is the potential to minimise the mass. Whilst composites have often been used for non-structural components (such as covers and non-load bearing panels), there is currently a strong drive for their use in structural applications. However, the inclusion of defects during manufacture, in particular porosity, often results in overengineered designs. To ensure composite structures are designed correctly, defects must be accounted for appropriately.

Previously, there have been significant experimental studies into how porosity affects the mechanical properties of composites.[30] However, not only does this have a high financial and time cost, there are also difficulties in the reproducibility of test panels. For instance, manufacturing laminates with the same void content is difficult, as well as controlling where the porosity generates or the shape and size etc. These difficulties have led to developments throughout the last decade towards numerical modelling, as it allows for the repeatability of virtual tests whilst having full control over the varying of specific parameters.

Whilst there is a strong advantage to using computer simulations with computational power greatly improving in recent years, there is still a trade-off between the simulation time and accuracy in representative models. Naturally, porosity-based models are generated at the microscale and often take the form of a 2D/planar model, such as those developed by Nikopour et al.[22] and Dong et al.[96] However, this results in voids being assumed to be infinitely long. Whilst μ-CT scans have shown that there can be significantly elongated voids (in the order of millimetres), this is not the only type of voids that has been reported[30]. Often, microvoids and short-length inter-ply

voids are present in a structure,[30] meaning that the assumption of only infinitely long voids present is not valid. To account for this type of void a 3D RUC is often generated and the stiffness of randomly selected matrix elements (amount based on the void volume fraction) is reduced, simulating voids. This inherently has several drawbacks, firstly, the size of the void is dictated by the element size and naturally, for accuracy reasons, elements are small respective to the model size. This may or may not be representative of the size of the voids found in the laminate being modelled. Secondly, the elements used in this type of model are typically either 3D brick or tetrahedral shaped. This means that the shape of the void is simulated to have flat sides with vertices and edges, which is not representative.[30] These drawbacks mean that the only parameter that can be representative is the void content and whilst this has been the focus of many studies, more recently there have been reports that the shape and size of voids are also very important on the impact on structural performance.[12,100] Thus, it can be concluded that not only the void content should be considered but also how the geometrical features of the porosity affect the mechanical response.

2.9.2. Knowledge Gap

Currently, the driving contributor that is monitored to assess the impact of porosity on a structure's mechanical response is the void content. This is seen in both academic research, where studies are mainly driven by the void content, and in multiple industrial contexts, where blanket limits are set such that the void content must always be below a specified threshold. In recent years, studies have shown that this is not the only porosity parameter that affects the mechanical response. Instead, it has become apparent that the geometrical properties of voids influence the magnitude of degradation that porosity has on a CFRP structure.[40] It is now clear that the void content is not sufficient to be able to accurately predict the reduction in material properties and thus, geometrical properties (such as void shape and size) must also be accounted for.

Currently, there is no practical solution to consider how the geometrical properties of the porosity affect the global laminate properties. It is not reasonable to invest a significant number of resources into developing a highly detailed model representing one specific section of a laminate. This is because firstly, the time invested into building the model would be unfeasible and secondly, the computation requirement

would also result in an unreasonable analysis time. To study the effect of voids requires models to be generated and adapted in reasonable time frames, such as hours or days at the most. The knowledge gap to be addressed in this thesis is to develop a practical modelling approach that can account for both void content and geometrical parameters of voids.

2.9.3. Novel Modelling Approach

The knowledge gap has shown that the numerical modelling of voids in CFRP must be developed to not only account for the void content, but to also be geometrically representative. While undertaking the literature review and accessing the current approaches, an inspiration for a new approach became apparent. This occurred when reviewing the publication by Huang and Talreja[40], where they modelled an isolated void in neat matrix to study how changing the major and minor axis lengths affected the elastic properties of CFRP. This study presented opportunities to address the geometrical influence of voids and by studying each void in isolation (i.e., not including other voids or fibres) the computation requirement is significantly reduced. However, the study had several shortcomings, first, only elastic properties were considered; there was no investigation into the reduction of strength that the void resulted in. Second, the shape of the void was limited to a cylinder, as illustrated in Figure 2-40, resulting in a void with parallel sides and flat surfaces at each end. The 90° edges at each end are likely why a strength analysis could not be achieved, since high stress concentrations would be present here.

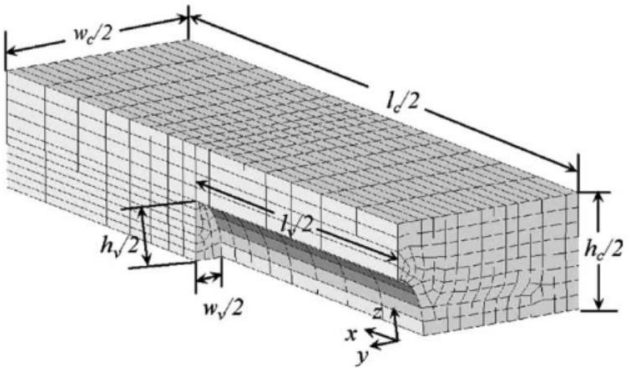

Figure 2-40 *Shape of the void considered in the study by Huang and Talreja.*[40]

This study was used as inspiration to conceptualise a new multiscale modelling approach such that a void(s) that is representative of the CFRP is modelled and a

strength analysis is used to determine the knockdown in strength of the matrix. This is the first stage of the approach. The second stage is to make use of a typical 'RUC', using the knocked-down matrix strength to predict knocked-down ply properties. A detailed explanation of this approach is given in Subsection 4.2.

This approach provides several benefits that address the knowledge gap. Firstly, three-dimensional geometry can be modelled in stage 1 with higher accuracy. Previously, this has been limited to either the shape of elements or a cylindrical void for three-dimensional studies. Secondly, in the transverse direction, both voids and fibres act as stress raisers of the matrix. Therefore, by excluding the fibres in the first modelling stage, an understanding of how the void geometry degrades the matrix can be understood. Also, by splitting the analysis into two separate models, this results in the possibility to scale the size of the models. E.g. if the fibres were included then this would define the element size (if the fibres were smaller than the voids), by not including the fibres, the element size is dictated by the size of the voids and therefore less elements would be required.

2.9.4. Research Question

Having determined a knowledge gap concerning modelling porosity in CFRPs and conceptualising a novel modelling approach, this presents a major research question to be answered by this thesis:

"*Can the conceptualised multiscale modelling framework accurately predict the resulting knock-down in strength of a CFRP structure due to the inclusion of porosity?*"

To answer this question four topics must be investigated, which are the following:

1. Can the multiscale modelling approach determine a change in strength due to varying porosity parameters, and consequently, how does the strength change as the parameters are varied?
2. What composite strengths are affected? Multiple parameters must be taken into consideration when evaluating the strength of a composite. For instance, the tensile or compressive strength in both the longitudinal and transverse directions. There is also flexural, short beam and torsional strength that defines

the strength of a composite. Therefore, the strengths to be evaluated using the modelling approach must be considered.

3. What geometrical form do the voids take, and how can this be represented in the modelling approach? The literature review highlighted that the geometry of the voids is an important factor in determining the knockdown in strength; therefore, the shape of the voids must be evaluated and accurately represented in the modelling approach.
4. How adaptable is the modelling approach to the porosity formed in different composite manufacturing methods? There are many different composite manufacturing approaches that result in differing porosity formation. It should be investigated how well the modelling approach can be adapted to represent voids from different manufacturing processes.

2.9.5. Research Plan

The following section details the plan that was set out to ultimately address the main aim of the thesis and answer the research question set. The plan was defined by addressing the topics mentioned above as well as the objectives defined in subsection 1.2.

1. Fully conceptualise and develop the modelling framework.

A high-level overview of the envisioned modelling framework has been presented above; however, this was required to be expanded upon to determine specifically how the modelling procedure works, including how boundary conditions and meshing were defined, as well as how the model strength is determined. Any scripting required for the modelling framework was also required to be developed.

Once developed, it was required that the model should be used to evaluate how porosity parameters affect strength, such as the void content by varying the void volume fraction, as well as the geometrical shape. The modelling framework should be preliminary validated through analytical solutions on the models that have been created.

2. Determine strength material properties that the modelling framework will be used to predict.

Not all strength properties are to be evaluated using this modelling framework, this is for two reasons. Firstly, in subsection 2.6.2, the literature review showed that not all strength properties are affected by porosity, most notably in the fibre direction. Secondly, due to the microstructure complexity, a single model is unlikely to be able to determine all material properties and must be developed to address specific properties accurately.

The tensile and compressive strengths were chosen as the key focus of the model development. The decision to address these strengths was two-fold: first, these are major strength parameters that are used in the classical laminate theory in composite design tools, such as ply calculators and FEM code. Second, whilst other strength properties are used in composite design, such as torsional, interlaminar and flexural strength, these are more complex failure mechanisms. Since the modelling framework is a novel concept, it was more appropriate to ensure that it can be used to accurately represent tensile and compressive loading first, before developing it for more advanced cases. It should also be noted that loading, such as flexural, can be investigated locally, such as either the tensile or compressive side of a beam/flexed structure. Therefore, the study could be simplified in such a way that this modelling framework could still be of use.

3. Conduct a series of theoretical studies investigating how geometrical parameters affect the strength.

The biggest driver for developing the modelling approach was to be able to address how geometrical properties that affect the strength. A series of studies were conducted where the shape of the void was varied. This was to show that the modelling framework can determine a change in strength as the geometry was varied and to investigate how the shape change affects the resultant strength. To validate the modelling framework, it was to be adapted in such a way that it can be compared to an analytical solution.

4. Manufacture laminates with various degrees of porosity, using two different processing techniques. Mechanically test the laminates and characterise the porosity.

Whilst comparing an adapted and simplified version of the modelling framework to analytical solutions can show if the approach shows potential, it is extremely beneficial to validate against empirical data. For this reason, an experimental campaign was conducted where laminates, with various degrees of porosity, were manufactured using both an autoclave and OoA processing technique. This was to highlight any differences, difficulties, or limitations that the modelling framework may be susceptible to. The porosity was to be characterised in a manner that allows for representative models to be built.

Whilst the primary reason to characterise the porosity of each of the laminates was for the use in the build of models, the data provides another research opportunity: to evaluate how the porosity changes under different manufacturing conditions. Due to the complexity of composite manufacturing, curing and microstructure, it is often hard to predict how the porosity will form. For instance, there has been a significant amount of research in studying and modelling processing conditions specifically for void formation. The data that was gathered for developing the models could also be used to provide insights into the effect of process conditions.

5. Undergo a correlation campaign where representative models of the tested laminates are built, and the FEM results are compared to the empirical data.

Using the porosity characterisation data of the manufactured laminates, representative models of each of the laminates were created. The porosity characterisation data should first be evaluated to determine how best the porosity can be represented accurately. Multiple models of the same laminate should also be generated where the porosity data is interpreted and processed in different ways to show how this affects the correlation. Conclusions should be drawn on how well the model correlates to the empirical data, as well as how sensitive the model is using different porosity representations.

6. Results should be fully discussed, and conclusions drawn.

As with any research project, the results from each of the topics investigated throughout the thesis were to be fully evaluated and compared to the main aim and

objectives. The implication of the results should be evaluated to show the significance of the findings in the context of modelling porosity in composites. Any unexpected results should also be evaluated with a discussion on why such a result became apparent. The limitations of each topic should be discussed, with particular attention given to the limitations of the modelling approach. Future work should also be considered that addresses either the limitations or builds upon the results that have been concluded in this thesis.

3. Common Experimental and Modelling Techniques

This chapter describes the techniques used throughout this thesis for laminate manufacture, specimen preparation and test procedures as well as the common operations used when modelling.

3.1. Manufacturing

3.1.1. Autoclave processing

One of the major manufacturing techniques that has been used throughout this thesis is curing prepreg layups in an autoclave. The manufacturing process starts by removing the roll of material from the freezer and defrosting it. After which, plies required for the laminate were manually cut out. The plies for each laminate were cut oversized by 40 mm in both the longitudinal and transverse directions to allow for sufficient excess material to be trimmed off. The plies were manually laid-up onto a flat metal mould using PTFE tape for demoulding. To achieve the same surface finish on both sides an additional thin aluminium sheet with the same PTFE tape was placed on top of the laminate. Identical surface finishes were required so that tabbing material could easily be bonded to the laminate surface. Previous testing had shown difficulty in the tabbing material adhering to the coarse surface formed from the breather cloth. By adding an additional plate on the top of the laminate, and below the breather cloth, provides an identical and smooth surface on both sides of the laminate. An unperforated release film was placed on top of the laminate before adding a breather fabric for even vacuum bagging, both supplied by Easy Composites, UK.[157] A schematic of how each of the parts are laid up is illustrated in **Figure 3-1**.

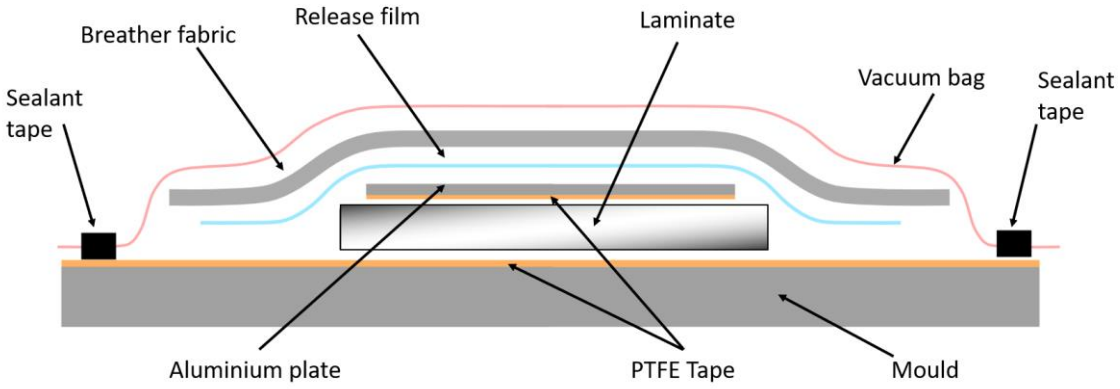

Figure 3-1 *Schematic of how the laminate is laid up into a vacuum bag.*

Each layup was vacuum sealed using a ring of bagging sealant tape around the laminate and vacuum bagging film over the top, two through-bag connectors were used to draw a vacuum. Pleats were used to take up any excess vacuum bagging film. A vacuum/leak test was completed on every laminate to ensure that there were no leaks before being placed into the autoclave. A limit of 1 mbar/min over a ten-minute test was chosen, based on previous experience, and if this was exceeded the vacuum seal was inspected/adjusted and retested. With a successful vacuum test, the layup was placed in the autoclave with two thermocouples attached to the layup(s) to monitor temperature. According to the material supplier recommendations, a dual dwell temperature cycle was used up to a maximum of 125 °C. The cure pressure was recommended to be set at 0.59 MPa; however, this was the parameter that was adjusted to vary the void content within the laminates. For this reason, the cure pressure was varied between a reduced vacuum bag only, set at 0.05 MPa, and the fully applied pressure of 0.59 MPa. An example of the temperature and pressure cycle used can be seen in **Figure 3-2**.

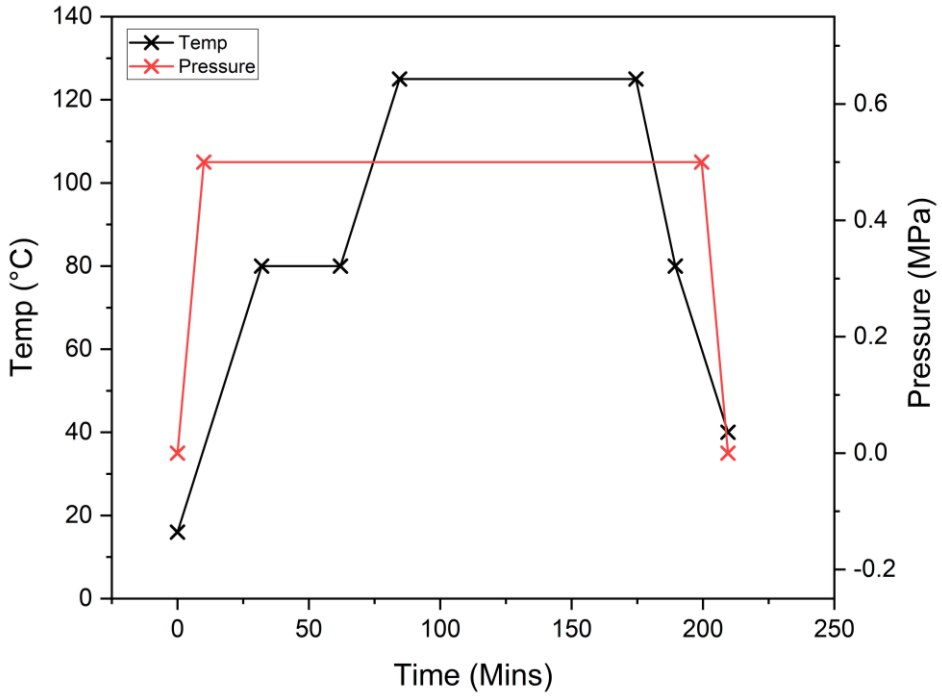

Figure 3-2 *Autoclave temperature and pressure cure cycle.*

3.1.2. Resin infusion processing

The second composite manufacturing process used in this thesis was resin infusion. The process starts similarly to that of the autoclave processing whereby the material, in this case the dry preform, is cut to size. Each ply is cut oversized by 20 mm in both directions and laid up on a flat glass mould that has been prepared using a mould release agent. Infusion mesh is laid over the regions where the inlet pipes are positioned, which is comprised of a vacuum hose connected to a spiral coil. The same pipe arrangement is also used for the outlet which is positioned approximately 100 mm from the end of the laminate to act as a buffer zone to allow full wet-through of the laminate. A peel ply is placed over the top of the layup and consumables, and a vacuum seal is applied. The resin infusion setup can be seen in **Figure 3-3** and **Figure 3-4**. The same vacuum/leak test that was performed for the autoclave-produced laminates was completed using the same conditions. If required, adjustments to the vacuum seal were made.

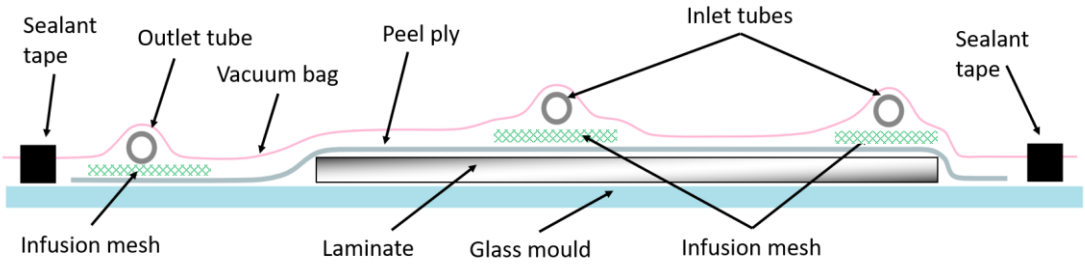

Figure 3-3 *Schematic of the setup used for resin infusion.*

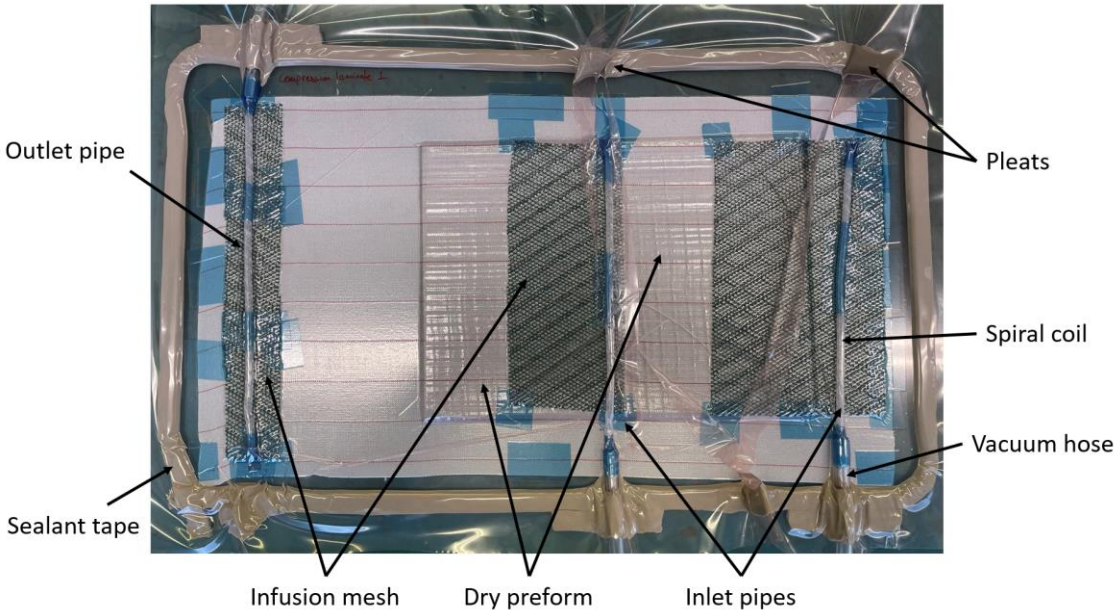

Figure 3-4 *Resin infusion arrangement.*

To prepare the resin prior to infusion, the resin and hardener were weighed out to an accuracy of ±0.01 g. The resin was next degassed and mixed with the hardener and further degassed. However, to vary the void content, the amount of degassing and stirring technique was varied (explained in further detail in Chapter 6). To infuse the resin-hardener mixture into the preform, the first inlet tube was inserted into the pot containing the mixture. With a vacuum being drawn, the first inlet was opened to draw the mixture into the preform. Once the mixture had just passed the second inlet tube, the first inlet was locked off and the resin pot was moved to the second inlet. The same process was repeated until a full wet-through was achieved. Using a glass mould allows the underside to be inspected to ensure that full wet-through has been achieved across the whole length of the laminate. Once full wet-through was achieved, all inlet and outlet tubes were locked off and the laminate was left for 24 hours to cure at room

temperature. Afterwards, as recommended by the resin supplier, a 6-hour post-cure was undertaken at 60 °C.

3.1.3. Specimen and laminate sizing

The dimensions for both the tensile and compressive specimens were given by the respective standards. The specimen dimensions are dependent on the fibre orientation (longitudinal or transverse to the load), which are illustrated and documented in **Figure 3-5** and **Table 3-1** respectively. The length and width of the laminates were set by the length and number of specimens required (including cutting wastage), respectively, plus surplus material to account for the laminate edges.

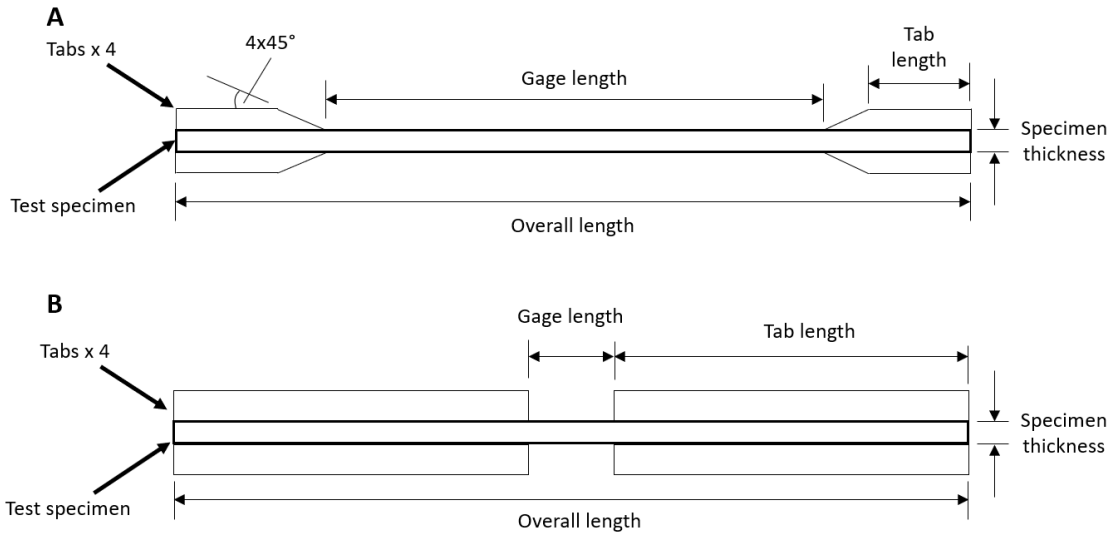

Figure 3-5 *Drawings for (**A**) tensile and (**B**) compression specimens.*

Table 3-1 *Reference dimensions of tensile and compressive specimens provided by the ASTM Standard.*

Test direction	Fibre orientation	Width / mm	Overall Length / mm	Specimen Thickness / mm	Tab Length / mm	Gage Length / mm	Bevel Angle / °
Tension	0°	15	250	1.0	56	138	45
	90°	25	175	2.0	25	125	45
Compression	0°	13	140	2.0	64	13	90
	90°	13	140	3.0	64	13	90

3.1.4. Tab bonding

Once the laminates had fully cured (from either process), tabs could be bonded onto the laminate. The reason that tabs were bonded onto the laminate before cutting specimens to size, was to prevent excessive grinding that would have been required if they were to have been bonded on afterwards. The size of the tabs were cut 10 mm oversized in the specimen length direction so that once they were fully bonded, the length could be cut to exact size. The width of the tabs were cut short of the width of the laminate so that when the first specimen was cut out, the laminate edge could be used as a datum for making the initial cut. The excess material to be cut is illustrated in **Figure 3-6**. Prior to bonding the tabs onto the specimens, all regions to be bonded were scuffed using 120-grit abrasive paper to improve the adhesion. The adhesive used to bond the tabs was Permabond's 2-Part Structural Adhesive ET538. A thin layer of adhesive was applied to both surfaces and then spring clamps were used to hold tabs in place, as shown in **Figure 3-7**. The tabs were left for a minimum of 24 hours before being unclamped.

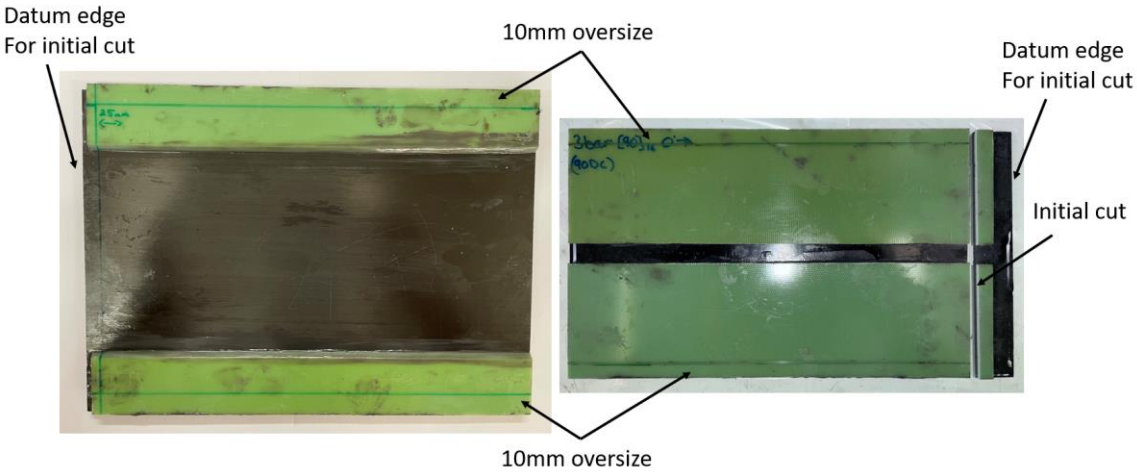

Figure 3-6 *Layout lines and datum edge to prepare laminate for specimens to be cut out.*

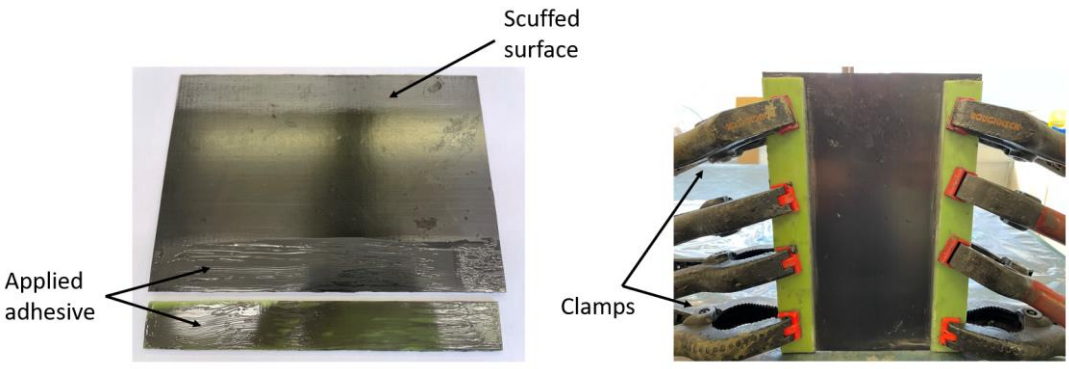

Figure 3-7 *Adhesion process to bond tabs onto CFRP laminates.*

3.1.5. Specimen preparation

Once the tabs were fully bonded onto the laminates, specimens could be cut to the correct size. All cuts were made using a bandsaw with an abrasive blade. First, one of the 10 mm overside lengths was cut off and then a fence on the bandsaw was set to the required length of the specimens. The length of the specimens was set to be 0.5 mm oversized to allow excess material to be removed when grinding. The datum side was then used to make the first cut along the length of each of the specimens. As there was a space under the laminate due to the additional thickness of the tabs on either end, additional support material was placed under the laminate to prevent any damage occurring during machining. After making the initial cut using the datum edge, the fence was set to the width required for the specimens, plus an additional 0.5 mm to allow for material to be removed during grinding. The surface finish after machining is very coarse, as can be seen in **Figure 3-8(A)**, which needs to be ground to a polished surface, as shown in **Figure 3-8(B)**. To do this, the machined surfaces are ground initially using 120-grit abrasive paper until all machining marks are removed. Afterwards, the sides are polished using a 240-grit abrasive paper. To ensure the same finish is applied to all specimens and to mitigate any variation, the same number of strokes (40) was applied to each specimen. Once all specimens were polished and ready to be tested, the cross-sectional area was measured. This was achieved by measuring the width and thickness at three points within the gage section, using digital callipers.

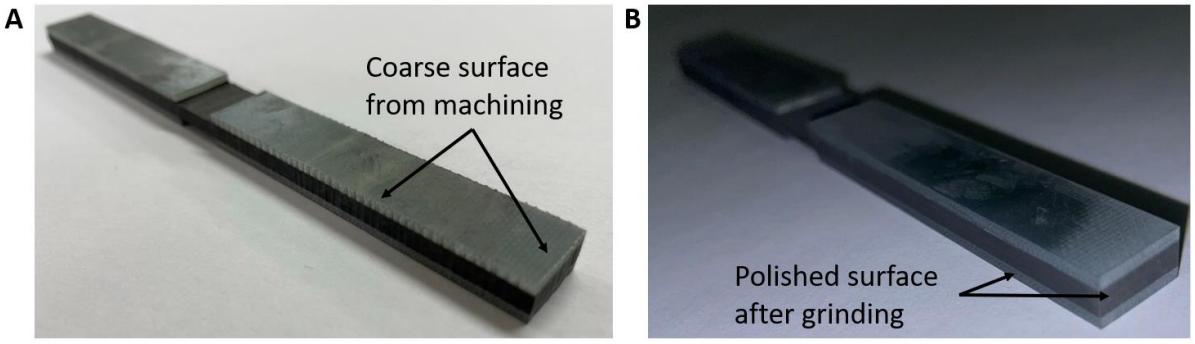

Figure 3-8 *Edge finish of the specimen (**A**) after machining, and (**B**) after grinding.*

3.2. Test Procedures

3.2.1. Tensile testing

All tensile testing was carried out using an Instron 8801 servo-hydraulic testing machine using a 100 kN load cell. Before inserting each specimen, the load reading on the control and measurement software for the machine was checked to be zeroed. Specimens were carefully inserted into the centre of the grips ensuring that there was no misalignment in the loading direction. The grips were tightened to clamp each specimen and due to the grip actuation mechanism, a small amount of compressive pre-load (approximately 10 N) was induced. Before each test, this load was returned to zero.

For tensile testing the ASTM standard D3039[158] was followed; therefore, load was induced into the specimens through a constant head displacement at a rate of 2 mm/min. The load was induced into the specimens until complete failure had occurred. Afterwards, the specimens were removed from the machine and failure mode was inspected and recorded. There are several different failure modes for tensile specimens, examples of which are illustrated in **Figure 3-9** with the corresponding failure codes recorded in **Table 3-2**. If any tensile specimens did not fail in accordance with the standard, such as failing at the grips, then a note was made to not include the data from that specimen when data processing.

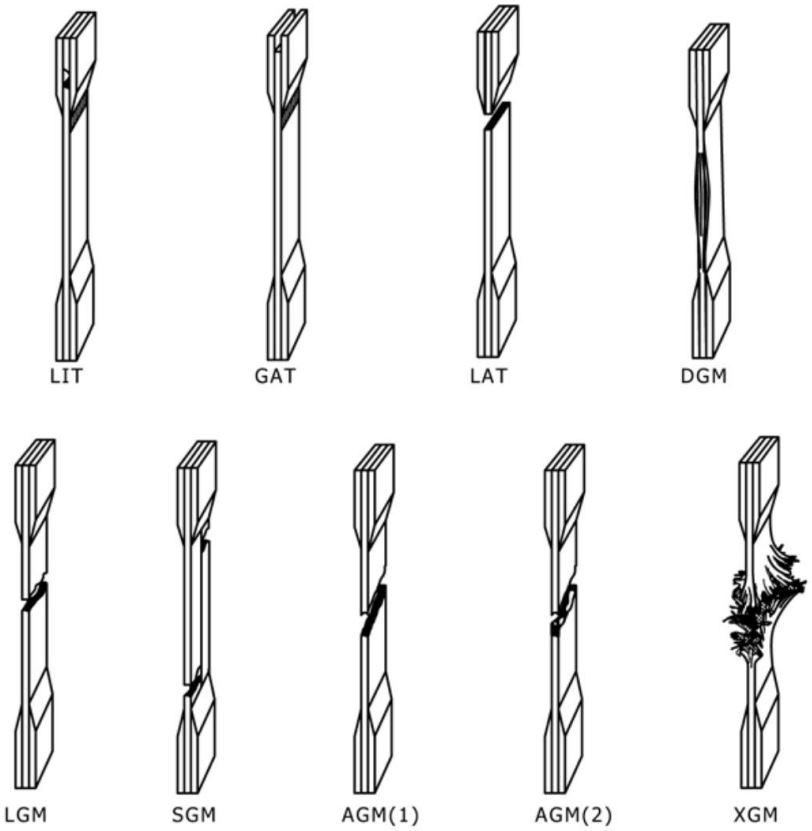

Figure 3-9 *Examples of different failure modes that can occur in tensile specimens with corresponding failure codes.*[158]

Table 3-2 *Failure codes for tensile specimens.*[158]

First Character		Second Character		Third Character	
Failure Type	**Code**	**Failure Area**	**Code**	**Failure Location**	**Code**
Angled	A	Inside grip/tab	I	Bottom	B
Edge delamination	D	At grip/tab	A	Top	T
Grip/tab	G	<1W from grip/tab	W	Left	L
Lateral	L	Gage	G	Right	R
Multi-mode	M(xyz)	Multiple areas	M	Middle	M
Long Splitting	S	Various	V	Various	V
Explosive	X	Unknown	U	Unknown	U
Other	O				

3.2.2. Compressive testing

Compression tests were conducted following the ASTM Standard D6641[159] which involved the use of a Combined Loading Compression (CLC) test fixture to determine the compressive strength and modulus. A schematic of the test fixture is illustrated in **Figure 3-10**. The test fixture works by clamping specimens between the left and right halves of the fixture using 8 bolts to a torque of 3.5 Nm. The upper and lower halves

of the fixture are free to slide along alignment rods, allowing the load to be induced through both shear and end loading.

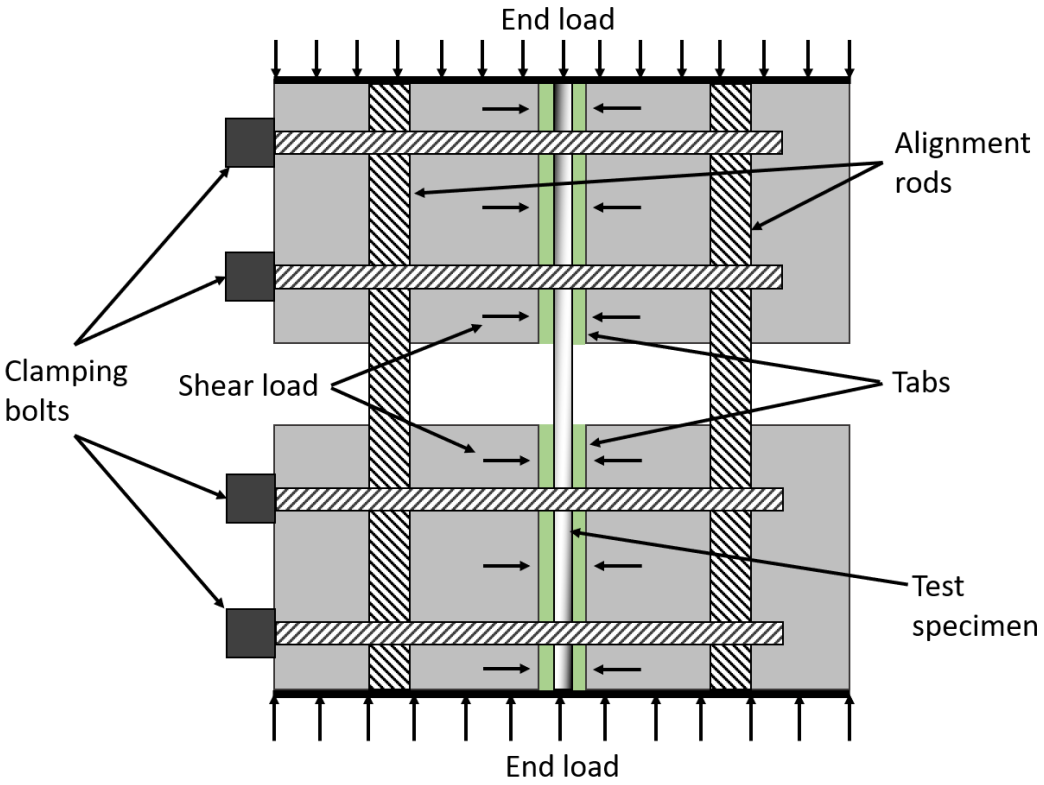

Figure 3-10 *Schematic of the CLC test fixture.*

All compression testing was carried out on a ZwickRoell Z050 electromechanical static testing machine coupled with a 50 kN load cell. The test fixture was placed into the test machine between two machined flat platens with alignment markings to ensure the placement was in the same location for each test. Before starting the test, the load measurement was checked to be zeroed and then the crosshead was positioned slightly above the test fixture. As per the standard, the load was induced through constant head displacement at a rate of 1.3 mm/min until complete failure occurred. Afterwards, the test fixture was removed from the test machine and the clamping bolts were loosened. The specimen was carefully removed from the test fixture and failure mode and locations were inspected. Examples of different types of acceptable and unacceptable failure modes are illustrated in **Figure 3-11**, with the corresponding failure codes summarised in **Table 3-3**. Trial testing has shown that any inaccuracy in the placement of the specimen in the test fixture can result in end crushing invalidating the test. Therefore, particular attention was given to both the specimen ends as well as

the gage section. If any specimens failed unacceptably, the specimen ID was noted, and the relevant data was not included in the post-processing.

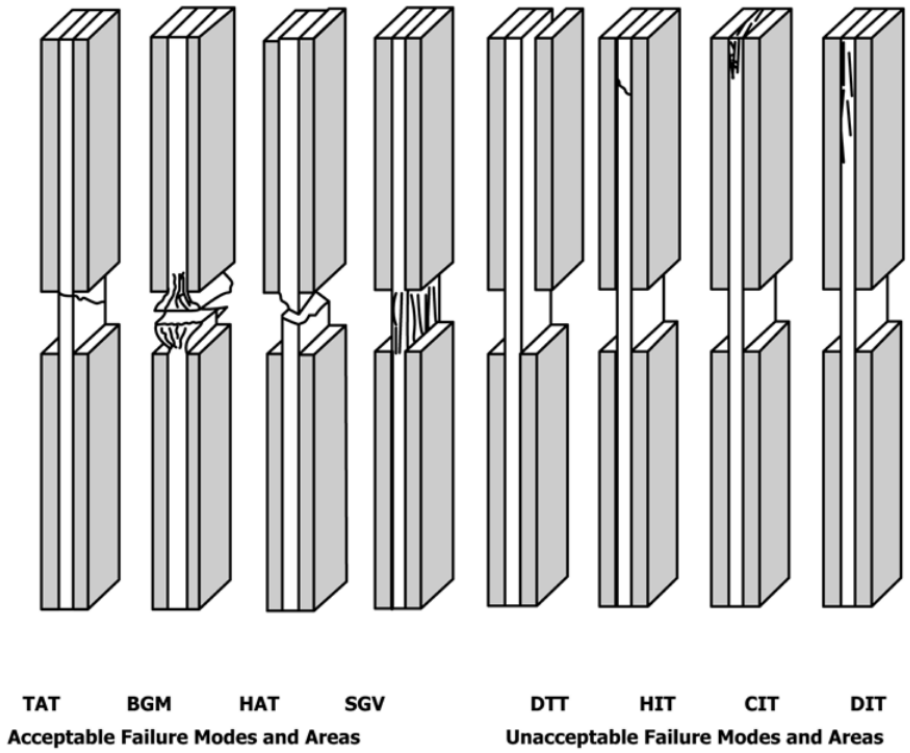

Figure 3-11 *Examples of the different acceptable and unacceptable types of compressive failure*[159]

Table 3-3 *Failure identification codes.*[159]

First Character		Second Character		Third Character	
Failure Mode	**Code**	**Failure Area**	**Code**	**Failure Location**	**Code**
Angled	A	Inside grip/tab	I	Bottom	B
Brooming	B	At grip/tab	A	Top	T
End-Crushing	C	Gauge	G	Left	L
Delamination	D	Multiple areas	M	Right	R
Euler buckling	E	Tab adhesive	T	Middle	M
Through-thickness	H	Various	V	Various	V
Kink bands	K	Unknown	U	Unknown	U
Lateral	L				
Multi-mode	M (xyz)				
Long Splitting	S				
Transverse shear	T				
Explosive	X				
Other	O				

3.2.3. Measurement apparatus and data processing

For both tensile and compressive testing, the load and displacement were recorded using data acquisition features built into the load control software. The measurements were recorded at a sampling rate of 5 Hz and processed using Excel. The maximum load for each specimen was determined, and along with the Cross Sectional Area (CSA) measurements, the ultimate strength of each specimen was determined using Equation (3-1), where F_{max}, P_{max} and A are the ultimate strength, maximum load recorded and CSA, respectively.

$$F_{max} = \frac{P_{max}}{A} \tag{3-1}$$

The strain of each specimen was measured using a video strain gauge system supplied by iMetrum to determine the Young's modulus. The system, as illustrated in **Figure 3-12**, comprised of an iMetrum camera coupled with either a general-purpose lens for tensile testing or a high magnification material testing lens for compression testing. Load and displacement data was also acquired by the system so that stress could be measured concurrently with the strain. The system works by tracking contrasting markings, such as a speckle pattern for full surface measurement or two dots acting as a 'virtual' strain gauge for an individual measurement. The latter was used for all types

of testing in this thesis where a gauge length of 60 mm and 8 mm were used for the tensile and compressive testing, respectively. An LED array light source was used to improve the contrast between the dots and the specimen. All measurements were recorded at a sampling rate of 5 Hz.

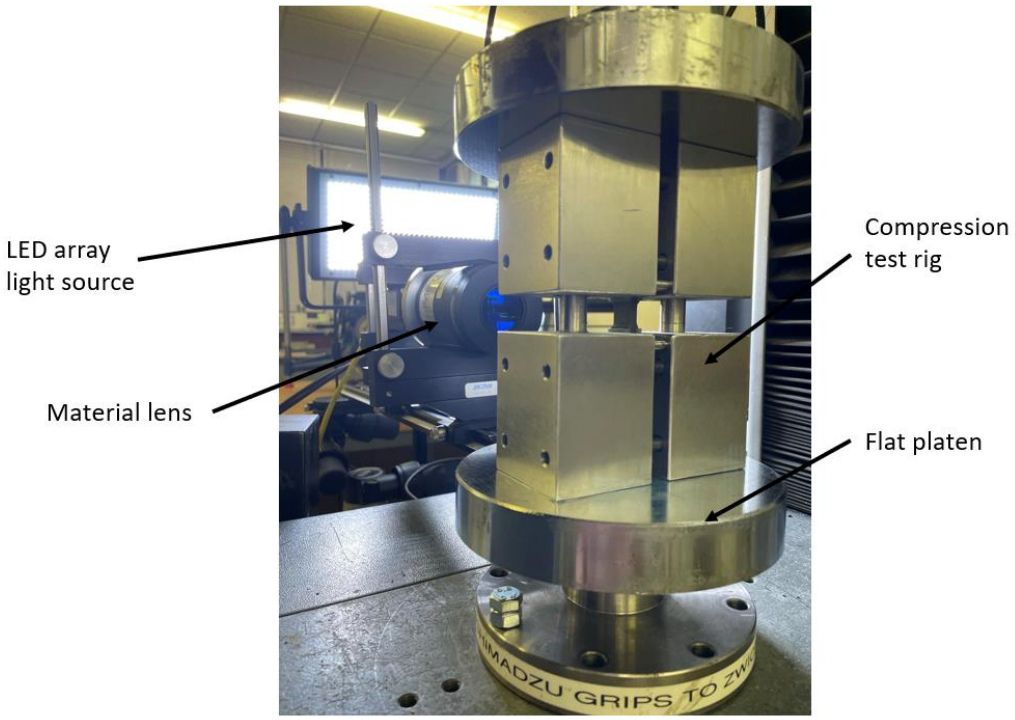

Figure 3-12 *Video strain gauge setup for compression testing.*

For each specimen, a Stress-Strain graph was plotted so that the Young's modulus could be determined for only the linear elastic region of each test. As the data is recorded just before the load is applied, and there is typically a small amount of slack in the test fixture, the Stress-Strain graph is used to identify the start of the elastic loading. Also, it is used to identify the maximum stress before any plasticity occurs. The Young's modulus was calculated using Equation (3-2), where E is the Youngs modulus, ΔS_{le}, $S_{max,le}$ and $S_{min,le}$ are the change in linear elastic stress, minimum and maximum linear elastic stress, respectively, $\Delta\in_{le}$, $\in_{max,le}$ and $\in_{max,le}$ are the change in elastic strain, minimum and maximum elastic strain, respectively.

$$E = \frac{\Delta S_{le}}{\Delta \in_{le}} = \frac{\left(S_{max,le} - S_{min,le}\right)}{\left(\in_{max,le} - \in_{min,le}\right)} \tag{3-2}$$

3.3. Porosity Characterisation

Several different approaches can be used to characterise the porosity within a laminate, as discussed in detail in Subsection 2.4. The characterisation technique chosen for the work presented in this thesis was optical microscopy. One of the main aims of this thesis is to account for the geometrical properties of voids which can be achieved through optical microscopy. Whilst techniques such as μ-CT can also be utilized to generate exceptionally accurate characterisation data, the process is limited in analysing small sample volumes and has very high setup times and associated financial costs. Therefore, it was determined that optical microscopy offers a good balance between accurate geometrical characterisation and efficient sample processing.

3.3.1. Sample preparation

To characterise the porosity of each laminate, samples must first be cut to size and polished. The samples were cut either directly from the surplus material that was not used for testing, or when this was not possible, tested samples were used. To ensure that the test did not influence the microscopy results, samples were taken from the gripped regions and if any cracks were present, that sample was discarded.

Three samples were cut from each laminate orthogonal to the fibre direction. Each sample was cut to a length of 25 mm as this allowed an adequate area for analysis along the cut surface (two per sample). The surfaces to be evaluated required polishing to a high surface finish. This was achieved through manual grinding using Mirka WPF wet and dry sanding sheets. 120 grit is used to remove the coarse machining marks left from cutting the specimens to size and then each sample is sequentially polished up to 4000 grit. Examples of the prepared samples are shown in **Figure 3-13**.

Figure 3-13 *Example of samples that were prepared for optical microscopy.*

3.3.2. Optical Microscopy

To evaluate the porosity through microscopy, a Leica DM LM microscope was used along with an iDS UI-1460LE-C-HQ digital camera to capture images. The camera was operated using a PC running Buehler OmniMet Modular Imaging System (OMIS) software which also had image postprocessing features to measure the size of the voids. Depending on the characterisation measurement, two different lenses were used on the microscope. To measure the void content, a 10X/0.25BD lens was used as this gave a good balance between imaging a large area and capturing accurate detail of voids. On the other hand, to measure the size of the voids, a 20x/0.40BD lens was used as this allows for higher accuracy when measuring the dimensions of each void.

3.3.3. Image processing

The imaging software connected to the microscopy was used to directly measure the dimensions of the voids. The dimensions measured were the major and minor axis lengths which were determined based on the void tips, as shown in **Figure 3-14** (**A**). The orientation of the voids was noted with reference to the load direction. To ensure the results were representative of the laminate, particularly since there is a random nature to a composites microstructure, a large sample size was measured for each laminate (the exact number is described in the relevant chapter), with measurements spread across the lengths of all samples. To analyse the spread in results a relative

frequency histogram was plotted for all datasets, with an example illustrated in **Figure 3-14** (**B**).

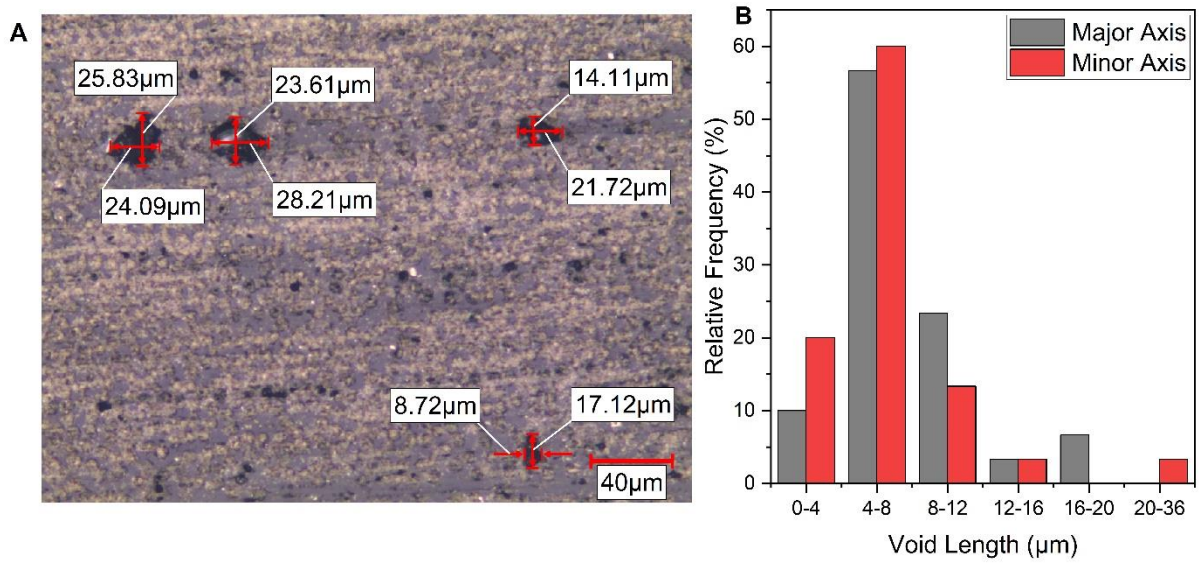

Figure 3-14 *Demonstration of void dimension. (**A**) shows an example image with the dimensions of the voids taken and (**B**) shows a relative frequency histogram of void dimensions for a laminate.*

The images that were used to calculate the void content were processed using a custom-written Python script which was run through the Spyder Integrated Development Environment (IDE). The script works by identifying voids as dark regions and isolates them from the rest of the image. An example of the process in use can be seen in **Figure 3-15**. The image processing starts by automatically loading the image to be evaluated and converting it to 8-bit greyscale. Each pixel is assigned a greyscale value within the range of 0 (black) to 255 (white). To improve the contrast between the outline of a void and the surrounding material, a Gaussian filter is applied. This works by systematically selecting each pixel and for a defined radius the average greyscale value is calculated. As the voids appear as dark regions, a greyscale threshold can be set to determine the porous regions; any pixel below the threshold value is converted to 0 (turning it black) otherwise it is converted to 255. The ratio between the number of pixels being 0 and 255 then gives the void content.

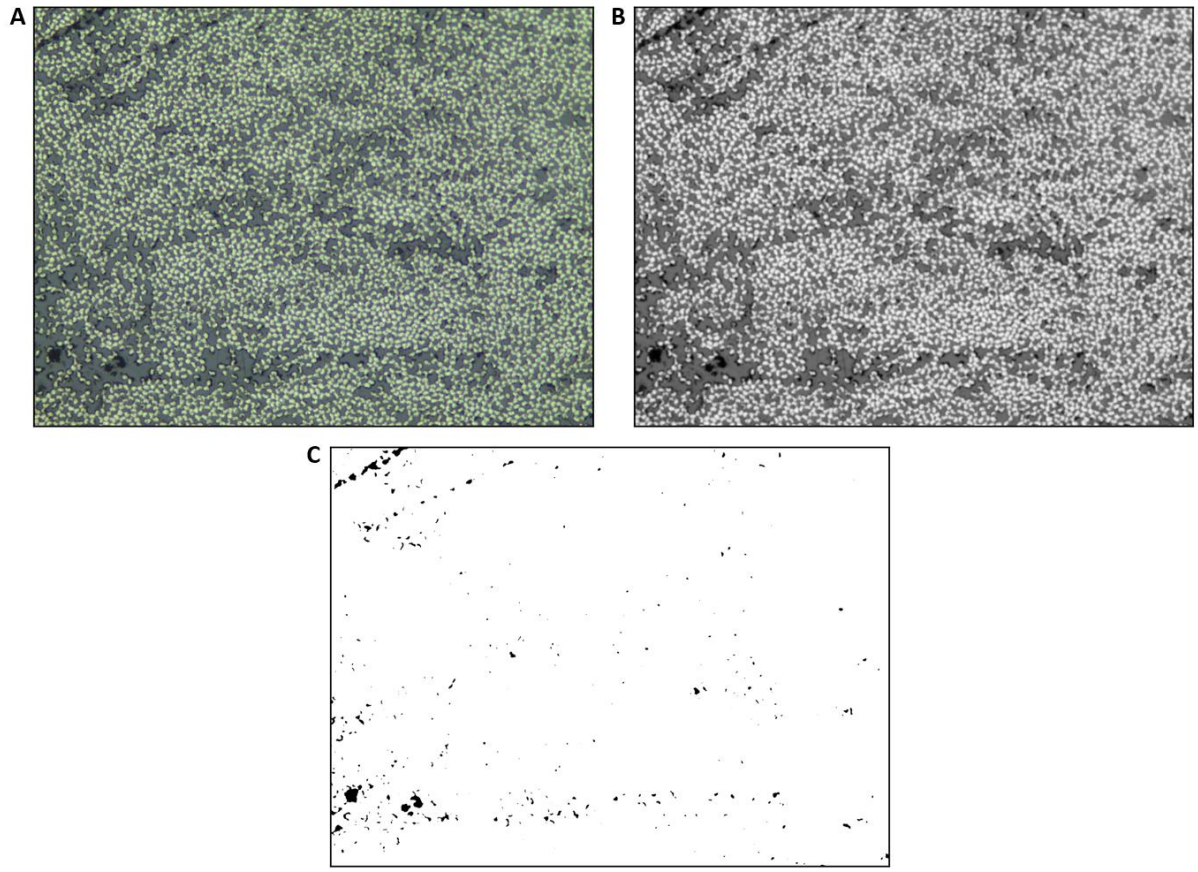

Figure 3-15 *Image processing stages to calculate the void content. (**A**) original image, (**B**) converted to greyscale and filtered, and (**C**) threshold image used to calculate void content.*

3.3.4. 3D Microscopy

The main drawback of using traditional optical microscopy is that only a 2D image can be evaluated; therefore, the depth of the voids cannot be measured. A common assumption is that voids are infinitely long; however, to determine the validity of this assumption for the voids found throughout this thesis, a 3D optical profiler was used. This process works by using a traditional microscope to image the surface; however, the depth of field is adjusted, and the resultant area of focus can be used to determine the change in surface height. The depth of field is adjusted such that the focus point starts at the highest point on a surface and ends at the lowest. At each increment, the region in focus is captured along with the relative height change compared to the initial increment. Once the full range is captured, a height map can be determined based on the incremental data. This process is fully controlled using dedicated software connected via a PC.

The system was supplied by SensorFar Metrology which comprised of a microscope using a Nikon TU Plan Flur 20x/0.45 lens with a ring light for additional lighting. The microscope is controlled using the dedicated software SensoScan which was used to program each scan, i.e., setting the scan range limits and adjusting lighting. The data from each scan was then post-processed and analysed using SensoMap. The scan was first levelled and if there was a small amount of missing data then these regions were interpolated. A combination of a depth profile plot (surface height along a line) and colour maps were used to determine the 3D geometry of a void. A 3D reconstruction of a region containing two voids can be seen in **Figure 3-16**.

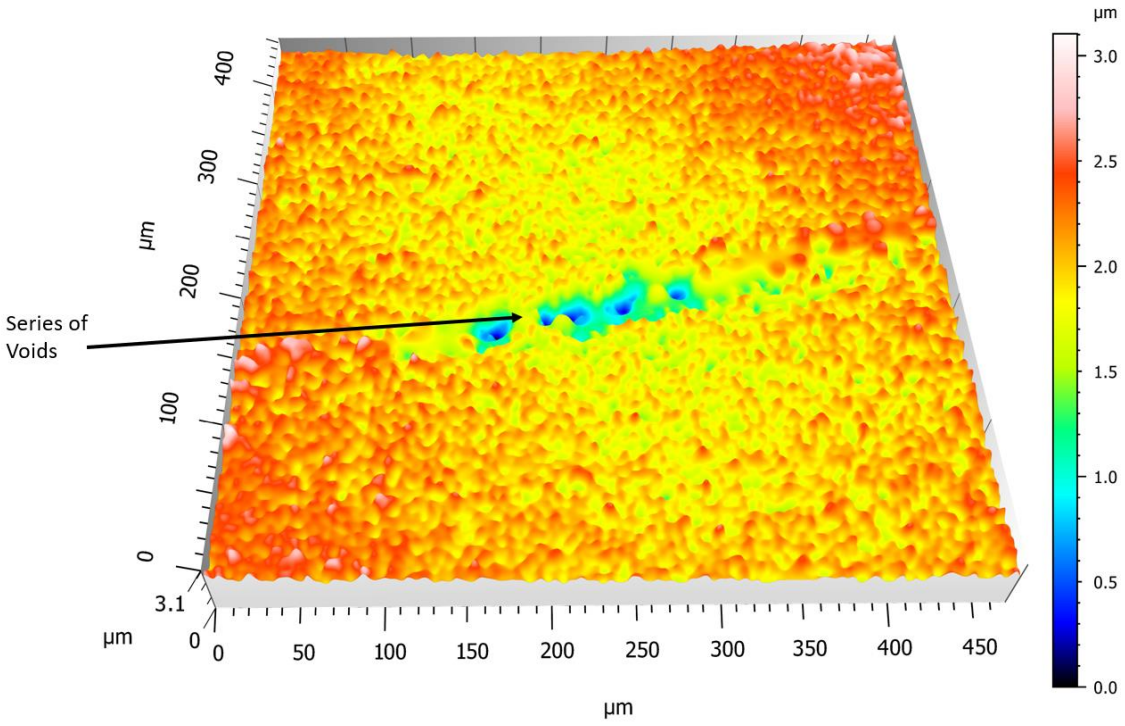

Figure 3-16 *3D reconstruction of a region containing voids.*

3.4. General Modelling Procedures

This section provides details on the more general modelling steps that are applied to all models (i.e., the procedure to create meshes and apply boundary conditions). This section does not provide specific details for certain analyses, or how the modelling framework, developed in this thesis, is set up. Specific analysis details for each model are discussed appropriately in the relevant chapter.

3.4.1. Initialization

All simulations conducted throughout this thesis were performed through Finite Element Analysis (FEA) using Abaqus/CAE 2019, with all solutions found using the Implicit solver with Abaqus/Standard. An AMD Ryzen 7 3700X CPU (8 core, 16 thread) was used to run the simulation and depending on the model element count, typically between 4-8 CPU cores were utilized per simulation.

Abaqus/CAE uses a dimensionless system; therefore, the working scale chosen was at the microscale. This meant that all geometrical dimensions were entered as μm, material properties and stresses had units of TPa, and load was defined using Newtons. Geometry was specified as 3D solid deformable and after being generated was partitioned into cells. Each cell allowed for different material properties or elements to be specified. The models created were linear elastic; thus, the material properties that were defined were the Young's modulus and Poisson Ratio. All simulations used a single general static time step with NLGeom (non-linear geometry) turned off.

3.4.2. Element selection

All simulations used 8-node 3D linear brick elements (C3D8), without reduced integration. Throughout the development in Chapter 4, it was found that absence of reduced integration increased accuracy without a noticeable impact on simulation run time. The models elemental mesh was generated by first specifying a global seed, which specifies the distance between element nodes along geometrical edges. For any regions that required a higher element count, the relevant geometry cells were partitioned to allow for local seed control along those edges, as illustrated in **Figure 3-17**. After defining element type and seeding, the mesh was generated.

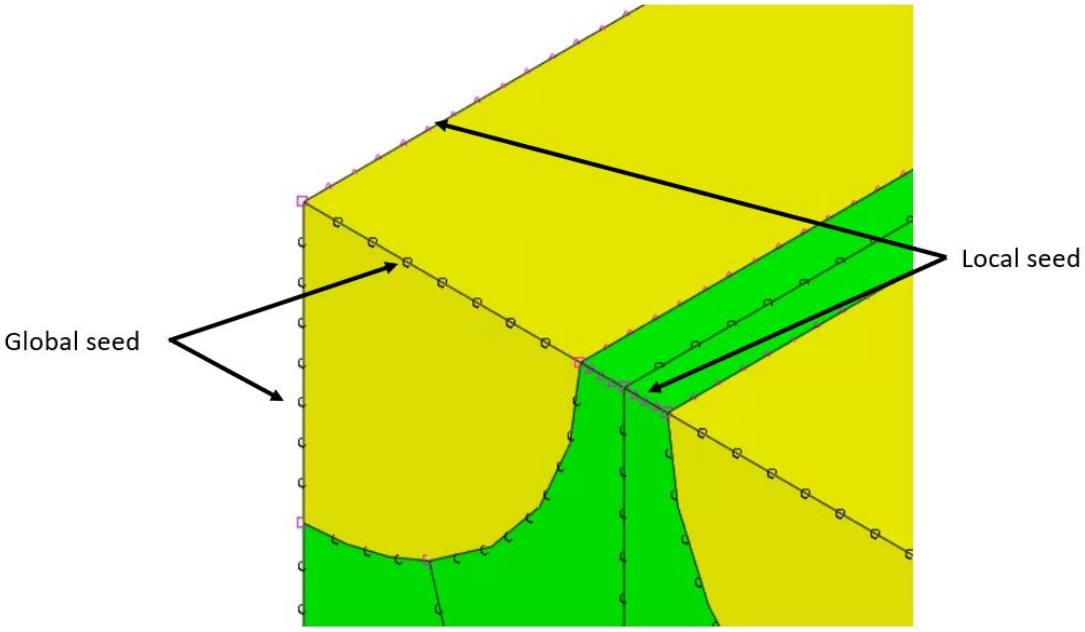

Figure 3-17 *Difference between global and local seed for mesh generation.*

To determine the most appropriate element size, a mesh convergency study was completed periodically, typically at the start of a new model or when significant updates to each model were implemented. The study was conducted by changing the elemental seed size and the stress distribution and maximum stress that was observed was recorded. The seed was initially set to generate a coarse mesh and sequentially adjusted to reduce element size. For each increment, the element count and maximum stress were recorded and plotted. The stress distribution and location of maximum stress were observed to ensure that the results were consistent. As well as monitoring the change in results, the element quality was also monitored, which included the element aspect ratio and corner angle. A typical mesh convergency study can be seen in **Figure 3-18**. The general trend is that using coarse mesh results in much lower stress values, which are initially significantly affected by a minimal change in mesh size. However, there is a turning point at which reducing the element size has a smaller impact on maximum stress. After which, increasing the element count only has a minimal impact on results, yet substantially increases simulation run time. A balance was found between computational efficiency and accuracy where the element size was targeted around/just after the knee point, as shown in the highlighted region in **Figure 3-18**.

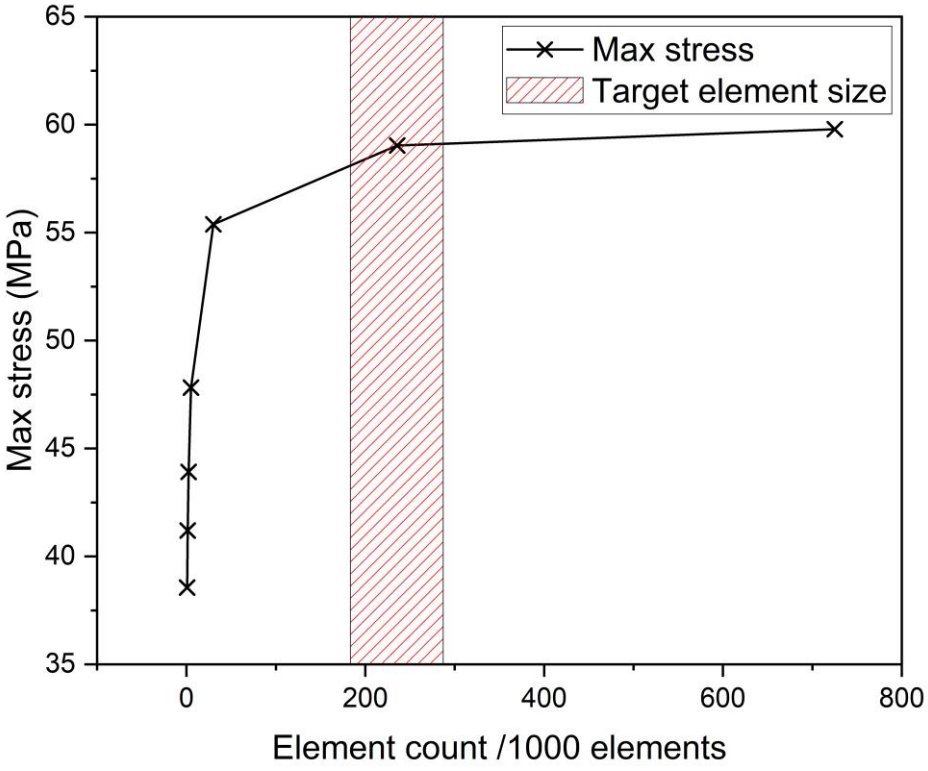

Figure 3-18 *Mesh convergency study showing the targeted element size range based on the change in maximum stress and element count.*

3.4.3. Boundary conditions

The load was induced into each model by constraining one surface and displacing the opposing side. The constraint was applied using a symmetric boundary condition as this allows orthogonal displacement and rotation; however, it restricts displacement and rotation in the load direction. For instance, if the load is applied in the X direction, then the symmetric boundary condition is defined according to Equation (3-3), where U1, UR2 and UR3 are displacements in the X direction and rotation about the Y and Z axis, respectively. This condition is important as it allows for Poisson effect to occur as well as any differences in elastic modulus throughout the model. Load was induced into the model by applying a displacement boundary condition to the surface opposing the constrained surface.

$$U1 = UR2 = UR3 = 0 \tag{3-3}$$

Micromechanical models are generally designed to be Representative Unit Cells (RUC), meaning that the geometry modelled is the smallest volume that is representative of the whole structure. One factor to be considered is the implementation of periodicity, i.e., a load applied to the unit cell on one side will also

experience the same load on the other corresponding side, as shown in **Figure 3-19** (**A**) and (**B**) where the RUC is represented by the blue square and 'virtual' RUCs are positioned adjacent on all sides if periodicity is present. This was achieved with Periodic Boundary Conditions (PBC), which work by linking nodes on adjacent surfaces. As one node is displaced, the corresponding node is moved by the same displacement vector, as illustrated in **Figure 3-19** (**C**) and (**D**). It should be noted that **Figure 3-19** is for illustrative purposes of how PBC's work and the applied load (particularly using mid-nodes) is not representative of the modelling framework developed in this thesis. To implement PBC a plugin was utilised, which can be found at the Github repository[160]. This plugin works by defining pairs of faces that contain the nodes to be tied. It systematically pairs corresponding nodes and applies a tie constraint. If more than one pair of faces is to have PBC applied, then any overlapping nodes which share the same edge must be defined and excluded.

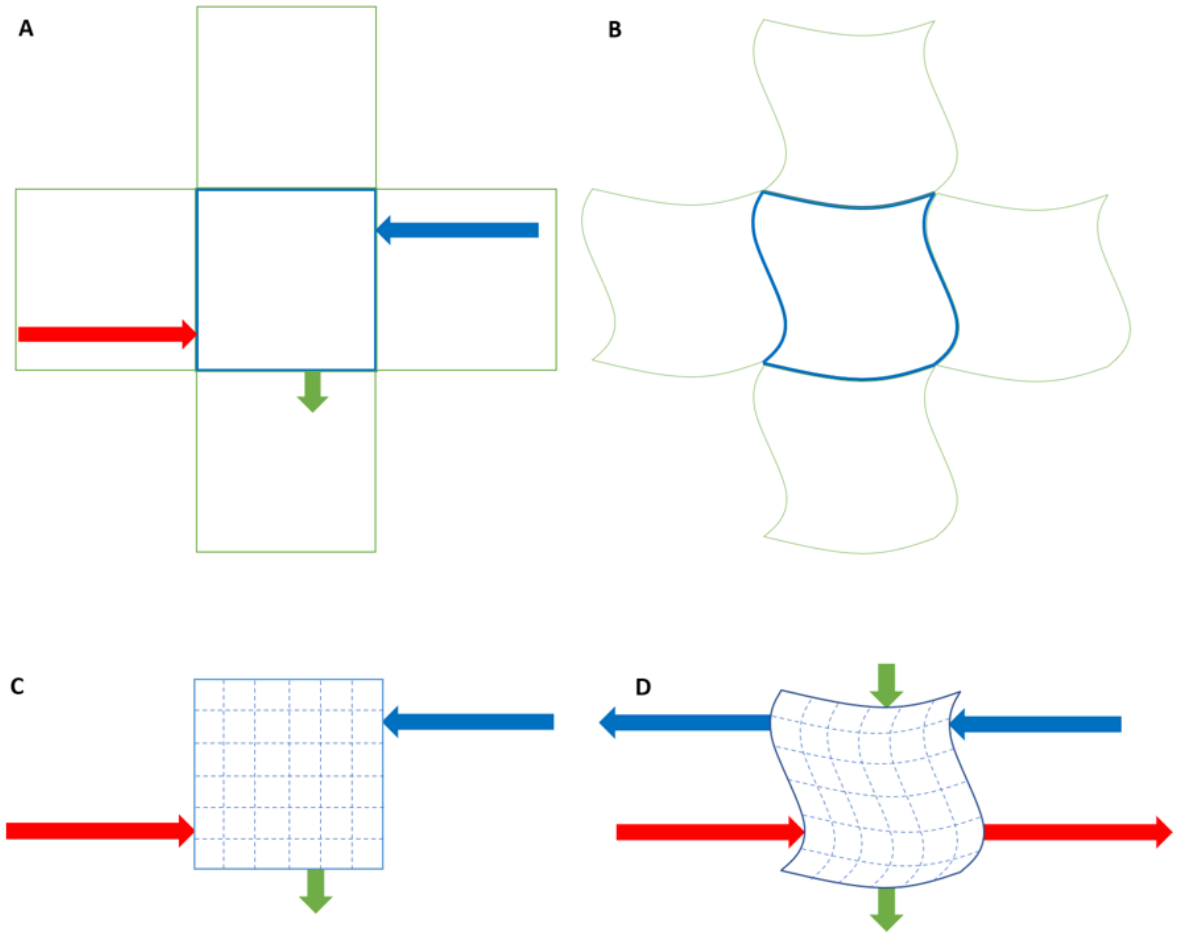

Figure 3-19 *Schematic of how periodic boundary conditions work. Parts **A** and **B** show how periodicity works on an RUC and parts **C** and **D** show a schematic of how PBC's work by linking nodes on adjacent surfaces to simulate periodicity.*

3.4.4. Reaction force measurement

The modelling framework that has been developed through this PhD determines the strength of the model. This is achieved by measuring the reaction force on the constrained surface. To do this, first, a nodal set is defined containing all nodes on the constrained face. In the pre-processor within Abaqus/CAE, a History-Output request is set up which records the reaction force in the loading direction (e.g., RF1 for load in the X direction), specifically for the constrained surface nodal set. After the model has been solved, within the visualisation environment an X-Y data plot is generated using the 'SUM ALL' function within the History-Output results request. This summates all the reaction forces within the set to output the overall force that has been applied to the model. This can then be used to calculate the model strength.

4. Model Development

4.1. Chapter Overview

This chapter develops the proposed novel modelling framework that accounts for the knockdown in the strength of unidirectional composite materials due to the inclusion of voids. Whilst previous modelling attempts found in the literature have mainly focused on the void volume fraction, the approach presented can account for accurate three-dimensional void characteristics. The chapter first explains the modelling framework, detailing the process involved. Next, preliminary models are presented studying the effect of varying the void volume fraction as well as geometrical properties. The chapter concludes by presenting a detailed investigation of each void characterisation parameter, validated using an analytical solution based on stress concentration theory.

4.2. Modelling Framework Concept/Overview

From reviewing the published literature on porosity in composites, specifically the current modelling techniques found in subsection 2.8, it was determined that there is a drive towards accurate and efficient FEA models. This means that both the void content as well as geometrical properties must be accounted for. One solution would be to generate a high-fidelity model, for example using μ-CT data; however, the computational requirement (and associated simulation run time) would be exceptionally high. Therefore, since the model setup and analysis would also be time-consuming, it would not be feasible for a design study to iterate through possible porosity scenarios. This provides the challenge of simplifying the model to conserve computational efficiency, while retaining a representative model.

The modelling framework conceptualised to address this challenge works on the assumption that voids act as stress raisers only on the matrix; thus, degrading the matrix properties. For this reason, the framework splits the modelling approach into two distinct stages, whereby first the fibres are removed from the model and only the

void(s) in neat matrix are modelled. This allows for '*effective*' matrix material properties to be predicted. The second stage is an RUC and uses the effective matrix material properties. A schematic of this approach is illustrated in **Figure 4-1**. These two stages are described in more detail as follows:

Stage 1. This stage is known as the '*Void Module*' and only considers the impact that the voids have on neat/pristine matrix. It is at this point that all the parameters that define the porosity being studied are considered. For example, this could be studying the effect of a single void, the spatial distribution of voids, a mixture of different voids, or arbitrarily shaped voids. It is at the user's discretion how best to represent the porosity that has been characterised. The benefit of this framework is that by being independent of the fibre geometry, means that a much larger model (dimensionally) does not require more elements since the element size can scale up with the size of the voids. If fibres had been included in the model, then the element size would be fixed (since fibre size does not change), and therefore, more elements would be required. An example of a void module containing three different voids is shown in the stage 1 part of **Figure 4-1**.

Stage 2. This stage is known as the RUC and is used to study how the inclusion of the fibres, and their distribution, act as stress raisers on the effective matrix calculated from the previous stage. Similar to the void module, the framework is flexible to allow different RUC's and it is at the user's discretion to decide how is best to represent the ply geometry, i.e., a single fibre or a randomly distributed fibre array can be used. An example RUC containing a central fibre and four-quarter fibres is shown in the Stage two part of **Figure 4-1**.

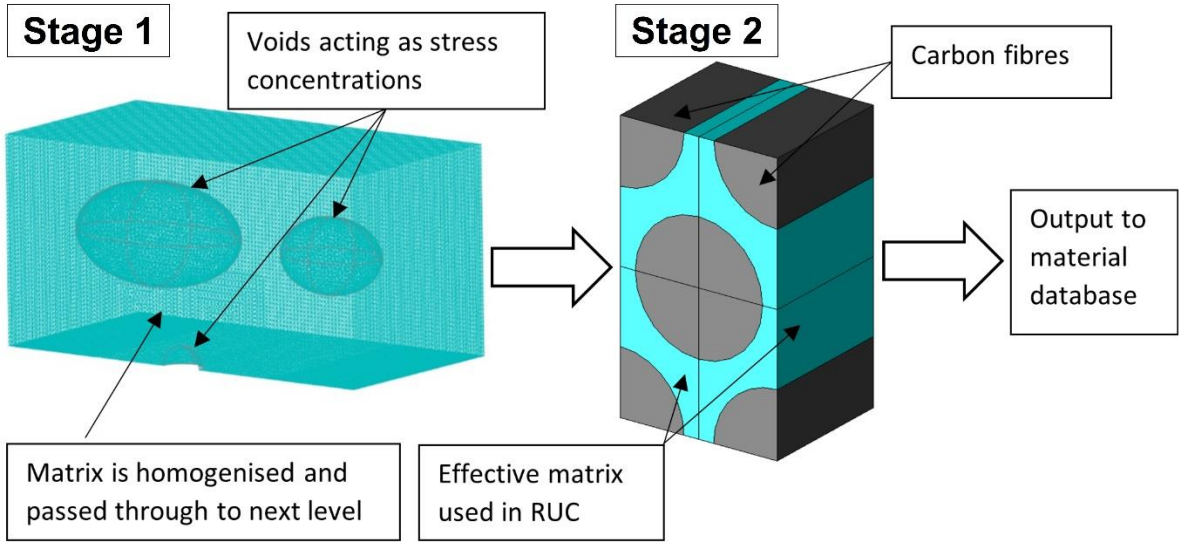

Figure 4-1 *Schematic of modelling framework, where the void module is shown in Stage 1 and an RUC using the effective matrix is shown in Stage 2.*

4.3. Analysis approach

A script was written to allow for the automation of both the induction of load and analysis of the model for both stages. An assumption was made that in the transverse direction, there is a brittle failure, which is in line with published literature.[84,161,162] Therefore, at the point when a single element fails, the analysis is stopped, and the strength of the model can be calculated. However, as this type of failure was an assumption, the script was designed such that, if required, it could be further developed to account for damage. To predict when a single element fails, the Von Mises yield criterion was used, as defined in equation (4-1), where where σ_{vm} is the Von Mises stress, and σ_{ij} (ij=11, 22, 33, 12, 23 and 13) are the stress tensor components. Whilst other failure models are available such as the Drucker–Prager yield model, as described in subsection 2.8.2.2, comparisons to equivalent analytical models have shown excellent correlation, as described later in subsection 4.5, and it was considered appropriate. The high-level workflow for the script was as follows:

- Incrementally increase the applied load in the model by increasing the displacement for each iteration.
- At each increment extract the stress components on each element.
- Use a stress criterion to determine if the element has failed.

- If no elements have failed increase the displacement and repeat until at least one element has failed.
- Once an element has been identified to have failed the simulation analysis is stopped.

To achieve this the following definitions were required:

- To apply the material properties.
- To apply displacement using a variable (so that the displacement can be updated between each iteration).
- Run the analysis.
- Use a 'for' loop to iterate through each element extracting the stress components which were used to determine the overall stress state of the element, identifying if it had failed.

The Von Mises yield criterion:

$$\sigma_{vm} = 1/\sqrt{2}\sqrt{(\sigma_{11}-\sigma_{22})^2+(\sigma_{22}-\sigma_{33})^2+(\sigma_{33}-\sigma_{11})^2+6(\sigma_{23}^2+\sigma_{31}^2+\sigma_{12}^2)^2} \quad (4\text{-}1)$$

A flowchart of the script can be seen illustrated in **Figure 4-2** and the full script can be found in Appendix A, section 8.2.

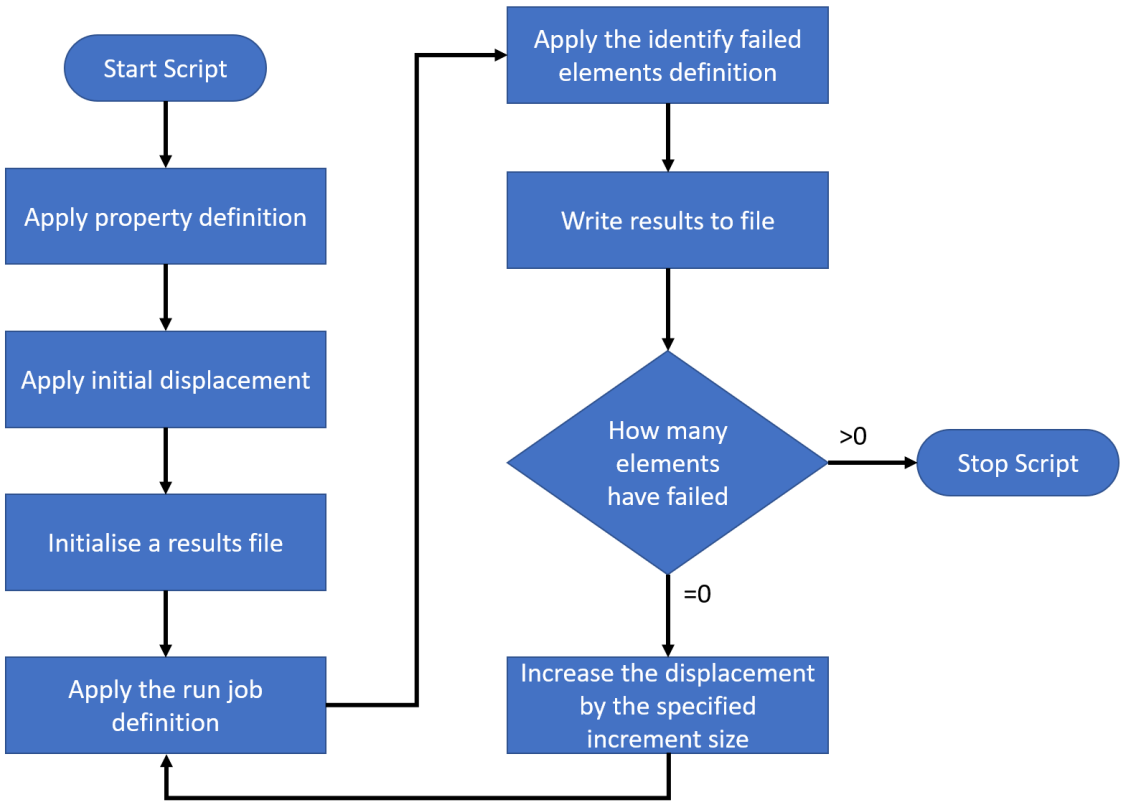

Figure 4-2 *Flow diagram explaining the working principle of the failure detection script.*

4.4. Preliminary Models

With the modelling framework conceptualised and a script written to determine the point at which failure occurs, a series of models were developed to investigate the model's response. At this point, only the reduction in strength was investigated. One of the main design principles for the modelling framework was to account for both the void content as well as geometrical features; therefore, both factors were investigated. Since the main focus of this modelling process is the stage 1 model and the homogenised matrix strength that it predicts, only this stage was modelled. Whilst the full modelling process could be followed through, for consistency reasons the RUC would be the same for each model and therefore becomes redundant.

The modelling framework assumes brittle failure, therefore, the strength of the model is equivalent to the applied load/stress at the point that a single element fails (which was set to a nominal value of 50 MPa). For the purpose of this study it is more appropriate to report the strength as an applied stress. This is because it allows for comparisons, in the later subsections, to an analytical model which relates the

maximum stress at a stress concentration to the applied stress (i.e. the model strength).

To investigate the effect of void content in isolation, a spherical void was modelled, the matrix surrounding it was reduced to increase the void volume fraction. To investigate how the shape of the void affects the strength, three models were set up: a spherical void getting larger and an elliptical void increasing in length along either the major or minor axis whilst the other axis was fixed. The schematics of these four studies are shown in **Figure 4-3**. The models were run following the general principles outlined in subsection 3.4 and the test matrix can be seen in **Table 4-1**.

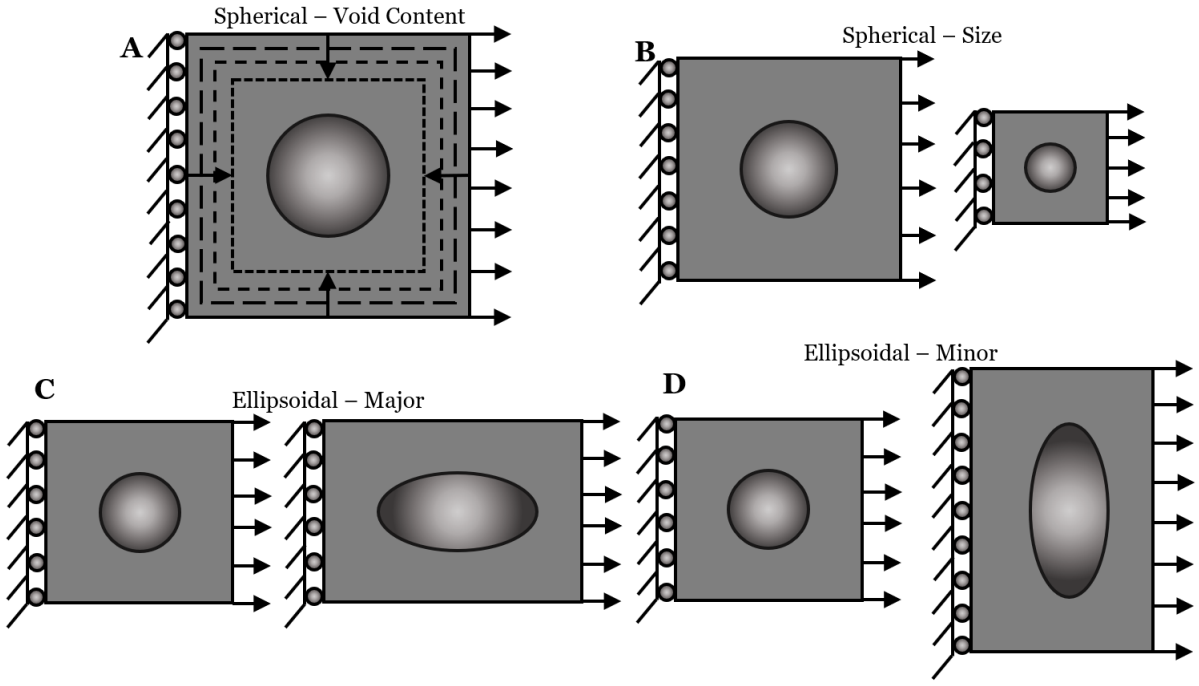

Figure 4-3 *Schematics of void content and void geometry studies. (**A**) Void content with constant void size, (**B**) Size with constant void content, (**C**) void shape in major axis and (**D**) void shape in minor axis.*

Table 4-1 *Test matrix for void parameter study using the modelling framework.*

Void Parameter	Void Type	Void Content / %	Void Dimensions / µm	Void Module Dimensions / µm
Shape	Spherical	0.15	5 x 5	35.21 x 35.21 x 35.21
		0.50		23.57 x 23.57 x 23.57
		1.00		18.71 x 18.71 x 18.71
		1.50		16.34 x 16.34 x 16.34
		2.00		14.85 x 14.85 x 14.85
		2.50		13.78 x 13.78 x 13.78
Shape	Spherical	1.50	1 x 1	3.27 x 3.27 x 3.27
			2.5 x 2.5	8.17 x 8.17 x 8.17
			5 x 5	16.34 x 16.34 x 16.34
			7.5 x 7.5	24.51 x 24.51 x 24.51
			10 x 10	32.68 x 32.68 x 32.68
	Ellipsoidal - Major	1.50	5 x 2.5	16.34 x 8.17 x 8.17
			5 x 5	16.34 x 16.34 x 16.34
			5 x 7.5	16.34 x 24.51 x 24.51
			5 x 10	16.34 x 32.68 x 32.68
			5 x 12.5	16.34 x 40.85 x 40.85
	Ellipsoidal – Minor	1.50	2.5 x 5	8.17 x 16.34 x 16.34
			5 x 5	16.34 x 16.34 x 16.34
			7.5 x 5	24.51 x 16.34 x 16.34
			10 x 5	32.68 x 16.34 x 16.34
			12.5 x 5	40.85 x 16.34 x 16.34

The effect of increasing the void content on the model strength can be seen in **Figure 4-4**, where there is a small and gradual reduction in strength. It was anticipated that as the void content increased, the strength would decrease. Whilst this was observed, the amount that the strength reduced by across the 0.15% to 2.5% range was significantly less than anticipated. After further investigations, detailed in subsection

4.5.1, the minimal effect was determined to be due to two factors. Firstly, the shape of the void is constant, and therefore the stress raiser does not change (this was by design for the study). Secondly, the amount of surrounding material was great enough that it could be approximated to be near infinite; therefore, any change only had a minimal effect. For an effect to be observed, the amount of material surrounding the void would need to be substantially reduced. The proposed study, where low surrounding material was present, was conducted in subsection 4.5.1. In short, the results showed that when there is minimal surrounding material present, a difference could be observed in the strength between models with different void volume fractions. However, after increasing the surrounding material the effect on strength converges and no further change occurs. It is in this region, where sufficient material is present around the void, where any change does not influence the required force to cause failure.

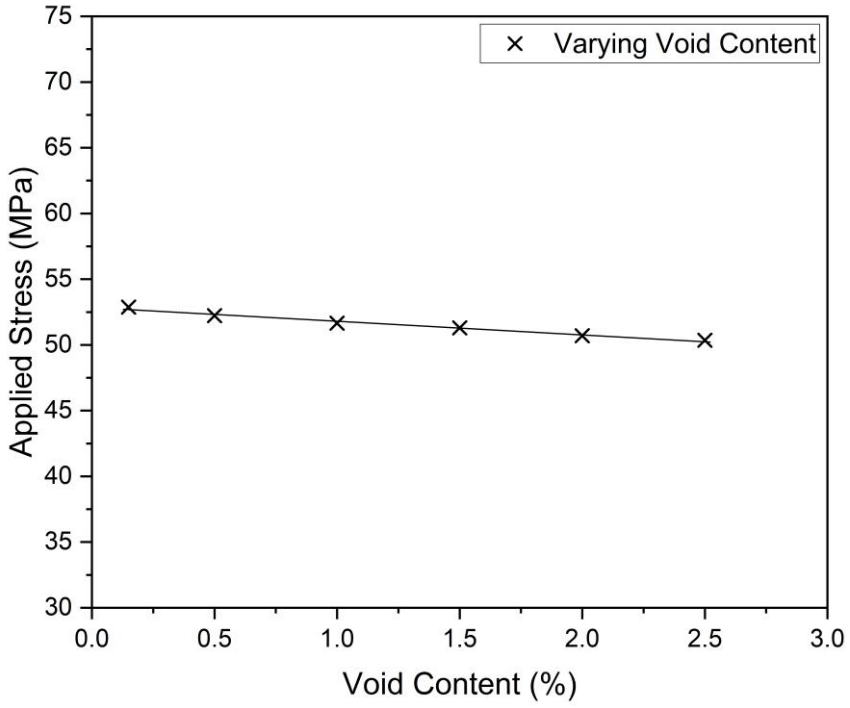

Figure 4-4 *Effect of increasing the void content on the required applied stress for a maximum stress of 50 MPa at the stress raiser in the stage 1 model.*

The results for the study where the shape of the void was changed, whilst keeping the void content constant at 1.5 %, can be seen in **Figure 4-5**. Thus, when the diameter of a spherical void was increased, no change in strength was observed. The explanation for this is linked to the shape of the void. Since the void is perfectly circular, i.e., the ratio between the 'notch' radius and the radius of the defect is constant in all models, as the diameter of the void increases, the same applied stress is required for a

failure/maximum stress to be observed. The stress concentration theory[163] is explained in detail in subsection 4.5.1.

In contrast, elongating the void along either the major or minor axis results in either a substantial decrease or increase in strength, respectively. Elongating the void in the major axis (in the same direction as the applied load) has the effect of reducing the stress concentration and minimises the change to the load path, resulting in a lower reduction in strength. Likewise, when the length of the void is increased along the minor axis (transverse direction to the applied load), this has the opposite effect, such that the stress concentration is increased and results in a greater reduction in strength. In both cases, there is a non-linear effect which is due to the void tip radius exhibiting a non-linear variation with void length. When the minor axis length is increased the stress concentration always increases; however, the rate of change of the radius reduces, which is why there is a plateauing effect, seen by the red curve of **Figure 4-5**.

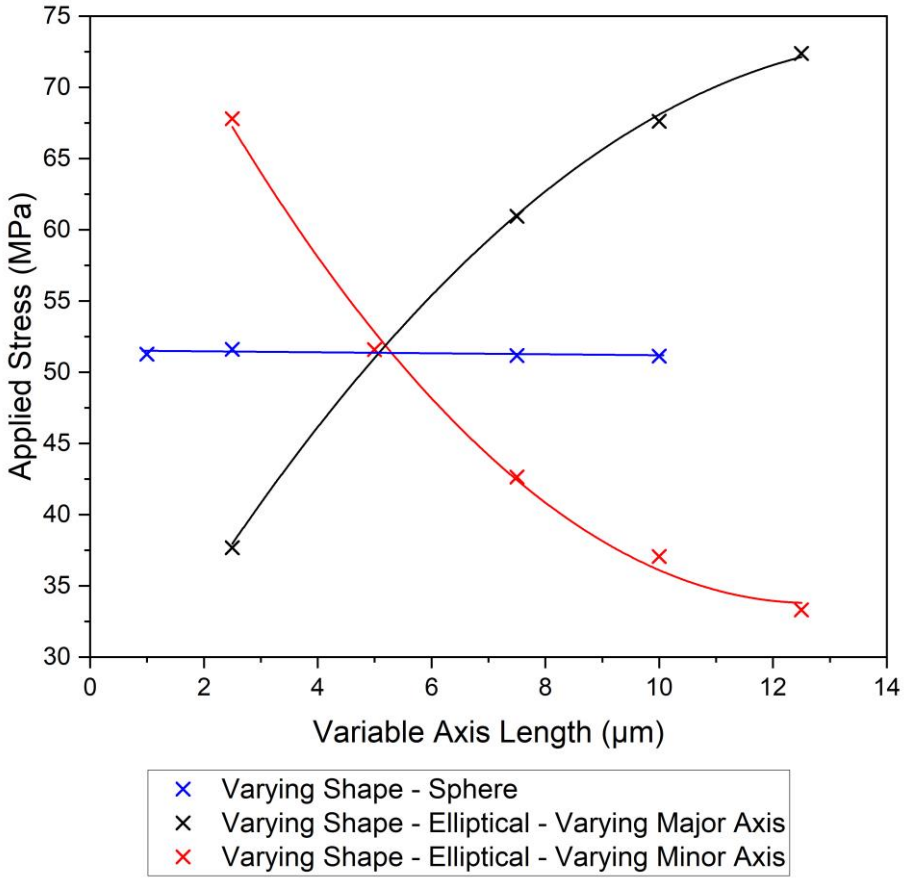

Figure 4-5 *Effect of varying the void shape on the required applied stress for a maximum stress at stress raiser of 50 MPa in the stage 1 model.*

4.5. Shape and Size Influence

The preliminary models showed that the geometry of the voids is a key parameter in determining the reduction in strength, and due to the void content set-up of the models, increasing void volume fraction resulted only in a minimal effect. Therefore, it was clear that further analysis was required to understand the magnitude that each parameter had on the resultant strength. To represent the stage 1 model, a finite thickness plate was modelled using a through hole to simulate a void, this allowed the model to be simplified and aiding the isolation/analysis of each variable. This also allowed direct comparisons between the shape of the 'void/notch' and stress concentrations, allowing comparisons to analytical models.

4.5.1. Constant Stress Raiser with Varying Void Content

The first parameter investigated was the void content. This was achieved through three parametric studies, where the width of a plate increased, and for each study, a different hole diameter was used, as illustrated in **Figure 4-6** (two-hole diameters and plate widths shown for illustration purposes). The three-hole diameters chosen were 10 μm, 15 μm and 20 μm and the plate widths increased from 15 μm, 20 μm and 30 μm respectively up to 100 μm. The boundary conditions were applied such that the models were constrained on one end and the opposing surface was loaded until an element reached 50 MPa, at which point the reaction force was measured to determine the applied stress.

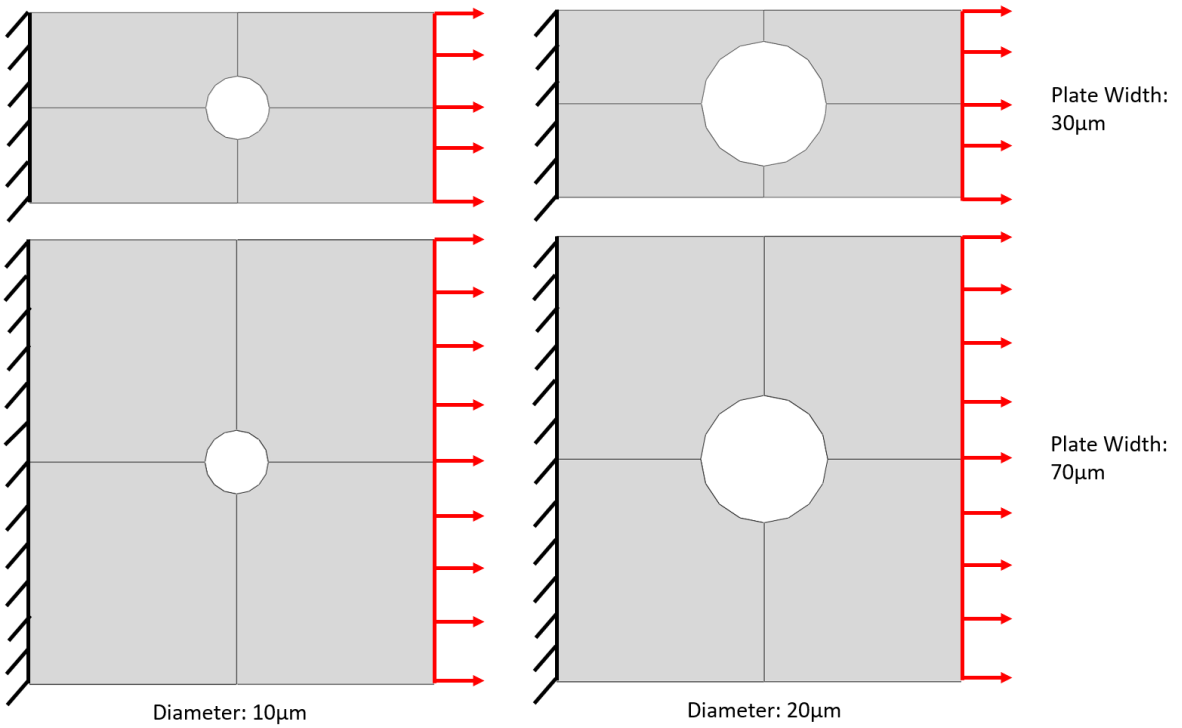

Figure 4-6 *Example of increasing plate width for two of the three different hole diameters.*

The results from these models can be seen in **Figure 4-7** where the first notable observation is that the models are much more sensitive to an increase in plate size at lower widths, however, after a certain point any further increase has a minimal effect on the results and the applied load rquired to achieve a peak stress of 50 MPa converges. The reason for this trend is due to the stress contours surrounding the void. As shown in **Figure 4-8**, there is a high stress concentration around the tip of the hole, nevertheless, at a certain distance away from the hole (along the dotted line in the figure) the stress reduces significantly. This resulted in the stress fields not changing when increasing the plate width. This is also illustrated by plotting the stress contour along a line between the top of the hole and the edge of the plate. This can be seen in **Figure 4-9** for the three different hole diameters, where there is initially a significant drop in the stress state of the elements before levelling off.

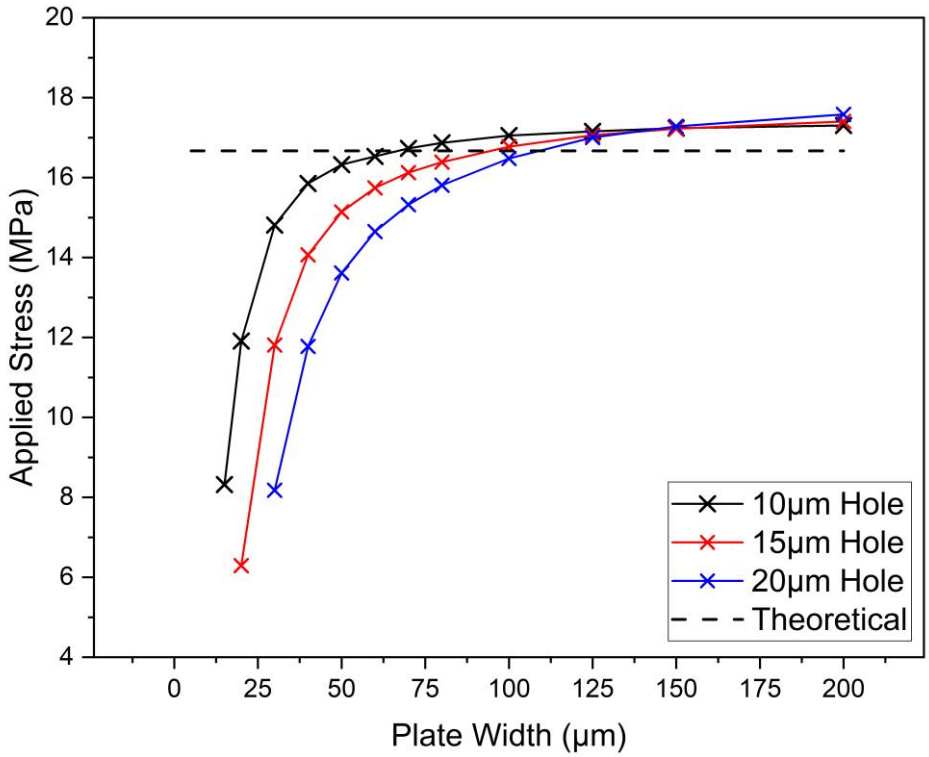

Figure 4-7 *Influence of increasing plate width, simulation of a reduction in void content, on the required applied stress for maximum stress of 50 MPa around stress raiser, at three different hole radii.*

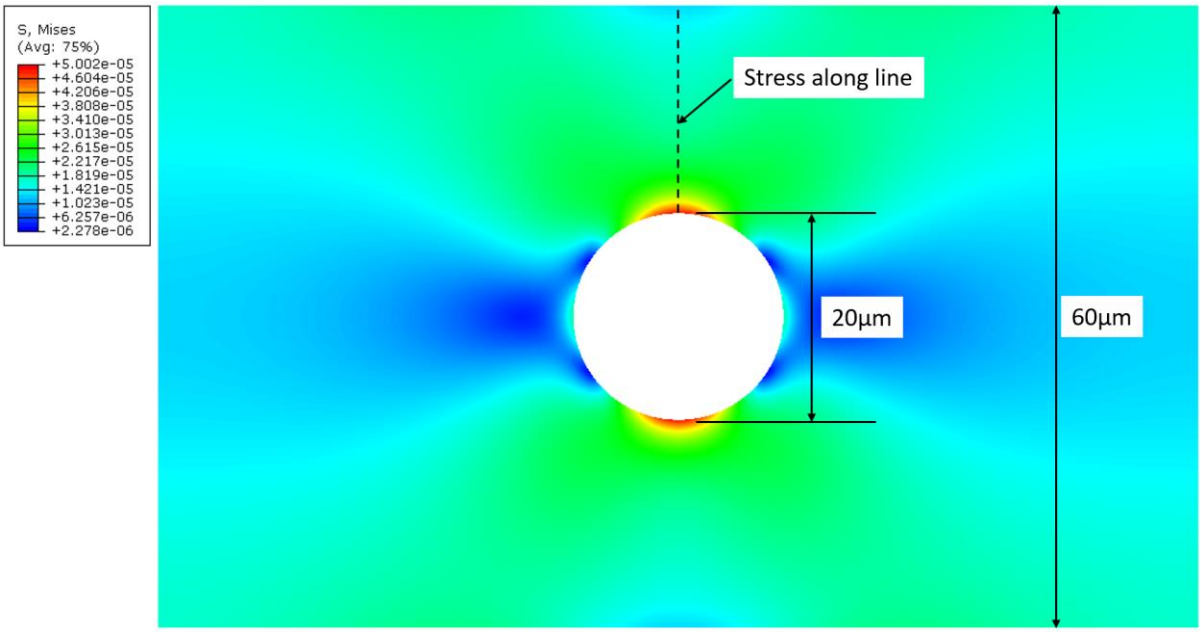

Figure 4-8 *Stress contour plot of a plate containing a 20 μm diameter hole with edges sufficiently far away from the central hole. After a certain distance away from the stress raiser there is only a minimal change in stress. The units of the legend are in TPa.*

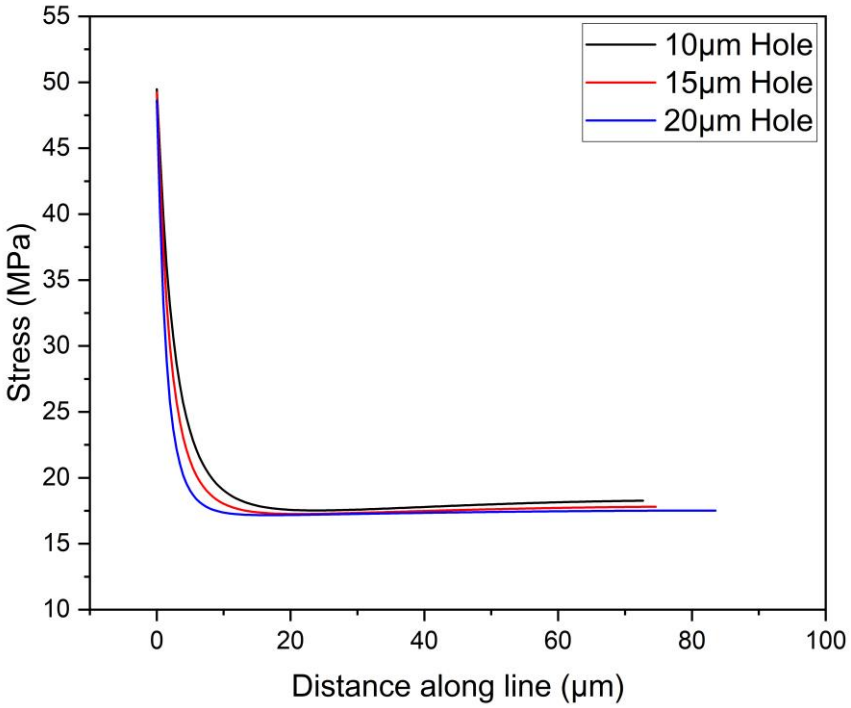

Figure 4-9 *Elemental Von Mises stress along the line between the tip of the hole and the edge showing a significant drop in stress initially before levelling off to a consistent stress state.*

Another observation of **Figure 4-7** is that at smaller plate widths, approximately 60 μm and less, the applied stress of the model is higher when the diameter of the holes is smaller. However, past this point, the applied stress converges to approximately 17.5 MPa. This is in line with the results found in Section 4.4, where increasing the void content had little to no effect on the results. This can be explained when considering stress concentrations and calculating the maximum stress at a stress concentration. As presented in Callister's *"Materials Science and Engineering: an Introduction,"*[163] the maximum stress at a stress concentration σ_m, such as the void extremity, is given by equation (4-2):

$$\sigma_m = \sigma_o \left[1 + 2\left(\frac{a}{\rho_t}\right)^{0.5}\right] \qquad (4\text{-}2)^{163}$$

Generally, σ_o, a and ρ_t are referred to as the applied stress, halve crack length and radius of the crack tip. However, in this work, it is more appropriate to use the terminology defect length and notch radius, for a and ρ_t, as this is more accurate to what is being represented. Whilst the theory is closely related to studying microscopic cracks, Callister[163] explicitly reports that the analytical model can be used for macroscopic features, such as corner radii or voids, which is also the case in this work.

Equation (4-2)[163] can be rearranged into equation (4-3), to determine the applied stress for a maximum stress at the stress concentration:

$$\sigma_o = \frac{\sigma_m}{\left[1 + 2\left(\frac{a}{\rho_t}\right)^{0.5}\right]} \tag{4-3}$$

Therefore, for a circular hole in a plate, such as in this example, the halve defect length and notch radius are the same (the radius of the hole). This means that for any size hole, the $\frac{a}{\rho_t}$ term becomes 1. For instance, when evaluating for a maximum stress of 50 MPa, substituting the geometrical parameters for a 10 μm or 15 μm hole into equation (4-3) results in the applied stress being the same:

$$\sigma_o = \frac{50}{\left[1 + 2\left(\frac{10}{10}\right)^{0.5}\right]} = \frac{50}{\left[1 + 2\left(\frac{15}{15}\right)^{0.5}\right]} = \frac{50}{[1 + 2(1)^{0.5}]} = \frac{50}{[3]} = 16.7\ MPa \tag{4-4}$$

Therefore, for a plate with a circular hole, equation (4-3) can be simplified to equation (4-5).

$$\sigma_o = \frac{\sigma_m}{[3]} \tag{4-5}$$

This shows that for the plate in this case study to have a peak stress of 50 MPa, the applied stress would theoretically be 16.7 MPa if a circular hole was present. This theoretical value is added to **Figure 4-7**. It can be seen that for all three diameters, the strength converges near to the theoretical strength with a 4.8% over prediction. This solution is only valid for plates that are assumed to be infinitely wide. The effect of shorter plates is apparent for the widths below 60 μm in this case, where the difference in hole diameter is apparent.

Instead of plotting the results in terms of plate width, it is also possible to use the defect volume fraction (synonymous with void content) as shown in **Figure 4-10(A)**. In this case, the defect volume fraction is determined based on the volume of the hole removed and the volume of the plate across the hole diameter, as illustrated in **Figure 4-10(B)**. It can be seen that for higher defect volume fractions (i.e., shorter plate widths), there is a difference in the applied stress for a peak stress of 50 MPa. However, as the plate width increases and the defect volume fraction reduces, the applied stress between the three series of models converges to approximately 17.5 MPa.

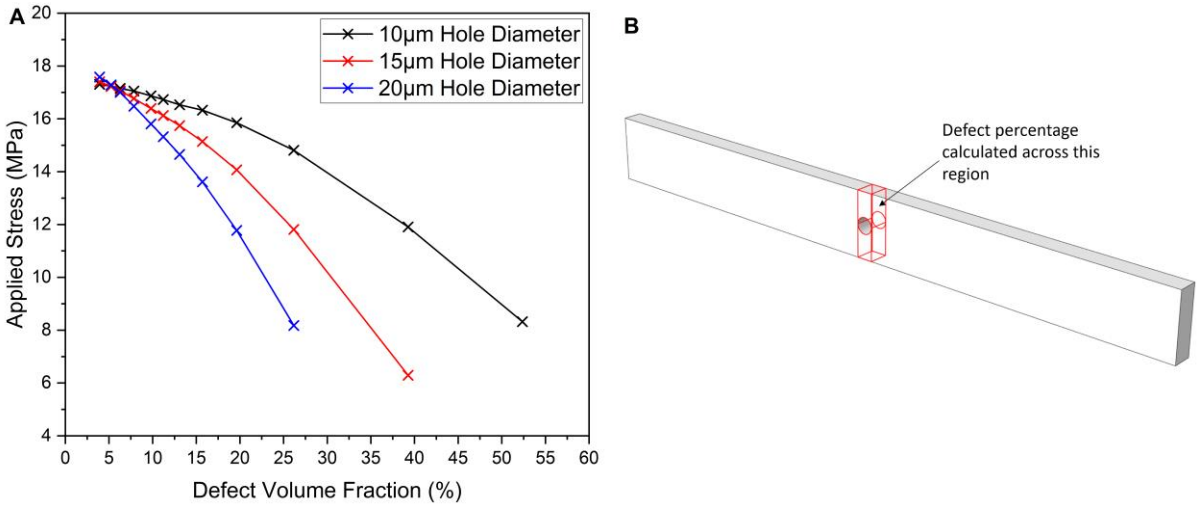

Figure 4-10 *Defect percentage on applied stress for a maximum stress of 50 MPa at the stress raiser. (**A**) The results of the three parametric studies presented (**B**) shows the location where the defect percentage is calculated.*

4.5.2. Influence of stress raiser

To understand how the maximum stress around a stress raiser changes due to a change in the geometrical features, itis important to understand how the geometry of voids affects the local matrix stress around the void. As shown in subsection 4.5.1 the geometrical parameter is made up of both the size of the void and the radius of the stress concentration at the tip of the void. To investigate these parameters a series of studies were performed, in the same manner as before by modelling a plate so that the model can be correlated to equation (4-3), and with various notches being adapted. The series of models included varying the size/length of the notch, the radius at the extremity of the notch and studying the tip radius of the notch in isolation. For all studies, the effect on the maximum stress, due to the stress concentration, was the dependent variable of interest.

4.5.2.1. Notch size

This study involved modelling a notch in the middle of a plate (using symmetry boundary conditions along the centre plane) whereby the length of the notch was increased and the effect on the stress at the notch tip was monitored. This was done by monitoring the force required to reach a predefined stress at the stress concentration. As the length of the notch was increased, the reduction in width was set

such that the volume of material removed was always constant. This was to ensure that the defect volume fraction was consistent in all models and did not influence the results. The baseline area (since plate thickness is constant across all models) is determined based on a spherical hole with a radius of 10 μm, giving an area of 314.16 μm². The notch length was increased in increments of 5 μm up to 25 μm. The geometry of all four models is illustrated in **Figure 4-11** and summarised, including the applied stress for a maximum stress of 50 MPa, in **Table 4-2**. To ensure an appropriate mesh was used, a mesh convergency study was conducted, where the results are presented in **Figure 4-12** and the chosen mesh is shown in **Figure 4-13**. In all models, it was ensured that there was a node at the notch tip, to ensure that this point was monitored accurately. Mesh statistics of the chosen mesh are summarised in **Table 4-3**. These models were also compared to the analytical solution using equation (4-2), where the notch tip radius was measured when defining the geometry in ABAQUS/CAE.

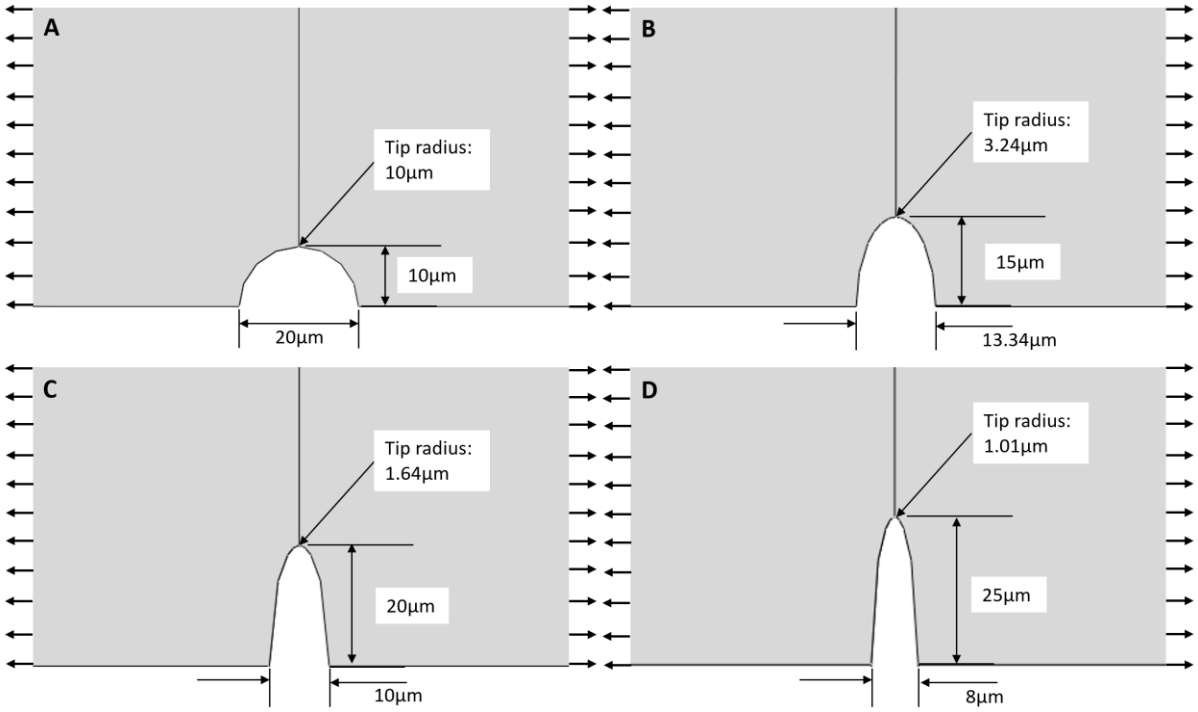

Figure 4-11 *Schematic of the different geometries used in the notch length study, arrows show load direction. N.B. not drawn to scale.*

Table 4-2 *Notch dimensions used in the study including the associated applied stress when the maximum stress at the stress concentration is observed.*

Notch width / µm	Notch length / µm	Aspect ratio	Notch tip radius / µm	FEA model applied stress / MPa	Analytical model applied / MPa
20.0	10	1.0:1	10	18.1	16.7
13.3	15	2.2:1	3.24	11.1	9.4
10.0	20	4.0:1	1.64	8.0	6.3
8.0	25	6.3:1	1.01	6.3	4.7

Table 4-3 *Mesh statistics for the chosen mesh.*

Avg. aspect ratio	Max. aspect ratio	Avg. min. corner angle / °	Worst. min. corner angle / °	Avg. max. corner angle / °	Worst. max. corner angle / °
1.09	3.24	88.89	20.93	91.11	165.11

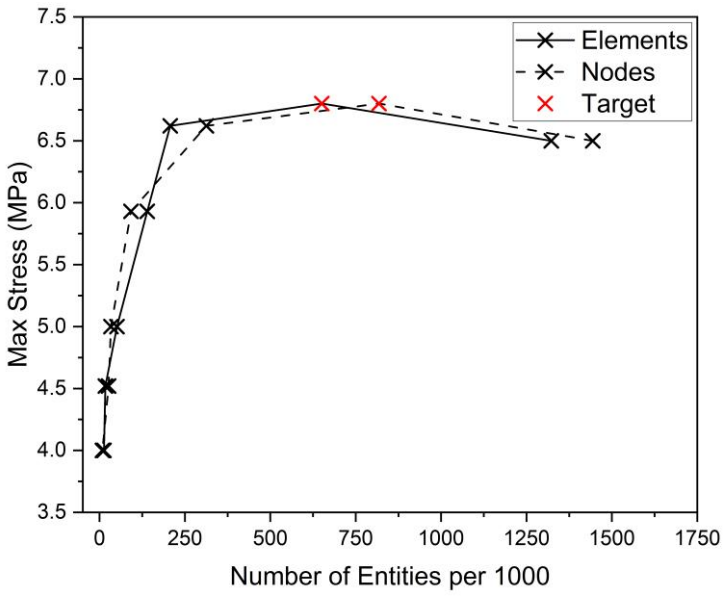

Figure 4-12 *Mesh convergency study of defect length models.*

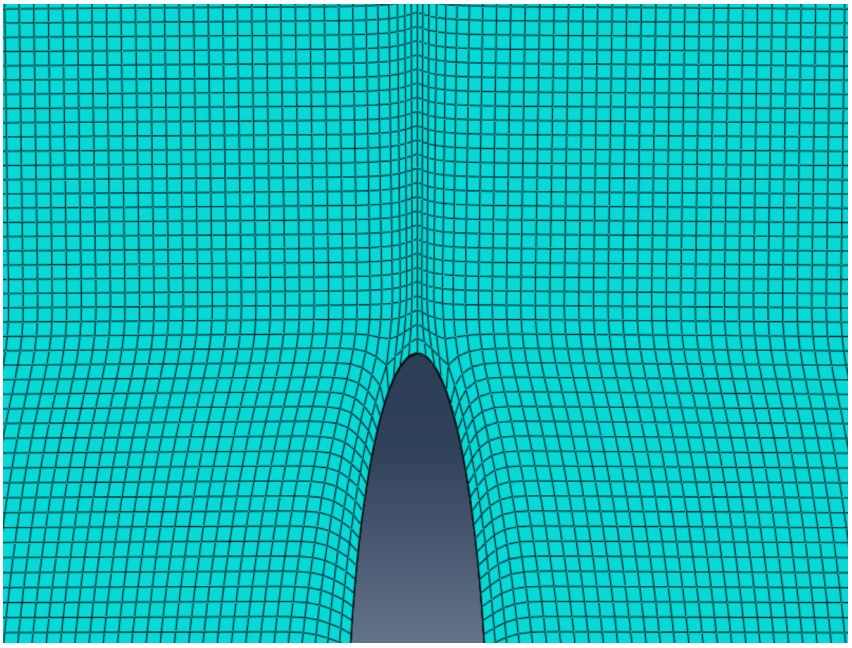

Figure 4-13 *Target mesh used to capture stress concentration.*

The results for both the FEA and analytical models can be seen in **Figure 4-14**, and a stress contour plot is also shown in **Figure 4-15**, where an exceptionally good correlation between both models can be seen. The FEA model follows the same non-linear trend as the analytical model with a correlation of between 0.9 and 3.1%. The results show that as the notch length is increased the applied stress required for a maximum stress of 50 MPa substantially reduces. The nonlinearity is likely due to a reduction in the rate of change of the notch tip radius with increasing notch length.

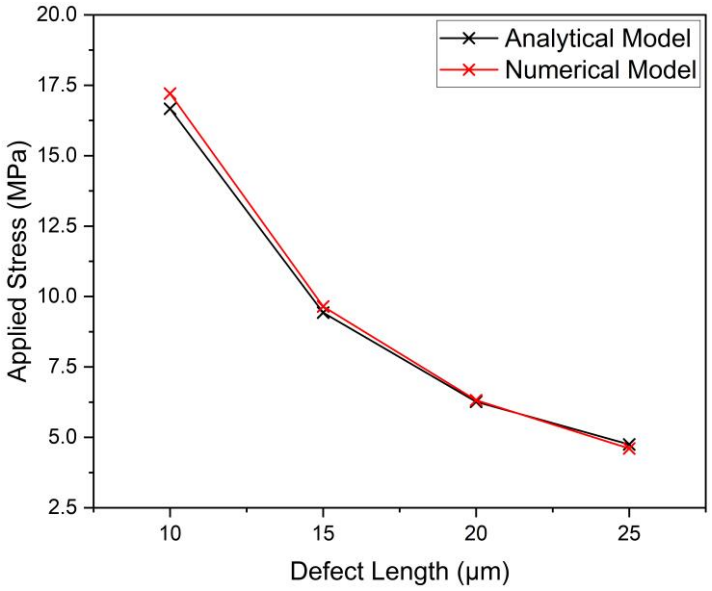

Figure 4-14 *Results of how increasing the notch length at a constant defect volume fraction affects the required applied stress for a maximum stress of 50 MPa at the stress raiser.*

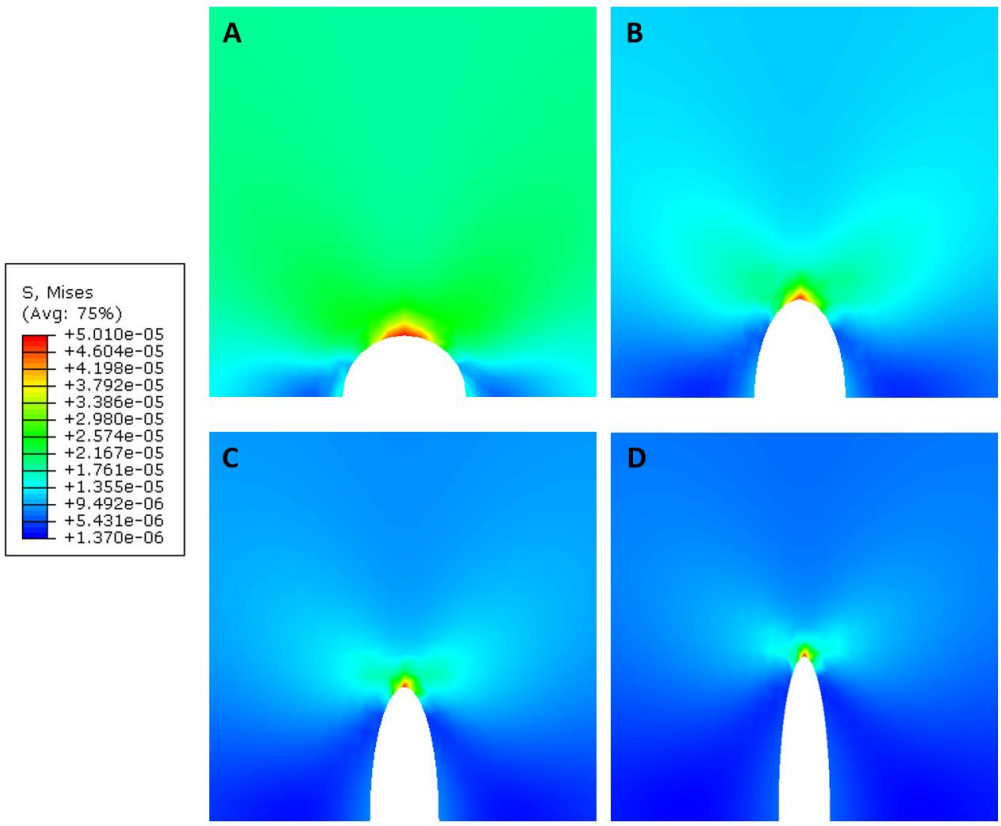

Figure 4-15 *Stress contour plots for models with notch lengths (**A**)10 µm (**B**)15 µm (**C**)20 µm and (**D**)25 µm.*

4.5.2.2. Slot with Variable Tip

The previous series of models in subsection 4.5.2.1 investigated how increasing the notch length with a constant defect volume fraction affected the results; however, two parameters were changed in each model: the notch length and notch tip radius. Therefore, the focus of the next study investigated how the notch tip radius affected the results at a constant notch length.

This was achieved by modelling a notch at a constant length and then reducing the radius of the notch tip. Previously, the notches were assumed to be elliptical and were defined by the major and minor axis, resulting in a variable radius along the major axis length. Therefore, to change the notch tip radius, several adjustments to define the geometry of a notch were made. First, a short slot of length 5 µm and 10 µm width were drawn and the coordinate of where the notch tip radius was located, as illustrated in **Figure 4-16**(**A**). The coordinate of the location for the notch tip was used for all studies. For each of the notch tip radii, a circle, with the radius of the required notch to be studied, was drawn such that the top of the circumference of the circle was

coincident with the notch tip coordinate, as illustrated in **Figure 4-16**(**B**). A series of lines and arcs were then drawn to connect the end of the slot and notch tip radii ensuring a smooth transition, as shown in Figure 4-16(**C**). The final notch profile is then shown in **Figure 4-16**(**D**).

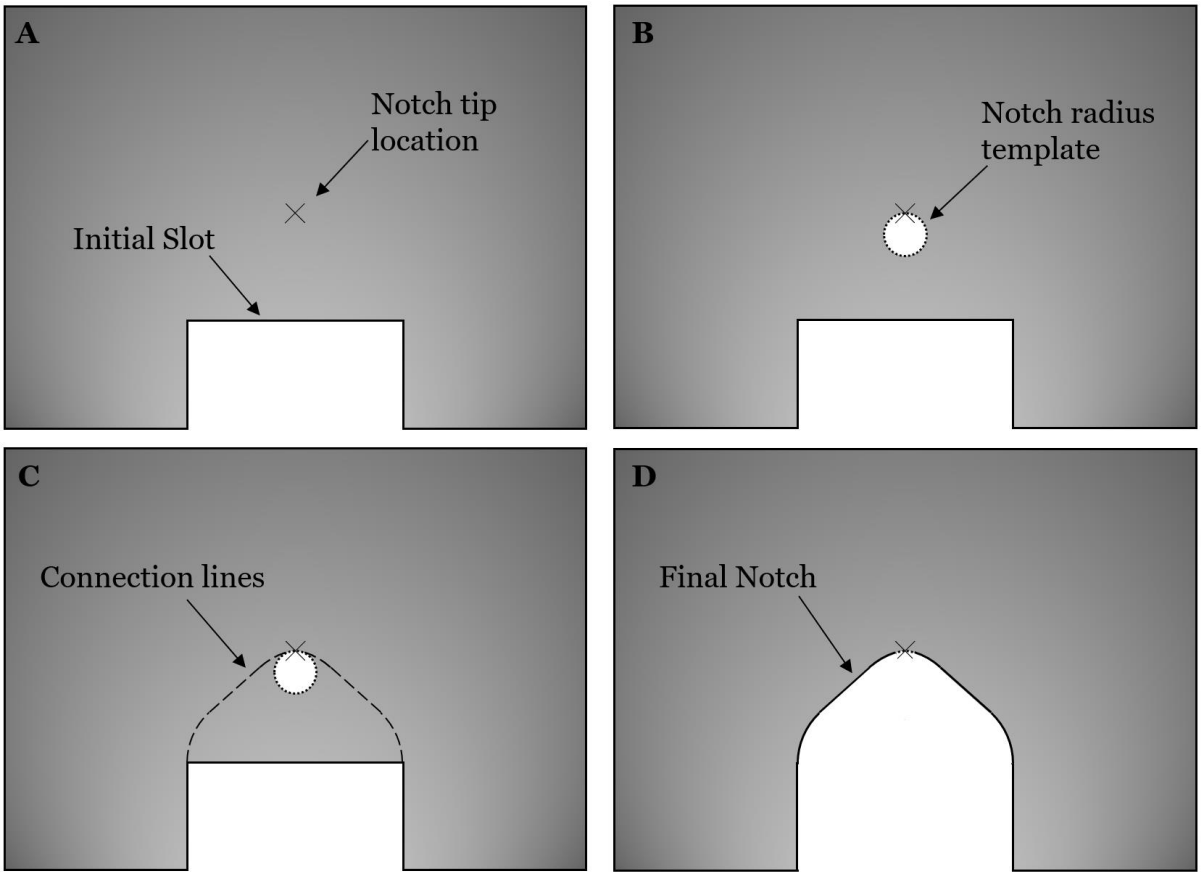

Figure 4-16 *Procedure to create the notch. (**A**) Initial slot and notch tip location, (**B**) circle used as a template for notch radius, (**C**) lines used to connect initial slot and tip radius, (**D**) final notch profile. (Not drawn to scale/proportion).*

Three notch tip radii were chosen for this study; 1.25 µm, 2.5 µm and 5 µm and the geometry is illustrated in **Figure 4-17**. This resulted in notches of similar size and aspect ratio, with the notch tip radius varied between the models.

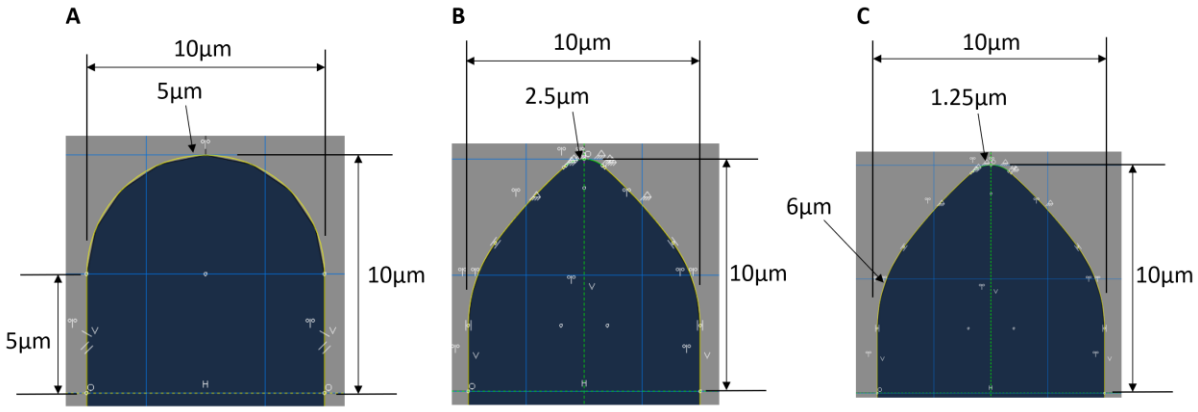

Figure 4-17 *Drawings of the three geometries used in the modelling where the stress raiser is changed by reducing the radius at the tip from (**A**) 5 µm, (**B**) 2.5 µm and (**C**) 1.25 µm. N.B. not drawn to scale.*

First, a mesh convergency study was conducted, to ensure correct behaviour was captured at the defect radius. The model with the smallest radius was chosen as a 'worst case' scenario. The results of the mesh convergency study are presented in **Figure 4-18**. The chosen mesh is shown in **Figure 4-19** with the mesh statistics summarised in

Table 4-4. The same boundary conditions for constraints were used as those in the previous simulations and the magnitude of displacement was set such that the predefined stress in the model reaches 50 MPa. As expected, the maximum stress is found at the tip of the defect where there is the stress raiser. As shown in **Figure 4-20** when the stress raiser is formed from a smaller radius, the strength is lower than when

a larger radius is used. The results show an approximately linear trend between applied stress and notch tip radius.

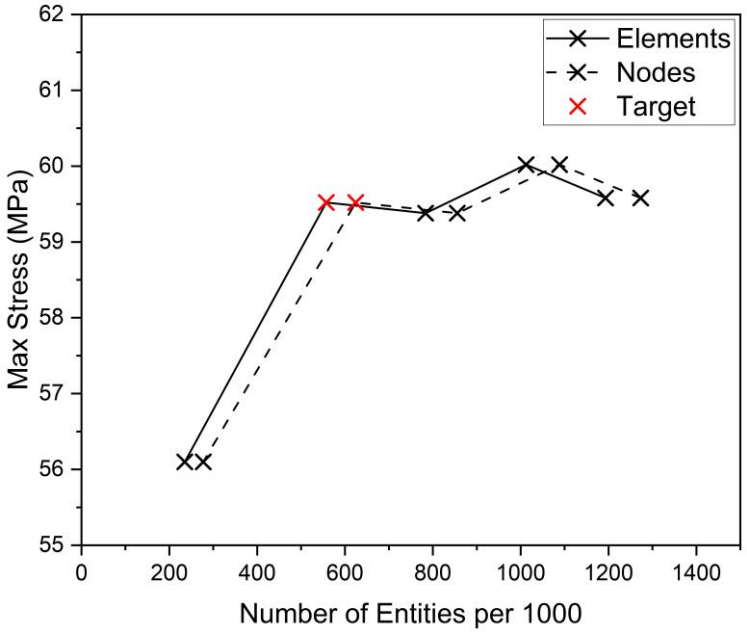

Figure 4-18 *Mesh convergency study of defect radius models.*

Table 4-4 *Mesh statistics for the chosen mesh.*

Avg. Aspect Ratio	Max. Aspect Ratio	Avg. Min. Corner Angle / °	Worst. Min. Corner Angle / °	Avg. Max. Corner Angle / °	Worst. Max. Corner Angle / °
3.47	6.28	77.68	41.89	104.04	143.10

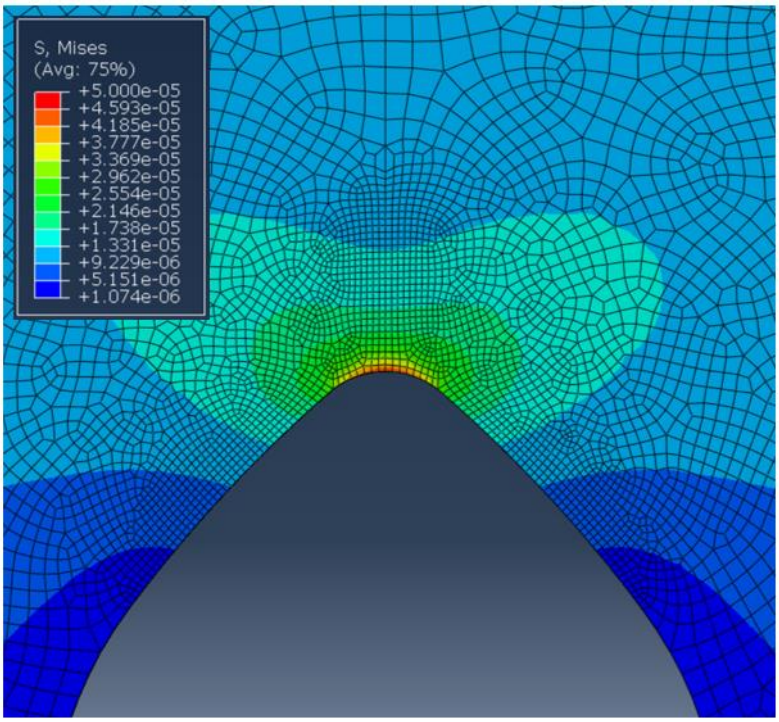

Figure 4-19 *Mesh around smallest defect radius, legend units are in TPa.*

To validate the model results, the analytical model from subsection 4.5.1 could also be used for comparison. In this case, the only variable that was changed in Equation (4-3) was the notch tip radius, since the notch length and maximum stress remained the same. Again, there is a good correlation of 3.2% between the analytical and numerical models, as illustrated in **Figure 4-20**. Previously, the numerical model followed the trend very closely to the analytical model, although, in this case, there is a slight divergence. This can be explained due to the change in geometry of the numerical mode; the geometry is not a perfect ellipse which is what is assumed in the analytical model.

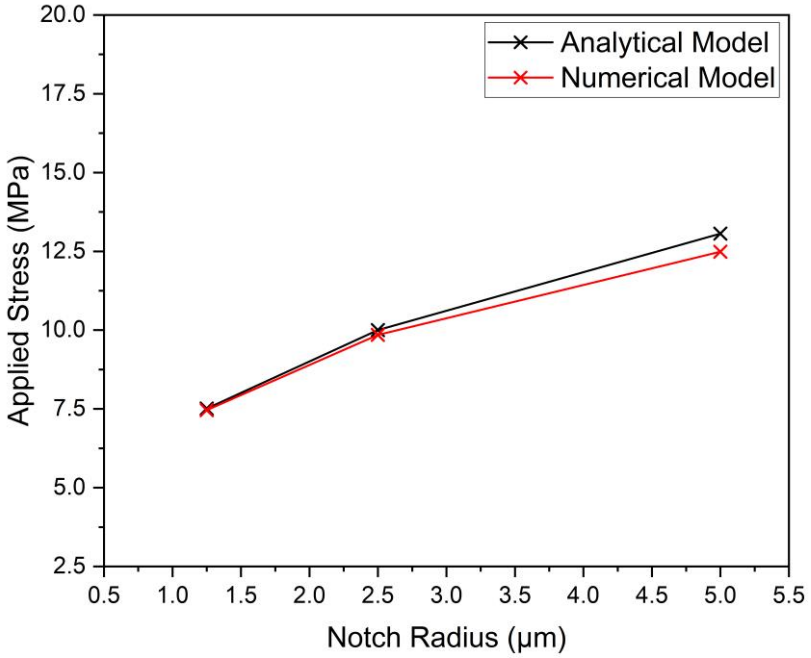

Figure 4-20 *Comparison between the analytical and numerical model of the required applied stress required for a maximum stress of 50 MPa at the stress raiser, as the notch radius increases.*

4.5.2.3. Notch study

There are two drawbacks with the previous approach. Firstly, whilst it does not affect the results, to generate the geometry an arbitrary/freeform approach must be taken, rather than modelling the notch as an ellipse. This also means comparisons to the analytical model are not completely like-for-like. Secondly, there is a limitation with the range of data points available limited by the slot width, it is not possible to create stress raisers that are larger than the width of the slot, meaning the slot width is a governing factor. For instance, in the above scenario, the slot width was 10 μm, therefore, it is not possible to have a stress raiser that has radii any larger than 5 μm.

For this reason, a different approach was adopted based on the concept that only the stress raiser needs to be modelled. To do this only the notch radius was modelled. As before, the location of the tip of the stress raiser is kept constant; therefore, to produce the stress raiser a circle is drawn offset from the model edge, such that the top of the circle coincides with the location of where the stress raiser has been set. A schematic of the process can be seen in **Figure 4-21** where the location of the stress raiser is kept constant, and the radius of the notch is increased. The applied stress was increased and measured until the stress at the notch radius reached 50 MPa.

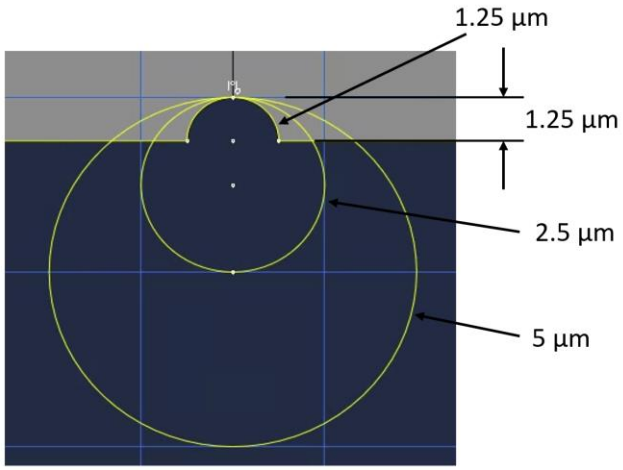

Figure 4-21 *Schematic of how the stress raiser is drawn to keep the location of the tip at the same point in all models. N.B. not drawn to scale.*

When generating the geometry, the location of the stress raiser was located 1.25 µm from the centre edge and symmetry boundary conditions were used at the centre line such that only one half was modelled. The radii used in this study ranged from 1.25 µm up to 10 µm. The results can be seen in **Figure 4-22** which shows an increasing trend, meaning that as the radius increases so does the required applied stress. The results agree with the findings from subsection 4.5.2.2 where the notch tip radii increases, the required applied stress also increases. The previous results showed a linear response, whereas the trend found in **Figure 4-22** has a small amount of non-linearity to it. This is likely a function of the $\frac{a}{\rho_t}$ term; the since a is kept constant and ρ_t increases, the function of the overall term reduces.

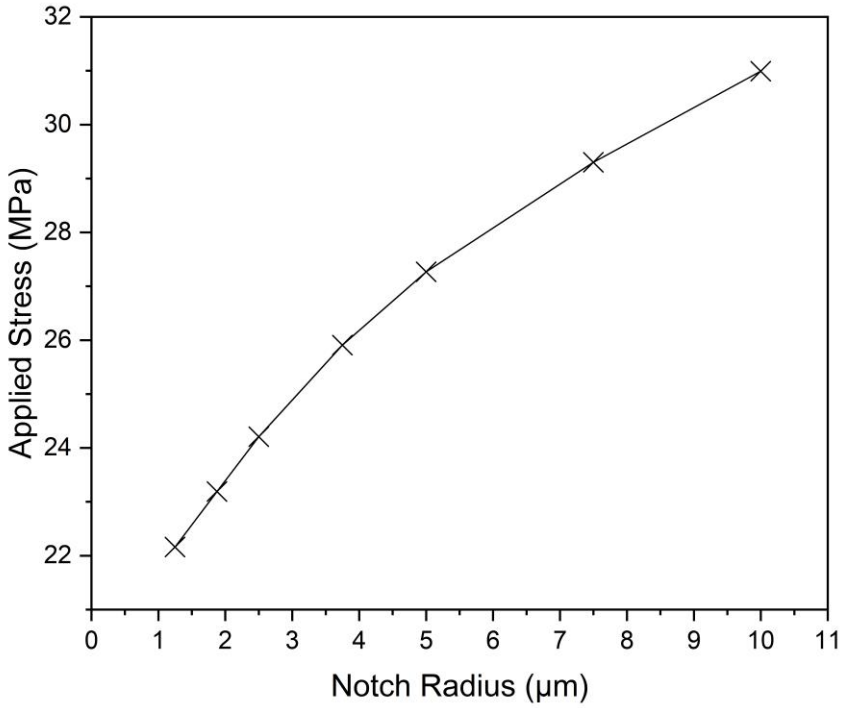

Figure 4-22 *Influence of stress raiser radius when only the top 1.25 μm is present on the required applied stress for a maximum stress of 50 MPa at the notch tip.*

4.5.2.4. 3D Notch study

The previous series of studies modelled a void as a notch in a finite thickness plate with no variation in the thickness direction. To improve the representation of a void, the plate used in previous models was replaced with a cube, and the notch was modelled into one of the sides, as illustrated in **Figure 4-23**. Like the study in subsection 4.5.2.3, the location of the notch tip radius was kept constant, and the radius of the notch was incrementally increased. Again, the force required to reach a predefined stress at the notch tip radius was monitored as the geometry was changed. The notch tip radius used in this study increased from 0.5 μm up to 10 μm and the location of the notch tip extremity was set at 0.5 μm from the surface edge. The cube had the dimensions 40 μm x 40 μm; however, symmetry boundary conditions were used at the centre to improve computation run time.

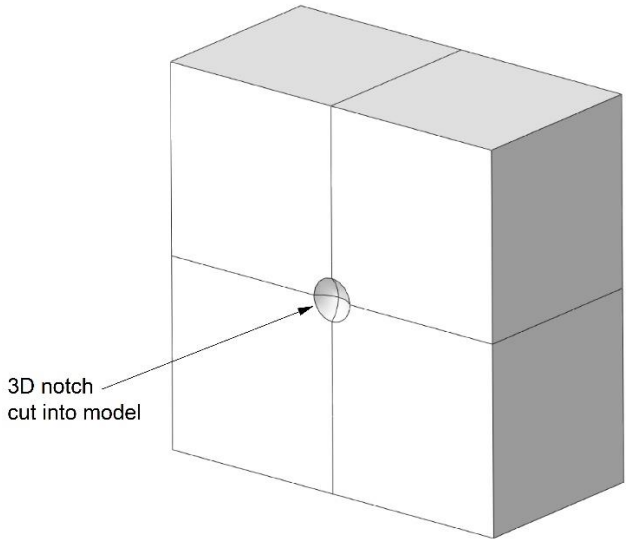

Figure 4-23 *Location and geometry of the 3D notch that cut into the side of the model.*

The results, shown in **Figure 4-24**, show a similar trend to the study in subsection 4.5.2.3, such that as the notch radius is increased, the strength also increases. A small amount of non-linearity is also present, as in the previous study. Again, this is attributed to a small change in the $\frac{a}{\rho_t}$ term.

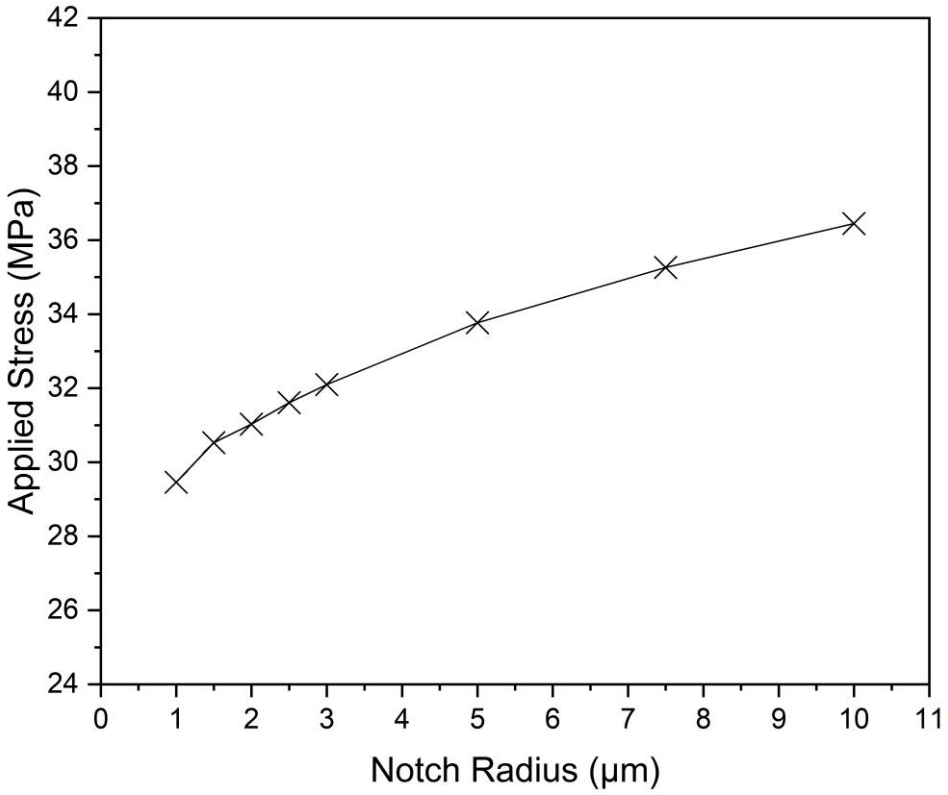

Figure 4-24 *Influence of 3D notch radius at three different edge distances, on the required applied stress for a maximum stress of 50 MPa at the notch tip.*

4.6. Modelling Approach Considerations

Having analysed several models looking into how the modelling approach accounts for changing void parameters (both full voids and individual void parameters), several considerations were identified. These include:

- A brittle failure criterion was implemented at this stage. Whilst this is conservative, it is often used in literature.[84,161,162] If at a later stage a different failure criterion is required or to account for damage progression, then the script could be updated accordingly.

- Another consideration is the loading mode. Currently, the development has been investigated purely in tension. The models are linear-elastic and so the same trend will be seen in either loading direction, except that the magnitude of strength will be different (i.e., the compressive strength will be higher than tensile, but follow the same trend). Therefore, the development that has been applied to the tensile models is also applicable to the compressive models.

- Currently, the modelling approach has been developed primarily by looking at the first stage, the void module. The overall modelling approach also considers the next stage where the fibres are introduced in the RUC, which outputs material properties to be used in a structural FE model. It would be possible to model a typical RUC; however, at this stage, it would not provide any additional information. This is because the same RUC would be used for all of the models and therefore would simply scale the results uniformly. At this point, the RUC does not need to be considered.

4.7. Chapter Summary

Porosity within composite materials is a major manufacturing defect such that after several decades of research there are still active developments being made into manufacturing processing and implications in performance. The main reason why there is continued research, particularly in understanding the impact of porosity, is due to the complexity of how voids are generated. This means that it is difficult and costly to test empirically, and simulations are a compromise between accuracy and computational efficiency. This chapter set out to address the first part of the overall

aim, which was to develop a modelling framework that can take account of accurate porosity characterisation data, such as the shape and size of voids, to be able to predict the reduction in strength.

This was successfully accomplished by developing a novel modelling approach which works on the principle of segregating the simulation into two distinct models. Firstly, the approach investigates how voids affect the strength of the matrix, without initially including the fibres. Not including the fibres means that the models result in lower element counts which allow for more complex/accurate geometry to be represented. Since voids affect the matrix dominant properties, this gives confidence that by studying the effect on the matrix is an appropriate approach. The stage 1 model is homogenised such that the '*knocked down*' strength of the matrix is determined; this is then used in an RUC where the fibre architecture is accounted for.

The modelling process was used in a preliminary study to investigate several parameters including varying the void content and aspect ratio of the voids. The results showed that the model was more sensitive to changing the shape of the void than adjusting the defect volume fraction. This resulted in further analysis investigating these parameters independently. The parametric studies showed the length and radius of the void influence the reduction in strength significantly more than increasing the void content. The studies were validated through a stress concentration analytical model where a good correlation was observed. This provides confidence such that the model can correctly capture the stress around the voids being modelled.

Overall, in this chapter, a modelling technique has been developed that can consider three-dimensional porosity parameters. The model has been used to show that as a void is changed in size, the strength of the model degrades and the trend that is observed can be explained based on the parameters that control the resultant strength. Whilst an analytical solution was used to validate individual parameter models, the next step was to validate the whole modelling process against experimental data.

5. Experimental Testing

5.1. Chapter Overview

The results presented in Chapter 4 have shown that there is a great opportunity to use the developed modelling approach to address the previous inaccuracies in void modelling representation found in the current literature. Chapter 5 details the experimental campaign designed to provide data for evaluating the accuracy and useability of the developed modelling approach. The experimental campaign involved the manufacture and mechanical testing of composite coupon specimens, as well as the characterisation of the microstructure. Two major manufacturing processes were used: autoclave cured prepreg and resin infusion. This allowed for the evaluation of how well the modelling approach represented both autoclave and Out-of-Autoclave (OoA) manufacturing processes.

5.2. Introduction

Confidence in a modelling process can only be achieved through validation and without showing good correlation results are not reliable. To validate a modelling process the validation must be representative of how the model would be used in a practical scenario. The use case for the modelling process that was presented in Chapter 4 is in composite design where the strength of the composite material is degraded by an unknown amount due to the presence of porosity. During the manufacture of a composite part, the porosity level is likely to be different to what was present in the samples that were used to derive the material properties. The porosity can differ across a part, if for instance, at a tight internal radius where the consolidation is not optimum. To mitigate this uncertainty high safety factors are used. Instead, the modelling process can be used to derive material strength properties that are more representative, reducing the need to overengineer a composite structure.

There are two major branches of composite manufacture, through autoclave processing, which produces high-quality components but with high cycle times. Or OoA approaches where cycle times can be greatly reduced but with an impact on part

quality (for instance higher porosity). In the experimental campaign, both approaches were used (resin infusion was used in the case of the OoA process) to evaluate the modelling approach with. Additionally, further research went into investigating the effect of porosity on the material properties of longitudinal laminates that were manufactured through autoclave processing. Due to the high variability of the microstructure from OoA processing, additional research went into characterising how the porosity varied across the resin-infused laminates.

5.3. Material Preparation

The model developed in this thesis has been designed specifically for tensile and compressive load cases, meaning that for the experimental campaign the corresponding ASTM standards D3039[158] and D6641[159], for tensile and compressive testing respectively, were followed. As the application of this model is to determine the transverse strengths at certain porosity parameters, transverse uniaxial testing was chosen. This subsection details how the laminates and specimens were manufactured and inspected through both autoclave and resin infusion processing.

5.3.1. Autoclave Manufacture

5.3.1.1. Tensile and Compressive Samples

For the autoclave manufacturing procedure, the material used was Skyflex K51 prepreg (USN200B)[89]. All autoclave produced laminates were manufactured following the procedures described in subsection 3.1.1. The porosity was controlled by varying the overall cure pressure (vacuum and autoclave applied pressure), which were 0.05 MPa, 0.19MPa, 0.39MPa and 0.59MPa. All laminates were manufactured to a size of 310mm x 310mm as this provided sufficient surplus material around the effects of the laminate, with the specimens being cut from the centre, to ensure no pressure-related edge effects were involved, as described in subsection 3.1.1.

The layups chosen for tensile testing were $[0]_5$ and $[90]_8$ for the longitudinal and transverse specimens, respectively. As outlined in subsection 3.1.2, five specimens were prepared for the longitudinal tests, whilst nine specimens were prepared for the transverse tests. Examples of the tensile specimens are shown in **Figure 5-1(A, B & C)**. The specimens were tested on an Instron 8801 servo-hydraulic testing machine following the procedure described in Section 3.2.1.

The layups chosen for the compressive testing were $[0]_{10}$ and $[90]_{10}$ for the longitudinal and transverse specimens, respectively. Five specimens were prepared for the longitudinal tests, whilst 18 specimens were prepared for the transverse tests. Examples of the compressive specimens are shown in **Figure 5-1(D&E).** The specimens were tested on a ZwickRoell Z050 testing machine following the procedure as described in Section 3.2 Test Procedures.

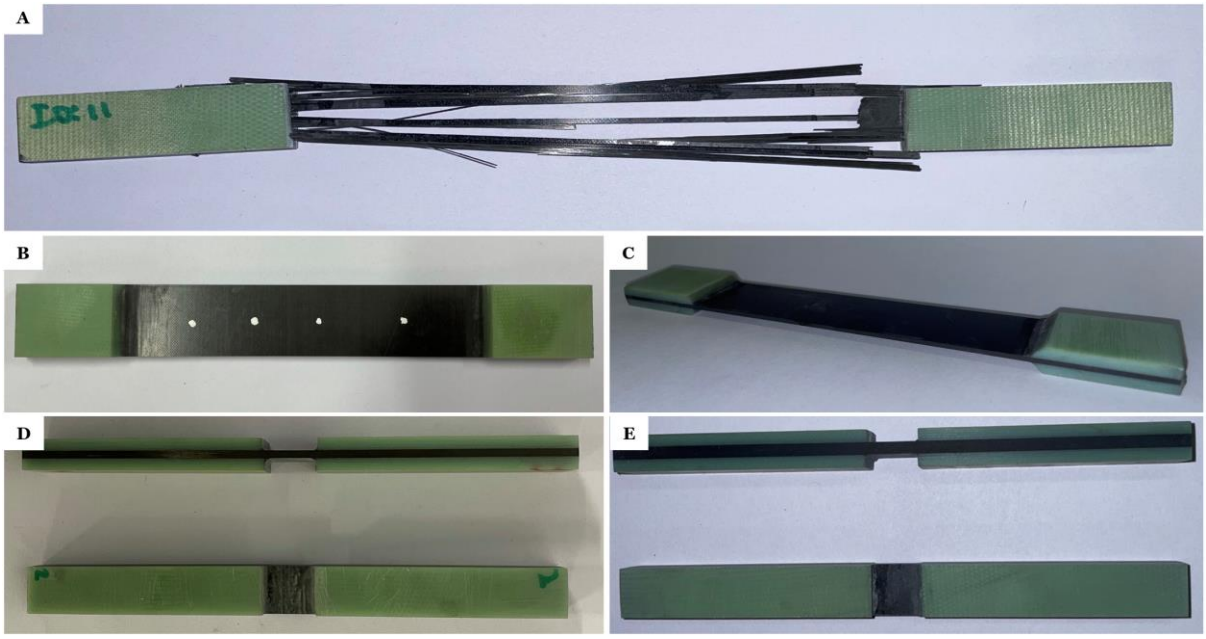

Figure 5-1 *Examples of (**A**) longitudinal and (**B** & **C**) transverse tensile specimens, and (**D**) longitudinal and (**E**) compressive specimens that were tested.*

5.3.1.2. DMA Samples

As the autoclave cure pressure was varied to change the porosity of the laminates, although the literature review suggests that this would not affect the matrix properties this assumption was validated experimentally. This was achieved through Dynamic Mechanical Analysis (DMA) of specimens cut directly from each of the laminates cured at different cure pressures. The results of the DMA tests allow an analysis of the matrix material to determine any variability between the samples.

A Perkin Elmer D800 Dynamic Mechanical Analyser was used for the DMA tests set up in single cantilever mode. Samples were cut from the 90° tension panels and tested along the fibre direction. Nominal sample thickness was 1.5mm and sample widths were between 3 and 4 mm. The DMA was operated under displacement control using a displacement of 50μm with an unsupported span of 15 mm. The samples were loaded

at a frequency of 1Hz and the temperature was ramped from 50°C to 180°C at a rate of 3°C/min. The Tg was determined by identifying the peak in the tan delta curve.

5.3.2. Resin Infusion Manufacture

5.3.2.1. Laminate manufacture

For the resin-infused laminates, a layup of $[90]_8$ was specified for the tensile specimens, where laminates of dimensions 265 x 290mm (fibre direction aligned with the 290mm side) were manufactured. This allowed for 10 specimens to be produced per laminate. The resin infused specimens for compressive testing had a layup of $[90]_{16}$ cut from laminates manufactured with dimensions 180 x 250mm (fibre direction aligned with the 250mm side), resulting in 15 specimens per laminate. The final tensile and compressive specimens prior to testing are shown in **Figure 5-2**. A description of the general resin infusion manufacturing process can be found in Section 3.1.2.

Figure 5-2 *Representative (**A**) tensile and (**B**) compressive specimens.*

Batches of laminates, with the same layup, were manufactured with different techniques to vary the porosity. These techniques included varying the time the resin was degassed before infusion, vigorously stirring the resin to encourage mechanical entrapment of air bubbles, and finally using a partial vacuum during infusion. The laminates were manufactured using either the techniques independently or in combination.

First, a baseline/optimum laminate (i.e., lowest porosity) was manufactured for both the tensile and compressive tests. This was achieved by first degassing the resin for 40 minutes to eliminate the majority of any dissolved gasses in the resin. The hardener

was then gently mixed in to minimise any mechanical entrapment of air and the mixture was then further degassed for 10 minutes. The next set of laminates were manufactured following the same process, however, the timings were reduced. In this case, the resin was degassed for 10 minutes before gently introducing the hardener and then the mixture was further degassed for 3 minutes. The third set of laminates were not degassed, yet when the hardener was introduced, the mixture was vigorously stirred for 2 minutes to encourage mechanical entrapment of air. Lastly, to manufacture the final set of laminates, the resin was again vigorously stirred and an additional pressure regulator was used during the infusion process. This was set so that only a 0.075 MPa vacuum was drawn.

An additional two compressive laminates were manufactured as during testing it was found that whilst the tensile laminates had a clear trend (details given in subsection 6.5) the compressive results required further testing with more data points. During manufacture, it was observed that when the resin was degassed before the hardener was added, the majority of dissolved gas was removed in the first few minutes. Therefore, to ensure a range of laminates were manufactured with differing porosity, not just laminates that were either degassed or not, two additional laminates were manufactured for compression testing. These laminates varied from the others by further reducing the length of time the resin/resin + hardener were degassed. For the first additional laminate, the resin was degassed for 1 minute and the resin and hardener mixture was degassed for an additional minute. In the second laminate, the resin was not degassed independently, but the mixture was degassed for 1 minute. **Table 5-1** presents a summary of each of the laminates with the corresponding porosity generation technique used. The laminate identification is denoted T.L.# and C.L.# for the tensile and compressive laminates, respectively, and the '#' represents the laminate number. These are the laminate I.D.s used throughout this chapter.

Table 5-1 *Techniques used to vary porosity across each of the laminates.*

Laminate I.D.	Degassing Duration	Mixing Approach	Vacuum Pressure / MPa
T.L. 1 & C.L. 1	40 minutes resin + 10 minutes mixture	Gentle	0.101
T.L. 2 & C.L. 2	10 minutes resin + 3 minutes mixture	Gentle	0.101
T.L. 3 & C.L. 3	N/A	Vigorous	0.101
T.L. 4 & C.L. 4	N/A	Vigorous	0.075
C.L. 5	1 minute resin + 1 minute mixture	Gentle	0.101
C.L. 6	1 minute mixture	Gentle	0.101

5.3.2.2. C-scan inspection of resin infused laminates

It was noticed that for two of the laminates (T.L.4 and C.L.4), full wet-through was not achieved towards the end of the infusion. It was determined that this was caused by the lower vacuum pressure resulting in a longer infusion time. This resulted in the resin becoming less viscous and harder to infuse before a full wet-through was achieved. To ensure uniformity across all specimens cut from the same laminate, regions where full wet-through was not achieved were discarded. Whilst dry patches on the lower surfaces of the laminates could easily be identified through visual inspection, any defective regions embedded inside the laminate were unknown. This also included the dry patches on the bottom as it was unknown at what point the resin stopped infusing inside the laminate. Therefore, by c-scanning each laminate, the identification and extent of any dry patches could be determined.

Each laminate was c-scanned using a single probe in pulse-echo mode with a system supplied by MIDAS NDT Systems Ltd. Each laminate was scanned using a 10 MHz probe overlapping by 25 % between each pass with the setup shown in **Figure 5-3**. ZEUS V3 software was used to post-process the recorded data so that the range of attenuation within the laminate was visible by adjusting thresholds. All laminates were scanned, however, the only defective regions that were identified were the dry patches

at the bottom of the laminate, as shown in **Figure 5-4**. This data was used to identify the non-defective regions of the laminates where specimens could be cut from.

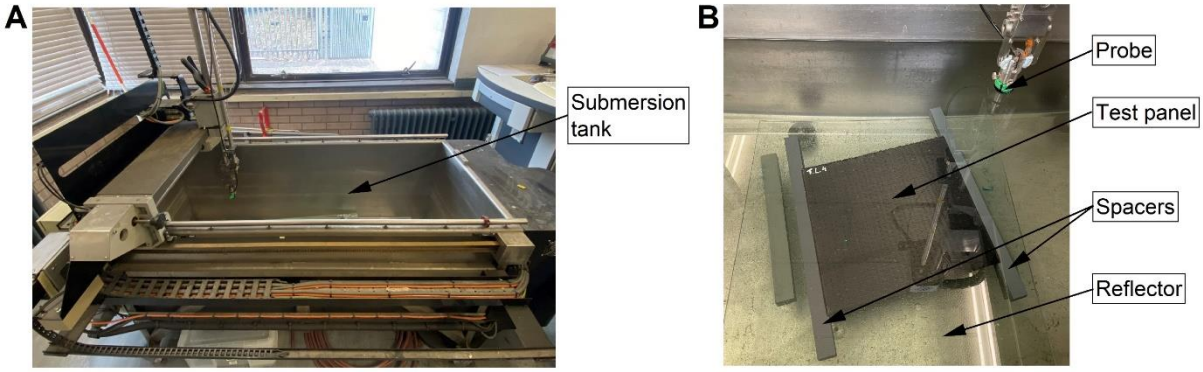

Figure 5-3 *C-scanning setup (**A**) shows the whole submersion tank and (**B**) shows the laminate and apparatus setup arrangement.*

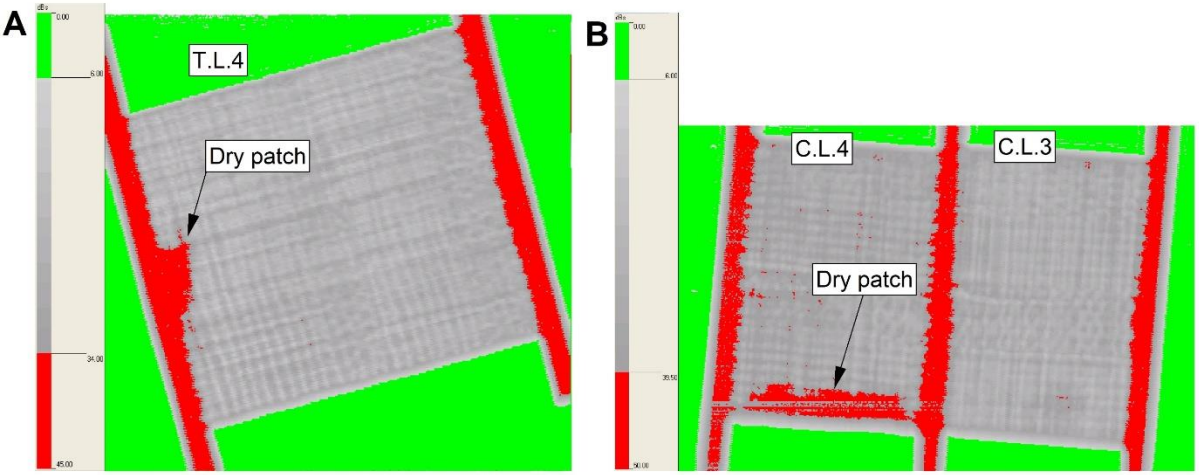

Figure 5-4 *C-Scan of (**A**) T.L.4 and (**B**) C.L.4 and C.L.3, showing dry patches that had been identified.*

5.3.2.3. Specimen preparation

Once satisfied that all laminates were of suitable quality, tabs were bonded onto each laminate before cutting specimens out. A description of the tabbing process can be found in subsection 3.1.3. The tabbing material used was 1.6mm thick G10 Epoxy Glass Fibre supplied by Fortex Engineering Ltd (1.6FR4-1218NA).[164] The geometry of the tabs is summarised in **Table 5-2**. A notable observation is that due to the difficulty in obtaining the correct failure of the tensile specimens within Chapter 5, the tabs were chamfered past the recommended 45° to an acute angle of approximately 30°. The longer chamfer length is designed to induce load into the gauge section gradually and result in the correct failure location.

Specimens were cut out of each laminate from the suitable regions that had been identified. The general procedure for cutting specimens from laminates, polishing, inspecting, and measuring them is described in subsection 3.1.4. The overall specimen dimensions are detailed in **Table 5-2**.

Table 5-2 *Specimen and tab geometry.*

Specimen type	Overall Dimensions	Gage section length	Tab length	Tab angle
Tensile	245 x 25 mm	35 mm	175 mm	30°
Compression	140 x 13 mm	13 mm	63.5 mm	90°

Due to the nature of resin infusion, drawing the resin through the preform under vacuum could have resulted in the effect of 'degassing' the resin. Also, there is a natural pressure gradient across the laminate where the inlet side is at near atmospheric pressure, whereas the outlet is at full vacuum. This means the consolidation across the laminate is not uniform, which could again lead to different void contents across each laminate. To ensure consistency across the laminate, specimen I.D.s were recorded in reference to the position along the length of the laminate. This allowed any trend in material property across the laminate to be identified when they were mechanically tested.

5.3.2.4. Neat epoxy resin samples

As explained in subsection 6.3.5, the constituent material properties are not always published, particularly for the matrix. This was true for the matrix system used in the autoclave processed laminates. As a matrix strength value was required, the modelling framework was used to derive the strength properties using the experimental data, as detailed in subsection 6.4.1. In a resin infusion process the matrix and fibre reinforcement are initially separate, which allowed for an opportunity to validate the procedure of predicting the matrix strength properties, through mechanically testing the resin.

Two plaques were cast using the same epoxy resin system that was used in the resin infusion process. The moulds to cast the plaques consisted of machined aluminium tooling plate fabricated to form a 'sandwich' type mould; where a 4mm central U-plate

was bolted between two 8mm outer plates, as illustrated in **Figure 5-5**. The plaques had nominal dimensions of 210 x 227 x 4mm.

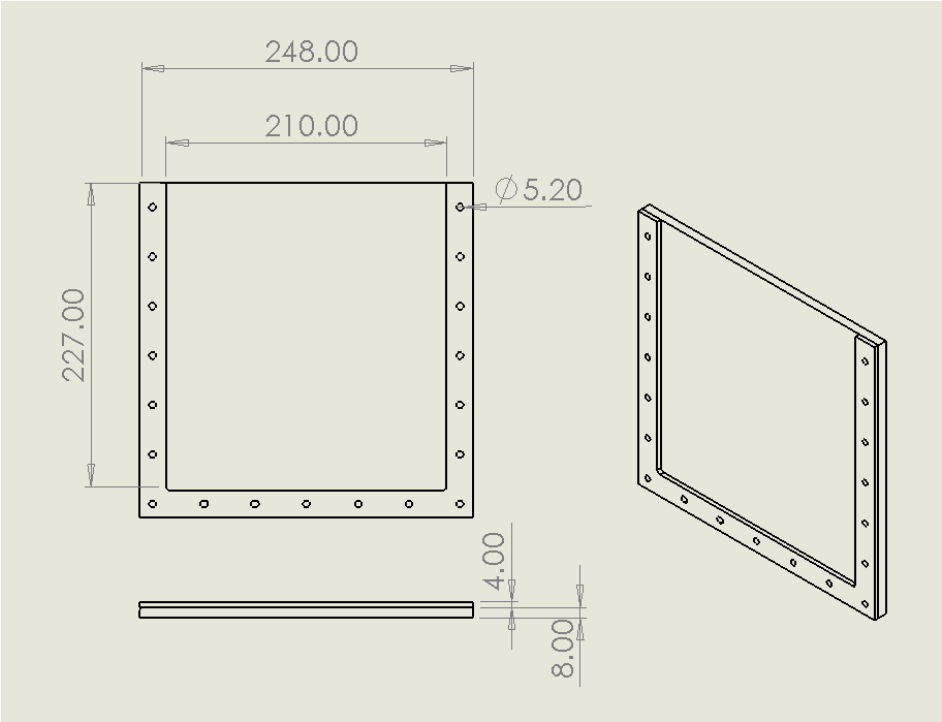

Figure 5-5 *Engineering drawing of the mold used to cast the resin plaques.*[165]

Since tensile and compressive strength properties were derived using the modelling procedure, it chosen to machine two types of specimens from the resin plaques so that both tension and compression tests could be undertaken. Following the test standard BS EN ISO 527[166] for tensile testing of polymer materials, 15 dumbbell shaped small specimens, of type 1BA, as illustrated in **Figure 5-6** were machined from each plaque. For the compression testing, ASTM standard D695[159] was followed and 11 cuboid specimens of dimension 12.7 x 12.7 x 4mm were machined from the remaining resin plaques.

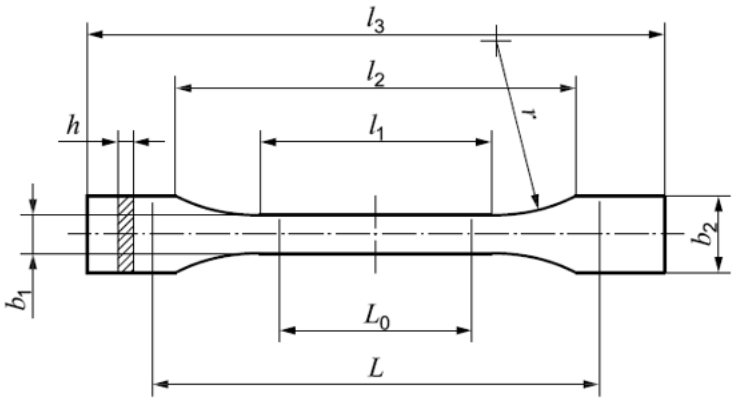

	Specimen type	1BA	1BB
l_3	Overall length	≥75	≥30
l_1	Length of narrow parallel-sided portion	30,0 ± 0,5	12,0 ± 0,5
r	Radius	≥30	≥12
l_2	Distance between broad parallel-sided portions	58 ± 2	23 ± 2
b_2	Width at ends	10,0 ± 0,5	4 ± 02
b_1	Width at narrow portion	5,0 ± 0,5	2,0 ± 0,2
h	Thickness	≥2	≥2
L_0	Gauge length	25,0 ± 0,5	10,0 ± 0,2
L	Initial distance between grips	$l_2{}^{+2}_{0}$	$l_2{}^{+1}_{0}$

NOTE The specimen types 1BA and 1BB are proportionally scaled to type 1B with a reduction factor of 1:2 and 1:5, respectively, with the exception of thickness.

Figure 5-6 *Tensile specimen shape machined from the resin plaques, as per BS EN ISO 527*[166] *test standard.*

5.4. Tensile and Compressive Test Procedure

The test setup and procedure (including apparatus, setup, load rates etc.) were followed in accordance with subsection 3.2. The testing was to determine the ultimate strength and Young's modulus of each of the laminates (and additionally the neat resin samples), therefore, the load and displacement were recorded from the test machines and the load (to calculate stress) and strain were measured by a video gauge system. Additionally, the test data (strength and stiffness) for the resin infused laminates were tracked along the length of the laminate (infusion direction).

5.5. Microstructure Characterization

The microstructure of each laminate was inspected for several reasons. Firstly, the void content was assessed to determine how the material properties were affected as this was varied. Secondly, the geometrical parameters were studied to observe if there is any change in void geometry due to different processing conditions and if this may contribute to any material property variation. The measured porosity parameters were

also used to build the stage 1 models in the following chapter. Lastly, the reinforcement was characterised to build the stage 2 models in the following chapter.

5.5.1. Void content analysis

The void content for the autoclave manufactured laminates was analysed using three separate samples, cut to 25mm in length, with an initial 18 images taken (6 from each sample) to capture a representative area. The initial results showed that there is a large amount of error (explained below) and therefore, for the 90° laminates to increase accuracy since these were the laminates of high interest for the modelling, the image count was increased to 60. Sample preparation and microscopy are outlined in subsections 3.3.1 and 3.3.2. The images were processed using a Python script, described in subsection 3.3.3, to isolate the voids and calculate the void content. A typical pre- and post-image can be seen in **Figure 5-7** where the post-image shows that any light scratch marks have been removed in the image processing, although both the small and large voids can be detected.

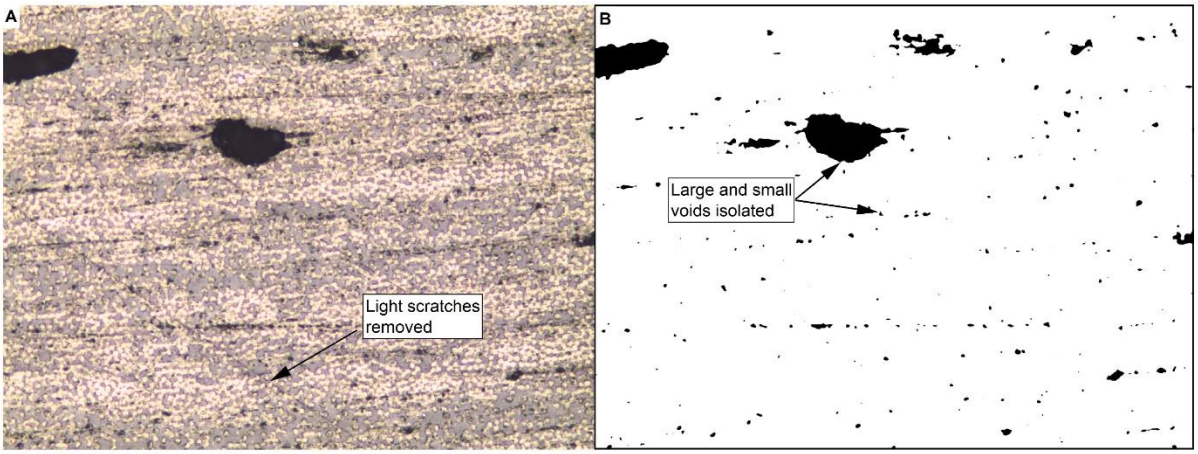

Figure 5-7 *Typical images used to calculate the void content of a sample where (**A**) is the original and (**B**) is the processed image.*

The void content results can be seen in **Table 5-3** where the error is defined by one standard deviation. As expected, as the cure pressure reduces the void content would increase. However, in some cases such as the 0.39MPa laminate the void content reduces as the cure pressure is reduced from 0.59MPa. For this reason, it is important to present results in terms of the void content rather than cure pressure. It can also be seen that there is a large range of results for nearly all laminates. However, this is due to the size of the images taken to sample the void content. To ensure voids were

accurately imaged a magnified field of view was required, however, doing so meant that only a small region of the laminate was inspected per image. As the density of void clustering will vary across the laminate, or if a larger void is present in the image, this results in a higher measurement error. To account for this error and ensure accurate results, a high number of images is required to map the laminate. Bodaghi et al.[52] suggests between 20-25 measurements to ensure accurate readings, therefore, the 60 images that were taken of the transverse laminates were deemed sufficient. Whilst the variability is high, the results show that there is more variability in laminates at a higher void content. Generally, for laminates with a void content below 1 %, their error is approximately ±0.5 %, however, when the void content is above 1 %, the variability can range from anywhere between ±1-2 %.

Table 5-3 *Void content results for autoclave manufactured laminates.*

Load Case	Void content for corresponding cure pressure / %			
	0.59 MPa	**0.39 MPa**	**0.19 MPa**	**0.05 MPa**
0° Tension	0.98±0.66	0.71±0.52	-	1.12±0.55
90° Tension	0.63±0.49	1.28±1.99	0.88±0.93	2.01±1.53
0° Compression	1.07±0.51	0.63±0.46	-	1.23±1.43
90° Compression	0.87±0.61	0.66±0.38	1.14±1.00	1.58±1.08

A higher fidelity void content inspection was undertaken for the resin infused laminates, such that the void content was measured not only for the whole laminate but also along the length (resin flow direction). The void content was measured at three locations (denoted A, B and C) for the tensile laminates and at four points (A, B, C and D) for compression laminates. The mean void content for each region of the laminates can be found in **Table 5-4**. The error is calculated based on a single standard deviation. The data is plotted as a line graph in **Figure 5-8**, with the error bars omitted for clarity.

Table 5-4 *Summary of measured void contents, including error (std. dev.) along both tensile and compressive laminate including the overall void content.*

Laminate I.D.	Void content – A / %	Void content – B / %	Void content – C / %	Void content – D / %	Range / %	Void content – Overall / %
T.L. 1	1.17 ± 0.47	0.85 ± 0.49	0.97 ± 0.62	-	0.32	0.99 ± 0.54
T.L. 2	3.31 ± 3.25	2.56 ± 2.72	1.20 ± 2.63	-	2.11	2.36 ± 2.63
T.L. 3	1.82 ± 1.25	2.55 ± 2.05	1.87 ± 1.69	-	0.73	2.08 ± 1.70
T.L. 4	1.07 ± 1.13	1.22 ± 0.82	1.71 ± 1.29	-	0.64	1.33 ± 1.13
C.L. 1	0.60 ± 0.49	0.57 ± 0.25	0.62 ± 0.25	0.62 ± 0.22	0.05	0.60 ± 0.32
C.L. 2	0.95 ± 0.34	0.88 ± 0.33	0.89 ± 0.29	0.89 ± 0.34	0.07	0.90 ± 0.32
C.L. 3	0.98 ± 0.37	1.16 ± 0.56	1.28 ± 0.58	1.05 ± 0.49	0.3	1.12 ± 0.52
C.L. 4	1.86 ± 2.35	1.53 ± 1.77	2.16 ± 1.48	2.22 ± 1.83	0.69	1.94 ± 1.88
C.L. 5	1.46 ± 0.81	1.41 ± 0.98	1.28 ± 0.72	1.28 ± 0.72	0.18	1.45 ± 0.90
C.L. 6	1.49 ± 0.81	1.75 ± 0.96	2.45 ± 1.84	0.89 ± 0.89	1.56	1.65 ± 1.31

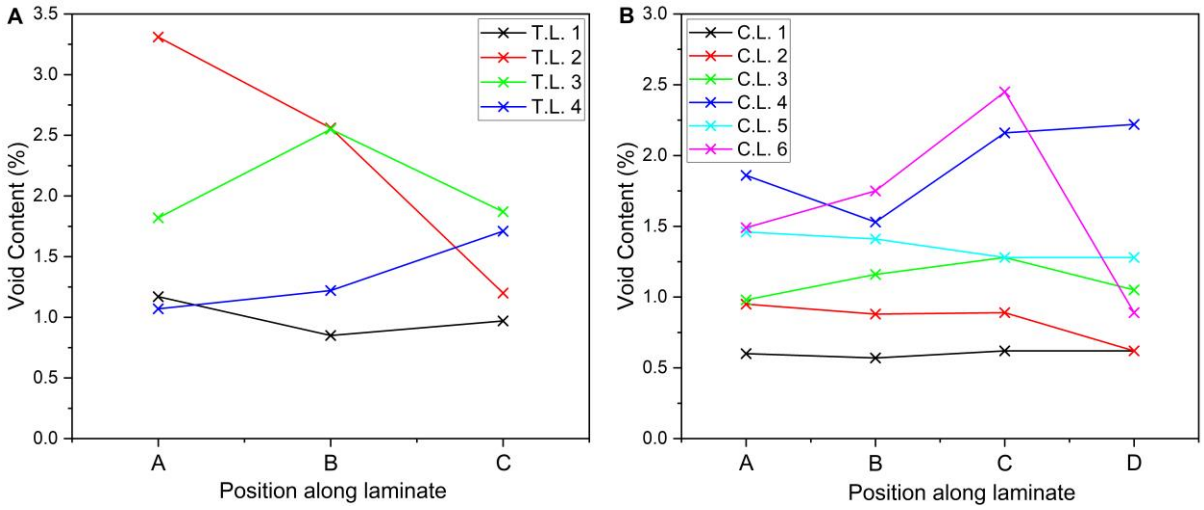

Figure 5-8 *Line graph of void content along (**A**) tensile and (**B**) compressive laminates.*

Table 5-4 shows there is a distinct difference in overall void content between each of the laminates. For the tensile laminates, there is a range between 0.99 % to 2.36 %, and for the compressive laminates, there is a range between 0.60 % to 1.94 %. In both series, there is a steady increase in void content between each of the laminates. The void content for the tensile laminates increased by an average of 0.45 % and for the compressive laminates, by 0.27 %. This can also be seen in **Figure 5-8** where there is a general increasing trend when comparing each of the line graphs, which is particularly noticeable in the compressive laminates. Interestingly, the increase in void content between each of the laminates does not always follow the manufacturing

order, i.e., it would have been expected that T.L.4 would have the highest void content. This is due to manufacturing variability, where factors such as infusion time or even room temperature and humidity, cannot be controlled and can result in a change in void content. Similarly, to the autoclave void content results, this shows the importance of reporting the void content when presenting results.

Figure 5-8 clearly shows how the void content varies along the length of a laminate. For the tensile laminates, T.L. 1 shows only a small amount of variation, a maximum range of 0.32 %, which is within the variation of 0.54 %. T.L. 3 and T.L. 4 have a larger range of 0.73 % and 0.64 %, respectively, which is again within the error. However, the overall error also increased to 1.70 % and 1.13 %, respectively. T.L. 4 similarly showed a slight increase in void content towards the end of the laminate. The most notable trend is that of T.L.2, where there is a steady decrease in void content along the laminate, with the largest variation across the whole laminate of 2.11 %±2.63 %.

The variation in void content across the compressive laminates is illustrated in **Figure 5-8**(**B**). There is very little variation across most of the laminates, particularly C.L.1-3 & 5, which all have a range of less than 0.2 %. C.L. 4 showed more variation, with a point in the middle of the laminate where the void content drops by approximately 0.5 %, however, this is a small amount compared to the average error of the whole laminate, of just under 1.88 %. The largest range was in C.L. 6 where the void content dropped from a maximum of 2.45 % to 0.89 % in a single step, giving a range of 1.56 %. This is the only laminate where the range in void content across the whole laminate is greater than the error, which was found to be 1.31 %.

In a few regions, the measured mean void content was smaller than the standard deviation, specifically in laminates T.L.2 and C.L.4. These are the laminates with the greatest void content for each series (tension and compression respectively), suggesting that there is a greater variation in porosity as the void content increases. As explained in subsection 2.2.3, there are two major types of voids (which differ by size) found in laminate C.L.4, and therefore depending on which type is captured in each image results in a larger standard deviation. This is a limitation of microscopy, where only a small region (approximately, 0.5x0.4 mm per image) can be evaluated at a time. Since the larger voids are only generated occasionally, they are not present in every image sampled. Therefore, when they are captured, it results in a large variation. As also explained in subsection 6.3.1.2, this was accounted for when modelled.

Another approach to determine the consistency of the void content between the laminates is to do a series of T-Tests comparing each region for a specific laminate. The specific T-Test was a two-tailed, non-paired equal variance with independent datasets. To determine if there is a statistical difference between the datasets, the P-Value threshold used was 0.05, such that any compared regions above this threshold are assumed not to be different.

The results of the T-Test can be seen in **Table 5-5**, where conditional formatting was applied such that values highlighted in green have a P-Value above 0.05 and those highlighted in salmon have a P-Value below 0.05. For the tensile results, there is an even split between regions which are statistically similar or different. When compared to **Figure 5-8**(**A**)**,** the T-Test confirms for T.L. 2 that position C shows a difference in void content compared to the other two positions. This is also true for T.L. 4, where there is a statistical difference in void content between position C and positions A and B. In these laminates, there is a general increase or decrease in void content (T.L. 4 and 2, respectively), whereas this is not seen with the other two laminates.

In comparison, the T-Test results for the compressive laminates show much more consistency between each region. Four out of the six laminates showed no statistical difference between each of the regions within the laminate. A notable observation is for C.L. 6, which showed a statistical difference between 5 out of the 6 regions. This correlates well with **Figure 5-8**(**B**)**,** where it was identified that there is little variation across most of the laminates, except for C.L. 6. This was also the only laminate to have a maximum range in void content larger than the measured overall error.

Table 5-5 *T-Test results for the tensile and compressive laminates. Cells highlighted in green represent no difference, and cells highlighted in salmon represent that there is a difference.*

Tensile T-Test				**Compressive T-Test**				
	Region	A	B		Region	A	B	C
T.L. 1	B	0.004	-	C.L. 1	B	0.772	-	-
	C	0.118	0.317		C	0.792	0.386	-
					D	0.758	0.325	0.950
	Region	A	B		Region	A	B	C
T.L. 2	B	0.262	-	C.L. 2	B	0.394	-	-
	C	0.000	0.004		C	0.385	0.963	-
					D	0.414	0.976	0.989
	Region	A	B		Region	A	B	C
T.L. 3	B	0.167	-	C.L. 3	B	0.0845	-	-
	C	0.922	0.186		C	0.007	0.379	-
					D	0.465	0.334	0.061
	Region	A	B		Region	A	B	C
T.L. 4	B	0.438	-	C.L. 4	B	0.482	-	-
	C	0.0163	0.0438		C	0.500	0.090	-
					D	0.444	0.090	0.862
					Region	A	B	C
				C.L. 5	B	0.823	-	-
					C	0.286	0.472	-
					D	0.968	0.860	0.337
					Region	A	B	C
				C.L. 6	B	0.192	-	-
					C	0.004	0.039	-
					D	0.002	0.000	0.000

Overall, there is good consistency in void content across most of the laminates. It was found the laminates with the lower overall void content were more consistent, and for the laminates with a higher overall void content, there was a larger range and lower P-Value. It was also found that the error increased as the void content was raised. This study was also able to identify several laminates where the change in porosity might affect the experimental results. Specifically, these laminates are T.L. 1, where the

porosity reduces nearer the outlet end of the laminate, and C.L. 6, where there is a large distribution of the results.

5.5.2. Void geometric analysis

One of the main objectives identified from the literature review, and the importance verified in Chapter 4, is accounting for the geometrical properties of the porosity. Only characterising the void content is insufficient to ensure an accurate representation is achieved when building a representative model. This subsection details how the relevant geometrical properties of the autoclave and resin infused laminates were characterised.

5.5.2.1. Void shape - autoclave processing

Typically, voids are of arbitrary shape as the void forms around the fibres. However, it is not practical to model voids in their exact shape due to two reasons. Firstly, it requires significant time investment to generate a 3D model of the various shapes, meaning that the only realistic approach is to use a μ-CT scanner. Nevertheless, it is unrealistic in a design scenario to own and/or run one due to cost, space and scan/postprocessing-time limitations. Secondly, even if an accurate representation of geometry can be modelled, due to the arbitrary shapes and small features result in element counts in the order of millions. For one-off research studies, these costly investments can be justified. However, for practical use cases, it is appropriate to make reasonable simplifications such as assuming voids are ellipsoidal. This assumption was by Mehdikhani et al.[57] where accurate μ-CT scans are simplified down into a void's major and minor axis and subsequently used in a 2D modelling process.

One approach to measuring the shape of voids is through microscopy, where a visual evaluation can be done to assess the general shape and dispersion of the voids. Typical images can be seen in **Figure 5-9** for the transverse specimens from the autoclave cured specimens where a selection of voids can be seen circled in red. Parts (**A**) and (**B**) are from tensile specimens cured at 0.59 MPa and 0.05 MPa, respectively, whilst parts (**C**) and (**D**) are from compressive specimens cured at 0.59 MPa and 0.05 MPa, respectively. The microscopy shows that the voids do not have perfect periodicity, but for the most part, they are evenly distributed. For instance, they do not always cluster

in ply boundaries or at a specific ply. From a modelling perspective, this means that a single void can be modelled and one can assume a uniform distribution of voids. Whilst the microscopy also confirms that the voids take an arbitrary form, they can be likened to an elliptical shape with various aspect ratios. This is a very common assumption to make when modelling porosity.[39,40,57,96]

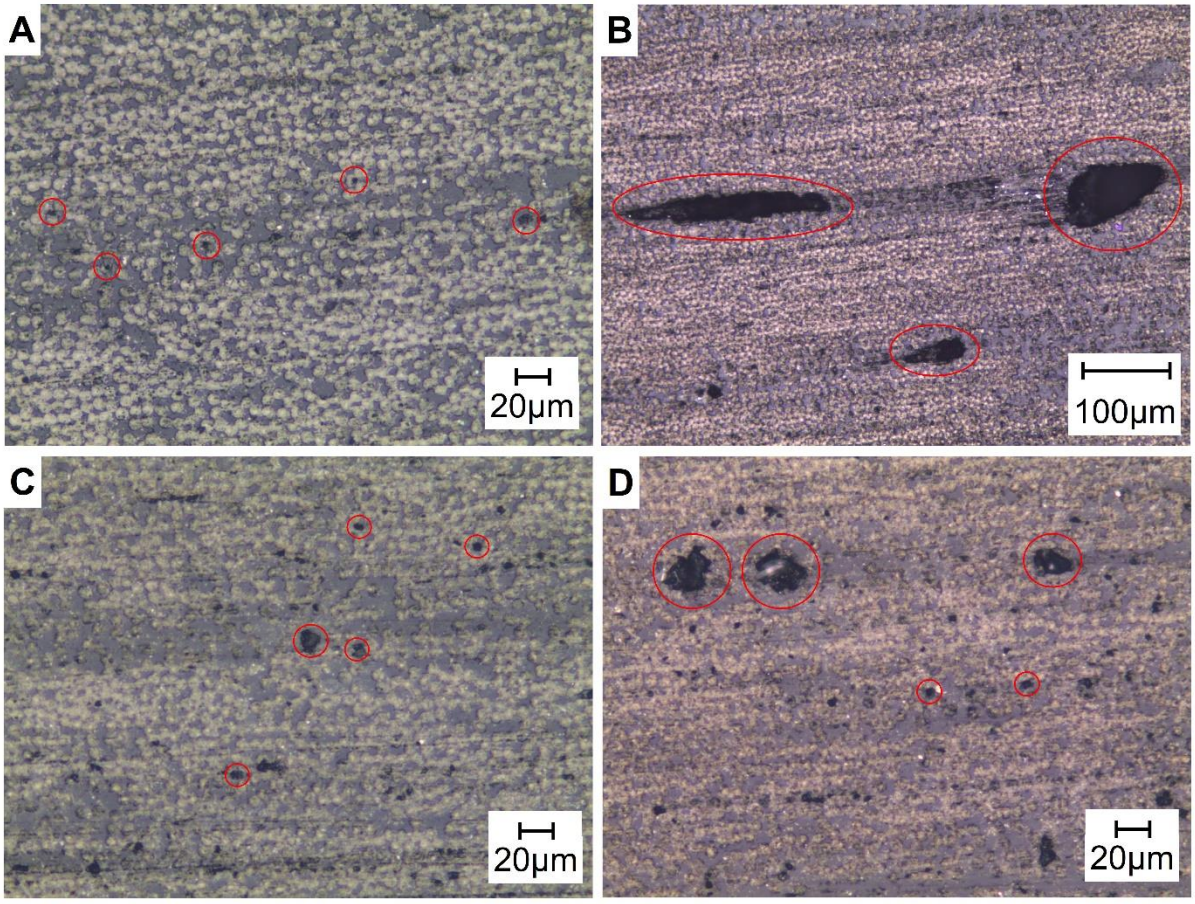

Figure 5-9 *Typical microstructure showing the shape of voids (circled in red) for: (**A**) 90° Tension 0.59 MPa, (**B**) 90° Tension 0.05 MPa, (**C**) 90° Compression 0.59MPa and (**D**) 90° Compression 0.05 MPa.*

A drawback to using general microscopy is that only a 2D image can be acquired, this means that the depth of voids cannot be evaluated. As previously stated, a common assumption, particularly in a 2D analysis evaluation, is that voids are infinitely long. However, from a visual inspection, often the bottom of the voids could be seen, particularly when adjusting the depth of field when focusing. For this reason, an optical metrology study using a 3D optical profiler was conducted. The 3D imaging microscope and associated software were produced by Sensorfar. The technique used is described in subsection 3.3.2. Several samples from the autoclave manufactured

laminates were investigated across multiple regions, however, due to the small diameters of the voids, there was difficulty in getting light inside. This led to limitations in the software recognising void surfaces. A ring light improved the lighting, yet there was still difficulty in gaining a full representation of the voids. For this reason, only a select number of larger voids were analysed, two examples can be seen in **Figure 5-10** and **Figure 5-11**. For both figures, part (**A**) is the initial topography map after being levelled and part (**B**) shows the voids isolated by lowering the upper limit such that any material above the void is excluded. The depth of voids can be read against the corresponding legend, where the bottom of the void is where the depth is measured. Parts (**C**) and (**D**) show the results of analysing a specific void including the maximum and mean depth.

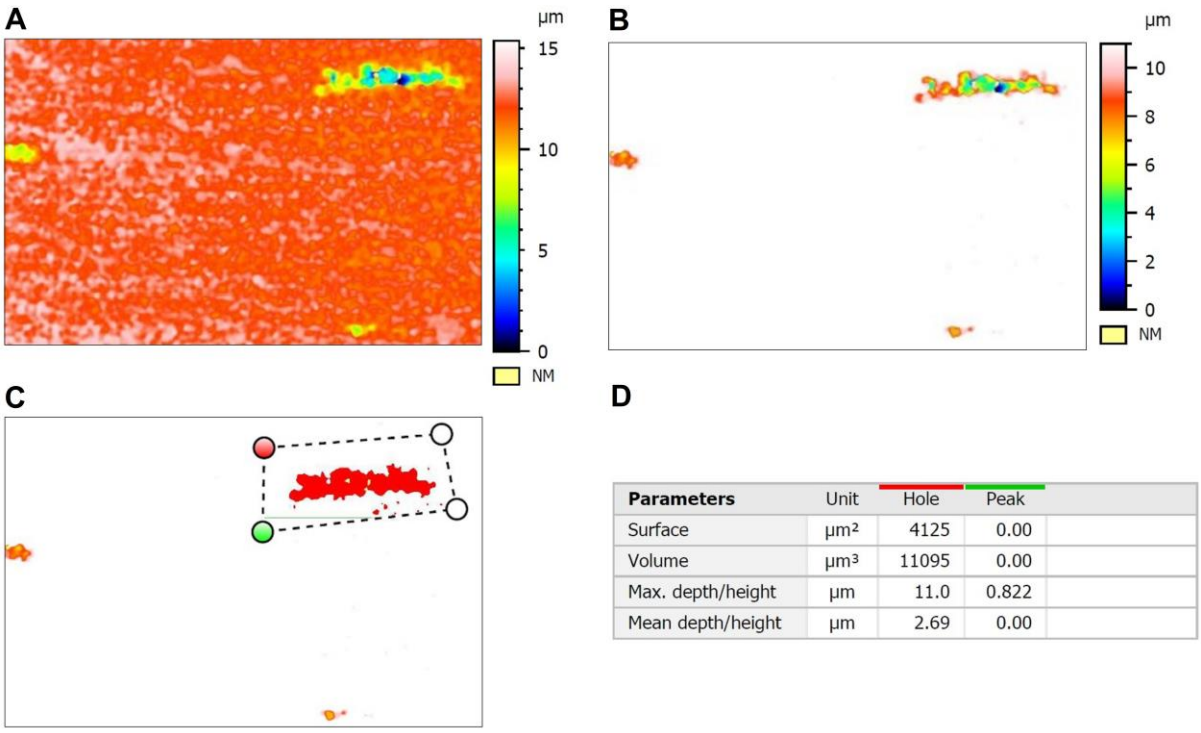

Parameters	Unit	Hole	Peak
Surface	µm²	4125	0.00
Volume	µm³	11095	0.00
Max. depth/height	µm	11.0	0.822
Mean depth/height	µm	2.69	0.00

Figure 5-10 *Region 1 - Topographical map showing the depth of voids. (**A**) Initial image after initial processing, (**B**) thresholds applied to isolate voids, (**C**) selection of a single void for analysis and (**D**) results of analysis.*

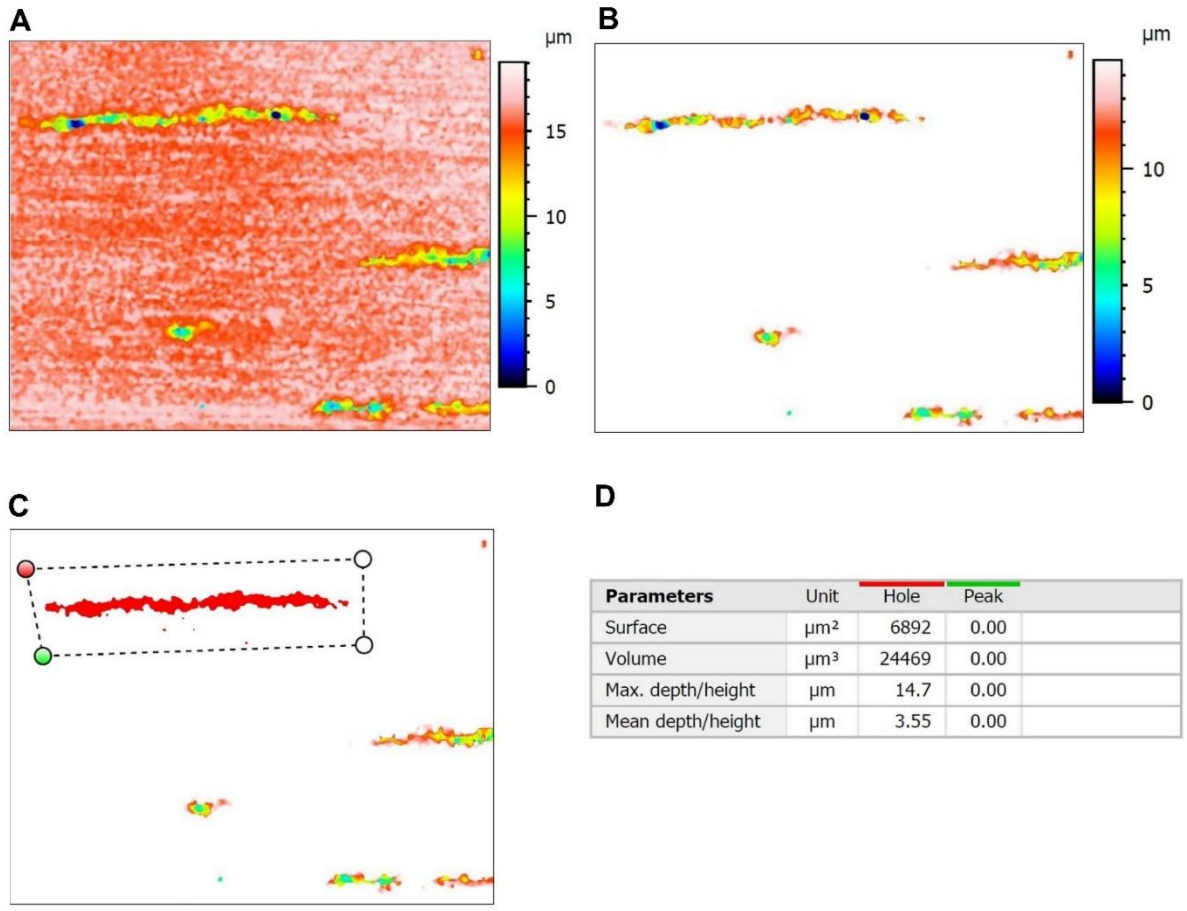

Figure 5-11 *Region 2 - Topographical map showing the depth of voids. (**A**) Initial image after initial processing, (**B**) thresholds applied to isolate voids, (**C**) selection of a single void for analysis and (**D**) results of the analysis.*

Due to measurement limitations, only a limited number of voids were analysed (less than 5). Therefore, it is not possible to get representative quantitative results, such as the average depth of a void, the depth-to-width ratio etc. Nevertheless, what can be found is that the assumption of infinity long voids is invalid, instead the depth is much shallower. This also validates that the bottom of the voids were able to be identified when adjusting the depth of field of 2D microscopy.

5.5.2.2. Void shape – resin infusion processing

The general shape and type of the voids (micro or discrete, as defined in Section 2.1) were also measured for the resin infused laminates. The void shapes were evaluated using the post-processed images used for the void content analysis as these images isolate the voids from the surrounding material.

Figure 5-12 illustrates representative post-processed images for the tensile and compressive laminates used to analyse the shape of the voids. The images selected for this figure are from the laminates with the lowest and highest measured overall void content. By visually analysing the post-processed images it was noted that there are three shapes that the voids will take, which are either spherical, elliptical or arbitrary. These shapes are illustrated in **Figure 5-13** where a region of the T.L. 2 laminate containing all three types has been magnified. For measurement purposes, the voids were assumed to take an elliptical shape. It was found that the void shapes were the same across all laminates, regardless of the manufacturing technique. This can be seen in **Figure 5-13** by comparing the low and high void content laminates (**A-B** and **C-D**).

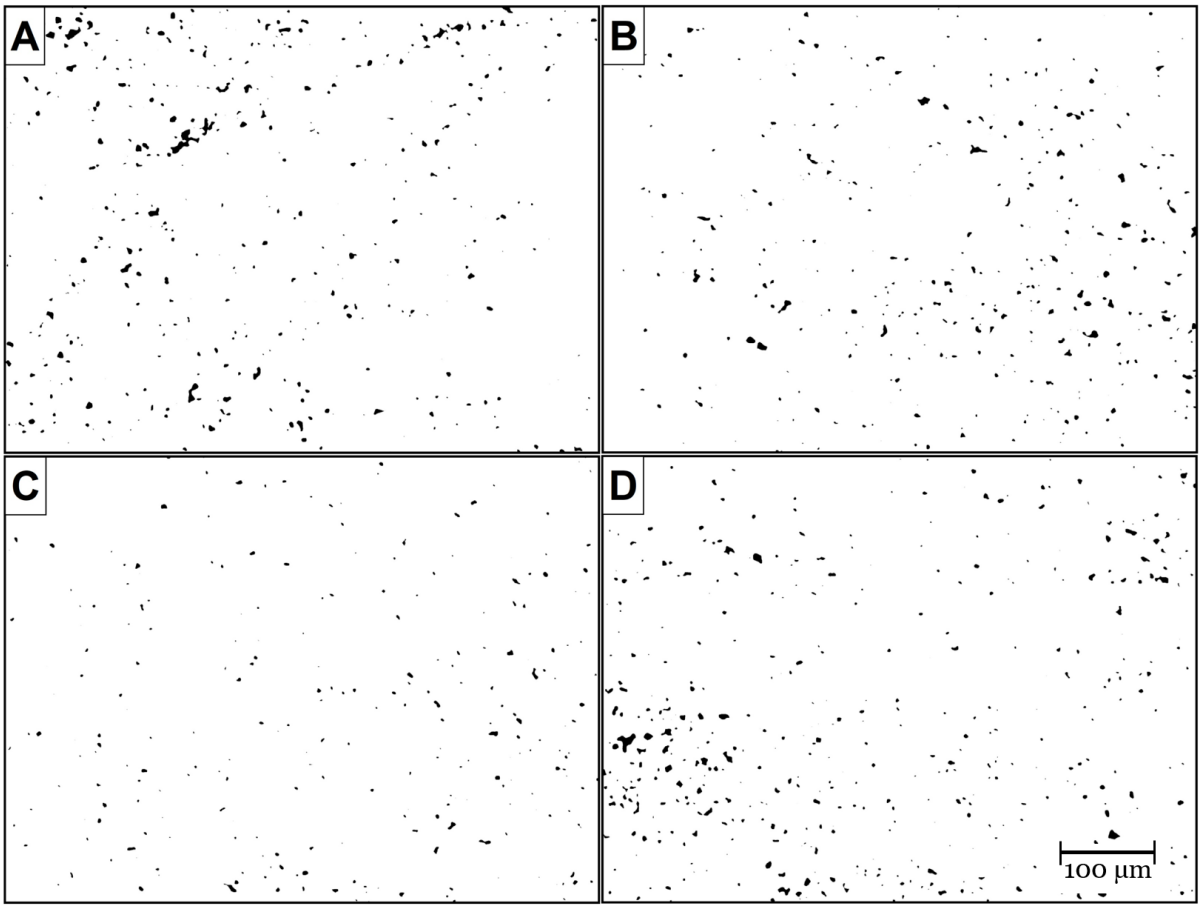

Figure 5-12 *Typical post-processed microscopy images to show the general shape and dispersion of voids from laminates: (**A**) T.L. 1, (**B**) T.L. 2, (**C**) C.L. 1 and (**D**) C.L. 4.*

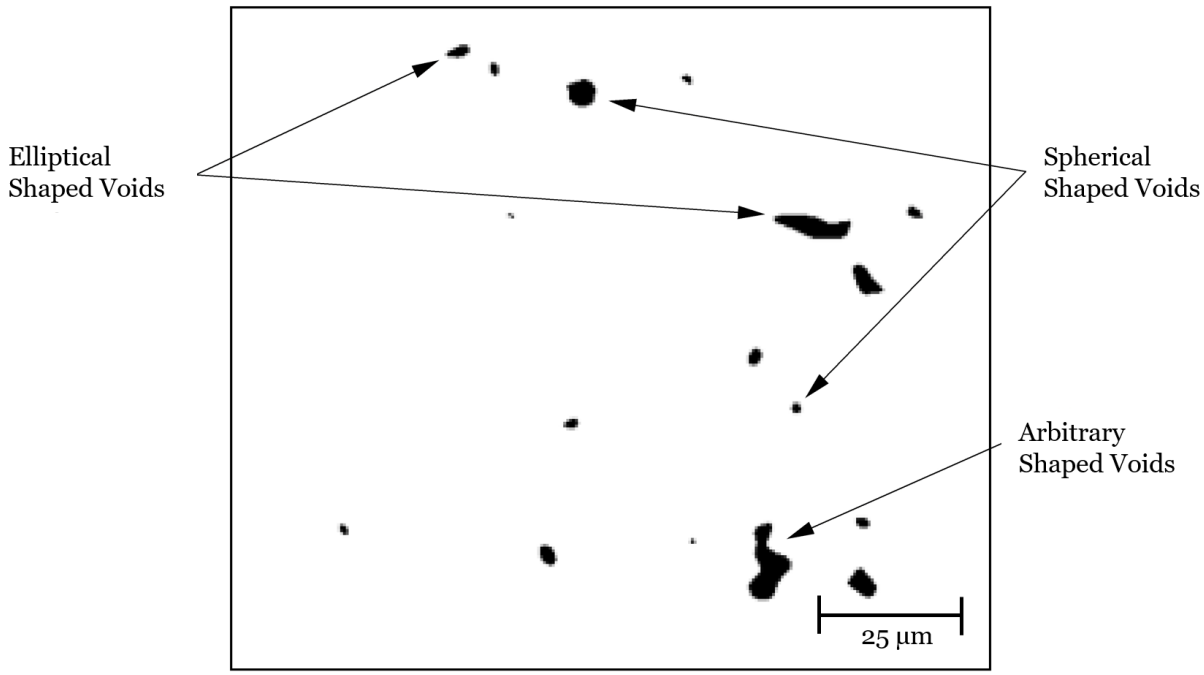

Figure 5-13 *Magnified region showing three types of void shape: Spherical, elliptical, and arbitrary.*

The type of voids seen in all laminates were microvoids (small voids of similar size to the fibres). It was visually observed when inspecting the C.L. 4 laminate, that as well as the numerous microvoids present, there were additional significantly larger discrete voids, as illustrated in **Figure 5-14**. These larger voids take either circular or elliptical shapes and therefore the same size measurement approach (length of minor and major axis) could be taken. Whilst the arbitrarily shaped voids cannot be explicitly defined by the major and minor lengths, for modelling purposes they are simplified to these dimensions. Therefore, when measuring them the 'average' length in each direction is estimated.

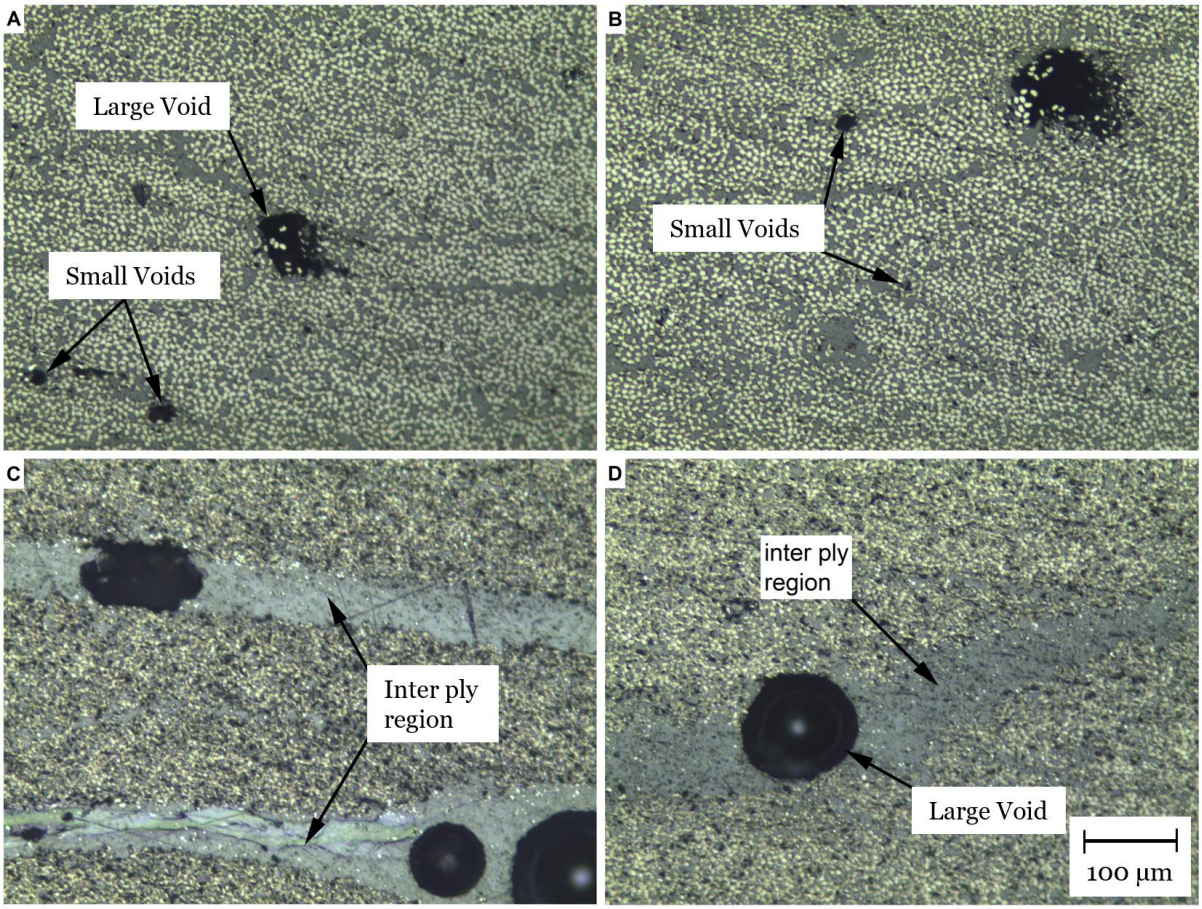

Figure 5-14 *A mixture of large (discrete) and small (micro) voids distributed in either (**A**) and (**B**) intra-ply or (**C**) and (**D**) inter-ply locations.*

As done for the autoclave processed laminates, the voids from the resin infused laminates were inspected using a 3D optical profile to measure the depth of several voids. This was to again determine the validity of whether voids are infinitely long or not.

The depth of 15 voids were measured where the major axis length ranged between 10µm to 30µm. Examples of the measured voids can be seen in **Figure 5-15** including both smaller and larger voids. The depth was measured from the sectioned surface and is assumed to be cut at the mid-point of the void, therefore the total void depth is calculated by twice the measured depth. The results are presented in **Table 5-6** where smaller voids (approximately 15µm in major axis length) have a mean total void depth of 3.0µm. For the void with a major axis length of 30µm, the total void depth was calculated to be 12µm.

There is, however, more error in the measurements for the smaller voids due to difficulty in reflecting light into and out of the voids required for the optical profiler to image. This means that the actual depth may be slightly deeper than what was measured. This is in contrast to the largest void that was measured, where the bottom was visible, and a high-accuracy measurement could be obtained. However, the main objective of this study was to determine if the voids are extremely elongated and should be assumed to be infinitely long. Whilst exact measurements were difficult to obtain, the results showed that the voids are not extremely elongated and should not be assumed to be infinitely long.

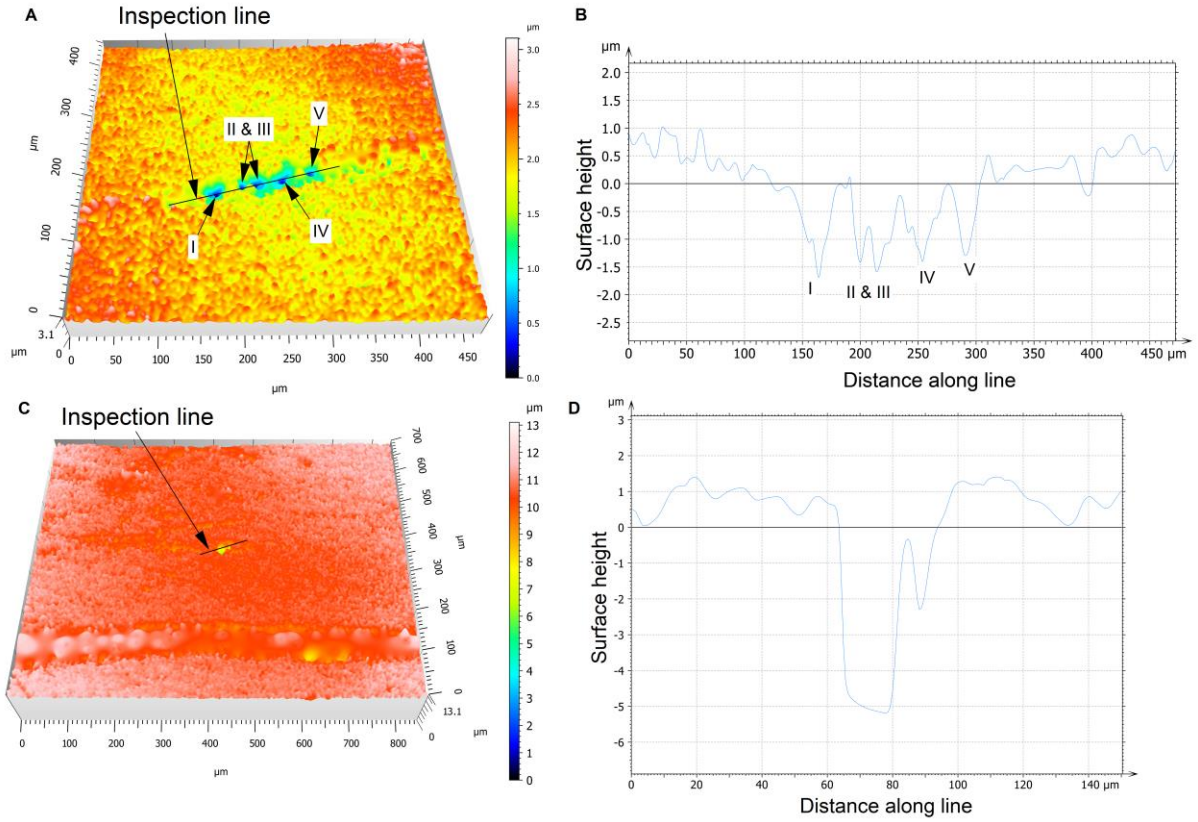

Figure 5-15 *Example of the depth of voids measured using the Sensorfar 3D optical profiler. Measurements of small and large voids are seen in (**A**) and (**C**) respectively, which show an amplified 3D render. An inspection line is positioned intersecting each void and the surface height along each line is measured and plotted in (**B**) and (**D**).*

Table 5-6 *Void depth results of the 15 measured voids, where depth is calculated as twice the measured distance from the sectioned surface to the bottom of the void.*

Void #	Major Axis Length / µm	Total Void Depth / µm
1	20	4.4
2	10	3.8
3	15	4.2
4	20	3.8
5	15	3.6
6	20	2.8
7	15	3.4
8	20	3.8
9	10	2.2
11	10	1.8
12	15	3.0
13	10	1.8
14	10	1.0
15	30	12

5.5.2.3. Void size - autoclave processing

Having established that the shape of the voids can be assumed to be elliptical the next step was to evaluate the range of sizes. This involved measuring the major and minor axis, with reference to the load direction. Measurement of void sizes is described in subsection 3.3.2. To ensure accurate representation, 30 voids were measured across 3 samples for each laminate. The mean dimensions of both the major and minor axes are presented in **Table 5-7**, including the major-to-minor length aspect ratio. Relative frequency plots of the void dimensions for each of the tensile laminates can be seen in **Figure 5-16** and compressive laminates in **Figure 5-17**.

Table 5-7 *Mean major and minor lengths of voids of all laminates, including the aspect ratio.*

Load Case	Cure Pressure	Mean Length (major axis) / µm	Standard Deviation (Major axis) / µm	Mean Length (minor axis) / µm	Standard Deviation (Minor axis) / µm	Aspect Ratio
Tension	0.59	7.86	3.53	7.01	5.98	1.12:1
	0.39	7.45	2.82	6.95	5.20	1.07:1
	0.19	21.54	15.23	18.84	14.77	1.14:1
	0.05	57.58	47.25	28.48	20.04	2.02:1
Compression	0.59	11.97	6.65	8.83	7.47	1.35:1
	0.39	10.14	5.10	6.11	2.80	1.66:1
	0.19	13.33	6.93	8.68	6.38	1.54
	0.05	25.72	20.16	18.86	11.86	1.36:1

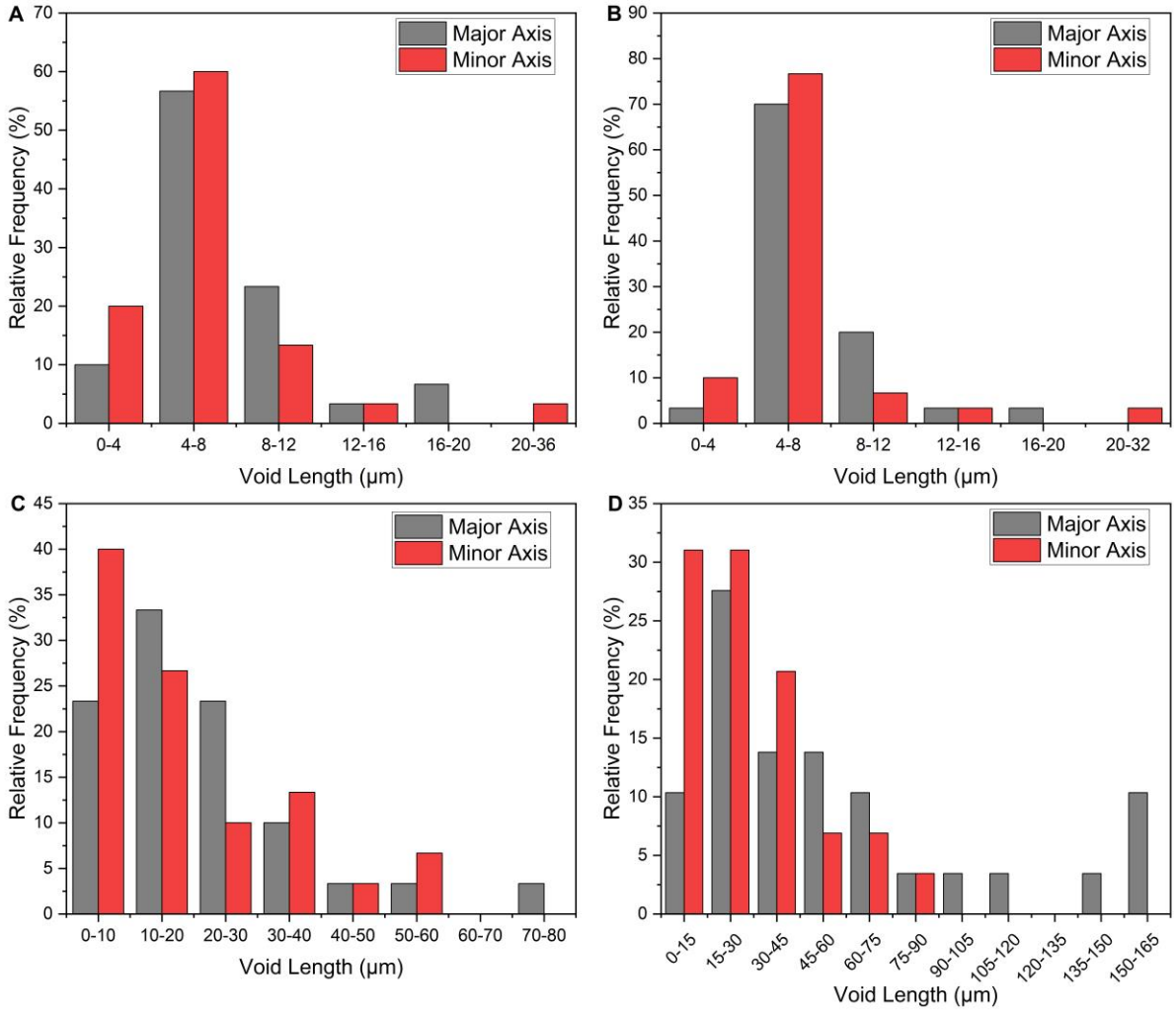

Figure 5-16 *Relative frequency plot of the major and minor dimensions of the voids in the following tensile laminates: (**A**) 0.59 MPa, (**B**) 0.39 MPa, (**C**) 0.19 MPa and (**D**) 0.05 MPa.*

For the tensile laminates that were cured at either 0.59 MPa or 0.39 MPa, the majority of the voids had dimensions in the range of 4-8µm in both the major and minor axis, with the mean value also falling in this range. However, as the cure pressure reduced, there was more variability in the results. Whilst the maximum measured voids of the 0.59 MPa and 0.39 MPa laminates were below 40µm, this increased up to 80µm and 165µm for the 0.19 MPa and 0.05 MPa laminates, respectively. The lengths for the two higher cure pressure laminates were mostly even between the major and minor directions (slightly larger lengths in the minor direction), however, for the lower cure pressures there was a higher percentage of longer voids in the major direction, this is particularly true for the 0.05 MPa cure pressure. This is likely due to the lower compaction resulting in longer voids.

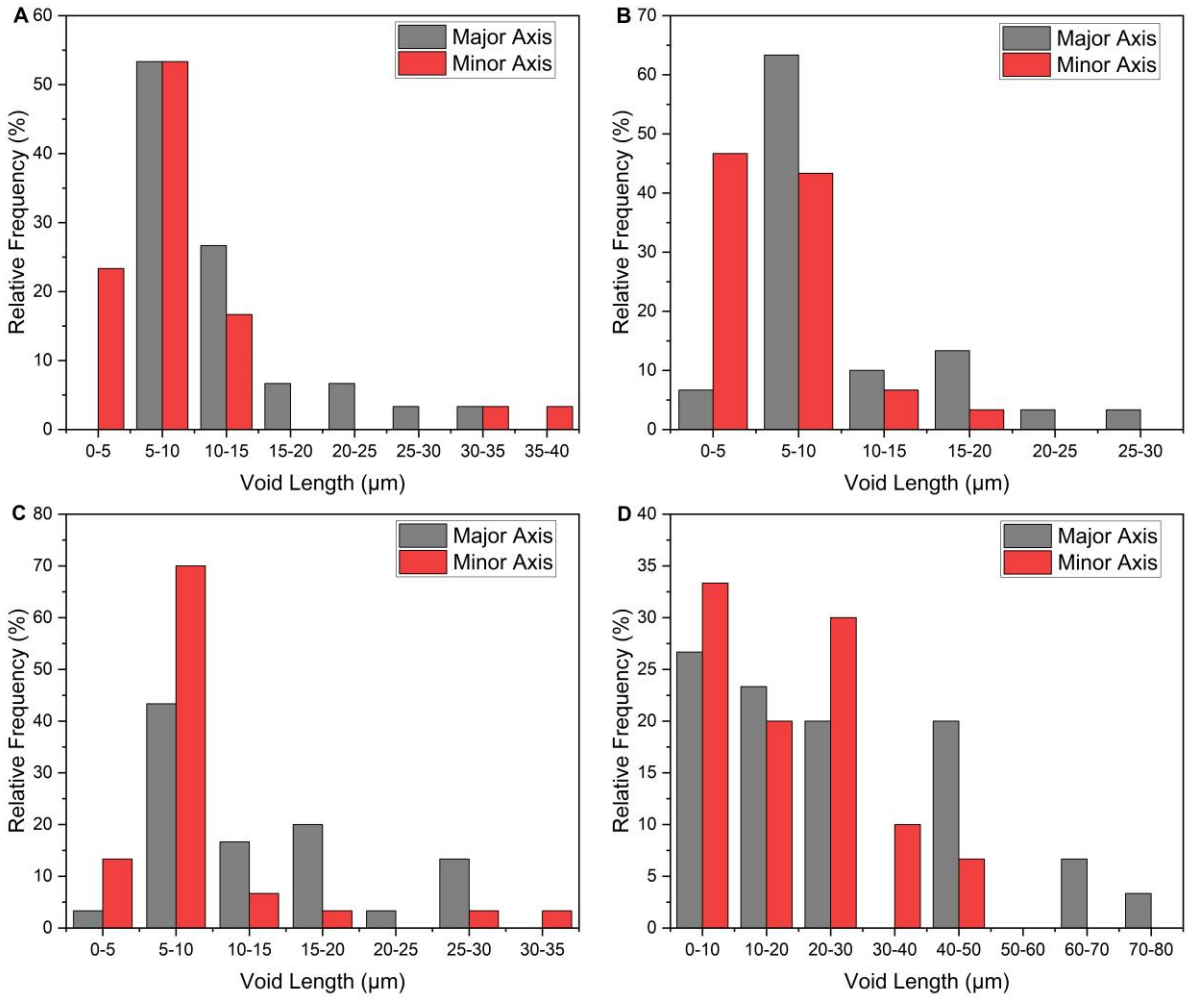

Figure 5-17 *Relative frequency plot of the major and minor dimensions of the voids in the following compressive laminates: (**A**) 0.59 MPa, (**B**) 0.39 MPa, (**C**) 0.19 MPa and (**D**) 0.05 MPa.*

The compression results also show that the majority of the voids have small dimensions with less than 10μm in both the major and minor directions in all laminates other than the one cured at 0.05 MPa. For the three higher cure pressure laminates the range in dimensions is up to 40μm, however, for the 0.05 MPa laminate, the major lengths can be seen up to 80μm. Again, this is likely because of the lower compaction due to lower cure pressure which results in elongated voids.

Whilst most voids fall approximately in the 5-10μm there is an increasing number of larger voids as the cure pressure reduces. This explains why there is a decay in strength reduction as porosity increases. As found in Chapter 4, there is a balance between the void size and void content such that increasing the size of the void reduces the stress intensity. This reinforces why both parameters must be considered.

5.5.2.4. Void size – resin infusion processing

The major and minor axes lengths of 60 voids per resin infused laminate were measured. From the shape analysis, it was found that for laminate C.L. 4, both micro and discrete voids were present in the laminate. As these two void types were present, both shapes were measured independently, labelled C.L.4 micro and C.L.4 macro. The mean length in both axes, error (calculated as a single standard deviation), and aspect ratio between the major to minor mean lengths, are recorded in **Table 5-8**. For all laminates the voids are of similar size (other than the discrete voids) where the mean major lengths are approximately 6.50 μm and the mean minor lengths are approximately 5.0 μm.

Table 5-8 *Size measurement results for the major and minor axis.*

Laminate I.D.	Mean Major Length / μm	Standard Deviation (Major axis) / μm	Mean Minor Length / μm	Standard Deviation (Minor axis) / μm	Aspect Ratio
T.L. 1	7.21	2.05	4.63	1.73	1.56:1
T.L. 2	6.01	1.71	4.05	1.38	1.48:1
T.L. 3	6.74	2.29	5.31	1.96	1.27:1
T.L. 4	6.04	2.16	4.70	1.83	1.28:1
C.L. 1	6.49	1.79	4.33	1.45	1.50:1
C.L. 2	7.09	2.32	4.66	1.80	1.52:1
C.L. 3	6.90	2.59	5.19	1.62	1.33:1
C.L. 4 (micro)	6.46	2.10	5.76	1.64	1.12:1
C.L. 4 (discrete)	142.39	92.77	75.88	58.15	1.88:1
C.L. 5	5.95	1.51	5.46	1.27	1.09:1
C.L. 6	6.32	2.22	5.49	1.91	1.15:1

Whilst the standard deviation recorded for each length suggested that the mean length is representative, it was also beneficial to present the range of results as a relative frequency histogram plot. This allows a greater understanding of the spread of recorded void lengths and the ability to identify any outliers. The histogram plots for the tensile and compressive laminates are presented in **Figure 5-18** and **Figure 5-19**, respectively. In almost all cases, for both the tensile and compressive laminates as well as in the major and minor axes, there is a single point at which the void lengths are most common. This can be seen by a single peak in the maximum relative frequency bins. The peak in the minor axis appears to be slightly tighter compared to the major axis, which is broader. This correlates with the error results in **Table 5-8** where the minor axis length has a mean standard deviation of 1.66 μm for all laminates, whereas the major axis standard deviation for all laminates is 2.07 μm. Also, in almost all plots,

the peak of the major axis occurs after the peak of the minor axis, again correlating with **Table 5-8** where the mean lengths for the major axis were always slightly longer.

Across both **Figure 5-18** and **Figure 5-19**, most peaks correlated with the mean axis length in **Table 5-8**. For instance, the peak for the major axis of all tensile laminates occurred in the 6-7.5 μm bin and the mean major axis lengths ranged from 6.01 to 7.21 μm. There are a few cases where the mean length is outside of the peak frequency bin, for example, laminate C.L.5 has a major axis mean length of 5.95 μm, yet the peak frequency bin is for lengths between 6-7.5 μm. As expected, all such cases can be explained by a small bias in the distribution resulting in the mean being slightly higher or lower accordingly. Whilst this is true, the relative frequency histogram plots use tight bins (up to a range of 2μm) and therefore the results overall correlate well with **Table 5-8**. This suggests that using the mean axis length to represent the porosity in the laminate is appropriate.

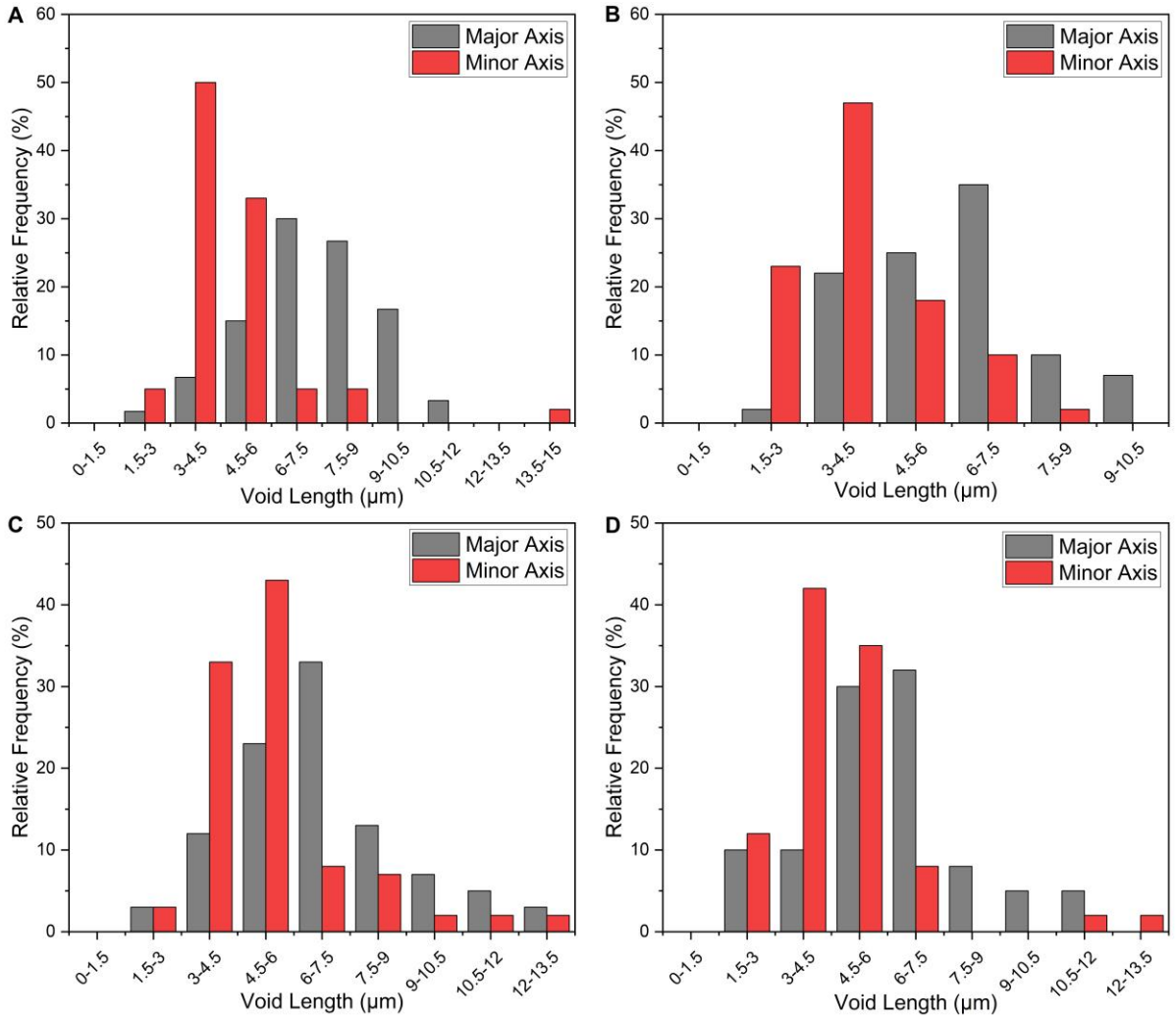

Figure 5-18 *Relative frequency histogram plot for laminates: (**A**) T.L. 1, (**B**) T.L. 2, (**C**) T.L. 3 and (**D**) T.L. 4.*

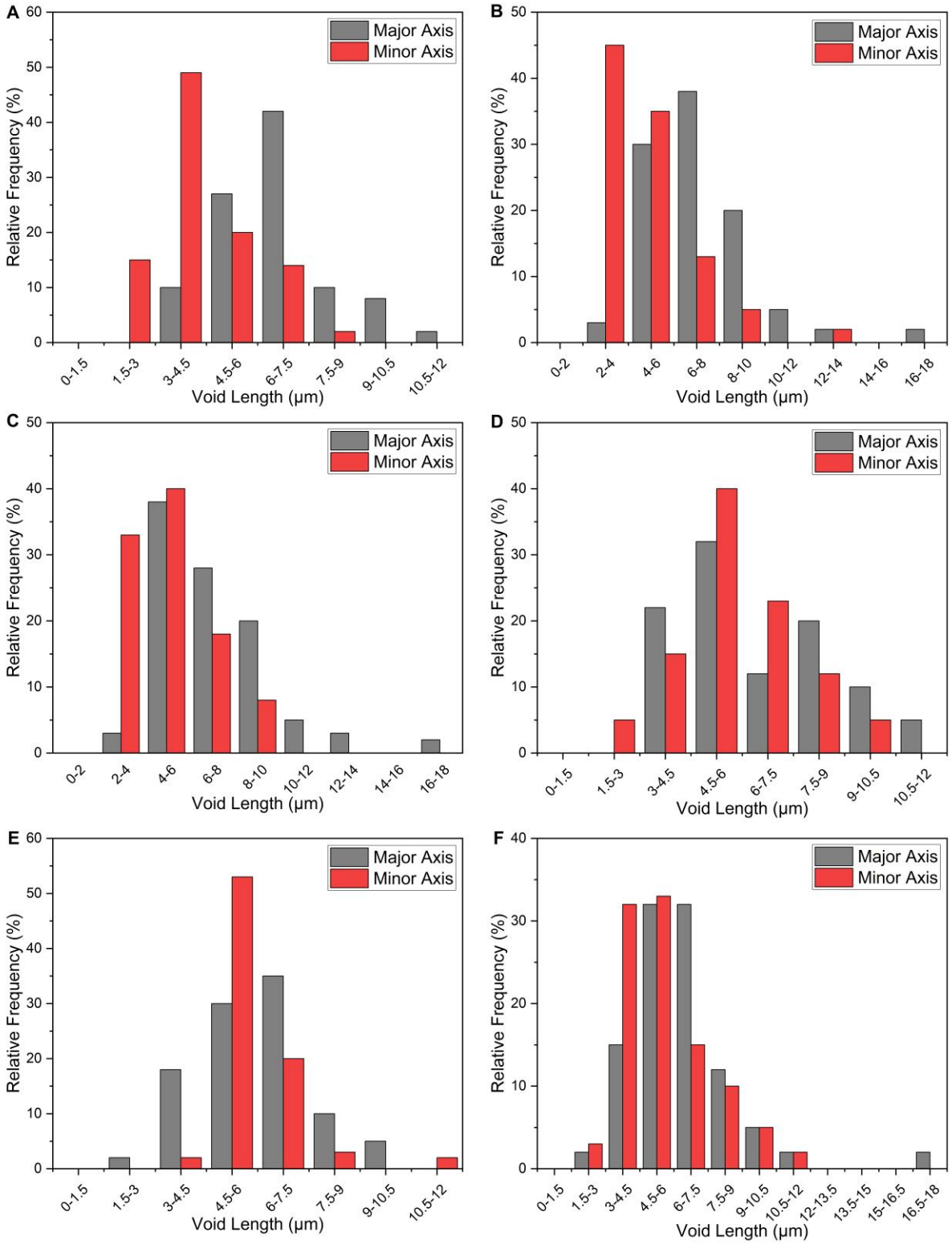

Figure 5-19 *Relative frequency histogram plot for laminates: (**A**) C.L. 1, (**B**) C.L. 2, (**C**) C.L. 3, (**D**) C.L. 4*, (**E**) C.L. 5, (**F**) C.L. 6. *N.B. only the micro-voids dimensions were used for laminate C.L. 4.*

The size results from **Table 5-8**, **Figure 5-18** and **Figure 5-19** suggest that a single void can be modelled as representative for all laminates. The only exception to this is for laminate C.L. 4, where two types of voids were identified. In this scenario, both

voids are modelled independently and have two separate Stage 1 models to understand their impact. The model with the lowest strength will be used as a 'worst case' and the corresponding results will be passed through to the Stage 2 model.

5.5.3. Fibre alignment analysis

The information to generate the stage two model (RUC) requires the matrix volume fraction to be known and the distance/angle between the fibres. The same material and processing conditions for the autoclave manufactured laminates were used by Almudaihesh et al.[167] who found that the resin content was calculated to be 40.64 %. The distance and angle between the fibres were measured using a microscope with a 50x lens as this allows high accuracy when measuring between the centres of the fibres. To measure the distance between the fibres, both horizontal and vertical lines were overlaid across the centre of the fibres as reference lines and the distance between these lines was measured. To measure the angle between the fibres, the centre of one fibre was selected and a horizontal baseline was drawn, then a centre-to-centre line was drawn between the fibres and the angle between the two lines was measured. Representative measurements can be seen in **Figure 5-20**.

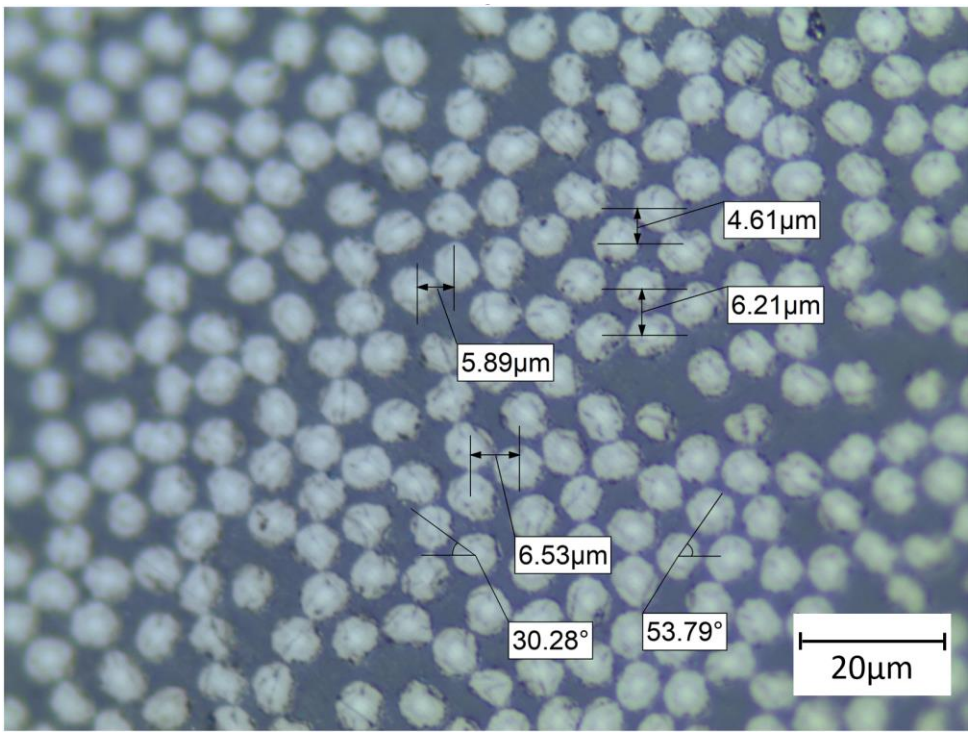

Figure 5-20 *Representative distances and angles between fibres.*

To check if different RUCs were required for the different cure pressures, the three measurements were repeated 15 times on each of the compression laminates. The compression laminates were chosen as they are thicker and therefore if any variation is present, it would have been more pronounced. The results, in **Table 5-9**, for all three measurements show little variation as cure pressure is reduced, meaning that a single RUC can be used for all models. In most cases, the distance between the fibres in both components is ~5μm, which reinforces the measurement angle of ~45°. In all results, the error is calculated as a single standard deviation.

Table 5-9 *Mean distances and angles between the fibres at four different cure pressures.*

Cure pressure / MPa	Mean Horizontal Distance / μm	Mean Vertical Distance / μm	Mean Angle / °
0.59	4.96±1.87	4.62±1.03	45.33±15.31
0.39	5.17±1.25	6.87±0.82	40.69±16.19
0.19	5.08±1.31	5.49±0.94	46.72±13.50
0.05	4.97±1.44	5.42±1.27	44.98±19.19

For the resin infused laminates, the radius of 30 fibres was measured which resulted in a mean measurement of 4.00 μm with a single standard deviation of 0.41 μm. Therefore, for modelling purposes, the fibre diameter was taken as 8.00 μm.

The next parameter considered is the fibre spacing, this was measured in two ways, firstly, the horizontal and vertical components between fibres were measured and used to calculate the angle, and secondly, the fibre angle between two neighbouring fibres (different fibre pairs to the one used for component measurements) was measured directly. The two approaches were used to cross-compare and ensure accurate measurements were taken. The fibre structure of five laminates was measured with 30 measurements for each component to ensure a representative measurement was recorded. The results are recorded in **Table 5-10** where for both measurement approaches there is a spread of results between approximately 60-70°. A large spread was expected as fibre distribution is non-periodic, however, in both approaches, a mean angle was determined at approximately 66°. There is no indication from these results that there is a difference in the fibre distribution; therefore, the same Stage 2 geometry can be used for all models.

Table 5-10 *Fibre structure measurements.*

Laminate I.D.	Horizontal Spacing / µm	Vertical Spacing / µm	Calculated angle / °	Measured angle / °
T.L. 1	2.15	6.33	71.3	59.4
T.L. 4	2.30	5.89	68.7	68.4
C.L. 1	2.95	5.28	60.8	63.5
C.L. 4	2.59	5.77	65.8	67.3
C.L. 6	2.28	5.19	66.3	69.3
Mean	2.45	5.69	66.6	65.7

The final parameter measured was the fibre volume fraction. The measurement was taken using 20 high-magnification images processed using Fiji ImageJ,[168] a scientific image postprocessing software, as described in Section 6.3.1.7. The mean result gave a fibre volume fraction of 54.82 % with a single standard deviation of 4.0%. This is in line with current literature, where Kazmi et al[169]. found typical fibre volume fractions for resin infusion laminates of approximately 52 %. Whilst the error is reasonably large, this was to be expected due to the non-periodic structure which included resin-rich zones and ply boundaries resulting in a higher matrix content and fibre-dense regions that have higher fibre volume fractions. As 20 images were used and each of these regions was captured, it was determined that the mean fibre volume fraction was representative.

5.5.4. µ-CT analysis

Accurate microstructure characterisation has been shown by this research to be extremely important. As the porosity characterisation was undertaken by 2D microscopy it was considered beneficial to µ-CT scan several samples from the autoclave cured laminates to validate the characterisation results. There were several aims of the study which included:

- Void content for each laminate.
- Void size distribution for one or more laminates.
- Accurate 3D geometry of the porosity from one laminate.
- Fibre volume fraction for one or more laminates.

For the most part, the μ-CT research was to validate the findings of the 2D microscopy and analyse any differences that may be identified. As the value for the fibre volume fraction of the autoclave cured laminates was taken from literature this was also to be validated. One of the largest benefits of characterising porosity through μ-CT scanning is that high-fidelity 3D models of the microstructure can be acquired, specifically of the porosity. For this reason, one of the aims was to use the μ-CT scans to create a high-fidelity model and compare the results to the model using data from 2D microscopy.

5.5.4.1. Scanning Setup

For each laminate, a sample with dimensions 2x4mm was cut out with the fibres orientated such that they were along the length of the sample. The ends of each sample were bonded to form a stack which was then enclosed in a CFRP tube. The purpose of the tube was to provide stability during scanning.

A Zeiss 160 kVp Versa 510 scanner was used at a spatial resolution of 700nm as this is approximately 10 times smaller than the most common voids and fibre diameters. The usable volume from each scan was positioned at the centre of each sample and covered a diameter of 666μm and a length between 950 and 980μm depending on the sample. The μ-CT scans were completed by the μ-VIS X-ray Imaging Centre at the University of Southampton, funded through the NXCT Free Beamtime Access Scheme, whom also recommended the appropriate scan settings and sample sizing.

5.5.4.2. Porosity evaluation

One of the main outputs from the μ-CT scans was to calculate a void content for each laminate, however, there was difficulty in identifying the voids. Only large and very elongated voids were captured, whereas the high number of smaller voids, seen from the microscopy, were not present. Before the parameters described above were agreed upon, previous scans were completed using different scanners, resolutions, and fibre alignment. In all these scans only the largest voids (greater than 50μm in width) could be detected. For this reason, the Zeiss 160 kVp Versa 510 scanner was chosen as it offers the highest resolution that the University of Southampton could provide. As there had been difficulty in capturing the smaller voids in previous trial scans, only the

four tensile specimens were scanned and if required the compression specimens could be scanned after.

Even at the highest resolution, the smaller voids were not captured, however, it was then considered that it was not a resolution issue as the fibres, which have a similar size, can easily be identified. Instead, it appears there is little difference between the attenuation of the matrix and void regions. The reason this became apparent was when studying the larger voids of the 0.05 MPa laminate, which can be seen in both the top-down view, **Figure 5-21**, and from a 3D render, **Figure 5-22**. It was expected that the attenuation across the void would be a continuous black/dark region, however, the greyscale colour (representing the attenuation) inside the void was the same as the surrounding matrix and only the edges of the void could be identified due to phase contrast edge enhancement. This can be shown by plotting the greyscale (which is 16-bit and therefore has 65,536 values[170]) along a line intercepting a matrix-rich zone and void as illustrated in **Figure 5-23(A&B)**. The graph showed very little difference in attenuation between the two zones, which was further confirmed by comparing the mean greyscale values of each region (matrix and void), this resulted in a 1.7 % difference between the two regions.

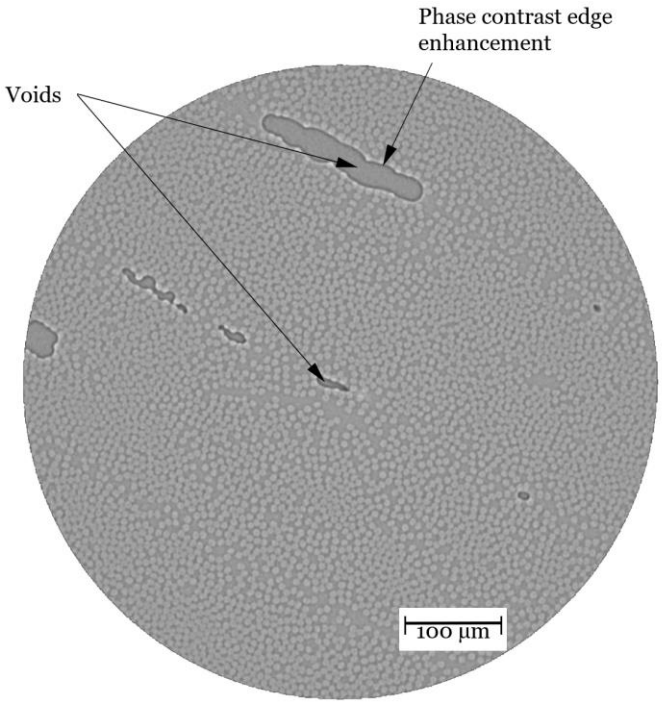

Figure 5-21 *A typical slice from a sample of the 0.05 MPa laminate showing the large voids able to be identified through the phase difference of the void and surrounding material.*

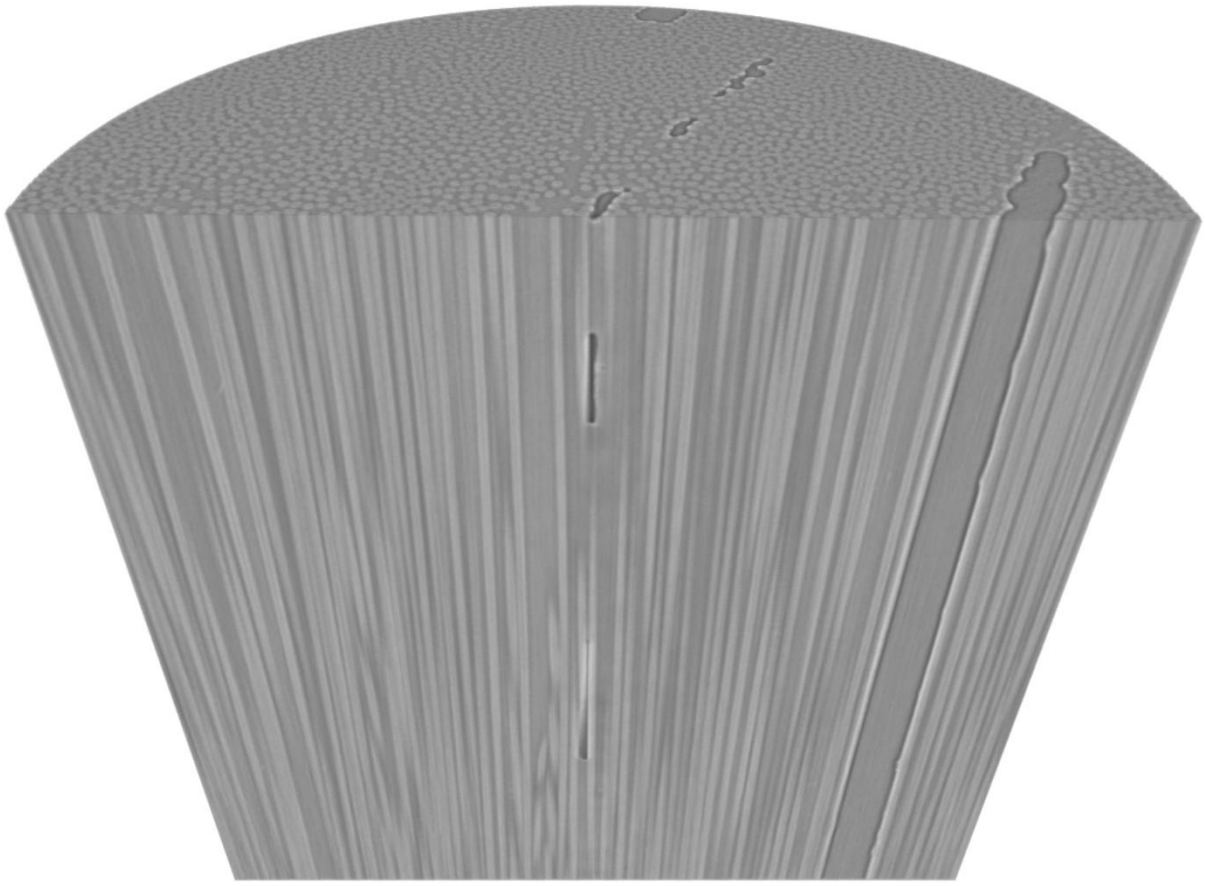

Figure 5-22 *3D cross-section render of the 0.05 MPa specimen of a specimen containing large voids.*

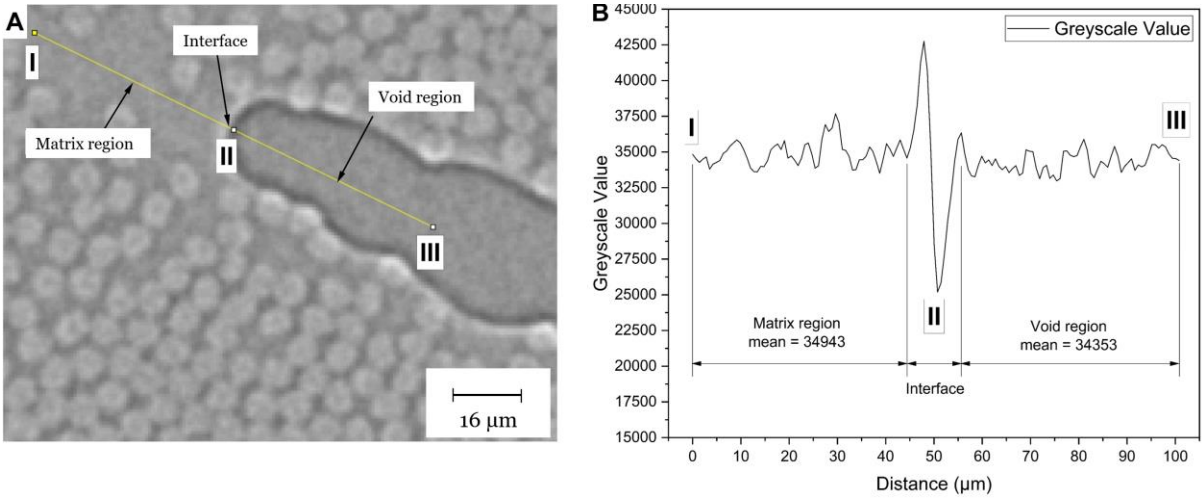

Figure 5-23 *Level of attenuation (greyscale value) across a line spanning both matrix and void regions, shows the interface between the two regions.*

5.5.4.3. Post-scan sample microscopy

To confirm that the regions that were scanned did contain voids, the samples were sent back to be sectioned at the scanned location and then polished and analysed. Due to the small size, it was not possible to cut the samples in half, therefore, each sample was bonded onto a Glass Reinforced Polymer (GRP) tab which was then carefully ground down to the centre point using a Chester 1-inch belt sander. A small amount of excess material was left to allow for polishing. Each sample was mounted in epoxy resin to aid handling and polished on a Struers Knuth-Rotor-3 polishing machine. It was important to ensure that the final polished surface was at the mid-point of the sample, therefore not all scratches were completely removed to prevent the removal of too much material.

Since the field of view of the images was small (approximately 200µm x 300µm), rather than taking a selection of images at different locations, the whole cross-section was imaged and then stitched together using the photo editing software Affinity Photo,[171] to form a single image to be evaluated. The microscopy of each sample can be seen in **Figure 5-24** to **Figure 5-27** with the previously measured void content in each figure caption for reference. The microscopy images show that for each sample there are many voids present, with the exception of the 0.59 MPa where there are only a few voids dispersed. However, in all cases, it was expected that the smaller voids would have been detectable particularly as they are of comparable size to the fibres and therefore the resolution was sufficient. A back-to-back comparison of the 0.39 MPa sample can be seen in **Figure 5-28** where the voids are clearly visible in the microscopy images but were not captured in the µ-CT scan. The main conclusion to be drawn is that in the microscopy images, all voids are present, whereas only the very large and elongated voids were detected from the µ-CT scans.

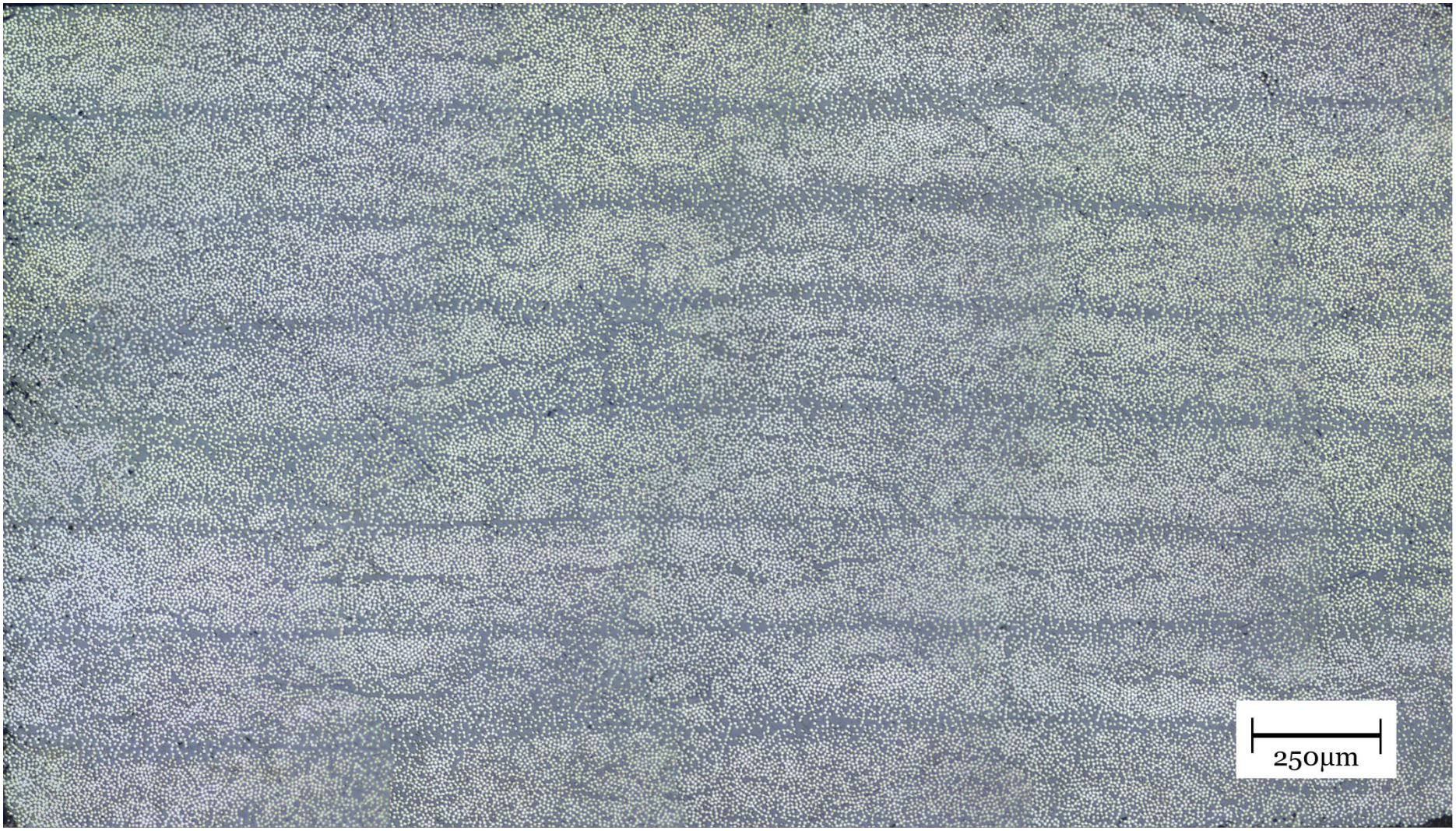

Figure 5-24 *Microscopy of the 0.59 MPa sample (void content of 0.63 %).*

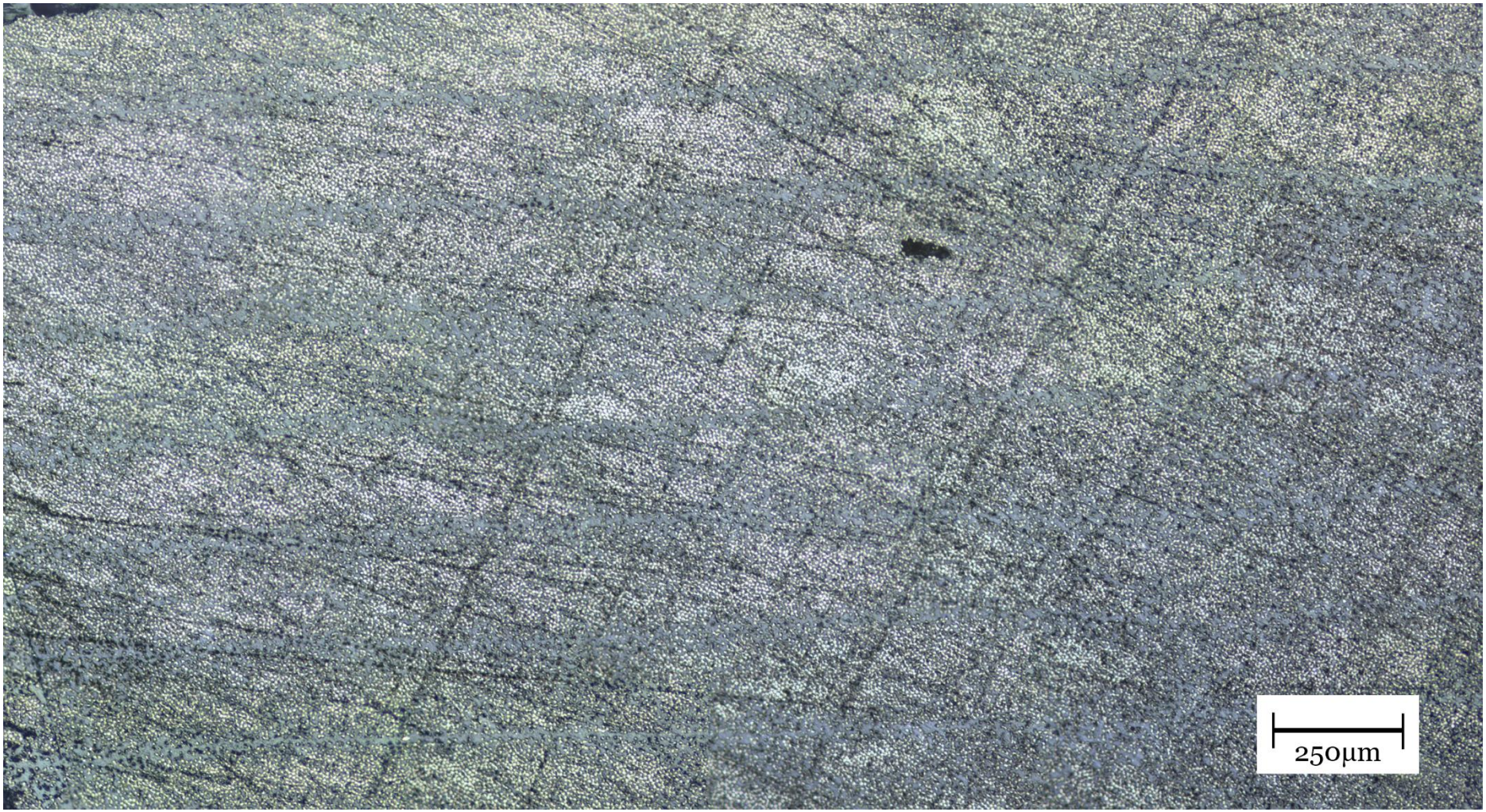

Figure 5-25 *Microscopy of the 0.39 MPa sample (void content of 1.28 %).*

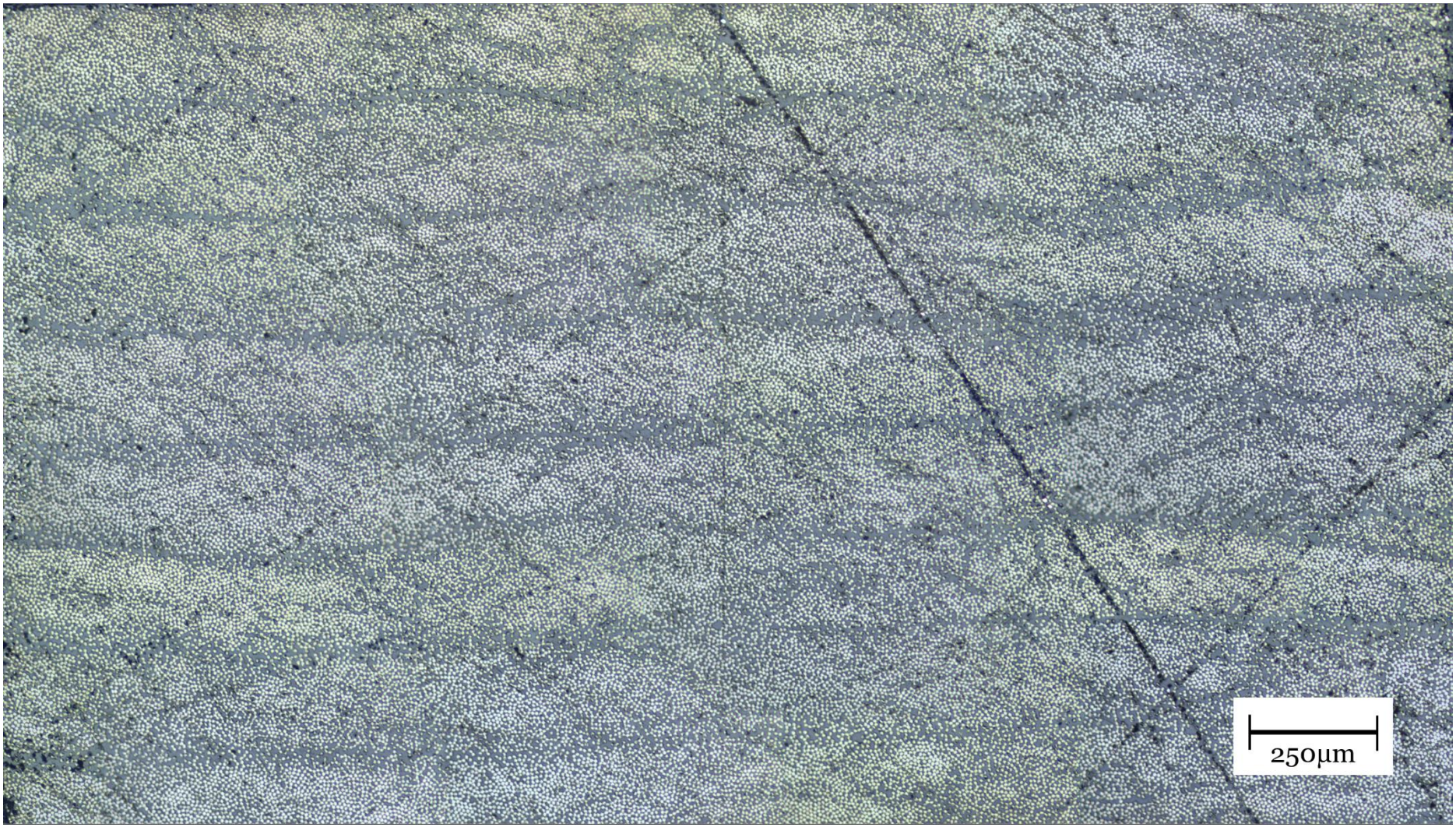

Figure 5-26 *Microscopy of the 0.19 MPa sample (void content of 0.88 %)*

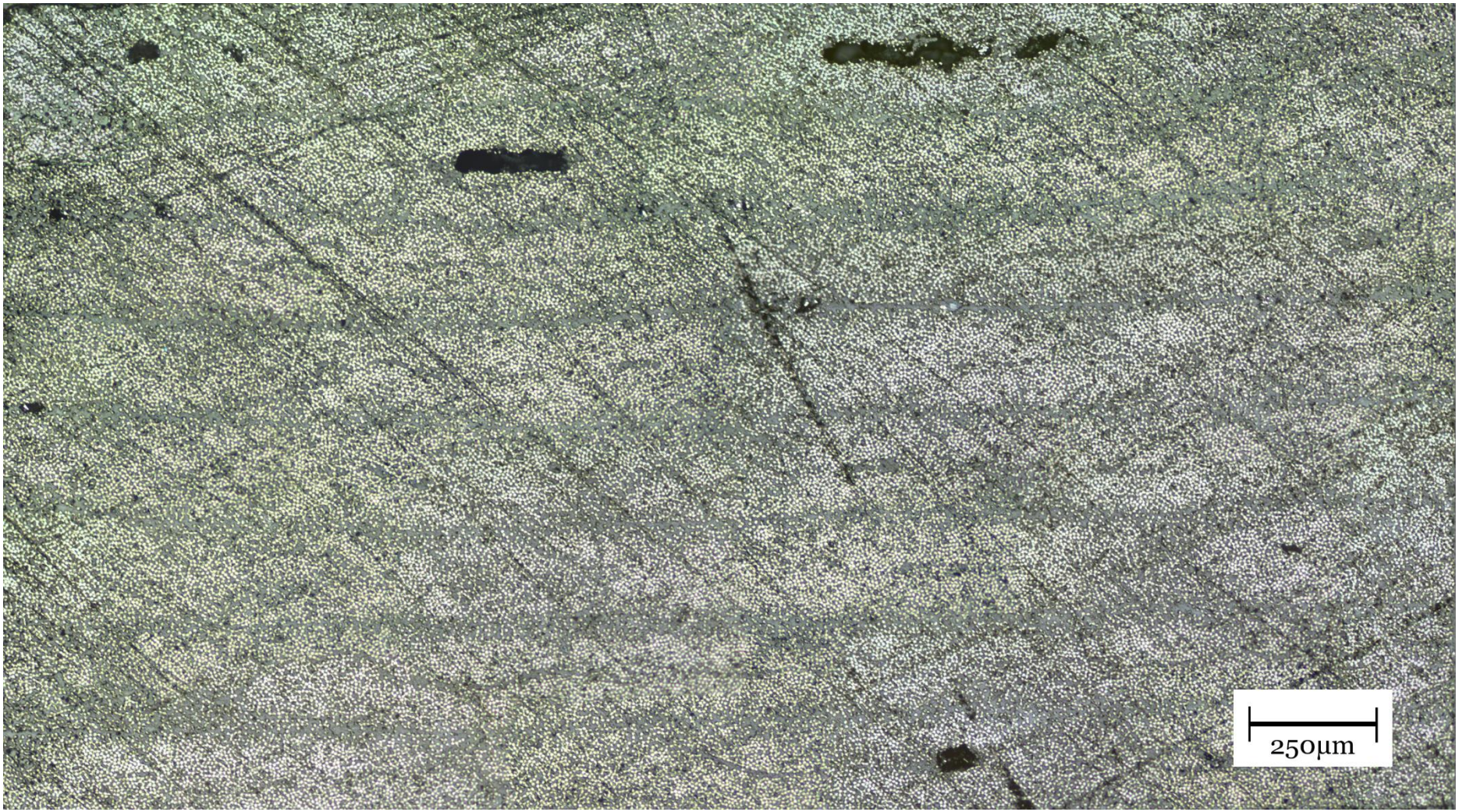

Figure 5-27 *Microscopy of the 0.05 MPa sample (void content of 2.01 %)*

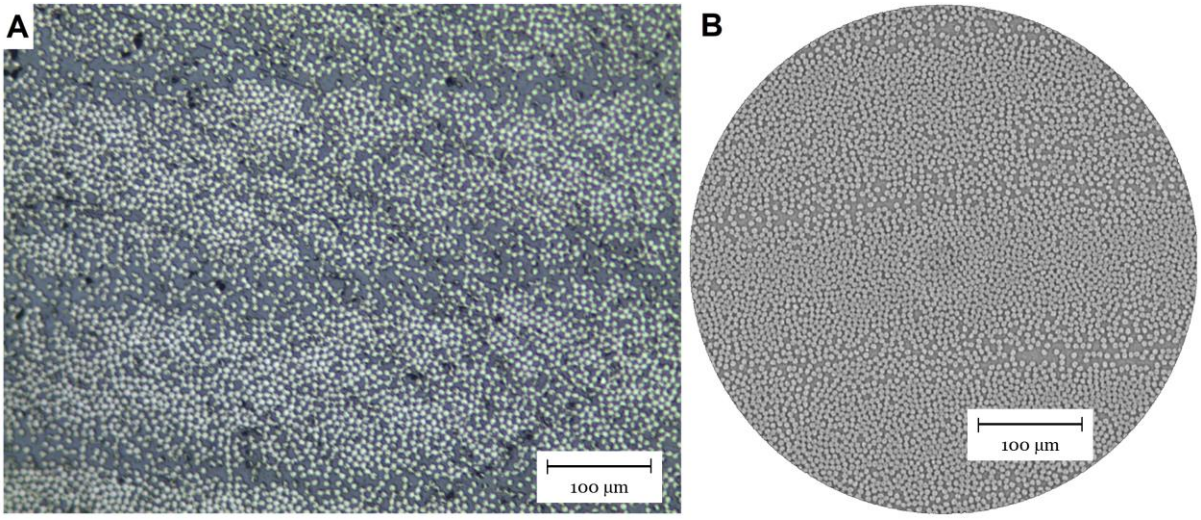

Figure 5-28 *Back-to-back comparisons of (**A**) microscopy and (**B**) µ-CT scan of the same sample showing small voids are not captured are not captured when µ-CT scanned.*

5.5.4.4. Fibre volume fraction assessment

The final objective of scanning the samples was to calculate the fibre volume fraction using Fiji ImageJ and compare this to the value used from the literature. Thresholding was applied to segregate the fibres from the matrix allowing a ratio between them to be calculated. However, when CFRP samples are scanned through µ-CT there is no definitive boundary between where the fibre edge is and the surrounding matrix. Also, an added difficulty is that for both the fibre and matrix regions there are significant levels of noise. These reasons mean that it is difficult to define with certainty where to apply thresholds, as can be seen in **Figure 5-29(A),** where a line is drawn intersecting several fibres and the corresponding greyscale values are plotted in **Figure 5-29(B)**. The noise of the fibre and matrix regions are overlaid in red and blue, respectively, and the sloped lines between these two regions represent the transition from fibre to matrix. To address the difficulties two measurements can be taken at a high and low threshold and therefore, it is possible to say with higher certainty that the fibre volume fraction is between these values.

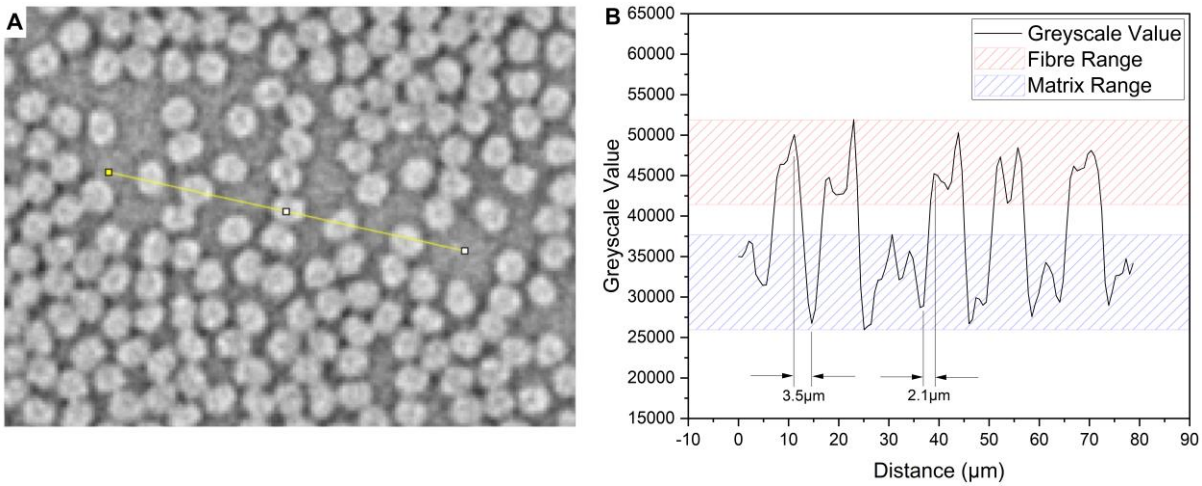

Figure 5-29 *Range of greyscale values for the matrix and fibre where (**A**) shows a line intersecting multiple fibres and (**B**) gives the corresponding greyscale values along the line. The red overlay shows the range of greyscale values for the fibre and the blue overlay shows the greyscale range for the matrix.*

The steps taken to calculate the fibre volume fraction can be seen in **Figure 5-30** where a magnified region of a scanned sample is shown in (**A**) for clarity and used throughout. (**B**) shows the threshold applied to separate the fibres from the matrix. The sliders in the popup window allow a certain greyscale range to be selected and this is where the upper or lower threshold is set for the calculation. Applying this threshold sets the fibres to white and the matrix to black (**C**), however often there is overlap and connected regions, therefore, the 'Watershed' function is used (**D**) to separate the connected regions. The fibres are then counted using the 'Analysis Particles' function. To ensure only the fibres are being counted a range is specified such that only regions with an area between 30µm² to 50µm² are counted, based on a fibre diameter being 7±1µm. Each fibre that is counted is recorded but also an overlay is applied to the original image (**E**), allowing the counted fibres to be checked and compared against the original image (**F**). As each fibre is counted the area is recorded which can then be summated to give the total area occupied by the fibres. Since the overall area of the scanned sample is known, the fibre volume fraction can be calculated.

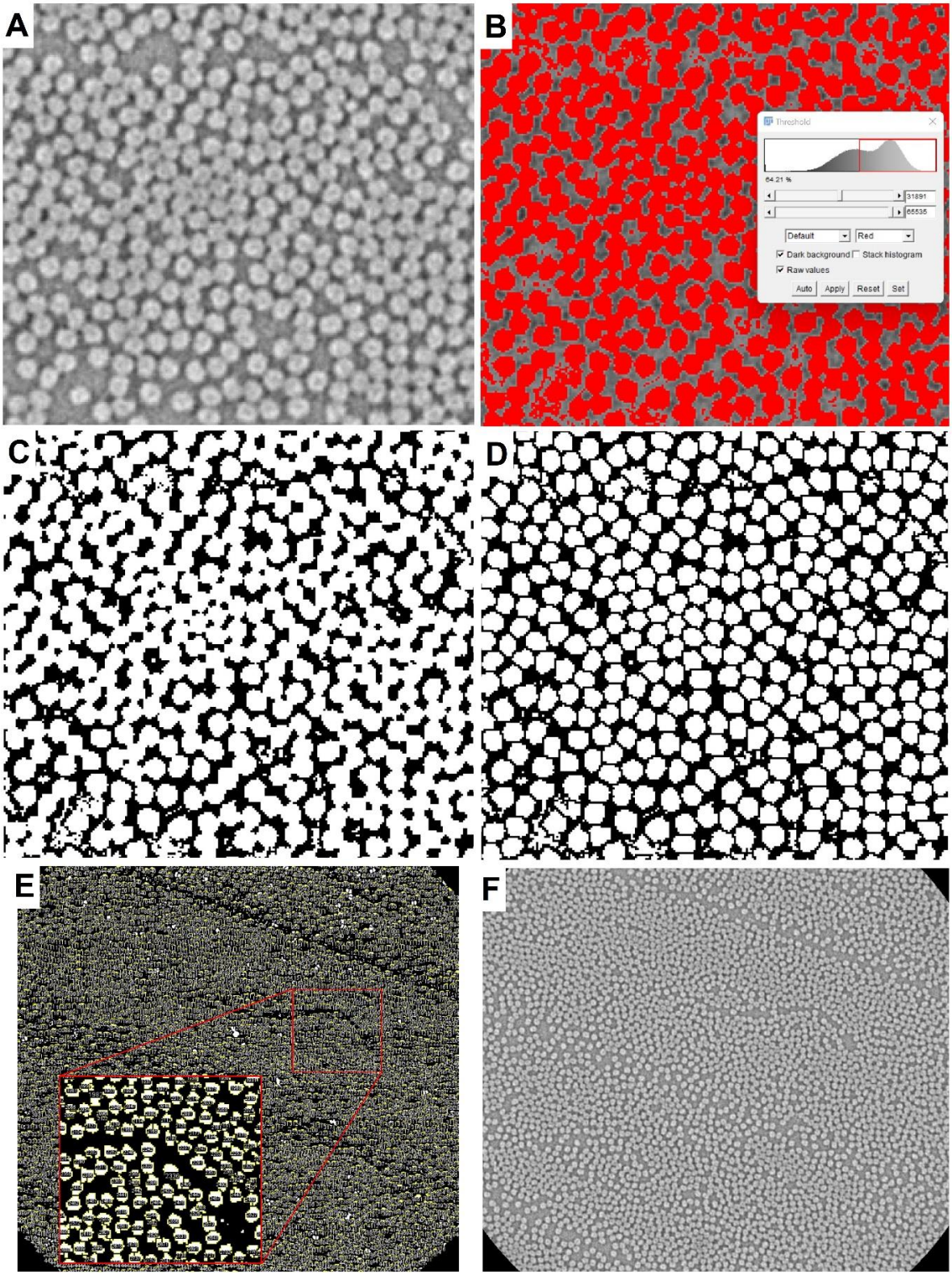

Figure 5-30 *Steps taken to identify fibres to calculate the fibre volume fraction. (**A**) is a magnified image of the fibres being analysed and (**B**) and (**C**) show the threshold applied. A 'watershed' function is applied (**D**) to segregate combined fibres and (**E**) shows the fibres that are counted by a numerical overlay (resin-rich zone is magnified for clarity) which can be compared to the original image (**F**).*

It was assumed that the fibre fraction is the same across all samples and therefore the 0.59 MPa sample was selected. The image stack from this scan produced 963 images, of which 10 evenly distributed images were selected for analysis. The mean results of the image processing can be seen in **Table 5-11** where the greyscale value used for the upper and lower threshold was recorded along with the number of fibres, the calculated fibre and the matrix volume fraction. The error was calculated based on one standard deviation. The fibre volume fraction gives a possible range between 59.2 to 61.2 % which, when considering a void content of 0.63 %, gives a matrix volume fraction between 38.2 to 40.2 %. This correlated well with the measured values of 39.8 to 41.6 % by Almudaihesh et al.[167] for the same material.

Table 5-11 *Results from processing the μ-CT scans to calculate the fibre volume fraction.*

Greyscale Threshold	Greyscale value	Number of fibres	Fibre volume fraction / %	Corresponding Matrix volume Fraction / %
Upper	30647±861	4990±174	59.2±2.0	40.2±2.0
Lower	28599±1143	4852±272	61.2±3.3	38.2±3.3

5.6. Experimental Testing Results

5.6.1. Mechanical testing of autoclave processed laminates

5.6.1.1.Tensile and Compressive Testing

Figure 5-31 and **Figure 5-32** present representative Load-Displacement and Stress-Strain graphs for the tensile and compressive specimens respectively. The failed specimens are shown in **Figure 5-33**, where the transverse specimens failed through a lateral and through-thickness failure type in the gage section for the tensile and compressive specimens respectively (LGM & HGV failure identification codes). Both the longitudinal tensile and compressive specimens failed through long splitting at the gage section (SGV failure identification code). The results of the increase in porosity against strength for the autoclave manufactured specimens can be seen in **Figure 5-34**. Overall, the results show that increasing porosity negatively affects the strength in the transverse direction, yet the longitudinal direction remains unaffected. The reason for investigating the impact of porosity in the longitudinal direction was that, whilst for tension it is known that porosity is not an issue, the research presented in subsection 2.7 showed that there is uncertainty in the level of sensitivity compressive strength has to porosity. The uncertainty is driven by the hypothesis that in

longitudinal compression the matrix supports the fibres from buckling, therefore by increasing the porosity it was possible that micro-buckling could be initiated at a lower load. On top of this however, contrary to this hypothesis, additional uncertainty came from the results of Hapke et al[26], where it was reported that an increase in strength was observed due to larger voids in longitudinal compression testing. The reasoning was based on the larger voids halting kink band propagation as the kink band buckles into the void. The different uncertainties gave further reasoning into investigating how porosity affects the laminates in different directions. However, as shown in **Figure 5-33**(**D**&**E**) and explained previously, the failure type was due to long splitting and there was no evidence of kink bands. The results in **Figure 5-34** show that there is not a definitive difference between the strengths of the longitudinal compression laminates. The transverse results show that as the void content increases the strength reduces nonlinearly for the compressive laminates, where a linear trend was observed for the tensile laminates.

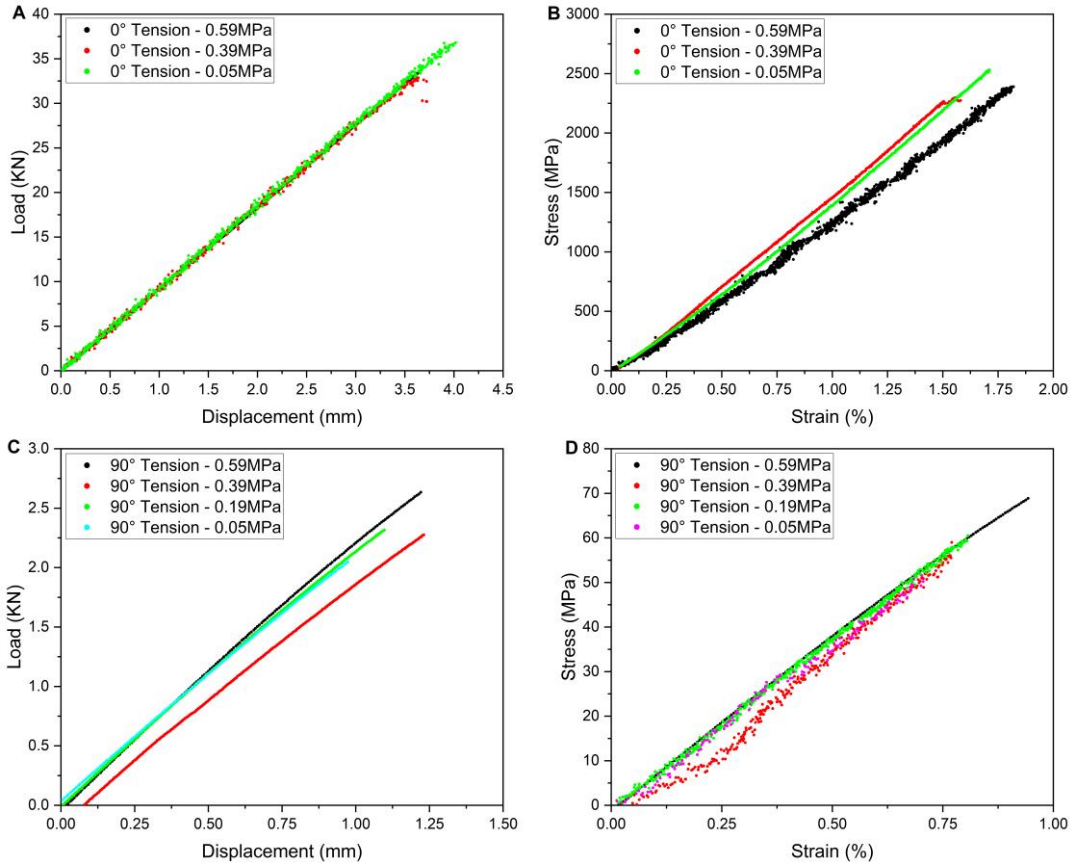

Figure 5-31 *Representative tensile loading graphs. 0° Load-Displacement (**A**) and Stress-Strain (**B**), and 90° Load-Displacement (**C**) and (Stress-Strain **D**).*

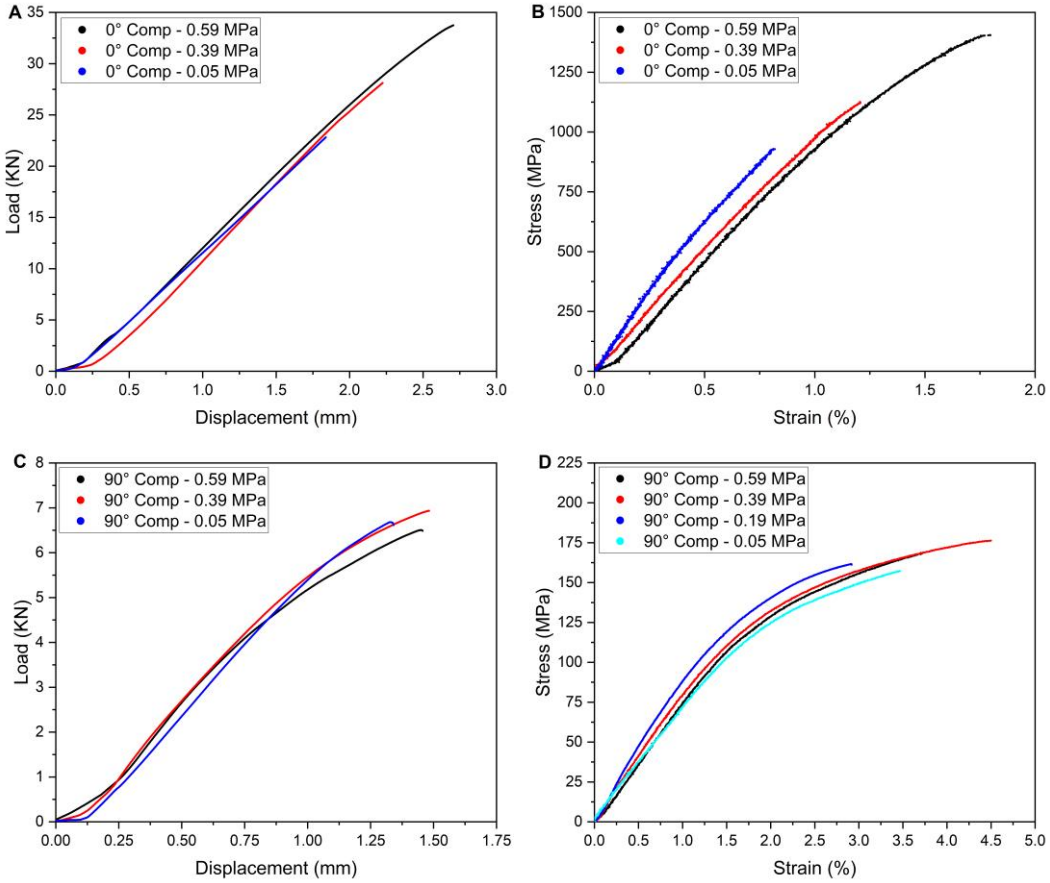

Figure 5-32 *Representative compressive loading graphs. 0° Load-Displacement (**A**) and Stress-Strain (**B**), and 90° Load-Displacement (**C**) and (Stress-Strain **D**).*

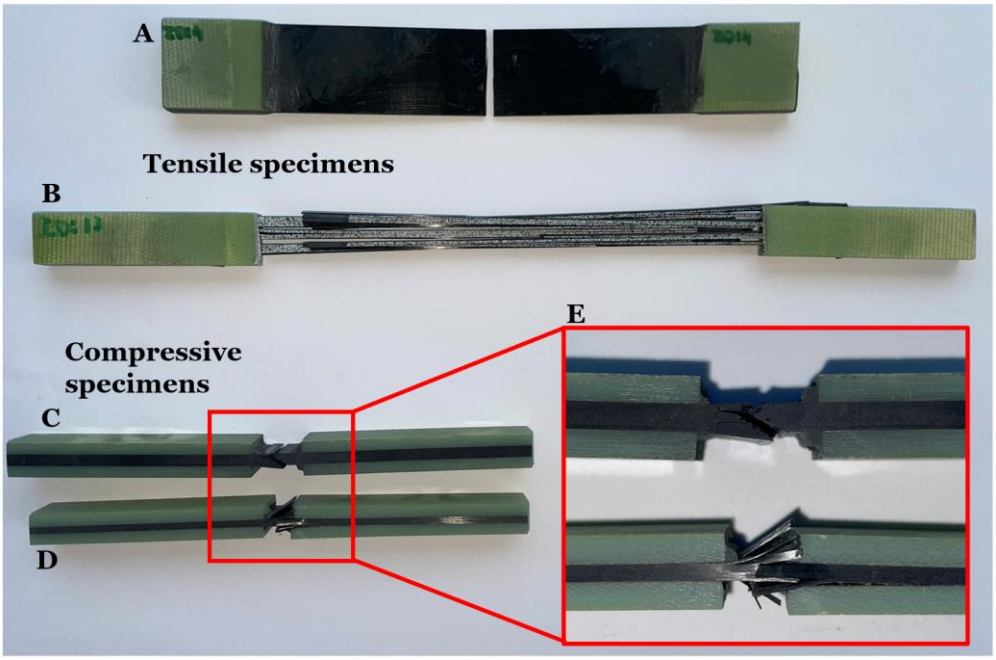

Figure 5-33 *Failed (**A**) transverse and (**B**) longitudinal tensile specimens, and (**C**) transverse and (**D**) longitudinal compressive specimens. **E** shows a zoomed-in region of the failed compressive specimens.*

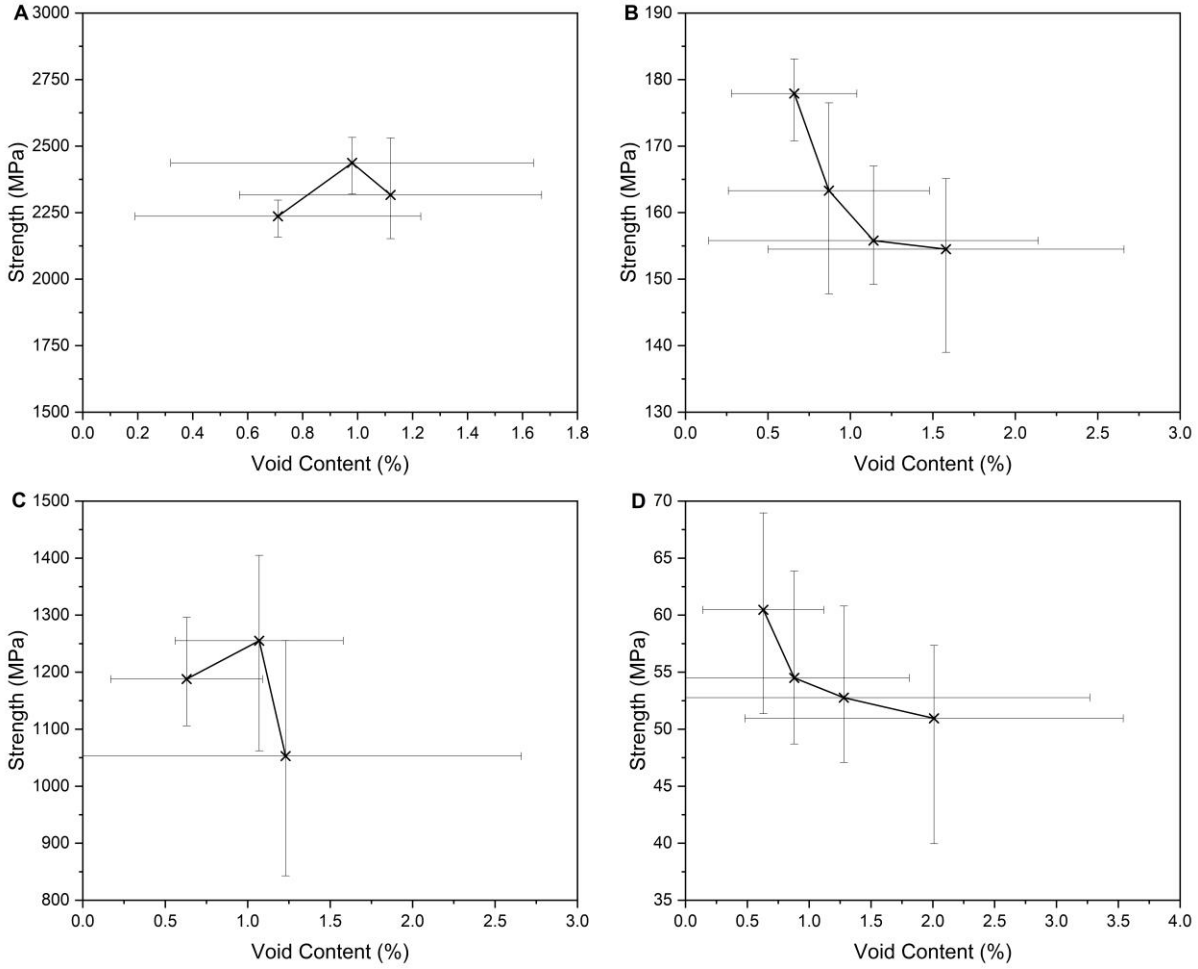

Figure 5-34 *Strength as a function of the void content for laminates: (**A**) 0° Compression, (**B**) 90° Compression, (**C**) 0° Tension, (**D**) 90° Tension.*

The modulus change due to variation in void content is presented in **Figure 5-35**. The results show that the modulus remains unaffected as the void content is increased. The literature presented in subsection 2.7, found that whilst some researchers reported that composite stiffness is degraded as porosity increases[97,99,172], others reported no effect.[21,71,100] This disagreement was the main reason for the experimentation, as it proves that for this material under the current conditions, the modulus is unaffected in all load cases. For this reason, the impact on the modulus is not incorporated into the modelling process.

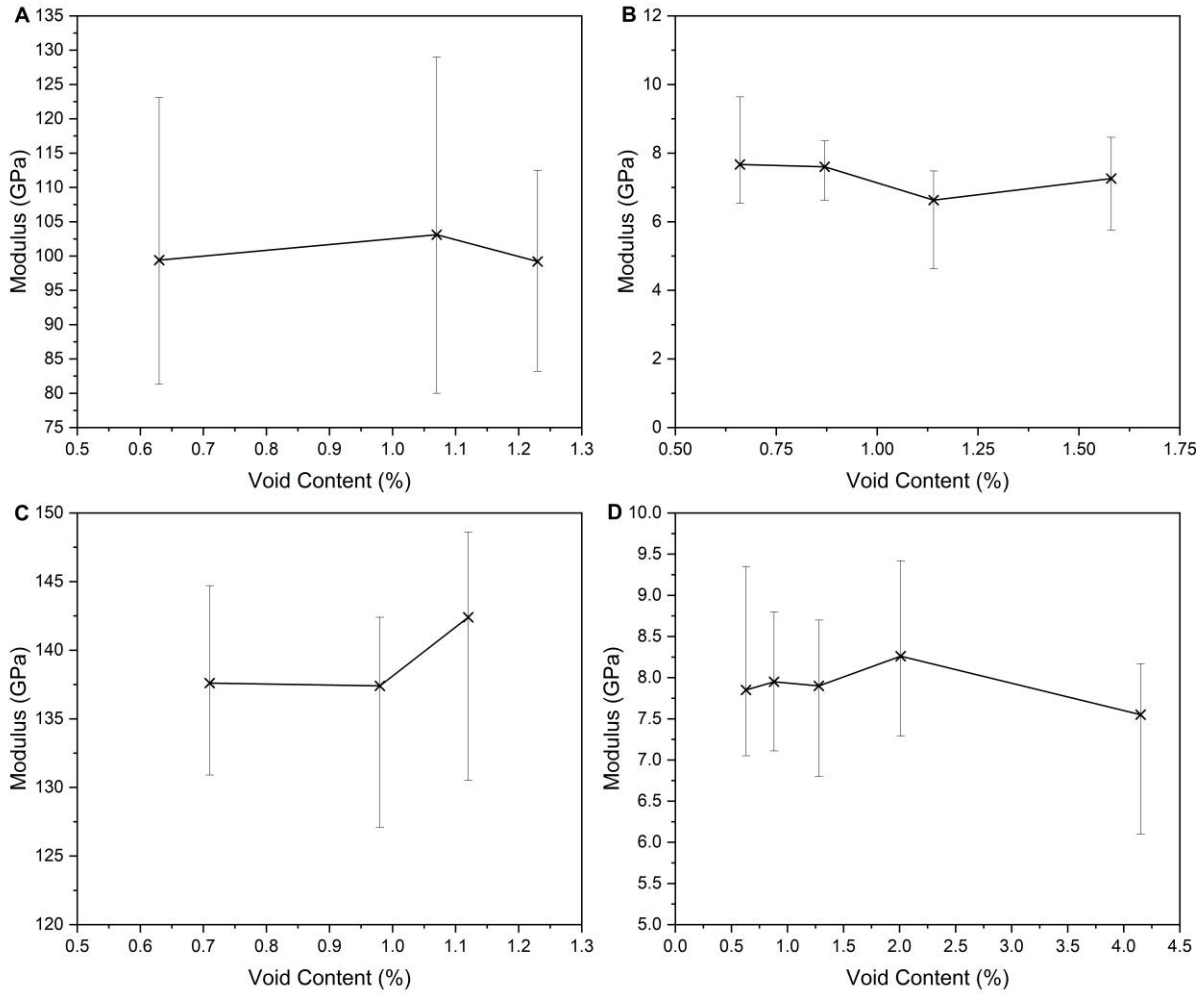

Figure 5-35 *Modulus as a function of the void content for laminates: (**A**) 0° Compression, (**B**) 90° Compression, (**C**) 0° Tension, (**D**) 90° Tension.*

5.6.1.2. DMA Testing

The results of the DMA tests are presented in **Figure 5-1**, which shows the glass transition temperature for two sets of autoclave processed laminates, cured at different cure pressures. The difference in the glass transition temperature between the laminates cured at 0.05 MPa and 0.59 MPa is 0.9°C and 0.2°C for the first and second sets respectively. The maximum difference in measured glass transition temperature for samples cured at the same cure pressure (to show measurement error) were 1.2°C and 1.5°C for the specimens cured at 0.05MPa and 0.19MPa respectively.

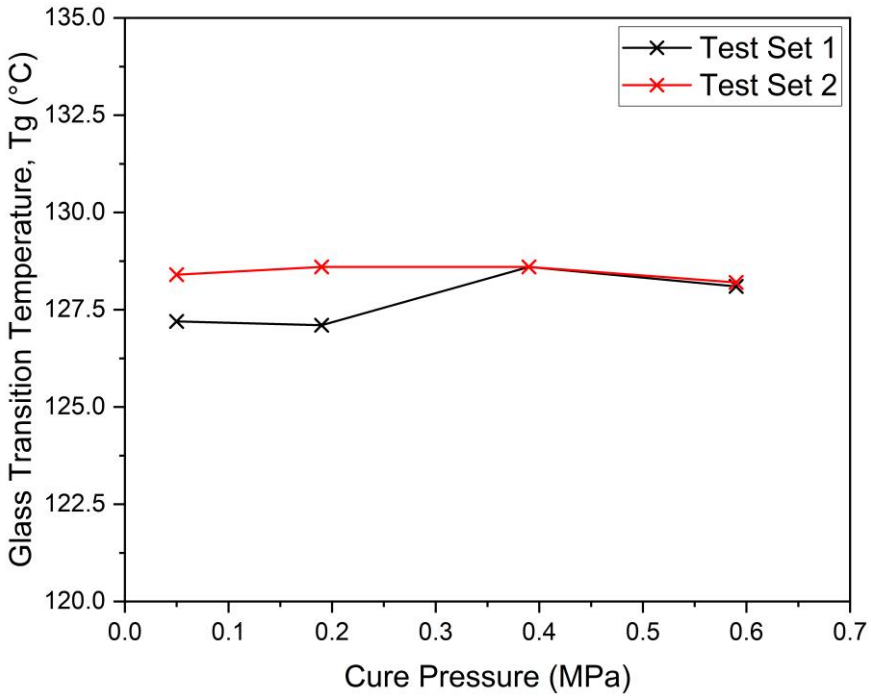

Figure 5-36 *Glass transition temperature results from the DMA testing of two sets of autoclave processed specimens cured at different cure pressures.*

5.6.2. Mechanical testing of resin infused laminate

5.6.2.1. Tensile and compressive testing

For both the tensile and compressive laminates that were manufactured through resin infusion, the specimens were tested in sequential order along the laminate length, starting at the outlet end and working towards the inlet. This was to identify if there was any significant variation/trend in strength along the length, and how this correlates with the variation in void content at the start, middle and end of the laminate. After each specimen was tested the failure mode and location were checked to determine if the correct failure was achieved. Examples of post-failure specimens are shown in **Figure 5-37**. All tensile specimens failed correctly with a lateral failure type within the gauge section (LGV). Only one compressive specimen failed incorrectly through end crushing, whereas the rest had a through-thickness failure mode within the gauge section (HGM). Representative Load-Displacement and Stress-Strain graphs are illustrated in **Figure 5-38**. It is clear from the graphs that both in tension and compression, the load response is linear-elastic and fails in a brittle-like fashion.

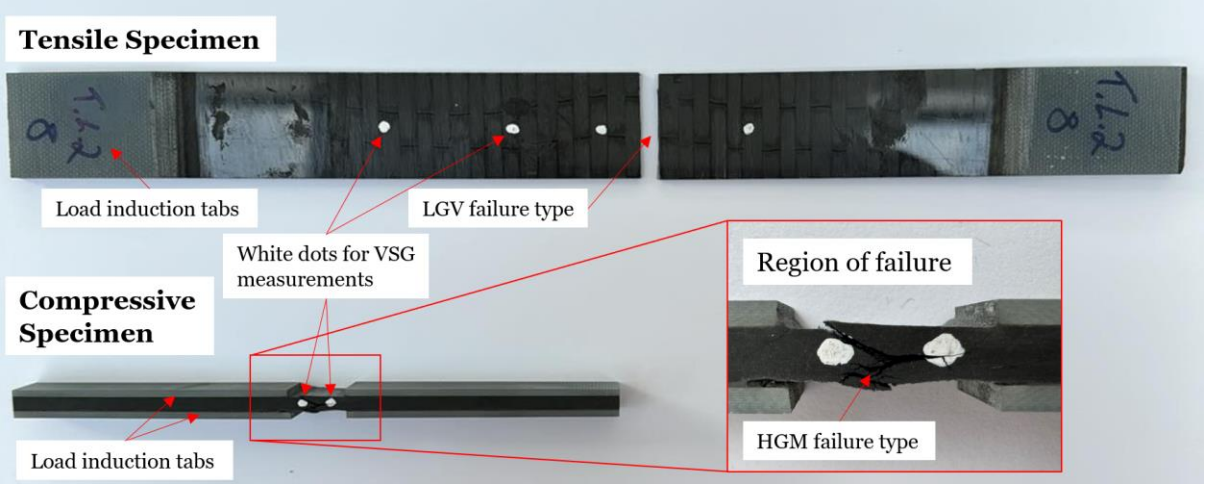

Figure 5-37 *Failed tensile and compressive specimens showing failure type.*

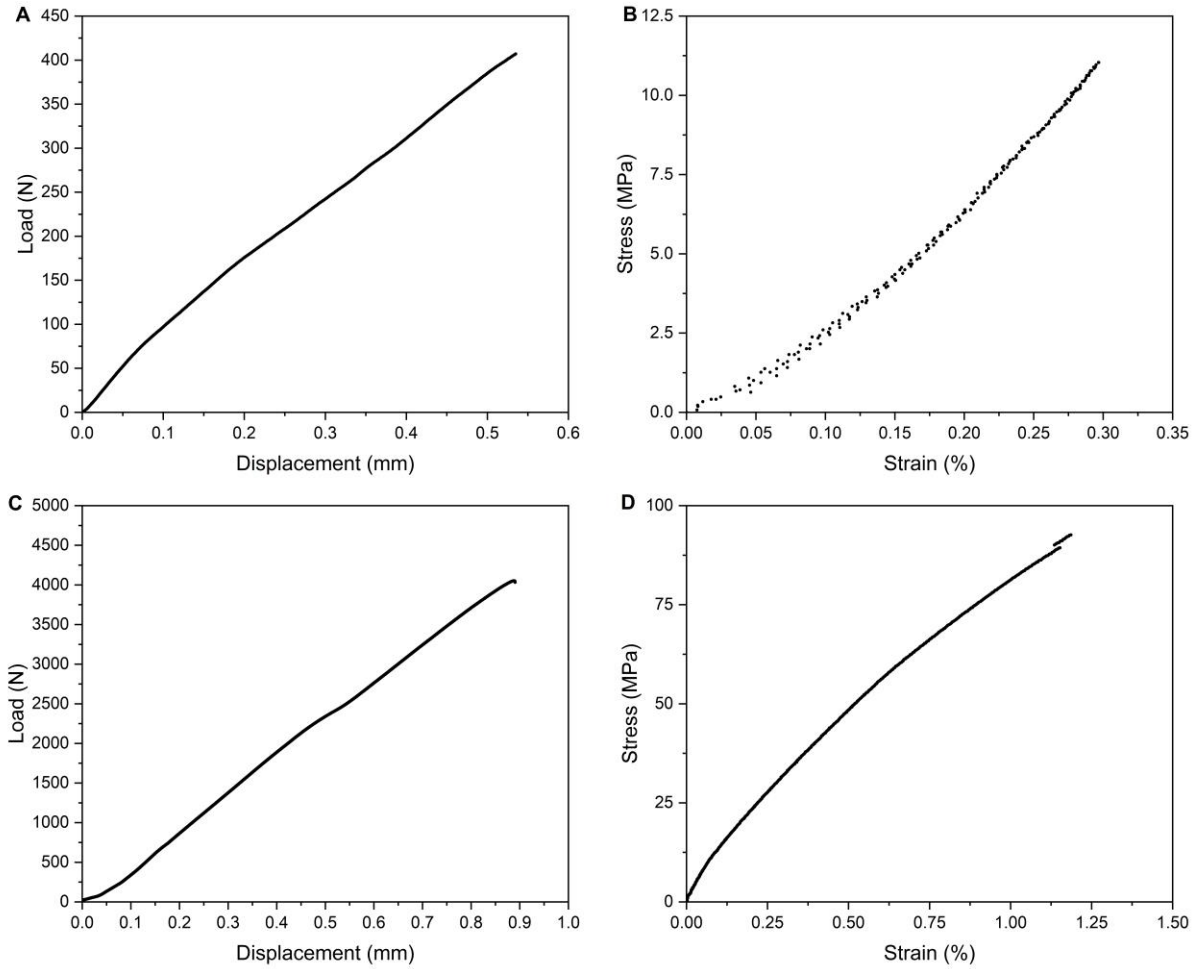

Figure 5-38 *Representative load response for the tensile and compressive tests. (**A**) Tensile Load-Displacement, (**B**) Tensile Stress-Strain, (**C**) Compressive Load-Displacement and (**D**) Compressive Stress-Strain.*

The specific strength for each tensile and compressive laminate can be seen in **Figure 5-39** and **Figure 5-40**, respectively. Overlaid on each plot is the overall mean as well as the upper and lower error defined as a single standard deviation. The results from the C-scan inspection identified the length of the dry patches for laminates T.L. 4 and C.L. 4, which is why these specimens are missing.

For all four tensile laminates, there does not appear to be a significant change in strength along the length of the laminate, other than the expected scatter in results. There may be a very slight increase in strength towards the inlet side of T.L. 3, however, only two of the six specimens on the inlet side are greater than the overall laminate mean and the void content results in **Figure 5-8**(**A**) do not suggest a variation in void content. Therefore, this trend was considered insignificant. Similarly, five out of the six compression laminates do not show a significant variation along the length of the laminate, other than the experimental scatter. For laminate C.L.3 however, it was observed that for the inlet and outlet, there is an increase and decrease in strength respectively. This is reviewed in more detail in the discussion chapter, but to use the data in the modelling stages, the first 3 specimens on the inlet end were removed from the study.

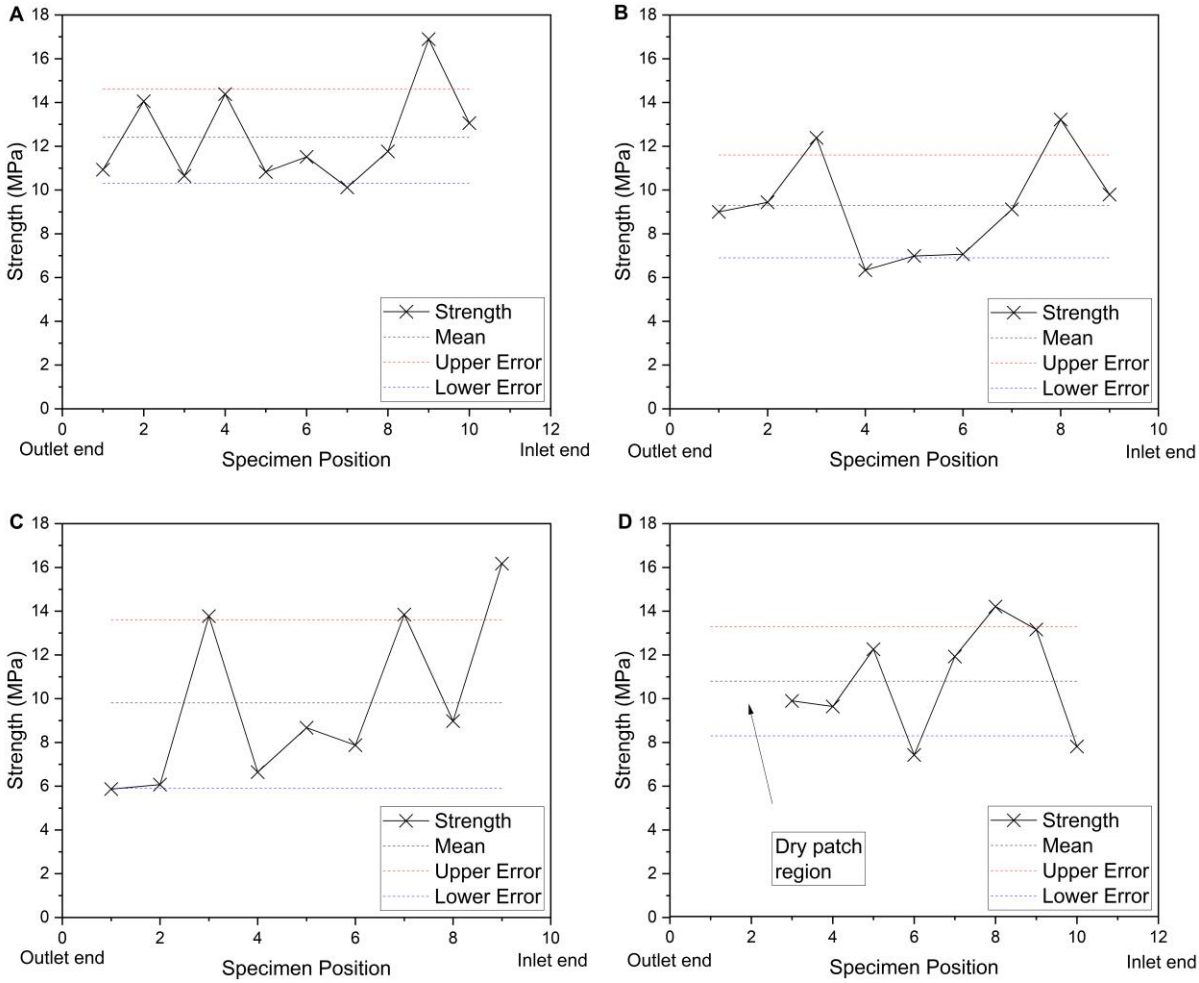

Figure 5-39 *Specimen strength (tension) along the length of the laminate for (**A**) T.L. 1, (**B**) T.L. 2, (**C**) T.L. 3 and (**D**) T.L. 4. The mean strength is overlaid in each plot, as well as the upper and lower error, defined as a single standard deviation. Consistent strength axis to show variation between laminates.*

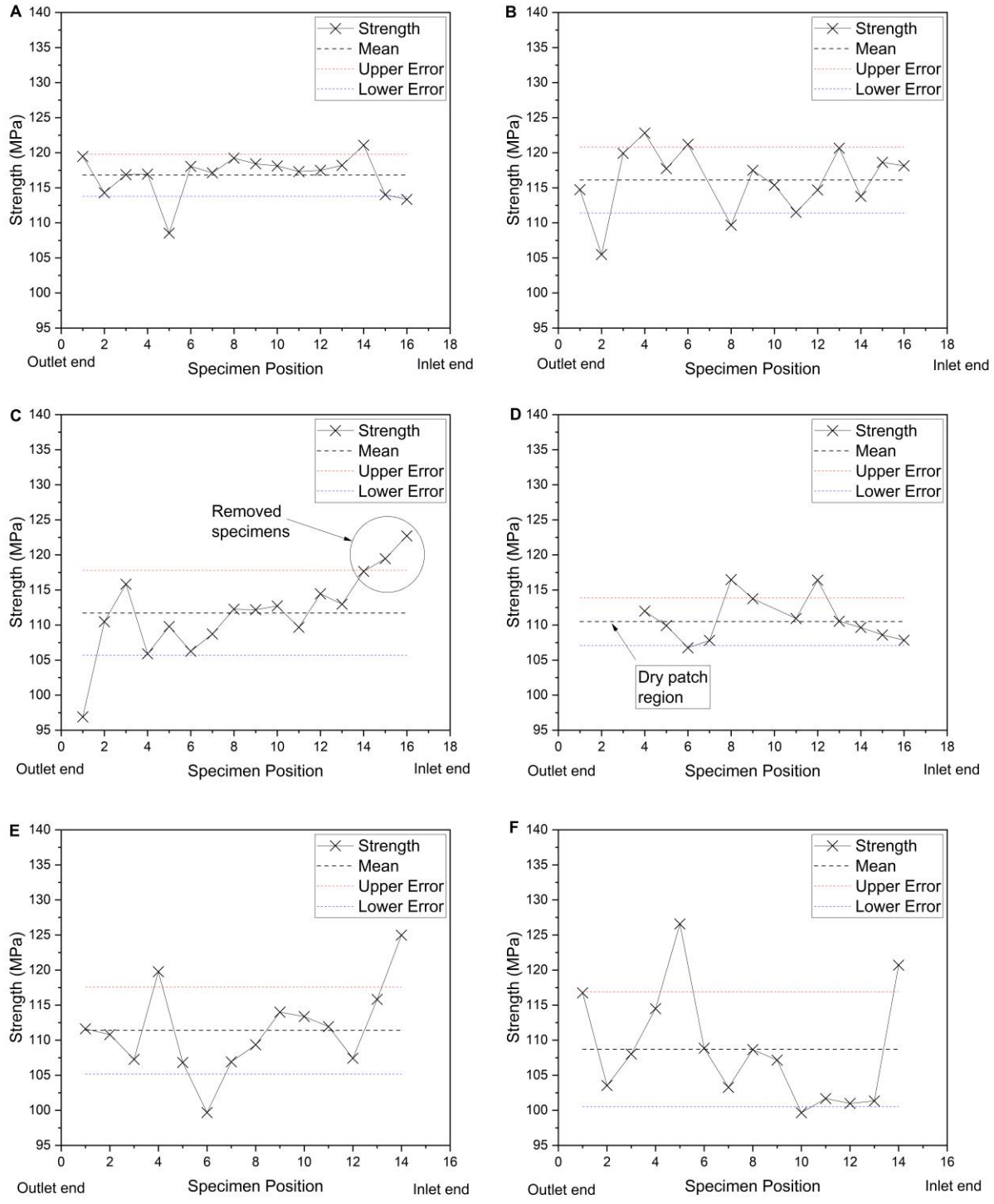

Figure 5-40 *Specimen strength (compression) along the length of the laminate for (**A**) C.L. 1, (**B**) C.L. 2, (**C**) C.L. 3, (**D**) C.L. 4., (**E**) C.L. 5 and (**F**) C.L. 6. The mean strength is overlaid in each plot, as well as the upper and lower error, defined as a single standard deviation. Consistent strength axis to show variation between laminates.*

The strength and modulus results for both the tensile and compressive laminates are summarised in **Table 5-12** and illustrated in **Figure 5-41**. The error is defined as a single standard deviation and the void content error bars are not included on the modulus results for figure clarity, as they are the same as on the strength plots. As expected, as the void content increases, both the tensile and compressive strength are reduced. When comparing the maximum and minimum recorded strengths, the tensile specimens appear to be significantly more sensitive to an increase in void content. The results showed that the tensile strength reduced by 2.3 MPa for every 1.0 % increase in void content, equating to 18 % of the maximum strength. In comparison, for a 1.0 % increase in void content, the compressive strength was reduced by 4.7 MPa, equating to a 2 % reduction in compressive strength.

The reduction in strength for the tensile laminates shows a linear trend, however, in comparison, there was a step down in the compressive strength at the 1.0 % mark. It is not considered that this irregular trend is a result of variations in void content, or void geometry (major to minor ratio only ranges between 1.09:1 to 1.52:1 across all laminates), but instead determined to be due to the larger experimental scatter in results in the compressive specimens when compared to the tensile specimens. This results in a linear trend observed but with a larger coefficient of determination (r^2 value).

The results do not show a notable increase or decrease in modulus as the void content increased for both tension and compression testing. Whilst there is a large percentage difference between the maximum and minimum values for each series, 18 % and 12% for tension and compression, respectively, this can be the result of a large amount of scatter in the results. Yet, when the overall trend is considered, the increase in void content does not have a significant effect.

Table 5-12 *Summary of tensile and compressive strength and modulus results, including the associated void content of each laminate for reference.*

Laminate I.D.	Laminate Void Content / %	Strength / MPa	Modulus / GPa
T.L. 1	0.99 ± 0.54	12.4 ± 2.15	3.86 ± 0.76
T.L. 2	2.36 ± 2.63	9.3 ± 2.36	4.72 ± 2.85
T.L. 3	2.08 ± 1.70	9.8 ± 3.84	4.22 ± 0.98
T.L. 4	1.33 ± 1.13	10.8 ± 2.48	4.70 ± 1.23
C.L. 1	0.60 ± 0.32	116.8 ± 3.0	7.21 ± 0.75
C.L. 2	0.90 ± 0.32	116.1 ± 4.7	7.14 ± 0.88
C.L. 3	1.12 ± 0.52	111.7 ± 6.0	7.62 ± 0.47
C.L. 4	1.94 ± 1.88	110.5 ± 3.4	7.01 ± 0.74
C.L. 5	1.45 ± 0.90	111.4 ± 6.2	7.98 ± 0.68
C.L. 6	1.65 ± 1.31	108 ± 8.2	7.27 ± 0.71

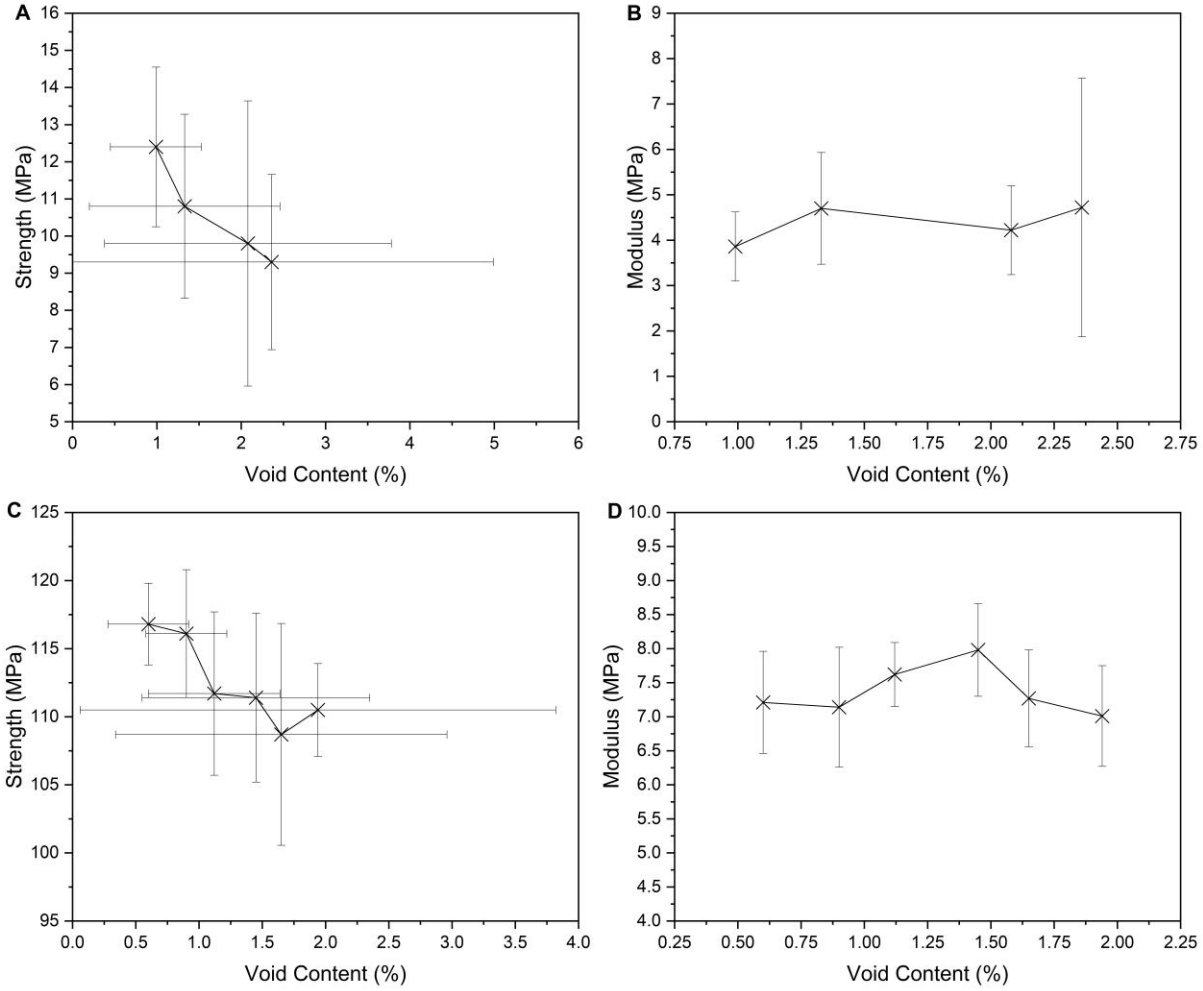

Figure 5-41 Results of how the void content affects the following mechanical properties: (**A**) tensile strength, (**B**) tensile modulus, (**C**) compressive strength and (**D**) compressive modulus.

5.6.2.2. Neat epoxy resin testing

The results of the tensile testing of neat epoxy resin are summarised in **Table 5-13**, where the error is defined as the standard deviation. Correlation to the model strength prediction and Young's modulus used (chosen from literature), as detailed in subsection 6.4.1, is also recorded. Stress-strain graphs of both plaques are shown in **Figure 5-42**, where an elastic region is present up to approximately 60MPa before becoming plastic up to a maximum of approximately 70 MPa. All samples failed in the gage section, as shown in **Figure 5-43**.

Table 5-13 *Tensile strength and Young's modulus results from the mechanical testing of neat epoxy resin.*

	Strength			Young's Modulus		
	Average (MPa)	**Model (MPa)**	**Correlation (%)**	**Average (GPa)**	**Model (GPa)**	**Correlation (%)**
Plaque1	66.88	57.10	-15.3	2.61	3.00	12.2
Plaque2	67.97			2.73		

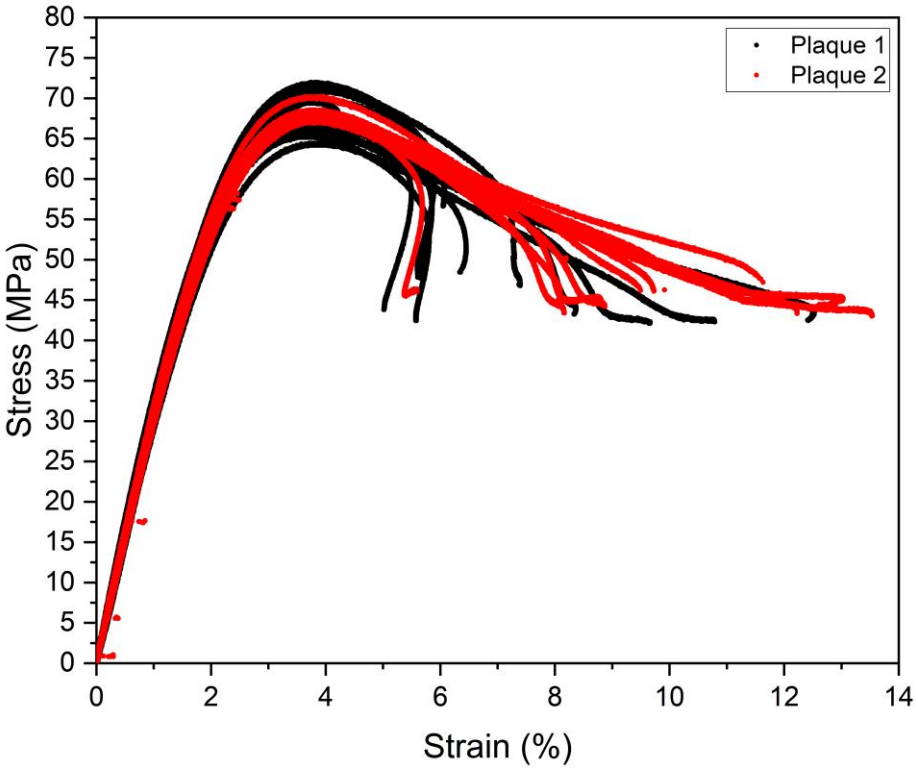

Figure 5-42 *Stress-strain graphs of the tensile tests, showing samples from both graphs.*

Compressive tests were also performed where an average strength of 98.8MPa was calculated. When compared to the compressive testing for the resin infused laminates, the 90° test specimens had a compressive strength up to 22% higher than that of the neat resin samples. Since the composite specimens contain fibres, which act as stress concentrations, it would be expected that the neat resin to have a higher strength. This indicates that the specimens failed prematurely and is not the true compressive strength of the resin. Additionally, post failure examinations indicated the compressive samples failed through in shear, observed by the diagonal line as illustrated in **Figure 5-43**, indicating that the specimens were not in pure compression. Further evaluations are made in the discussion chapter.

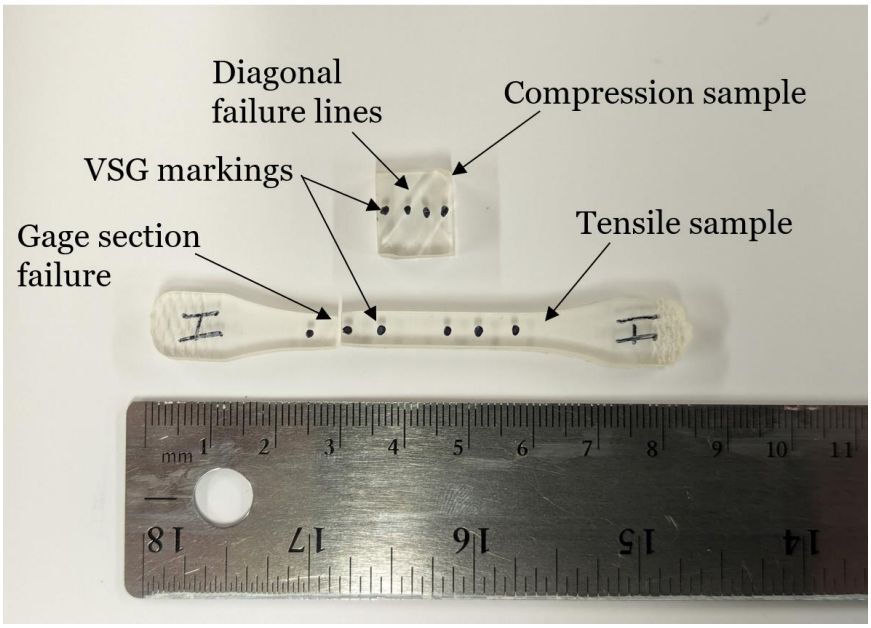

Figure 5-43 *Failed tensile sample.*

5.7. Chapter Summary

This chapter detailed the experimental campaign undertaken to provide material property and microstructure characterisation data on composites containing various levels of porosity. The chapter was split into three main sections: the manufacture of the laminates, characterisation of the microstructure and the mechanical testing of the composite specimens from each of the laminates.

Composite manufacturing can be split into two major processes: either in or OoA. Void generation will differ depending on which type of manufacturing process the composite is manufactured through. Autoclave processed laminates will be more consolidated and therefore have lower void contents and more consistent porosity distribution, whereas the opposite is true for OoA laminates. Therefore, laminates were manufactured using both techniques to determine how well the modelling framework could correlate to both approaches.

Two sets of four laminates were manufactured using a unidirectional prepreg cured in an autoclave. Each of the laminates were assigned a cure pressure, to vary the level of porosity, ranging from 0.05MPa to 0.6MPa. One set of laminates was assigned for tensile testing, whilst the other set was assigned for compression testing. Similarly, two sets of laminates were manufactured through resin infusion for tensile and compressive testing. The porosity was adjusted by reducing the degassing time and

how vigorously the hardener was mixed into the resin. In total, four tensile and six compressive laminates were manufactured.

The microstructure was characterised to determine the void content, shape, size, and fibre distribution. For the autoclave processed laminates, it was assumed that porosity formed evenly across the whole laminate (the outside 25mm of each laminate was discarded to account for edge effects), therefore the microstructure was measured 'globally' to determine data for the whole laminate. In contrast, it was hypothesised that as the resin infused into the laminate, there may be a difference in porosity formation along the length of the laminate (infusion direction). For this reason, a more detailed characterisation process was undertaken. The tensile laminates were characterised at three regions (near the inlet, outlet and middle of laminate) and the compressive laminates were characterised at four regions (near the inlet, outlet and two inner regions). The characterisation process involved sectioning the composite orthogonal to the fibres and polishing the surface. This allowed for optical microscopy to be used to determine each of the parameters. Several μ-CT scans were undertaken to determine the same porosity parameters to validate the characterisation process. Whilst the scan resolution was sufficient to identify features with a diameter of 10μm, the minimal difference in attenuation of the matrix and void regions resulted in the voids not being able to be detected. The edge of large void regions could only be identified due to phase interference between the matrix and void. The μ-CT scans were used to determine the fibre volume fractions and the results correlated well with the literature for the same material.

Tensile and compressive mechanical tests were undertaken to determine how the strength of the laminates changed as the porosity varied. Both longitudinal and transverse testing was undertaken for the autoclave manufactured laminates. This was to determine that only considering the transverse direction in the modelling framework was correct. The results showed that only transversely loaded composites were affected by voids. For this reason, only the transverse strength of the resin infused laminates was tested. Whilst the main focus was on investigating how the strength varied, the elastic modulus was also measured as there have been conflicting reports in the literature on whether an increase in porosity increases the elasticity of the composite or not. The elastic modulus was measured for both the autoclave and resin

infused laminates. The results showed that increasing the level of porosity does not affect the elastic modulus, and all results are within the margin of error.

6. Model Representation

6.1. Chapter Overview

This chapter details how the results from the experimental campaign were used to build representative transverse strength models of both the autoclave and resin infused laminates. The chapter is split into describing specifically how the models were set up, including geometry, boundary conditions and meshing, and then presents the modelling results.

6.2. Introduction

The use of composites in structural applications requires precise modelling to ensure components behave as expected. This calls for representative material properties, however, the material properties presented in datasheets are the ideal/nominal, which may not be representative of the actual structure manufactured. One reason why material properties may deviate is due to the inclusion of porosity (resulting from environmental humidity, insufficient consolidation or poor manufacturing processes). For this reason, it is important to be able to predict what the actual material properties are, before having certainty in a composite design.

The results from Chapter 5 showed that the increase in porosity has a negative effect on the transverse strength. The results of Chapter 4 found that the void content and geometrical properties (stress concentrations) both contribute to the failure strength. This chapter aims to realise representative models for all autoclave and resin infused laminates, by considering the porosity parameters of each laminate, building the associated models and correlating the results to the experimental data.

6.3. Model Setup

Having completed all experimental work, including microstructure analysis, for both the autoclave processed and resin infused laminates, all required data was available to build representative models of the testing. The common modelling steps (such as the

time step and history output setup) are detailed in Section 3.4. The first step was to build the Stage 1 models.

6.3.1. Stage 1 Geometry

6.3.1.1. Autoclave models

From the microscopy analysis results in subsection 5.5.2.1, it was determined that voids were evenly distributed, therefore, a single void could be modelled. To build the geometry for the stage 1 models, the calculated void content was used in combination with the measured lengths. As it was not possible to measure the depth of the voids, it was assumed that the depth of the voids was the same as half of the minor axis length, i.e., has a circular cross-section. Therefore, knowing the dimensions of a representative void and the void volume fraction, the volume fraction of the matrix that the void is embedded in can be calculated.

The volume of a void is calculated using equation ((6-1)) where V_v is the void volume, a, b and c are the major and minor radii of the void, where it was assumed that the two minor axes are the same, therefore $b = c$. By calculating the volume of the void, the total volume could be calculated using equation ((6-2)) where v_c is the void content.

$$V_v = \frac{4}{3}\pi \times a \times b \times c = \frac{4}{3}\pi \times a \times b^2 \quad (6\text{-}1)$$

$$V_t = \frac{V_v}{v_c} \quad (6\text{-}2)$$

Having determined the total volume of the void, allowed for the outer dimensions of the void module to be calculated, which was done using the same aspect ratio as the void. As a single void was being modelled, symmetry boundary conditions could be used in two planes, reducing the model size by 75 %. The void parameters for each laminate and the corresponding void module dimensions are presented in **Table 6-1**, the void module dimensions are presented without symmetry (i.e., the full model).

Table 6-1 *Void parameters used to create the void module for the stage 1 model.*

Load Case / MPa	Void Content / %	Major Axis Length / µm	Minor Axis Length / µm	Full Void Module Dimensions / µm
Tension – 0.59	0.63	7.86	7.01	34.30 x 30.59 x 30.59
Tension – 0.39	1.28	7.45	6.95	25.67 x 23.95 x 23.95
Tension – 0.19	0.88	21.54	18.84	84.09 x 73.55 x 73.55
Tension – 0.05	2.01	57.58	28.48	170.69 x 84.43 x 84.43
Compression – 0.59	0.87	11.97	8.83	46.91 x 34.6 x 34.6
Compression – 0.39	0.66	10.14	6.11	43.57 x 26.25 x 26.25
Compression – 0.19	1.14	13.33	8.68	47.74 x 31.09 x 31.09
Compression – 0.05	1.58	25.72	18.86	82.61 x 60.58 x 60.58

6.3.1.2. Resin infused models

The same conclusions regarding evenly distributed voids were drawn for the resin infused laminates. In nearly all cases the results showed a normal distribution indicating that a single void could be modelled as representative. The visual inspection also showed that the distribution of voids was, whilst not perfectly periodic, evenly spread out, i.e., they did not only occur within or between the plies. The only exception where a single void was not considered representative was for laminate C.L. 4, where there were two types of voids identified; microvoids which were common in all other laminates, and large discrete voids. Two separate models were created, each representing one type of void, and the results from the model which failed first were used. This is using the assumption that the laminate fails due to brittle failure. To differentiate between the two sizes of void modules, since different element sizes are required, the model containing the large discrete void representing laminate C.L.4 is named the macro void module, and all other void module models are named micro void modules.

To generate the void module for the stage 1 geometry, the same process used in subsection 6.3.1.1 was followed. The representative minor and major lengths of the void being modelled were first to first calculate the volume of the void which, along with the void content, determined the amount of matrix required for the model. Secondly, the aspect ratio between the two lengths was used for the overall aspect ratio of the model (i.e., the model length to width). As a single void was modelled, and therefore symmetry is present, a quarter model containing symmetry boundary

conditions was used. A summary of the void module geometry is documented in **Table 6-2**.

Table 6-2 *Summary of geometrical parameters used for each void module.*

Laminate I.D.	Void Content / %	Major Axis length / µm	Minor Axis length / µm	Full Void Module Dimensions / µm
T.L. 1	0.99%	7.21	4.63	27.06µm x 17.38µm x 17.38µm
T.L. 2	2.36%	6.01	4.05	16.89µm x 11.38µm x 11.38µm
T.L. 3	2.08%	6.74	5.31	19.75µm x 15.56µm x 15.56µm
T.L. 4	1.33%	6.04	4.7	20.55µm x 15.99µm x 15.99µm
C.L. 1	0.60%	6.49	4.33	28.79µm x 19.18µm x 19.18µm
C.L. 2	0.90%	7.09	4.66	27.46µm x 18.07µm x 18.07µm
C.L. 3	1.12%	6.90	5.19	24.85µm x 18.71µm x 18.71µm
C.L. 4 – micro	1.94%	6.46	5.76	19.38µm x 17.28µm x 17.28
C.L. 4 – Discrete	1.94%	142.39	75.88	427.11µm x 227.61µm x 227.61µm
C.L. 5	1.45%	5.95	5.46	19.7µm x 18.06µm x 18.06µm
C.L. 6	1.65%	6.32	5.49	20.00µm x 17.40µm x 17.40µm

6.3.2. Stage 2 Geometry

6.3.2.1. Autoclave models

To create the geometry for the RUC to be used in the stage 2 models that were representing the autoclave results, the fibre characterisation results from subsection 5.5.3 were used. The results showed that there was little difference in the structure as the cure pressure was changed, therefore the same RUC was used in all simulations. The parameters required to generate the RUC are the fibre volume fraction, fibre diameter and spacing/angle between the fibres. Based on the image processing and literature results[167] the use of a 40 % matrix volume fraction in the model was adopted and the fibre diameter was provided from the supplier's datasheet as 7µm.[173] The fibre angle measurements concluded that an angle of 45° between the fibres was representative. To incorporate the correct angle between the fibres, the RUC formation chosen involved two quatre fibres modelled in opposing corners of a square. As the angle between the fibres is 45° then all sides are the same length. To determine the lengths of the sides, the fibre volume fraction is used in association with the fibre diameter. As there is no variation in the thickness direction, to calculate the geometry the 2D area is used. Firstly, the area of two-quarter fibres is calculated, and then based

on the fibre volume fraction the CSA of the RUC is calculated. As the RUC was a square the length of the sides was simply calculated using the square root of the area. This resulted in the length of the sides being 5.66µm. As there was no variation in the thickness direction, the RUC was extruded to 5.66µm such that it was a cube. A drawing of the RUC can be seen in **Figure 6-1**.

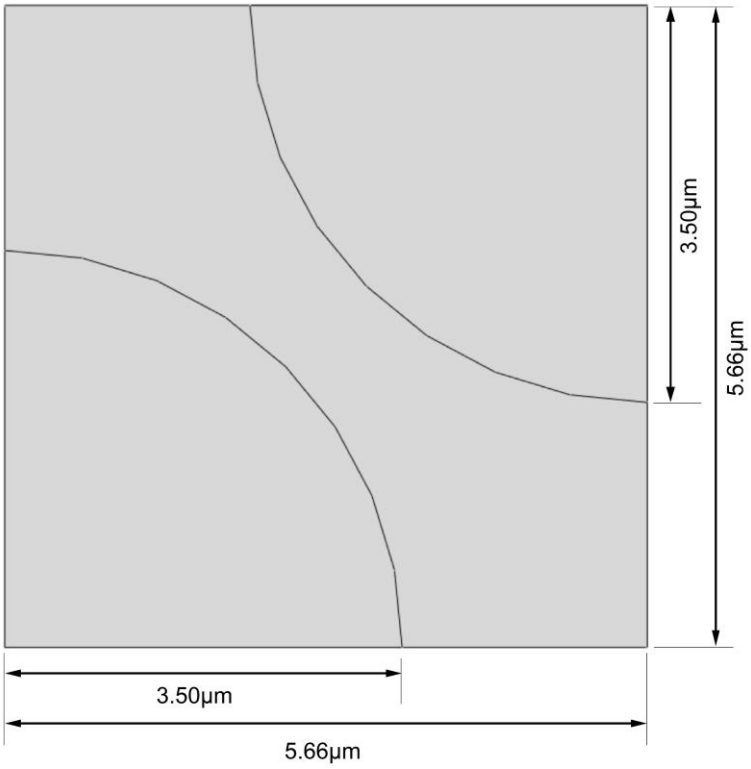

Figure 6-1 *Dimensions of the RUC. N.B. Not drawn to scale.*

6.3.2.2. Resin infused models

To generate the geometry for the RUC for the resin infused models the characterisation results from subsection 5.5.3 were used. One of the main considerations when characterising the fibre distribution was the difference between the laminates. However, the results did not indicate a notable difference, therefore, the same RUC was used for all simulations. A summation of the fibre distribution results used to generate the RUC is documented in **Table 6-3** and a drawing of the RUC is illustrated in **Figure 6-2**.

Table 6-3 *Geometrical parameters used to generate the RUC for the Stage 2 model.*

Fibre Diameter / µm	Fibre Angle / °	Fibre Volume fraction / %
8.00	65	55

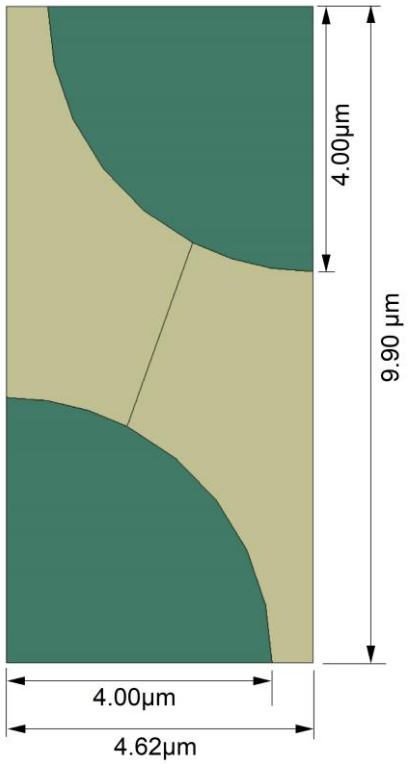

Figure 6-2 *Drawing of the RUC showing used for the Stage 2 model.*

6.3.3. Boundary conditions

The same boundary conditions were applied to the autoclave and resin infused models, detailed as follows. Both stage 1 and 2 models were constrained using symmetry boundary conditions as this restricts displacement in the loading direction yet allows for Poisson's effect to take place. Load was applied through a displacement boundary condition applied to the opposing surface. Due to a single void being modelled, symmetry boundary conditions were applied in two perpendicular planes. A detailed description of these boundary conditions can be found in Section 3.4.4. Periodic boundary conditions were applied to the stage 2 model to preserve periodicity, as described in subsection 3.4.3. Surfaces where the boundary conditions were applied are illustrated in **Figure 6-3**.

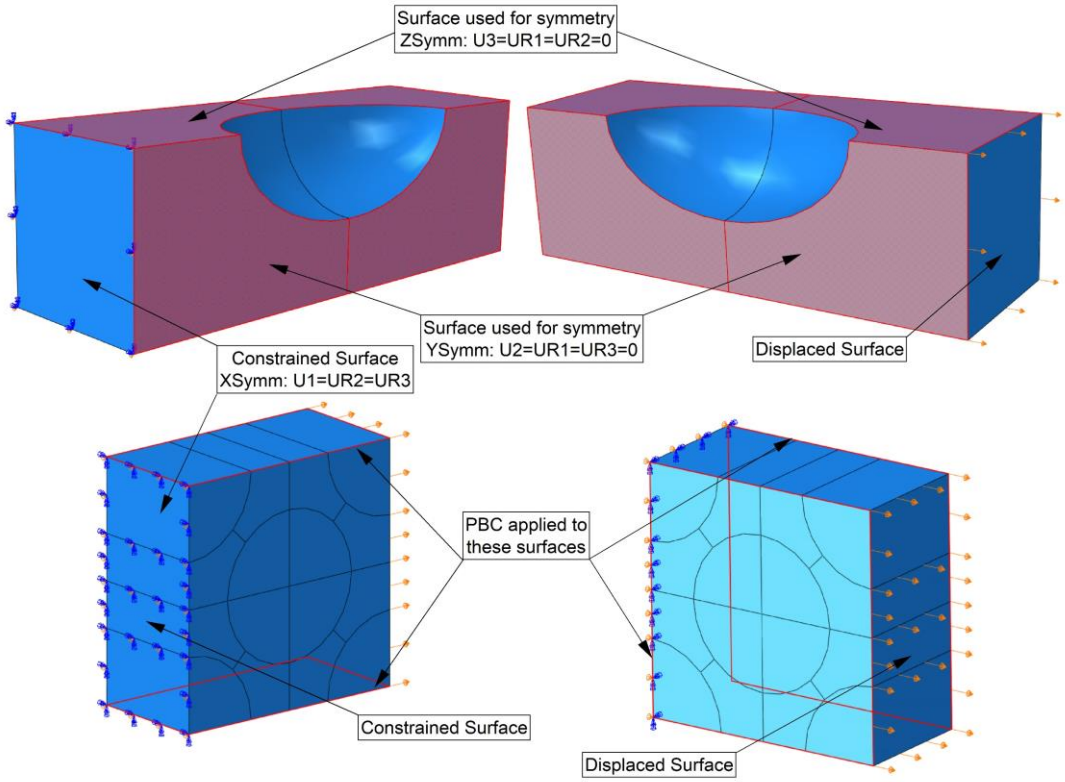

Figure 6-3 *Surfaces where boundary conditions are applied.*

6.3.4. Meshing

The elements used for all autoclave representative models were 8-node 3D linear brick elements (C3D8), without using reduced integration, as described in subsection 3.4.2. Mesh convergency studies were conducted to identify the appropriate element size. The model used for the mesh convergency study was the 90DT 0.39 MPa laminate as this model had the smallest void aspect ratio (where the smaller aspect ratio requires a higher refinement of elements to capture accurately). The results of the mesh convergency study of the void module and RUC are illustrated in **Figure 6-4** (**A**&**B**) respectively. The mesh size that was deemed appropriate is illustrated with the red cross, where this element size was used across all models. The full statistics of the chosen mesh from the mesh convergency study are summarised in **Table 6-4**, including element quality statistics. Examples of the elements are presented in **Figure 6-5** and **Figure 6-6** for the void module and RUC respectively.

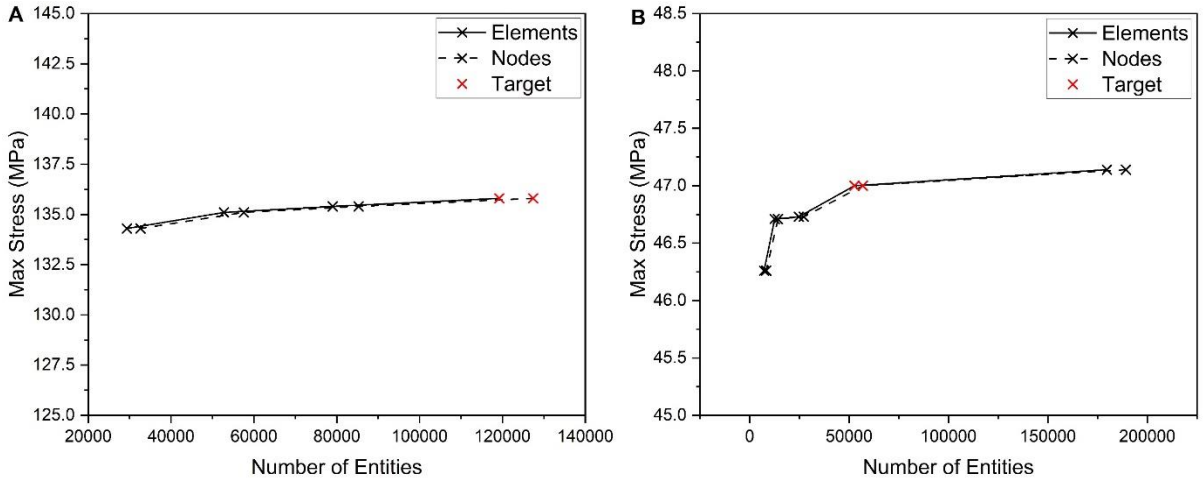

Figure 6-4 *Mesh convergency studies of the (**A**) void module and (**B**) RUC, where the target mesh size is identified with the red cross.*

Table 6-4 *Statistics of the models used for the mesh convergency study.*

Model	Avg. Aspect Ratio	Max. Aspect Ratio	Avg. Min. Corner Angle / °	Worst. Min. Corner Angle / °	Avg. Max. Corner Angle / °	Worst. Max. Corner Angle / °
Void Module	1.08	2.47	84.65	59.83	95.25	114.18
RUC	1.27	2.40	83.21	53.00	96.67	133.02

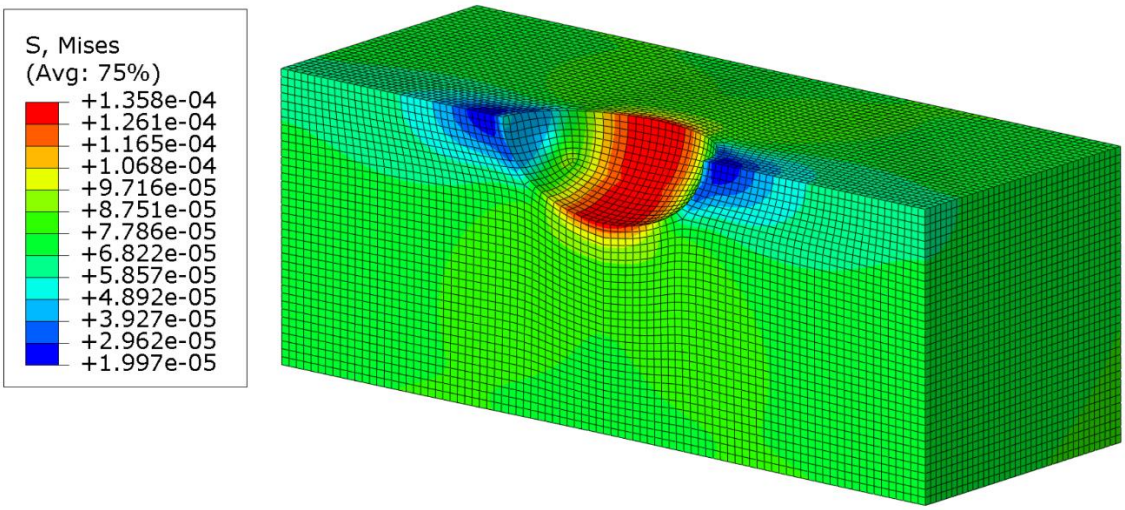

Figure 6-5 *Illustration of the chosen mesh, including stress contours, for the void module. (Units in TPa).*

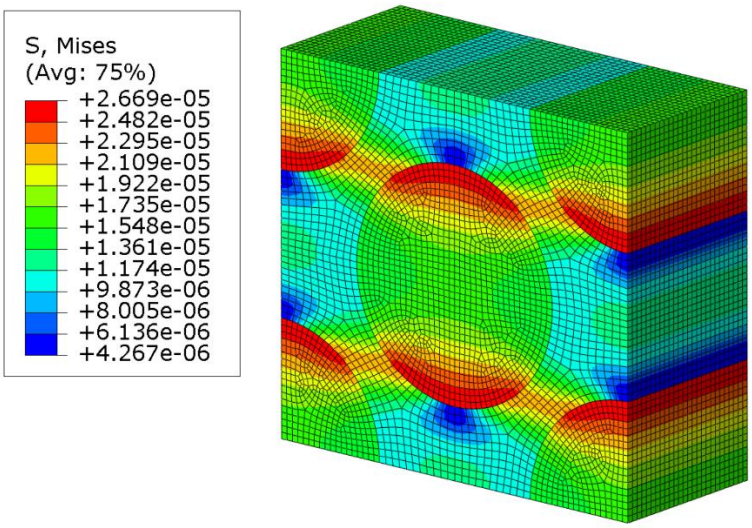

Figure 6-6 *Illustration of the chosen mesh, including stress contours, for the RUC. (Units in TPa).*

The same 3D 8-node linear brick elements without reduced integration (C3D8) were used throughout the models representing the resin infused laminates, for both stages. A mesh convergence study was conducted to determine the appropriate element size for each of the model series. The results of the mesh convergency studies are shown in **Figure 6-7**, and **Figure 6-8** to **Figure 6-10** show examples of the generated mesh on the micro void module, macro void module and RUC models respectively. Nominal element sizes were 0.3 μm for all stage 1 models, except for the macro void module, where a nominal element size of 3 μm was used due to a much larger void size. The element count across all stage 1 models was approximately 100,000 elements. The stage 2 module used a nominal element size of 0.25 μm resulting in the generation of 30,914 elements and 34,188 nodes. The mesh generation procedure is detailed in Section 3.4.3. The full statistics of the chosen mesh from the mesh convergency study are summarised in **Table 6-5**, including element quality statistics.

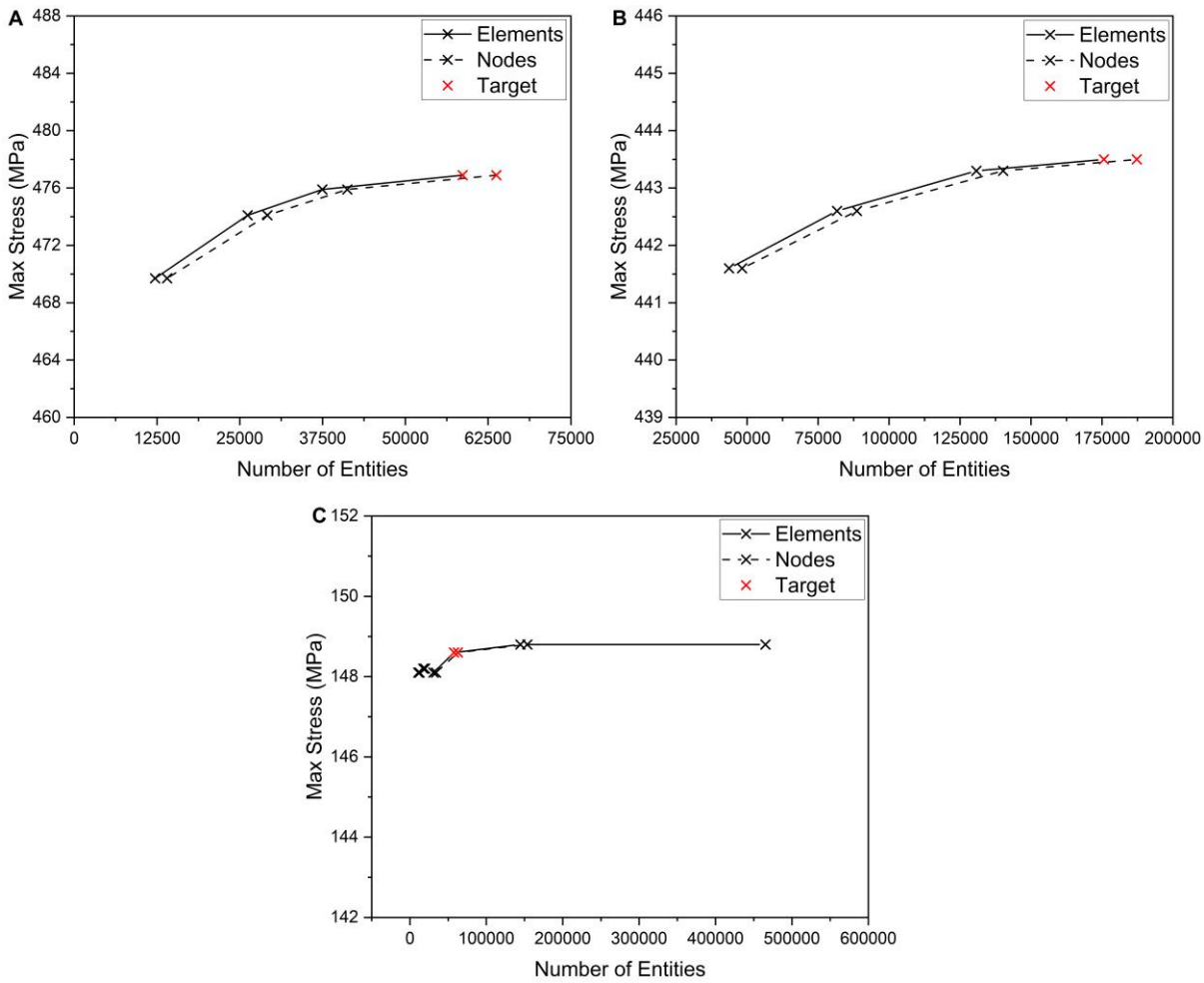

Figure 6-7 *Mesh convergency studies for the (**A**) micro void module, (**B**) macro void module and (**C**) RUC. The target mesh size for the respective models is highlighted in red.*

Table 6-5 *Statistics of the models used for the mesh convergency study.*

Model	Avg. Aspect Ratio	Max. Aspect Ratio	Avg. Min. Corner Angle / °	Worst. Min. Corner Angle / °	Avg. Max. Corner Angle / °	Worst. Max. Corner Angle / °
Micro V.M.	1.10	2.57	84.35	58.24	95.56	58.24
Macro V.M.	1.06	3.51	85.49	46.38	94.58	120.55
RUC	1.29	3.16	82.39	44.53	98.06	131.05

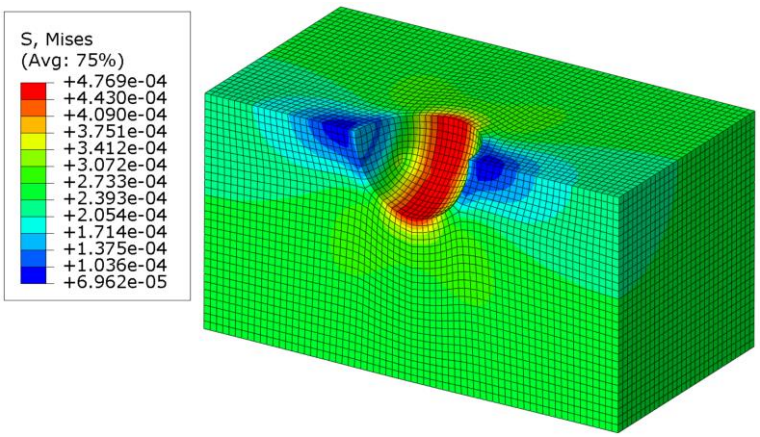

Figure 6-8 *Chosen mesh generation for the micro void module model, showing stress contours. (Units in TPa).*

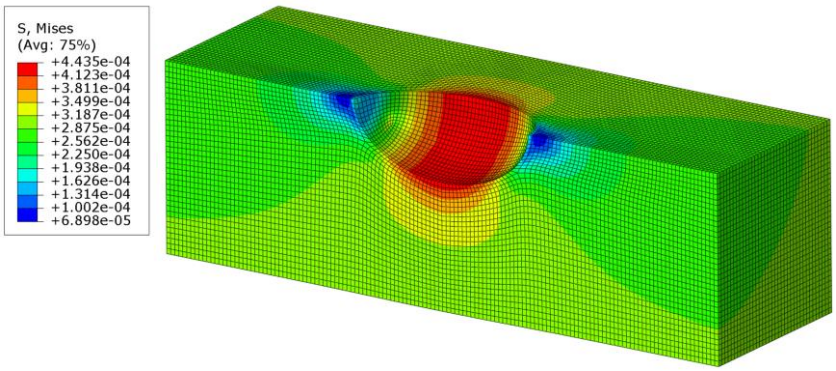

Figure 6-9 *Chosen mesh generation for the macro void module model, showing stress contours. (Units in TPa).*

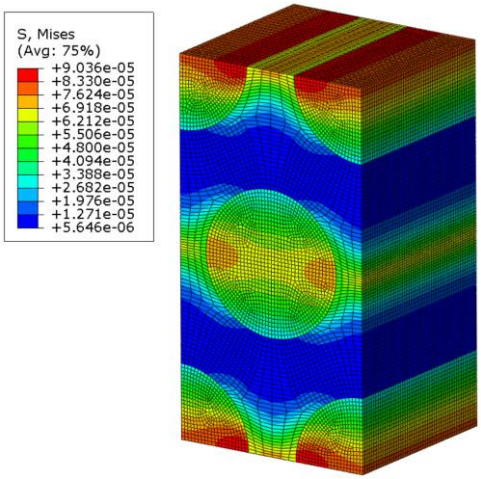

Figure 6-10 Chosen mesh generation for the RUC model, showing stress contours. (Units in TPa).

6.3.5. Constituent material properties

Due to confidentiality surrounding prepreg materials, most of the constituent material properties for the autoclave processed material were not published, only macro-scale/ply properties were available. The only properties supplied were the strength and stiffness of the fibres and no matrix properties are made public. However, estimates for the missing information can be ascertained through published literature. The Poisson's ratio of carbon fibre filaments was recorded as 0.2,[174,175] between 0.34 and 0.38 for the matrix[161,174,175] and the stiffness of the matrix has been recorded between 2.75 and 3.35 GPa.[161,174–176] The values used in the simulation are recorded in **Table 6-6**.

Table 6-6 *Material properties used in the simulation were found from either datasheets or literature.*

Constituent	Young's Modulus / GPa	Poisson's Ratio	Tensile Strength / MPa	Compressive Strength / MPa
Fibre	235	0.20	4.12×10^3	N/A
Matrix	3.0	0.35	232.4[a]	327[a]

[a] Model strength prediction.

The tensile and compressive strength of the matrix were not published, and whilst typical values could have been estimated based on literature, as have other material properties, it was possible to estimate them using the model and the experimental results. This was achieved by following the modelling procedure in reverse order where the experimental results were used to derive the homogenised matrix strength, using the RUC in stage 2, and then pristine matrix properties were derived using the relevant porosity parameters in stage 1. The associated matrix strengths that are presented in **Table 6-6** are the results from subsection 6.4.1 where this procedure is documented. It should be noted that this was not a form of 'tuning/correlating' the model as only a single data point was used independently from the rest of the results. For instance, if this process was done for all data points and then an average was taken, then this would be 'tuning/correlating' as data from all results were used. However, in this case, no information was used from all other results other than the one being used.

Resin infusion requires the selection and combination of both the fibres and resin (rather than being supplied as a single pre-manufactured material such was the case for prepreg). Therefore, the constituent properties were less limited. The fibres used

in the study were HiMax FCIM312 supplied by Hexcel,[177] however, the datasheet for this fabric[178] did not specify which exact fibre is used. Instead, based on the various fibres that Hexcel supplies, an estimation for Young's modulus and tensile strength could be achieved[179]. These datasheets did not provide the Poisson's Ratio for the fibres, however, the literature used for the fibres properties of the prepreg material was used instead. The only relevant property that was listed on the material property datasheet for the epoxy resin[180] was the tensile strength. The modulus and Poisson's ratio were selected based on the literature reviewed for the autoclave material properties. Since the compressive strength of the matrix was not listed in the material property datasheet, the same 'inverse' modelling approach to determine the strengths was undertaken. To evaluate the accuracy of this approach, the same procedure was also followed for the tensile strength. A result of 57.1 MPa was predicted which was comparable to the range presented by the datasheet (65.5-73.5 MPa). A summary of the material properties used is documented in **Table 6-7**.

Table 6-7 *Summary of the constituent material properties used in the models.*

Constituent	Young's Modulus / GPa	Poisson's Ratio	Tensile Strength / MPa	Compressive Strength / MPa
Fibre	300	0.20	5.0x10[3]	N/A
Matrix	3.0[161,174–176]	0.35[161,174,175]	65.5-73.5, 57.1[a]	429.8[b]

[a] Model strength prediction.
[b] Compressive strength comes from subsection 6.4.1.

6.3.5.1. Matrix strength determination

As detailed in subsection 6.3.5, the matrix tensile and compressive strength had to be determined. A single data point from both the compressive and tension results was taken and whilst any could have been used, the data from the laminates with the lowest void content was chosen.

To determine the tensile strength of the pristine prepreg matrix (for the autoclave representative models), the RUC was loaded until the calculated strength of the model matched the experimental strength of 60.4 MPa. At that point, the matrix element with the highest stress was 79.13 MPa. The same process was done in compression where the RUC was loaded to 177.9 MPa, matching the experimental results, which resulted in a maximum stress of 232.4 MPa. The location of the maximum stressed elements can be seen in **Figure 6-11**.

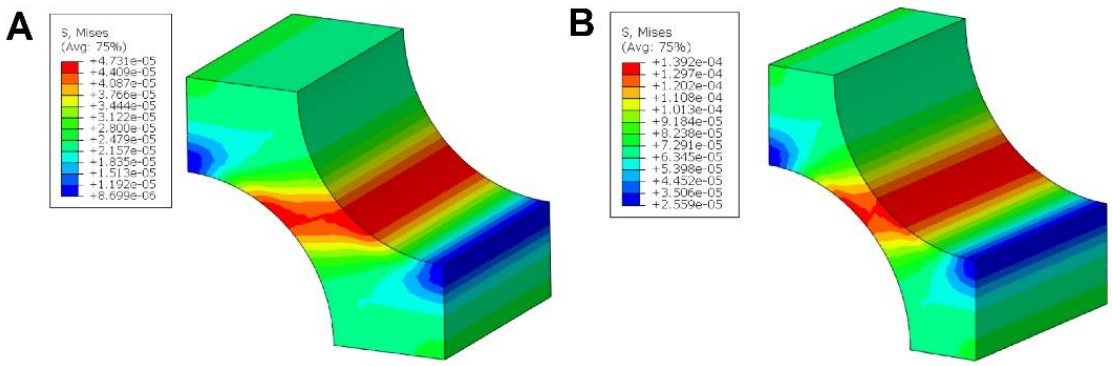

Figure 6-11 *Von Mises stress distribution and maximum stress within the matrix elements of the RUC. (**A**) represents the tensile model with a deformation scale factor of 28 times and (**B**) represents the compression model at a scale factor of 9 times. The units are in TPa.*

The matrix elements with the maximum stress represent the homogenised stage 1 strength, therefore the respective stage 1 models were loaded until the calculated strength matched the maximum stress from the stage 2 model. At this point, the maximum stressed element within the stage 1 model was recorded as this represents the pristine matrix strength. The model predicts a tensile strength of 143.2 MPa and a compressive strength of 357.9 MPa. These results were cross-referenced with typical values found in literature where Hobbiebrunken et al[176] measured tensile strength of 135±21 MPa for thin strands of epoxy resin (to minimize the inclusion of defects found in macro tests) and predicted a compressive strength of up to approximately 327 MPa.

The same procedure was followed to determine the matrix strengths of the resin infused laminates. Whilst the supplier datasheet did report tensile strengths, the opportunity was taken to compare how well the model can predict the strength. For both the tensile and compressive strength, the laminate with the lowest void content laminate was chosen to base the strength prediction on (T.L. 1 and C.L. 1).

The RUC in stage 2 was loaded in tension until the global stress state (combination of the reaction force and CSA) matched the experimental strength, at which point the maximum matrix stress was 35.5 MPa. The void module was then loaded in tension until the global stress state matched the 35.5 MPa of the RUC. At that point, the maximum stressed matrix element was 57.1 MPa, which is taken as the tensile strength of the resin. The supplier datasheet reports a matrix tensile strength of between 65.5-73.5 MPa, resulting in the model predicting the strength of approximately 8MPa lower

than what is reported. It was considered that these results are comparable. The same process was followed in compression where the RUC predicted a homogenised matrix stress of 290.4 MPa and subsequently, the void module predicted a pure resin compressive strength of 429.8 MPa.

6.4. Model correlation to experimental results

6.4.1. Autoclave representative models

Having determined the strength properties of the matrix it was possible to use these values to predict the transverse strength for each laminate. The homogenised knocked-down matrix strength from the stage 1 model and transverse strength from the stage 2 model are presented in **Table 6-8**.

Table 6-8 *Results from the Stage 1 and 2 models of the autoclave representative models. *Represents the models used to calculate pristine matrix properties.*

Model Representation		Stage 1 Strength / MPa	Stage 2 Strength / MPa
Tension	0.59 MPa*	79.1	60.5
	0.39 MPa	78.9	60.3
	0.19 MPa	76.9	58.7
	0.05 MPa	78.9	60.3
Compression	0.59 MPa	214.3	163.8
	0.39 MPa*	232.4	177.9
	0.19 MPa	222.3	169.9
	0.05 MPa	209.2	159.8

To compare how the model correlates to the experimental testing, both sets of results were plotted on a graph as shown in **Figure 6-12**. The data points for the lowest void content correlate perfectly, as these were the points used to predict the matrix strength. When comparing the remaining results two features were evaluated. Firstly, the overall trend and secondly how well each specific model compares to the corresponding experimental data point.

For the tensile series, it was found that there was a small decrease in strength observed between the three lowest void content models and the last model increases in strength. This increase in strength is explained by the histogram, shown in **Figure 6-13** where there are a small number (~15%) of large, elongated voids compared to the majority of significantly smaller voids. This has the effect of skewing the mean measurement to be larger. For instance, the larger voids have a major axis length of between 135-165µm,

compared to the major axis length of the smaller voids, which make up ~80% of the laminate, of up to 45µm. This gives a mean measurement of 58µm resulting in the representative void having a major axis length that is larger than ~80% of all the voids. Representative voids of the two types are shown in **Figure 6-14** As shown in subsection 4.4, a void with a larger aspect ratio in the loading direction results in a smaller stress concentration. This has the effect of requiring a higher applied stress/load for the same maximum stress found at the stress concentration/void. Therefore, since the large and elongated voids had the effect of reducing the stress concentration this resulted in the predicted strength increasing. Also, all tensile models overpredict the strength to just outside of the experimental error, again, this is likely due to taking the mean of all values for the same reason. For the compression results, three of the four models correlate very well with the experimental results, however, there is one model which overpredicts the strength. Since the modelling approach is sensitive to the geometry of the void, the discrepancy is likely to be due to non-representative void dimensions being used. These results show that taking the mean value is likely to not be the most representative and other statistical approaches should be investigated.

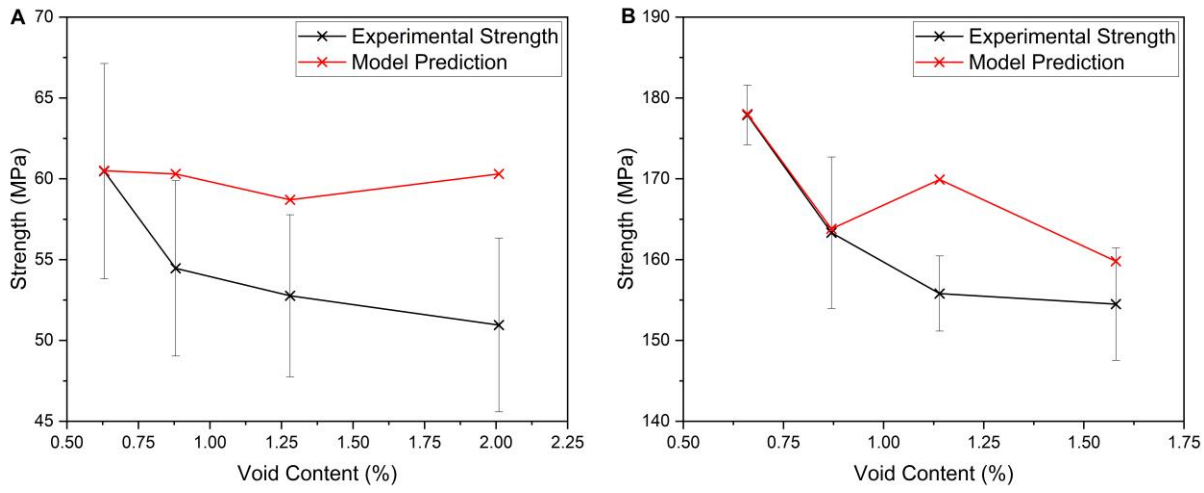

Figure 6-12 *Modelling results for (**A**) tension, and (**B**) compression, correlated against the experimental results, presented as a function of the void content.*

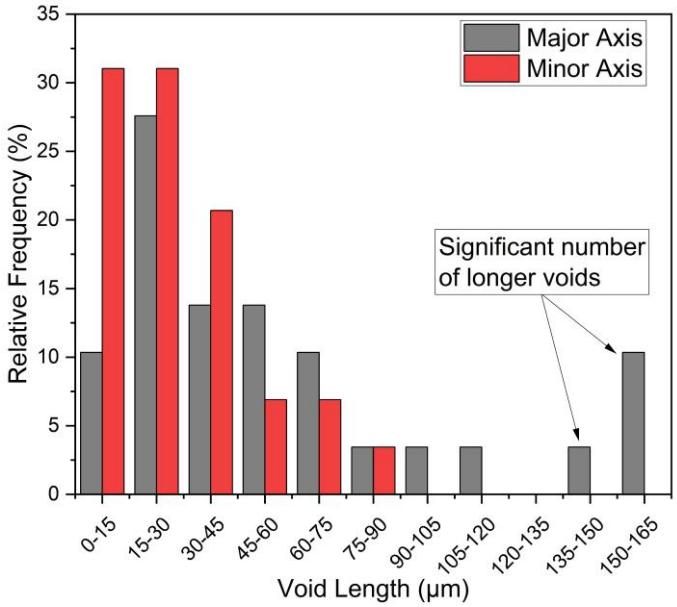

Figure 6-13 *Relative frequency histogram plot of the void size distribution of the 0.05 MPa tensile laminate showing that a significant number of voids are extremely elongated.*

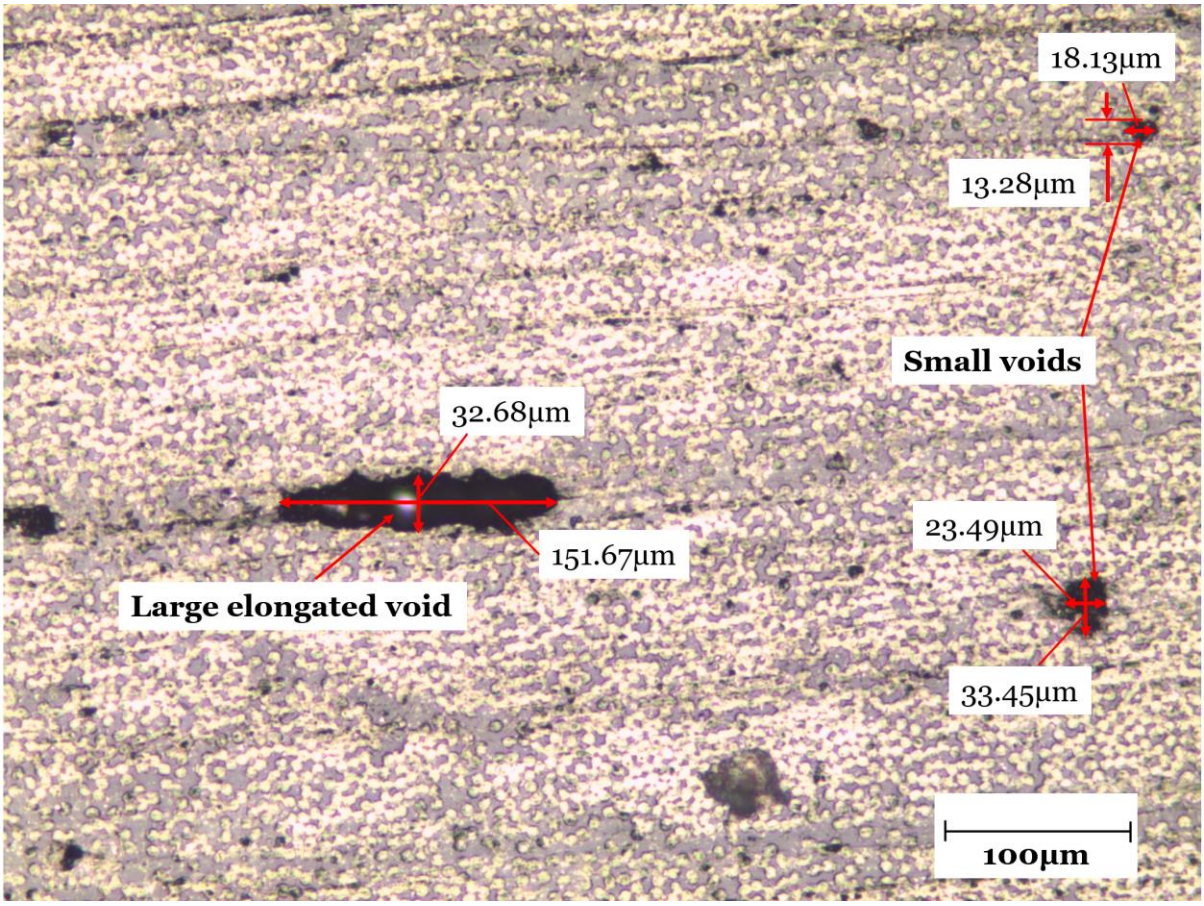

Figure 6-14 *Representative large and small voids observed that form in the 0.05MPa laminate.*

6.4.1.1. Porosity characterisation with various statistical approaches

It was clear that for both the tensile and compressive series of models, taking the overall mean void dimensions is not always the most appropriate. This led to the investigation of different statistical approaches, including:

- **Mean – All:** This is the approach used in the previous section, where the mean of all measurements was taken.
- **Mean – Std. Dev:** This is taking the mean of measurements that fall within one standard deviation of the overall mean. This has the effect of removing any outlying values as shown in **Figure 6-13**.
- **Median:** This is using the middle value of all measurements.
- **Mean – Lower Third:** This is ordering all measurements in ascending order and taking the mean of the smallest third. This is working on the assumption that failure is initiated from the smallest voids which would have the highest stress concentration. It is also seen from the histograms that in most cases the majority of voids are within this region.

The void dimensions for each statistical approach are summarised in **Table 6-9**. The full stage 1 void module geometry for each model is detailed in Appendix C.

Table 6-9 *Representative void dimensions for each statistical approach.*

Laminate Designation	Mean – All / µm	Mean – Std. Dev / µm	Median / µm	Mean – Lower Third / µm
90DT - 0.59 MPa	7.86x7.01	6.76x5.79	6.98x5.55	4.78x3.71
90DT - 0.39 MPa	7.45x6.95	6.45x5.6	6.82x5.33	5.08x4.24
90DT - 0.19 MPa	21.54x18.84	16.99x11.21	19.08x12.29	8.08x7.04
90DT - 0.05 MPa	57.58x28.48	36.74x19.23	41.39x23.08	16.4x10.81
90DC - 0.59 MPa	11.97x8.83	9.11x6.7	9.59x6.51	6.84x4.68
90DC - 0.39 MPa	10.14x6.11	7.96x5.29	8.64x5.56	5.86x3.64
90DC - 0.19 MPa	13.33x8.68	9.79x6.62	10.94x6.5	6.87x5.25
90DC - 0.05 MPa	25.72x18.86	13.94x13.79	19.66x16.23	8.43x6.71

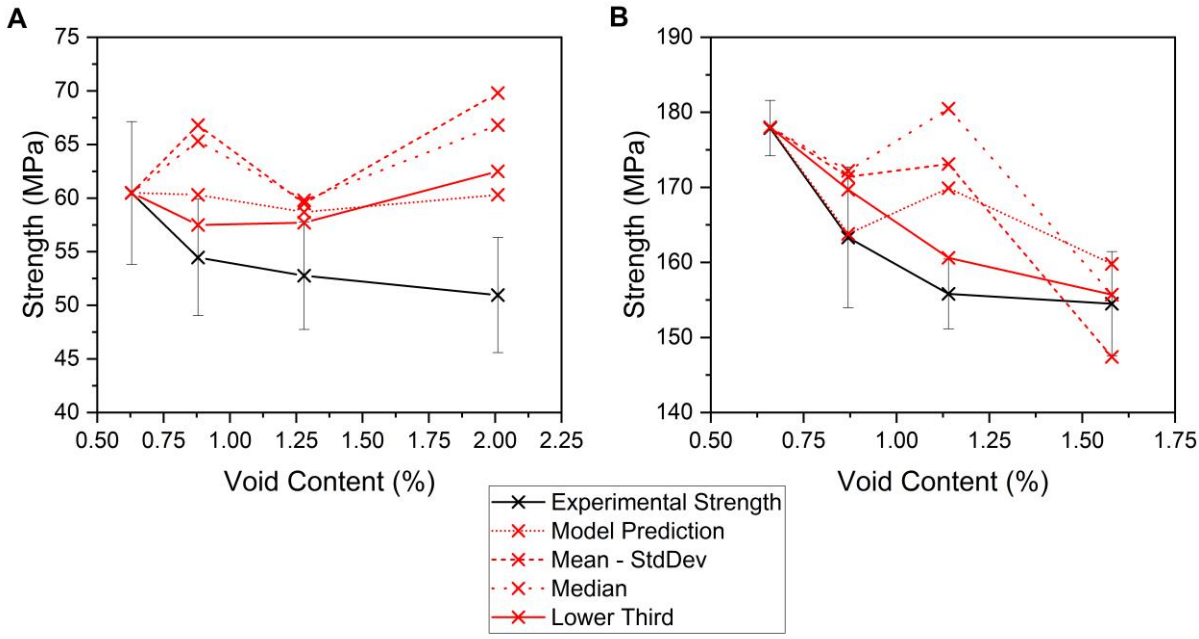

Figure 6-15 *Model correlation to experimental results using different statistical approaches, for (**A**) tension and (**B**) compression.*

The correlation between the FEA models and the experimental results can be seen in **Figure 6-15**. Whilst most all models show an over-prediction, the modelling approaches that build the stage 1, which use all values such as Mean-All and Median, significantly over-predict. This can be explained by the inclusion of the larger and elongated voids which results in the associated representative void having an aspect ratio larger than the majority of voids (as explained previously in subsection 6.4.3). The larger aspect ratio results in a reduced stress concentration requiring a larger force to reach failure. On the other hand, the approach that specifically only uses the lower third of measured values was found to correlate best across almost all results. When only considering the smaller voids results in the best correlation, giving further confidence that it is the smaller voids with higher stress concentrations (due to the smaller aspect ratio compared to the elongated larger voids) that dominate the failure behaviour. The only exception to using this approach was for the 0.05 MPa tensile laminate. When analysing the associated relative frequency histogram plot, **Figure 6-13**, it can be seen that for both the minor and major axis lengths, within the lower third of measurements, there is a broad spread, rather than a normal distribution. As such, the histogram shows that the majority of voids had a major axis length of between 15-30µm and a minor axis length of 0-45µm. It was for this reason that it was chosen to update the model using a spherical void of diameter 20µm. The correlation

using the Lower Third approach and updated modelling geometry for the 0.05 MPa tensile model can be seen in **Figure 6-16**.

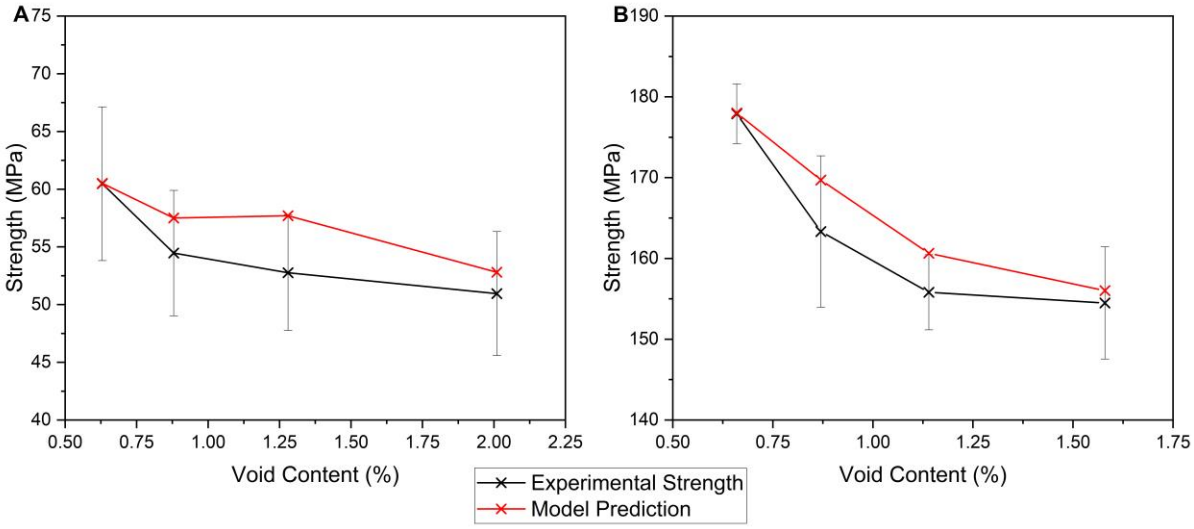

Figure 6-16 *Final model correlation to experimentally recorded values, for (**A**) tension and (**B**) compression.*

A very good correlation was found when comparing the FEA model to the experimental results. Overall, both series of models predicted a degradative trend with increasing void content and the compressive models captured the non-linearity found in the experimental results. As shown in **Table 6-10**, all models had a good correlation to the experimental results where the tensile predictions were all within 10 % and the compressive predictions were within 4 %. Almost all models predicted strengths within the experimental variability with only the model representing the 0.19 MPa laminate falling just outside of the error bars.

Table 6-10 *Correlation between the mean experimental strength and the strength predicted by the model.*

Load Case	Void Content / %	Mean Experimental Strength / MPa	Model Strength Prediction / MPa	Correlation / %
Tension – 0.59 MPa	0.63	60.47±6.66	60.5	0.1
Tension – 0.39 MPa	1.28	52.76±5.43	57.5	5.6
Tension – 0.19 MPa	0.88	55.33±5.01	57.7	9.4
Tension – 0.05 MPa	2.01	50.95±5.37	52.8	3.6
Compression – 0.59 MPa	0.87	177.9±9.4	178.0	0.1
Compression – 0.39 MPa	0.66	163.3±3.7	172.2	3.9
Compression – 0.19 MPa	1.14	155.8±4.7	180.5	3.1
Compression – 0.05 MPa	1.58	154.5±6.9	155.7	0.8

Whilst there is a general decrease in strength as void content increases, there is one model where the strength slightly increases. This can be due to other parameters, such as major and minor axis length, being changed between the models, yet only the strength of the material is plotted against void content. This means that each of the models will correlate differently to the experimental data, and for this study, the model representing the 0.19 MPa laminate (0.88 % void content) had a better correlation than the model representing the 0.39 MPa laminate (1.28 % void content)

Overall, by considering both the void content as well as void geometry, the modelling framework can accurately predict the strength of the laminates with varying degrees of porosity. These results show that when accurate porosity characterisation data is available, the modelling framework can accurately predict the knockdown in transverse strength.

6.4.2. Resin infused representative models

The resin infused representative models were next evaluated, where **Table 6-11** documents both the void module and RUC strengths for each laminate, as well as the experiential strength for the respective laminate. As documented in subsection 5.5.5,

only specimens 1-13 were considered for laminate C.L. 3 as it was found that the remaining specimens have a different void content. Therefore, the model is only representative of specimens 1-13. The correlation between the model prediction and the experimental results is illustrated in **Figure 6-17**.

Table 6-11 *Strength predictions of Stages 1 and 2 including the experimental results.*

Laminate I.D.	Stage 1 Strength / MPa	Stage 2 Strength / MPa	Experimental Strength / MPa
T.L. 1 [a]	35.49	12.40	12.40
T.L. 2	35.06	11.90	9.26
T.L. 3	32.13	11.22	9.77
T.L. 4	31.95	11.17	10.80
C.L. 1 [b]	290.4	116.8	116.8
C.L. 2	286.4	114.1	116.1
C.L. 3	273.4	109.3	109.9 [B]
C.L. 4 – Micro	254.7	102.1	110.5
C.L. 4 – Discrete	289.3	115.7	110.5
C.L. 5	255.3	102.1	111.4
C.L. 6	256.8	103.0	108.8

[a] Represents model used to calculate pristine matrix properties.
[b] Mean of specimens 1-13 from laminate C.L. 3.

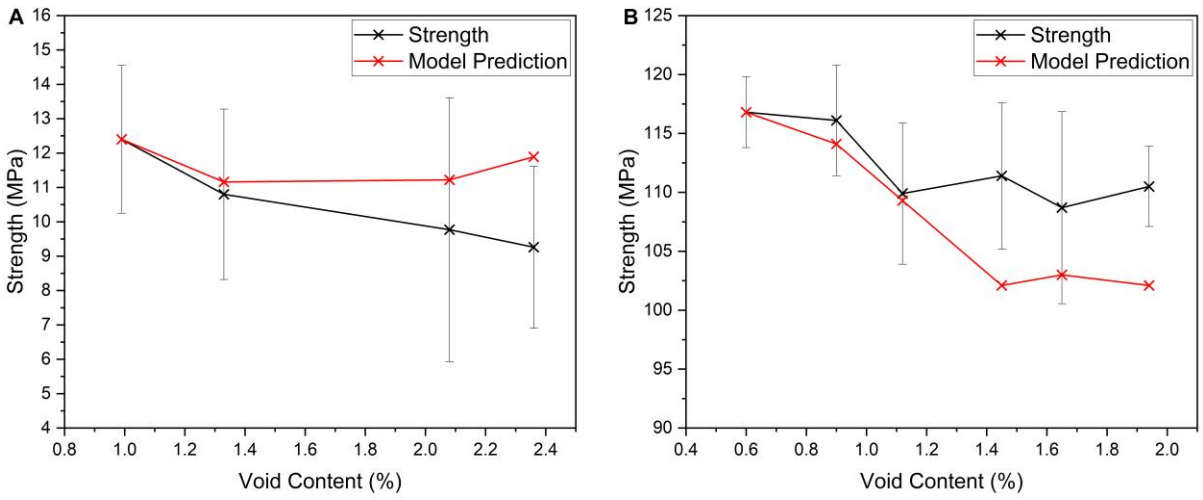

Figure 6-17 *Correlation between the model and experimental results for (**A**) tension and (**B**) compression.*

For both the tensile and compressive models there is a good correlation at lower void contents. The model correlates extremely well for void contents up to 1.2 % in both cases, however, past this point, the correlation deviates. This is likely due to the variation in void content and strength across the laminate; this is evaluated further in the discussion chapter.

6.5. Chapter Summary

This chapter aimed to describe how the results of the experimental campaign were used to build representative models using the developed modelling framework. The microstructure parameters used to build the models were the void content and void size as well as the fibre distribution.

For each laminate, a representative model was built to compare against the experimental test results. For the modelling, it was assumed that the voids were evenly distributed, and therefore, just a single representative void was modelled. The geometry of the stage 1 model was determined based on the overall void content and aspect ratio of the void, which was assumed to be elliptical. The geometry of the stage 2 model was determined based on the fibre distribution measurements and to enforce periodicity, periodic boundary conditions were implemented. Mesh convergency studies were undertaken for each set of models.

To use the model the matrix strength must be known, however, due to the confidentiality requests from the manufactures, this information was classified. To resolve this, the modelling framework was used in reverse, in combination with the experimental data from one of the laminates (lowest void content), for each set of tests (load case and manufacturing process). This allowed for the modelling process to be used to determine the matrix strength.

Initially, for the voids within the autoclave manufactured laminates, it was determined from the histograms that the void dimensions followed a normal distribution and therefore the mean lengths were taken, however, this resulted in poor correlation to the experimental strength. For this reason, multiple statistical approaches were evaulated, and it was determined that by only considering the smallest voids (i.e. the ‘lower third’ of voids measured) the results correlated the best.

When determining the representative void size for the resin infused laminates, it was established that the most appropriate representation for a single void was to use the mean dimensions. This was due to the central peak in each of the histograms suggesting that a normal distribution was present. The modelling approach was able to accurately predict the reduction in strength for void contents up to 1.2 % for both the tensile and compressive laminates. For laminates with higher void contents, the model does not correlate as well; this was concluded to be due to higher variation and more complexity and as such, only modelling a single void is not representative of the whole laminate.

7. Discussion

7.1. Chapter Overview

The purpose of this chapter is to review and interpret the relevant results that have been presented in this PhD thesis, highlight the implications and benefits of the research, and acknowledge the limitations of the research.

7.2. Research Aim and Summary of Key Finding

This subsection gives a high-level summary of the key findings, which are then examined in more detail in the following subsection.

Manufacturing defects in composites are common and while significant research has been undertaken to reduce them, they cannot be avoided completely. Therefore, various defects must be considered when designing composite structures, particularly for load-bearing purposes. One such defect is porosity, which has been shown to degrade various mechanical properties. The overarching aim of the research within this thesis was to evaluate if the proposed modelling framework, conceptualised from investigating the current state-of-the-art porosity modelling approaches, could accurately determine the reduction in transverse strength in composites containing porosity.

The first objective that was investigated using the modelling framework was to validate if it can predict a change in strength and investigate how void geometry affects strength reduction. The results showed that the geometry of a void affects the strength and that there is a correlation between the stress concentration factor and strength knockdown. Recent research has begun to identify that the geometry of voids is also important in determining the strength knockdown factor, as found here. For instance, Little et al.[12] and Stamopoulos et al.[100] demonstrated that the strength of different composites containing the same void content can vary due to differences in the geometrical properties of the porosity. To ensure that the model was calculating the stress

accurately, the model was adapted to be representative of a plate and the results were compared successfully with an analytical solution.

The next objective involved exploring which composite properties were affected by porosity through mechanical testing. In this work, the tensile and compressive strength and modulus were calculated in the longitudinal and transverse directions for two different manufacturing processes. The results showed that only the transverse strength in tension and compression was significantly affected by porosity, and no effect could be observed on the longitudinal strength and all elastic moduli. Additional DMA tests were performed to establish if there was any variation in the mechanical properties of the cured matrix due to varying the applied pressure. The results showed no variation was present.

The porosity within all laminates was characterised to determine which material properties were affected, but also to use the characterisation data as inputs into the modelling framework. The void content, geometry of the voids and fibre distribution were measured. From the optical microscopy it was observed that the void geometry was approximately ellipsoidal in shape, as previously illustrated in **Figure 5.9**, within Chapter 5. Therefore, by using this approximisation the major and minor axis were measured, with reference to the loading direction. A detailed characterisation study for the porosity within the resin infused laminates was undertaken to determine if there was a significant variation along the length of the laminate. Whilst the majority of the laminates showed no significant variation, one of the laminates exhibited a difference in void content at the in-inlet end of the laminate. This region was excluded as inputs into the models and only the regions with uniform porosity were compared.

The final objective was to conduct a correlation campaign where the developed modelling framework was used to predict what the laminate transverse strength is for the given porosity parameters and compare it to the experimental results. It was found that the models correlated very well for the autoclave processed laminates, and for the resin infused laminates that contained a void content of below ~1.2%. Through undertaking the correlation campaign, it was found that it was important to use the correct statistical representation of the porosity within the laminates. For instance, whilst using the mean void dimensions was appropriate for the resin infused laminates, it was more appropriate to use the void dimensions from the ‘lower third’

of voids measured. When other statistical approaches were used, lower correlation was achieved.

7.3. Results Discussion

7.3.1. Novel Model Conceptualisation

Following the literature review, the initial objective was to conceptualise a novel approach for predicting the effect on the mechanical properties of composites containing porosity. The literature review showed that there are typically two approaches to modelling the effect of porosity: either a 2D model where voids are modelled as gaps in the matrix, such as the models presented by Vajari[181] and Chowdhury et al.[182], or a 3D mode where matrix elements are selected, as done by Zhang et al.[183], where the modulus is degraded to represent a void. Both approaches can be used to vary the void content by adjusting the volume fraction of gaps/defective elements. However, both approaches have a significant flaw, they are not able to accurately represent the geometry of the voids. In the 2D models, the voids are modelled as infinitely long. For the 3D models, the voids must take the shape of the elements and so possess flat sides and sharp edges/vertices. In both cases, it is not possible to accurately capture the local stress field around the voids.

In recent research,[12,100] it has been suggested that the shape of voids is also a factor in how porosity affects the degradation of the material properties. Therefore, by not accurately representing the geometry, and solely focusing on the void content, the models may not be fully representative. To address this, a novel approach was conceptualised, based on the assumption that voids act as stress concentrations on the matrix, causing a detrimental impact on the composite strength. The approach first evaluates how voids act as stress raisers in neat matrix, i.e. without considering the fibres, results in a 'knocked down' matrix strength that can then be used in a conventional RUC to give ply properties.

There are several advantages to this modelling framework. First, unlike the previous models already established, there is no modelling-specific limit on how well the geometry can be represented. Any shape/size/distribution of voids can be included in the modelling approach. Instead, the limitation is on the characterisation processes to determine the geometry representing the voids (such as the 2D optical microscopy that

cannot measure depth, or μ-CT that has difficulties in identifying small voids). Another advantage of this approach is the computational efficiency. Not including fibres in the first stage of the model and only focusing on modelling the void in the matrix greatly reduces the element count in the model. This is because, to ensure the accuracy of the model, a sufficient number of elements/nodes should be located around any geometrical feature, such as a void or fibre. Therefore, by not including the fibres these additional elements are not required.

This multistage modelling framework is the focus of this PhD thesis and set the main aim which was to determine if it can be used successfully to predict the effect on the mechanical properties of voids in composites.

7.3.2. Model Development

The first study using the modelling framework was an investigation into how varying the porosity parameters previously mentioned affected the strength. First, a study was conducted where a single spherical void was modelled, and the amount of surrounding matrix was varied. It was expected that as the volume of the matrix was reduced, in turn increasing the void content, the strength would decrease. Instead, the amount that the strength was reduced by was negligible. It was later determined, after investigating the relation of stress concentrations to this work, that the minimal change in strength was due to the large amount of material surrounding the void/stress concentration and any subsequent variation to the void volume fraction had no effect on the results. The next study involved changing the aspect ratio of the void, and again the results could be explained using stress concentrations. As the void aspect ratio increased either in the transverse direction or in the longitudinal direction, the required applied stress to achieve a given maximum stress at the stress concentration would either decrease or increase, respectively. These results show that since voids act as stress concentrations, the geometry of the void is important to determine at what load failure will occur.

To ensure that the model calculates the stress in the model correctly, a series of models were set up and compared to a representative analytical model. A limitation of the analytical model is that it can only be used for 2D/plate-like structures. Therefore, rather than modelling voids in their full three dimensions, they were simplified to ‘defects/notches’ in plates. Whilst this was a simplification, the same modelling

procedures were used (meshing, boundary conditions, force calculation etc.) and so it could be considered the same modelling approach.

The results from the numerical and analytical models showed a very good correlation, with all numerical predictions within 5% of the analytical solution. The analytical solution suggests that two main parameters affecting the maximum stress at a stress concentration are the radius of curvature of the stress concentration, and the defect size. Studies were set up to investigate both parameters, and the results showed that whilst they both affect the maximum stress for a given applied load, their contribution differs. It was found that as the defect/notch size increases, the required stress for a given maximum stress at the stress concentration reduces non-linearly, as previously illustrated in **Figure 4-14** within Chapter 4. This could be explained such that as the size of the defect increases, the rate of change of the radius at the stress concentration reduces (i.e. the change in stress concentration reduces) and; therefore, the change in applied load for a given maximum stress reduces. On the other hand, it was then found that the effect of the stress concentration radius has a linear effect. As the stress concentration radius either reduces or increases the load required for the maximum stress to be reached increases or decreases, respectively, as previously illustrated in **Figure 4-20** within Chapter 4,. These results suggest that whilst both parameters (size and radius) are important and contribute to stress located at a stress concentration, voids that are sharper and have higher stress concentrations are likely to be more detrimental than larger voids in their impact on strength. It should also be noted that the analytical model suggests that if the void is spherical, then regardless of how big or small it is, it will always have the same stress concentration factor.

The studies that had been undertaken to investigate the void parameter contributions were solely focused on the stage one model, i.e., how a void degrades the pristine matrix properties. However, the overall modelling framework also includes the next stage, where the homogenised matrix properties are used in an RUC to provide the ply properties based on the porosity being modelled. The second stage of the modelling approach was not included since its effect would only be to scale the strength accordingly as the same RUC would be used; therefore, this does not provide useful and novel research.

Nevertheless, the results have shown that it is not solely the void content that is important, but also the geometry of the voids plays a significant role in the impact of

strength. This had been identified in the literature review with previous focus on the void content; however, recent publications have demonstrated that the geometrical properties must also be considered. This research has shown that these parameters must be accounted for accurately to have a representative model, as the results can otherwise vary significantly.

7.3.3. Experimental Testing

The objective of the experimental campaign was to validate and confirm which mechanical properties were affected by porosity, investigate how the porosity forms geometrically, and characterise the microstructure (porosity and reinforcement) to be able to use as inputs into the modelling framework in the subsequent chapter. Two manufacturing processes were used to produce laminates with various degrees of porosity. This was to determine how well the modelling framework correlates with laminates manufactured either with or without the use of an autoclave.

There are a variety of different load cases that define a composite strength, such as flexural, torsion or interlaminar shear strength. Due to time constraints, it was not practical to investigate in great detail the effect of porosity on all mechanical properties; therefore, tension and compression tests were chosen. These were chosen as they are the dominant mechanical properties used in the calculations for composite layup design/classical laminate theory[184]. In addition to this, it was considered that the modelling framework could already be used for structures in flexural loading since, by the nature of the load, there will be regions of the structure in either tension or compression. Thus, it would be possible to use the modelling framework locally on different regions of the structure/position in layup. Consequently, it was determined to be more appropriate to ensure that the modelling framework could be used in tensile and compressive load cases before developing it for more complex loading.

The literature review showed that the transverse strength in both tension and compression is affected by voids; however, there were conflicting reports on whether the longitudinal compressive strength is affected[25,30]. Likewise, there was also disagreement as to whether voids affect the elastic modulus in all load cases. For this reason, it was chosen to test both the strength and elastic modulus in both the longitudinal and transverse directions to determine exactly what is affected. This was done for the laminates processed using an autoclave. Since the results showed that

only the transverse strength was affected, only transverse specimens were manufactured through OoA processing and instead, the effort was focused on the porosity inspection.

To evaluate how the mechanical properties were affected by the porosity, before evaluating the mechanical testing results, the porosity was characterised for each laminate. The porosity parameter characterisation was undertaken through microscopy. Whilst this is a common approach, it can only be used to evaluate the microstructure in 2D, meaning depth was not considered. This affects all parameters as the overall void content and void geometry include void depth. The first approach to address this drawback was using an optical profiler as this was able to show that the voids were not infinitely deep as some studies suggest.[57] A second approach was to use µ-CT scans as this is a common approach to characterise porosity at high fidelity. µ-CT scans were done for several of the autoclave processed laminates. Unfortunately, it was not possible to identify the large number of small voids since there was not a distinct difference in attenuation between the matrix and void/material free region. This could only be identified since a few large voids were identifiable due to phase contrast edge enhancement where the attenuation at the edge of the void fluxtuates resulting in the outline of the voids being present. The µ-CT scans were used to measure the fibre volume fraction which correlated very well with the results found in the literature.

Consequently, as shown in the literature[71,172], it was expected that as the autoclave cure pressure reduced the void content in the laminate would increase. Whilst this was generally the case, in a few cases this trend was not observed. For instance, the transverse tensile laminate cured at 0.19 MPa had a lower void content measurement than the same laminate cured at 0.39 MPa. This was also observed for the transverse compression laminates cured at 0.39 MPa and 0.59 MPa. The reason for these inconsistencies can likely be attributed to the manufacturing process not being completely controlled. For instance, the laminates were not manufactured/laid up in an environmentally controlled room meaning the temperature and humidity could vary. Particularly if the humidity in the room on a given day was higher, then this in turn could likely result in higher moisture being trapped between the plies of the layup and result in the laminate having a higher void content. This has been shown in literature where Anderson and Altan[19] demonstrated that by increasing the humidity

during prepreg processing, the void content increased. Another factor to consider is that the laminates were laid up by hand; therefore, the pressure applied when rolling a 'squeegee' after applying each ply could vary. If less pressure was applied when laying up one laminate, this again could result in a higher void content. Ultimately the strength of the laminate is studied against the void content, not the processing pressure.

When measuring the void content, a high error was observed, as expected. Due to the nature of microscopy, only a 'snapshot' of a given region is captured. Since the voids do not generate perfectly periodically each region imaged will vary. In the case where there are large voids present in the laminates (such as when little pressure was applied or the resin was not degassed prior to infusing), depending on the number of large voids captured in the image would significantly change the measurement of that image. To minimise this error, a significant number of images were taken and processed.

To vary the porosity for each laminate, the autoclave cure pressure was adjusted. This successfully resulted in different void contents for each laminate; however, one uncertainty was whether the change in cure pressure affects the mechanical properties of the matrix. It was hypothesised that as the cure pressure reduced the cross-link density of the polymers would consequently reduce. This in turn would result in a change in the matrix's elastic modulus. Whilst this technique for varying void content is a common approach seen in literature[30,71,172], to ensure that the technique is valid and is not introducing additional variables into the study, the hypothesis was investigated. This was done in two stages, first, a detailed literature review was conducted to determine the cure mechanics of epoxy resin and any studies investigating the influence of cure pressure on elastic modulus. Secondly, experimental tests were conducted to determine if any variation in the matrix between samples cured at different pressures was present.

The literature search concluded that by increasing the cross-link density the elastic modulus should increase[86]. However, when it was investigated what process parameters affect the cross-link density, it was determined that only the cure time, temperature and hardener-to-resin ratio affect the cross-link density.[80,81] Instead, it was found that the purpose of the pressure during the curing process is to improve the consolidation of the layup so that the void content is reduced and to extract excess

resin.[69,90] Thus, these findings suggest that reducing the cure pressure will not have an effect on the elastic modulus of the matrix used in the autoclave processed laminates.

To further valid this conclusion, experimental tests were performed to study any variance in elastic modulus as the epoxy resin cures. Initially, the resin used for the infusion laminates was trialled; however, this resin system was designed for room temperature cure and when cured at elevated pressures the temperature could not be controlled (even when full cooling was applied), as the additional pressure resulted in elevated temperatures. Since the literature review showed that cure temperature does affect the matrix's mechanical properties, accurate and valid comparisons cannot be made. Additionally, due to safety concerns associated with the uncontrolled temperature of curing resin, further attempts were aborted. Instead, DMA tests were employed using the remaining material from the autoclave cured laminates, that had been cured at different pressures, to determine the glass transition temperature for each laminate. As illustrated in **Figure 7-1**(**A**), the results showed that there was no trend between the cure pressure and the glass transition temperature of the laminates. In the research presented by Bandyopadhyay et al.[81] their results showed a correlation between the crosslink density and the glass transition temperature as well as the crosslink density and Young's modulus, as illustrated in **Figure 7-1**(**B**). Since the results of the DMA tests have shown no trend between cure pressure and glass transition temperature, it can be concluded that there is no significant variation in crosslink density between the laminates cured at different cure temperatures, and therefore the elastic modulus is consistent between the laminates. This correlates with the literature review in subsection 2.6, where the influence of pressure on the matrix cure was investigated. It was found that the range in pressure applied, does not influence the matrix cure but rather is used to improve consolidation and reduction of void content.

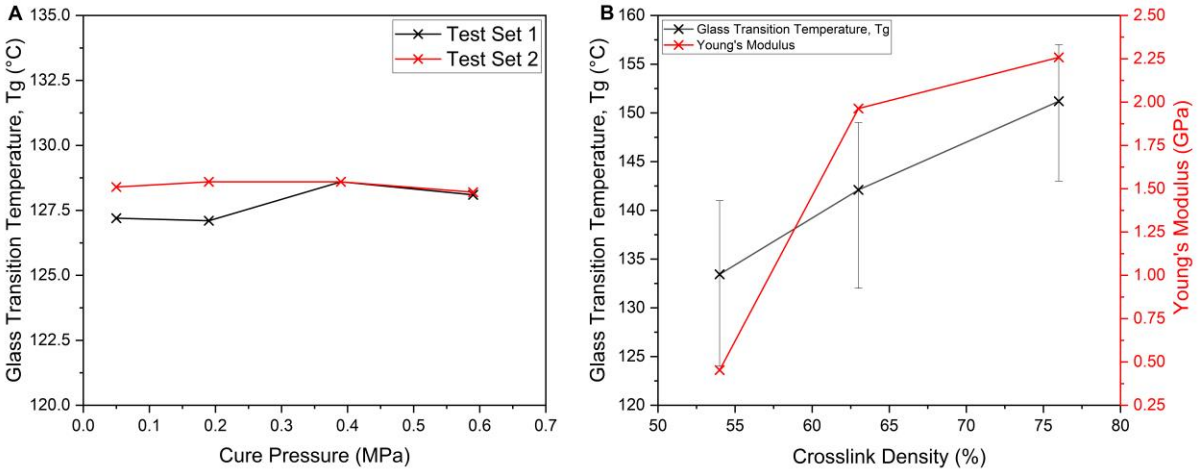

Figure 7-1 (**A**) Glass transition temperature variation due to cure pressure, and (**B**) relation between crosslink density and glass transition temperature and Young's modulus.

A more detailed investigation was undertaken for the laminates that were manufactured through resin infusion, to study how the void content varies along the infusion length. This was investigated as it was considered that the draw of the vacuum may degas the resin, resulting in a lower void content at the outlet end to the inlet end. Also, due to the less controlled nature of resin infusion, it could be expected to have more variation within the laminate. For 7 out of the 10 resin infused laminates, the results showed only a minor fluctuation in void content along the length. The minor fluctuation can be attributed to the high measurement variation as previously discussed. The three laminates that had a notable change in void content were all manufactured to have a higher void content percentage. It was found that for these laminates with higher void content fractions, the error was also larger, which suggests that higher void content fractions lead to higher local variation (not to be confused with variation across the length of the laminate). When comparing the range in void content across the laminate infusion length to the measurement error, it was found that the range falls within the error. For this reason, it cannot be concluded that there is a variation in void content along the length of the high void content laminates, only that there is high local variation in the same region.

As well as measuring the void content, the geometry of the porosity was studied. The results for both the autoclave and resin infusion showed that whilst there is variation in the dispersion, the voids are spread evenly throughout the laminate, i.e., they do not only exist at ply boundaries, or at the centre/outer plies. The shape of the voids within the autoclave processed laminates were ellipsoidal whereas for the resin infused

laminates spherical, ellipsoidal and arbitrarily shaped voids were present. These observations are consistent with the literature.[57,185] This again suggests that the void form resulting from OoA processing is more complex. The dimensions of the voids were measured by their major and minor axis. This was achievable for the spherical and elliptical voids; however, this is a simplification for the arbitrarily shaped voids since it is not possible to measure and recreate the exact shapes for all of the arbitrarily shaped voids. Instead to account for these voids their approximate length and width were measured.

The void size measurement results for the voids within the autoclave processed laminates showed that the porosity was made up significantly of small voids (approximately 5-10 μm in length). However, in the lower pressure cured laminates, such as the 0.05 MPa laminate, there was a notable number of larger voids, up to 165 μm in length, resulting in a skewed normal distribution. In contrast, the size distribution for the voids from the resin infused laminates showed a normal distribution. Capturing the correct distribution is important as it is used to determine how to correctly represent the porosity in the modelling framework.

The void content for each laminate was used to compare the strength of each laminate. The results of the autoclave manufactured laminates showed that whilst the transverse direction was significantly affected, there was no notable correlation between void content and strength in the longitudinal direction. There is a general agreement in the research community that the longitudinal tensile strength is unaffected by voids, which has been confirmed by these results, as the load is carried predominately by the fibres. Nevertheless, there is disagreement as to what extent the longitudinal compressive strength is affected. The reasoning is that whilst the load is again predominately carried by the fibres, the matrix still has a role in supporting the fibres from buckling and without the matrix (due to porosity), the fibres are more likely to fail prematurely through micro-buckling of individual fibres. Although, as shown by these results, only the transverse direction was affected and therefore, was only considered in the subsequent modelling work.

For the resin infused laminates, the testing was focused on the transverse direction and the strength was measured along infusion length. This was to supplement the research on how the void content varied along the length of the laminate. For all the laminates, where the specimens were loaded in tension, no significant trend or

variation was found other than the expected experimental variation. The same was true for five out of the six compressive laminates where no significant variation along the length of the laminate was observed. However, for laminate C.L.3 , there appeared to be a localised increase and decrease in strength at the inlet and outlet ends, respectively. It is likely that at the outlet end there is just a single specimen that has failed at a lower strength, which occasionally occurs in the other laminates (for instance specimen number 5 and 2 for laminates C.L. 1 and C.L. 2, respectively). This resulted in a false indication of decreasing strength. Conversely, this cannot be said for the inlet end as there is a general increase in strength from specimens numbered 13 to 16. These are the last 4 specimens in the laminate and when compared with the void content analysis, there does appear to be a reduction in void content towards the inlet end. The nearest measurement to the inlet end was taken from specimen 14, which explains why a more significant void content reduction was not recorded (as it is expected that the void content continues to reduce further towards the inlet end). From a modelling perspective, these regions need to be analysed independently; therefore, in the subsequent modelling section, only specimens 1 to 13 were considered. Whilst it would be possible to also model the inlet region with further porosity evaluation, there are only a few experimental data points, thus, an accurate representation of the strength in this region cannot be determined. Further evaluation of this region was beyond the scope of this study and was not considered.

The modulus was also measured in all test configurations, again since there is disagreement in the research community[20,98,111] and to ensure that this does not need to be accounted for. If it was affected, then this would need to be included in the modelling process as this information will be required at the component design. The results showed that there was no significant impact made on the modulus as the porosity was increased for all test configurations.

7.3.4. Model Representation

The objective of the model representation chapter was to use the porosity characterisation data that had been gathered to predict the failure strengths of the laminates using the proposed modelling approach. The model predictions would then be correlated with the experimental results to determine to what extent the modelling framework can predict the reduction in transverse strength.

Separate models were generated for each specific laminate which were built using the void content, void size and fibre distribution data from the microstructure analysis. Since the strength of the matrix was unknown for both the autoclave and resin infused laminates, one tensile and compressive model was selected for both processing conditions and used to independently determine the tensile and compressive strength for each of the resin systems. Additionally, the remaining models for both tension and compression were simulated, using the determined strength value, and compared to the experimental results.

Using the modelling approach in a 'reversed' direction to determine the matrix strength properties introduces an uncertainty into the modelling process. Since the data from only one set of tests was used (it was chosen to use test data from the laminate with the lowest void content) this does not have the effect of 'tuning' the model to the experimental results, i.e., each model is independent of the others. However, the accuracy of the model will dictate how accurate the matrix strength prediction is, which consequently affects the performance of the model. To ensure that the predicted values were accurate, two approaches were taken.

First, they were compared to the values of similar material published in the literature to confirm that they were reasonable. Secondly, tensile and compressive tests were conducted on the matrix used in the resin infusion tests. This was to validate that the properties that the model predicts are representative of the material used in the experimental testing. Two resin plaques were manufactured to increase specimen numbers for additional certainty, as well as checking for any variation in manufacturing. The results showed no variation between the plaques and therefore no manufacturing issues were identified. The results of the tensile testing found that was an acceptable correlation of -15.3 % for the strength prediction and 12.2 % for the Young's modulus. The difference can be attributed to the model simplifying the failure to being brittle and instantaneous failure occurring, whereas the test results show the material turning plastic before final failure.

In addition to the tensile testing, it was attempted to conduct compression tests, however, the results indicated that the specimens did not fail correctly (i.e. not in pure compression) and could not directly be compared to the FEM predictions. The mean compressive strength was determined to be 98.8 MPa, with a standard deviation of 21.5 MPa. The large error is attributed to some specimens failing with a failure strength

notably higher than the mean strength (with strengths observed as high as 193.7MPa). Additionally, the transverse compressive strength of the resin infused laminates (where the matrix strength is dominate) across all specimens had a mean strength of 112.5 MP and maximum observed strength of 126.6MPa. This results in transverse compressive strengths that are 12.2 % and 22.0 % higher than the measured neat resin strength respectively. It was expected that the neat resin strength to have a higher strength in compression than the transverse compressive strength of the resin infused laminates due to the addition of the fibres and voids. This suggests that the neat resin samples failed prematurely. When inspecting the compression samples diagonal failure could be observed, indicative of the samples being loaded in shear and not pure compression. This can be attributed to the friction between the samples and the platens not allowing for expansion, due to Poission's effect, at the loaded ends. By observing that the samples failed in shear, it is possible to predict the compressive strength by comparing the shear and compressive strength of similar materials. By evaluating the material properties presented in the book chapter "*Mechanical Properties of Polymeric Materials*"[186], it can be understood that the compressive strength is approximately 1.97 times greater than the shear strength. By applying this to the sample that failed with the highest strength, on the basis that it had the least number of internal flaws, gives a compressive strength of 383.3 MPa. This gives an acceptable model correlation of 12.1 %. The analysis of both the tensile and compressive mechanical testing of neat resin suggests that the model predicted strengths are representative and the procedure to determine strengths from the experimental data is validated.

For the autoclave processed laminates, initially, it was found that the model was over-predicting the strength, this was particularly true for the tensile laminates. On review, it was determined to be due to how void size distribution was being characterised. The mean length of major and minor axes was taken as representative. This would be true if a normal distribution was present' however, in this case, the distribution was misrepresented in favour of the smaller voids. This was most notable in the major axis where there were several larger and more elongated voids. By including these voids in the mean calculation, the geometry of the representative void became more elongated. When considering stress concentrations, a more elongated void would require a higher load to reach the same maximum stress, which explains why the model overpredicts the strength.

Subsequently, it was determined that greater care was needed when choosing the correct void size distribution; therefore, a study was undertaken to evaluate the most appropriate distribution to be representative of the void sizes. The results from the analyses found that using the lower third of measurements yielded the best correlation. It was determined that the strength of the composite in the transverse direction (which is matrix dominant) is dependent on the stress concentrations resulting from the smallest voids, rather than around the large and elongated voids where the stress concentration is lower. The final results of the models representing the autoclave processed laminates showed good correlation; all models predicted a strength that was within the measurement error and the predictions were within 10 % of the experimental mean. This shows that the model is dependent on accurate geometry information for good correlation.

The models that were built to represent the resin infused laminates showed good agreement with the experimental results for lower void contents, up to 1.2%. However, past this point, the model deviates. The lower correlation at higher void contents was determined to be due to the void formation being more complex in that porosity range. This also suggests that OoA processes result in complex and varied void formation, particularly at the higher void contents. For instance, the void content results of the tension laminates with the lower void contents showed less variation; however, when the void content was increased, more variation in the void content was present. Whilst the void content variation did not appear to have a significant influence on the laminate's strength, it is possible that due to the high variation in measured void content, the void content used was not representative. Similarly, the lower void content compressive laminates had very little void content variation, whereas the higher void content laminates, in particular C.L.4 and 6, had much more variation. It would also be expected that laminates with higher void content, particularly with variation across the laminate, would be geometrically more complex, i.e., a larger range of shapes, particularly more arbitrary. The difficulty in accurately characterising the porosity without higher accuracy measurement equipment results in less representative geometry being used and higher deviation from laboratory results. This also goes some way to show the difficulty in modelling the effect that porosity has on mechanical properties, and why low void content thresholds are set for structural composites (such as the 1.0% limit on aerospace structures). Whilst there was difficulty in the model predicting the strength past 1.2%, the model correlates well for laminates

with lower void contents, which is the range in which the model would most likely be used for.

7.4. Research Limitations

This subsection details any limitations of the research presented throughout this thesis and the implication that the limitation has on the results.

One such limitation was the failure criteria used to determine the failure of each stage. It was assumed that the matrix of the composite fails through brittle failure and, as such, when it was identified that a single element had reached the maximum allowable stress, it was considered that total failure had occurred. This is not an unreasonable assumption to take, the results of experimental campaign for the composite laminates results showed little plasticity when the specimens were loaded in the transverse direction, where the failure behaviour is matrix dominant, particularly in tension. However, assuming brittle failure as the failure criteria limits further study into damage propagation. For instance, studying how damage propagates between voids if multiple voids are included in the stage 1 model, or the matrix-fibre interaction if damage was to propagate around the fibres. These are detailed and specific studies that were beyond the scope of this PhD project; however, to investigate such topics the failure criteria would need to be adapted. The modelling framework has been designed such that there is low difficulty to use different failure criterion; the stress tensors for each element are determined which are used in the various failure criterion (in the current case Von Mises Yield Criterion is used).

Another limitation of the modelling approaches that were taken was that only a single void was considered representative of the global laminate porosity. This is a simplification since the void measurement results showed a large variation in the void sizes. The stress concentration theory that was considered in Section 4.5 assumed that there is a single stress concentration on an infinite plate. This is not representative of how porosity forms in composites; the microstructure characterisation results showed that multiple voids form in close proximity to each other. In practice, having voids within close proximity of other voids would result in higher stress concentration. For instance, Hensaw et al.[187] investigated this principle by considering holes in composite plates. Their results showed that the stress concentrations around a hole significantly

increase when secondary holes are in close proximity. They also found that the arrangement was important; the increase in stress concentrations was magnified when the secondary hole was out of alignment with the primary hole to the load. Likewise, Davis et al.[188] investigated how the stress concentrations in a homogeneous material (for their study rocks were used) change as the void separation distance changes. Their results agree with those of Hensaw et al.,[187] such that when voids are closely packed and formed in an offset arrangement from the applied load, higher stress concentrations result. This shows that considering only a single void, when the microstructure has shown multiple voids in are in close proximity, is likely to result in an overprediction in strength as the stress concentrations will be higher than if only a single void was present. The focus of the thesis has been on the development of the modelling approach and so, whilst the analysis that has been performed has been simplified in this regard, it has allowed the development to progress. It is noted that including the effects of multiple voids should be considered in further advancements. A benefit of the modelling framework is that it allows for more complex geometry to be modelled, and as such multiple voids of various shapes and sizes can be situated in the stage 1 model and this phenomenon can be addressed.

Throughout the thesis, only tensile and compressive strengths were considered, whilst numerous other strength properties define a composite such as flexural, torsional and interlaminar shear strength. It was determined appropriate to only consider tension and compression loading for two main reasons: first, as this is the development of the modelling framework and is a novel approach, it was considered more appropriate to ensure that the framework correlates well in tension and compression before advancing to more complex loads. Second, tensile and compressive strengths are the main strength factors when considering classical laminate theory which is predominately used in the design of composite structures. For these reasons, it was considered appropriate to only use the model to predict the tension and compression strengths.

Throughout the thesis, 2D microscopy was the main contributor to characterise the porosity. Whilst this is a common approach used,[30] the main limitation to using 2D microscopy is that the depth of the voids cannot be measured. Two attempts were made to address this issue, the use of a 3D optical profiler and μ-CT scanner. The 3D profiler was able to show that the voids were not infinitely long, as has been suggested

by other researchers; however, the full depth could not be measured since the voids had to be sectioned to measure the depth. To measure the porosity geometry without sectioning the voids, μ-CT scans were undertaken. The resolution was not sufficient to accurately distinguish small voids (micrometre scale) and only large voids (millimetre scale) could be detected.

8. Conclusions and Future Work

This chapter concludes this thesis by highlighting the current state of the art, identifying the knowledge gap and summarising the aims of this study. The key research findings are then summarised in relation to the project aims including any limitations. This chapter finishes by proposing future research opportunities that build upon this work.

8.1. Summary of Conclusions

There is a strong drive towards using composite materials in automotive applications to improve both efficiency and reduce the impact on the environment. However, a major obstacle is the significant manufacturing variability and associated deviation of mechanical performance. One variability is porosity, where many researchers have investigated the effect on different mechanical properties. Whilst there is disagreement as to what extent the modulus is affected, there is a good consensus that the transverse strengths are significantly affected. Predicting the effects on relevant mechanical properties is essential in efficient composite designs. Initial modelling processes, which are still very common, are 2D models whereby fibres and voids are distributed throughout a plane and are assumed to be infinitely long. More recently, there has been a focus on increasing the accuracy of void geometry representation. To model voids in 3D, the most common approach is by randomly selecting several elements and degrading their properties to near zero. After reviewing the relevant literature, it is apparent that there is a drive towards developing modelling approaches that not only account for the void content, but also accurate geometrical parameters. This set the overall aim of the project to develop a modelling framework that can predict the effect of porosity on the strength of carbon fibre reinforced polymer materials.

Based on the reviewed literature, a modelling framework was developed and validated against experimental data. The following concluding remarks of this thesis can be summarised as follows:

- The first objective was to conceptualise the modelling framework. The modelling framework can accurately represent void geometry by splitting the procedure into two main stages; first, the effect of voids acting as stress concentrations on pure resin is investigated and homogenised into the 'degraded matrix' and second, how the degraded matrix affects an RUC.
- The second objective was to use the modelling framework to predict how the geometrical parameters (void shape and size) affect the strength of a composite. A series of models were developed whereby voids of different shapes and sizes were modelled. The results showed that the shape of the void acts as a stress concentration and significantly influences the local stress around the void. The local stress was analytically compared with good correlation (less than 5% difference).
- The next objective was to conduct an experimental campaign to determine the effect of porosity on the mechanical properties. The relevant data gathered could then be used to validate the modelling process. The study investigated two composite manufacturing processes, autoclave prepreg curing and resin infusion. The results showed that the longitudinal properties were unaffected by voids, even in compression, as some studies have suggested. Literature has shown disagreement in whether the modulus is affected by voids; however, the results found that it was also unaffected. The only property that increasing porosity affects was the transverse strength in both tension and compression. For the autoclave processed samples, a non-linear trend in the compressive results was attributed to the shape of the voids being elongated resulting in lower stress concentrations around the voids. This gives further evidence that the void geometry must also be considered, rather than only void content.
- To build representative models, an objective was set to characterise the porosity of each laminate. This was accomplished for all laminates such that the void content, shape, size and distribution were analysed.
- The final objective was to use the porosity characterisation data to build representative models. The results from the models representing the autoclave manufactured laminate showed that the best correlation was found when only the smaller voids (which represent the majority found in the laminate) were considered. The models representing the resin infused laminates showed good correlation for laminates containing void contents up to 1.2%, which is within

the allowable void content range that structural composites are manufactured to.

8.2. Future Work

The work presented in this thesis are the findings of the development of a novel micromechanics multiscale modelling framework focusing on porosity in composites. Several areas of interest have been highlighted where further investigations could be continued, which are summarised in the following points:

- **Matrix characterisation**. The biggest difficulty in the current work was not knowing the exact strength of the matrix. This value was required for the stage one model as it was used to determine when an element had failed, at which point the homogenised strength could be calculated. Characterising the material properties of the matrix will allow for a more accurate model.
- **Incorporation of plasticity**. This is an expansion of the previous point where higher accuracy material properties are used. The modelling in this thesis used a linear brittle failure assumption as there was no plasticity observed in the tensile stress-strain graphs and only a small amount was present in the compressive load cases. Whilst a brittle failure assumption is in alignment with published studies, it is a simplification, and some researchers account for plasticity. Using test data to accurately incorporate plasticity within the model material properties will result in a more robust model. Further work could also investigate fibre-matrix cohesion as this is another area that is frequently studied.
- **Porosity representation**. Another factor that should be investigated is how the representation approaches used affected the results. This was initially shown in Chapter 5, where the results revealed that different statistical approaches used to represent the porosity resulted in significant differences. It would be extremely beneficial to further this work by including more complex porosity geometry, such as multiple voids and arbitrary voids, etc. This also coincides with the current research trends of investigating the effect of geometrical properties rather than void content.
- **High-fidelity models using μ-CT**. This is a continuation of the previous point of identifying a better representation of porosity. μ-CT scans used to

generate accurate porosity formation could be used to compare how well the simplification approaches correlation. Whilst this was attempted in Chapter 5, it was found that extensive trials to get accurate data were required and beyond the scope of this project. It would be extremely beneficial to invest time into conducting this research and comparing how a high-fidelity model compares to that of the simplified approach.

- **Fibre architecture**. Only unidirectional composites were investigated; however, woven composites are typically used on complex geometries due to their excellent draping and shear properties. Nevertheless, it is also in these regions where voids are often generated due to difficulties in consolidation. It would be an interesting study to investigate how robust this modelling approach is for more complex RUC.
- **Real structures.** Finally, it would be extremely beneficial to conduct a study into the porosity formed in actual structures, how these compare to 'laboratory' flat laminates and use of the model to predict the reduction in strength. This modelling process has been designed for structural design;therefore, it would be beneficial to evaluate the robustness in a 'real-life' scenario and use the results to update and develop the modelling framework accordingly.z

9. References

1. Savage, G. Formula 1 Composites Engineering. *Engineering Failure Analysis* **17**, 92–115 (2010).
2. Jacob, A. Built in Italy: the Lamborghini Avendator. *Reinforced Plastics* **57**, 29–31 (2013).
3. Climate at a Glance | National Centers for Environmental Information (NCEI). https://www.ncei.noaa.gov/cag/global/time-series/globe/land_ocean/ann/12/1880-2022?trend=true&trend_base=10&begtrendyear=1880&endtrendyear=2022.
4. Participation, E. Climate Change Act 2008. https://www.legislation.gov.uk/ukpga/2008/27/part/1 (2008).
5. A European Green Deal | European Commission. https://ec.europa.eu/info/strategy/priorities-2019-2024/european-green-deal_en.
6. European Commission. COMMUNICATION FROM THE COMMISSION TO THE EUROPEAN PARLIAMENT, THE COUNCIL, THE EUROPEAN ECONOMIC AND SOCIAL COMMITTEE AND THE COMMITTEE OF THE REGIONS. (2020).
7. The Paris Agreement | UNFCCC. https://unfccc.int/process-and-meetings/the-paris-agreement/the-paris-agreement.
8. The Department of Business, Energy, and Industrial Strategy (BEIS). *Energy White Paper Powering out Net Zero Future*. 170 https://assets.publishing.service.gov.uk/government/uploads/system/uploads/attachment_data/file/945899/201216_BEIS_EWP_Command_Paper_Accessible.pdf (2020).
9. Grzesiak, S. & Sulich, A. Car Engines Comparative Analysis: Sustainable Approach. *Energies* **15**, 5170 (2022).
10. Edgren, F. Composites 2021. https://congress.cimne.com/composites2021/frontal/ProgramPrint.asp?id=Fr01 (2021).
11. Huang, H. & Talreja, R. Effects of void geometry on elastic properties of unidirectional fiber reinforced composites. *Composites Science and Technology* **65**, 1964–1981 (2005).
12. Little, J. E., Yuan, X. & Jones, M. I. Characterisation of voids in fibre reinforced composite materials. *NDT & E International* **46**, 122–127 (2012).

13. Park, C. H., Lebel, A., Saouab, A., Bréard, J. & Lee, W. I. Modeling and simulation of voids and saturation in liquid composite molding processes. *Composites Part A: Applied Science and Manufacturing* **42**, 658–668 (2011).
14. LeBel, F., Fanaei, A. E., Ruiz, É. & Trochu, F. Prediction of optimal flow front velocity to minimize void formation in dual scale fibrous reinforcements. *Int J Mater Form* **7**, 93–116 (2014).
15. Olivier, P., Cottu, J. P. & Ferret, B. Effects of cure cycle pressure and voids on some mechanical properties of carbon/epoxy laminates. *Composites* **26**, 509–515 (1995).
16. Lundstrom, T. S., Gebart, B. R. & Lundemo, C. Y. Void Formation in RTM. *Journal of Reinforced Plastics and Composites* **12**, 1339–1349 (1993).
17. Centea, T. & Hubert, P. Modelling the effect of material properties and process parameters on tow impregnation in out-of-autoclave prepregs. *Composites Part A: Applied Science and Manufacturing* **43**, 1505–1513 (2012).
18. Grunenfelder, L. K., Centea, T., Hubert, P. & Nutt, S. R. Effect of room-temperature out-time on tow impregnation in an out-of-autoclave prepreg. *Composites Part A: Applied Science and Manufacturing* **45**, 119–126 (2013).
19. Anderson, J. P. & Altan, M. C. Formation of voids in composite laminates: Coupled effect of moisture content and processing pressure. *Polym. Compos.* **36**, 376–384 (2015).
20. Lukaszewicz, D. H.-J. A. & Potter, K. D. The internal structure and conformation of prepreg with respect to reliable automated processing. *Composites Part A: Applied Science and Manufacturing* **42**, 283–292 (2011).
21. Li, S. J. *et al.* The influence of cure pressure on microstructure, temperature field and mechanical properties of advanced polymer-matrix composite laminates. *Fibers Polym* **15**, 2404–2409 (2014).
22. Nikopour, H. A virtual frame work for predication of effect of voids on transverse elasticity of a unidirectionally reinforced composite. *Computational Materials Science* **79**, 25–30 (2013).
23. Afendi, M., Banks, W. M. & Kirkwood, D. Bubble free resin for infusion process. *Composites Part A: Applied Science and Manufacturing* **36**, 739–746 (2005).
24. Cinquin, J., Triquenaux, V., Rouesne, Y. & Iw, E. Porosity influence on organic composite material mechanical properties. in 8 (2007).
25. Kosmann, N., Karsten, J. M., Schuett, M., Schulte, K. & Fiedler, B. Determining the effect of voids in GFRP on the damage behaviour under compression loading using acoustic emission. *Composites Part B: Engineering* **70**, 184–188 (2015).
26. Hapke, J., Gehrig, F., Huber, N., Schulte, K. & Lilleodden, E. T. Compressive failure of UD-CFRP containing void defects: In situ SEM microanalysis. *Composites Science and Technology* **71**, 1242–1249 (2011).

27. Carrera, E., Petrolo, M., Nagaraj, M. H. & Delicata, M. Evaluation of the influence of voids on 3D representative volume elements of fiber-reinforced polymer composites using CUF micromechanics. *Composite Structures* **254**, 15 (2020).
28. Clyne, T. W. & Hull, D. *An Introduction to Composite Materials*. (Cambridge University Press, 2019).
29. Tang, X., Whitcomb, J. D., Li, Y. & Sue, H.-J. Micromechanics modeling of moisture diffusion in woven composites. *Composites Science and Technology* **65**, 817–826 (2005).
30. Mehdikhani, M., Gorbatikh, L., Verpoest, I. & Lomov, S. V. Voids in fiber-reinforced polymer composites: A review on their formation, characteristics, and effects on mechanical performance. *Journal of Composite Materials* **53**, 1579–1669 (2019).
31. Birt, E. A. & Smith, R. A. A review of NDE methods for porosity measurement in fibre-reinforced polymer composites. *insight* **46**, 681–686 (2004).
32. Bascom, W. D. & Romans, J. B. Microvoids in Glass-Resin Composites. Their Origin and Effect on Composite Strength. *I&EC Product Research and Development* **7**, 172–178 (1968).
33. Cilley, E., Roylance, D. & Scheider, N. Methods of fiber and void measurement in graphite-epoxy composites.pdf. in *American Society for Testing and Materials* 237–249 (1974).
34. Patel, N. & James Lee, L. Modeling of void formation and removal in liquid composite molding. Part I: Wettability analysis. *Polymer Composites* **17**, 8 (1996).
35. Patel, N. & Lee, L. J. Modeling of void formation and removal in liquid composite molding. Part II: Model development and implementation. *Polym. Compos.* **17**, 104–114 (1996).
36. Thomas, M., Joseph, B. & Kardos, J. Experimental characterization of autoclave-cured glass-epoxy composite laminates .pdf. *Polymer Composites* **18**, 283–299 (1997).
37. Tretiak, I., Kawashita, L. F. & Hallett, S. R. Predicting short beam shear strength reduction in carbon/epoxy laminates containing voids. *Composite Structures* **290**, 115472 (2022).
38. Machado, J. M., Tavares, J. M. R. S., Camanho, P. P. & Correia, N. Automatic void content assessment of composite laminates using a machine-learning approach. *Composite Structures* **288**, 115383 (2022).
39. Mehdikhani, M., Straumit, I., Gorbatikh, L. & Lomov, S. V. Detailed characterization of voids in multidirectional carbon fiber/epoxy composite laminates using X-ray micro-computed tomography. *Composites Part A: Applied Science and Manufacturing* **125**, 105532 (2019).

40. Huang, H. & Talreja, R. Effects of void geometry on elastic properties of unidirectional fiber reinforced composites. *Composites Science and Technology* **65**, 1964–1981 (2005).
41. ASTM Standards. *Test Methods for Void Content of Reinforced Plastics*. http://www.astm.org/cgi-bin/resolver.cgi?D2734-16 doi:10.1520/D2734-16.
42. D20 Committee. *Standard Test Methods for Density and Specific Gravity (Relative Density) of Plastics by Displacement.Pdf*.
43. D30 Committee. *Test Methods for Constituent Content of Composite Materials*. http://www.astm.org/cgi-bin/resolver.cgi?D3171-22 doi:10.1520/D3171-22.
44. Campbell, F. C. *Manufacturing Processes for Advanced Composites*. (Elsevier, New York, 2004).
45. Campbell, F. C. Nondestructive Inspection and Repair: Because Things Do Not Always Go As Planned. in *Manufacturing Processes For Advanced Composites* 42 (2004).
46. Stone, D. E. W. & Clarke, B. Ultrasonic attenuation as a measure of void content in carbon-fibre reinforced plastics. *Non-Destructive Testing* **8**, 137–145 (1975).
47. Hamidi, Y. K., Aktas, L. & Altan, M. C. Effect of packing on void morphology in resin transfer molded E-glass/epoxy composites. *Polym. Compos.* **26**, 614–627 (2005).
48. Zhan-Sheng Guo, Ling Liu, Bo-Ming Zhang, & Shanyi Du. Critical Void Content for Thermoset Composite Laminates. *Journal of Composite Materials* **43**, 1775–1790 (2009).
49. Olivero, K. A., Barraza, H. J., O'Rear, E. A. & Altan, M. C. Effect of Injection Rate and Post-Fill Cure Pressure on Properties of Resin Transfer Molded Disks. *Journal of Composite Materials* **36**, 2011–2028 (2002).
50. Barraza, H. J., Hamidib, Y. K., Aktasb, L., O'Rear, E. A. & Altan, M. C. Porosity Reduction in the High-Speed Processing of Glass-Fiber Composites by Resin Transfer Molding (RTM). *Journal of Composite Materials* **38**, 195–226 (2004).
51. Effect of processing parameters and void content on mechanical properties and NDI of thermoplastic composites. *Composites Part A* 13 (2019).
52. Bodaghi, M., Cristóvão, C., Gomes, R. & Correia, N. C. Experimental characterization of voids in high fibre volume fraction composites processed by high injection pressure RTM. *Composites Part A: Applied Science and Manufacturing* **82**, 88–99 (2016).
53. Gao, Y., Hu, W., Xin, S. & Sun, L. A review of applications of CT imaging on fiber reinforced composites. *Journal of Composite Materials* **56**, 133–164 (2022).
54. Dilonardo, E., Nacucchi, M., De Pascalis, F., Zarrelli, M. & Giannini, C. High resolution X-ray computed tomography: A versatile non-destructive tool to characterize CFRP-based aircraft composite elements. *Composites Science and Technology* **192**, 108093 (2020).

55. Naresh, K., Khan, K. A., Umer, R. & Cantwell, W. J. The use of X-ray computed tomography for design and process modeling of aerospace composites: A review. *Materials & Design* **190**, 108553 (2020).
56. Elkolali, M., Nogueira, L. P., Rønning, P. O. & Alcocer, A. Void Content Determination of Carbon Fiber Reinforced Polymers: A Comparison between Destructive and Non-Destructive Methods. *Polymers* **14**, 1212 (2022).
57. Mehdikhani, M. *et al.* The effect of voids on matrix cracking in composite laminates as revealed by combined computations at the micro- and meso-scales. *Composites Part A: Applied Science and Manufacturing* **117**, 180–192 (2019).
58. Carraro, P. A., Maragoni, L. & Quaresimin, M. Influence of manufacturing induced defects on damage initiation and propagation in carbon/epoxy NCF laminates. *Advanced Manufacturing: Polymer & Composites Science* **1**, 44–53 (2015).
59. Nikishkov, Y., Airoldi, L. & Makeev, A. Measurement of voids in composites by X-ray Computed Tomography. *Composites Science and Technology* **89**, 89–97 (2013).
60. Lambert, J., Chambers, A. R., Sinclair, I. & Spearing, S. M. 3D damage characterisation and the role of voids in the fatigue of wind turbine blade materials. *Composites Science and Technology* **72**, 337–343 (2012).
61. LeBel, F., Ruiz, É. & Trochu, F. Void content analysis and processing issues to minimize defects in liquid composite molding. *Polym. Compos.* **40**, 109–120 (2019).
62. Chen, D., Arakawa, K. & Xu, C. Reduction of void content of vacuum-assisted resin transfer molded composites by infusion pressure control. *Polym. Compos.* **36**, 1629–1637 (2015).
63. Kang, M. Formation of microvoids during resin-transfer molding process. *Composites Science and Technology* **60**, 2427–2434 (2000).
64. Patel, N. & Lee, L. J. Effects of fiber mat architecture on void formation and removal in liquid composite molding. *Polym. Compos.* **16**, 386–399 (1995).
65. Ruiz, E., Achim, V., Soukane, S., Trochu, F. & Breard, J. Optimization of injection flow rate to minimize micro/macro-voids formation in resin transfer molded composites. *Composites Science and Technology* **66**, 475–486 (2006).
66. Labat, L., Bréard, J., Pillut-Lesavre, S. & Bouquet, G. Void fraction prevision in LCM parts. *Eur. Phys. J. AP* **16**, 157–164 (2001).
67. Lawrence, J. M., Neacsu, V. & Advani, S. G. Modeling the impact of capillary pressure and air entrapment on fiber tow saturation during resin infusion in LCM. *Composites Part A: Applied Science and Manufacturing* **40**, 1053–1064 (2009).
68. Lee, D. H., Lee, W. I. & Kang, M. K. Analysis and minimization of void formation during resin transfer molding process. *Composites Science and Technology* **66**, 3281–3289 (2006).

69. Liu, B., Bickerton, S. & Advani, S. G. Modelling and simulation of resin transfer moulding (RTM).pdf. *Composites Part A* **27A**, 135–141 (1996).
70. Centea, T., Grunenfelder, L. K. & Nutt, S. R. A review of out-of-autoclave prepregs – Material properties, process phenomena, and manufacturing considerations. *Composites Part A: Applied Science and Manufacturing* **70**, 132–154 (2015).
71. Liu, L., Zhang, B.-M., Wang, D.-F. & Wu, Z.-J. Effects of cure cycles on void content and mechanical properties of composite laminates. *Composite Structures* **73**, 303–309 (2006).
72. Koushyar, H., Alavi-Soltani, S., Minaie, B. & Violette, M. Effects of variation in autoclave pressure, temperature, and vacuum-application time on porosity and mechanical properties of a carbon fiber/epoxy composite. *Journal of Composite Materials* **46**, 1985–2004 (2012).
73. Netzel, C., Hoffmann, D., Battley, M., Hubert, P. & Bickerton, S. Effects of environmental conditions on uncured prepreg characteristics and their effects on defect generation during autoclave processing. *Composites Part A: Applied Science and Manufacturing* **151**, 106636 (2021).
74. Gu, Y., Li, M., Zhang, Z. & Sun, Z. Void formation model and measuring method of void formation condition during hot pressing process. *Polym Compos* **31**, 1562–1571 (2010).
75. Kardos, J. L., Dudukovic, M. P. & Dave, R. Void growth and resin transport during processing of thermosetting — Matrix composites. *Advances in Polymer Science* (1986) doi:10.1007/3-540-16423-5_13.
76. Grunenfelder, L. K. & Nutt, S. R. Void formation in composite prepregs – Effect of dissolved moisture. *Composites Science and Technology* **70**, 2304–2309 (2010).
77. Agius, S. L., Magniez, K. J. C. & Fox, B. L. Cure behaviour and void development within rapidly cured out-of-autoclave composites. *Composites Part B: Engineering* **47**, 230–237 (2013).
78. Lukaszewicz, D. H.-J. A., Potter, K. D. & Eales, J. A concept for the in situ consolidation of thermoset matrix prepreg during automated lay-up. *Composites Part B: Engineering* **45**, 538–543 (2013).
79. Lukaszewicz, D. H.-J. A., Ward, C. & Potter, K. D. The engineering aspects of automated prepreg layup: History, present and future. *Composites Part B: Engineering* **43**, 997–1009 (2012).
80. Jin, F.-L., Li, X. & Park, S.-J. Synthesis and application of epoxy resins: A review. *Journal of Industrial and Engineering Chemistry* **29**, 1–11 (2015).
81. Bandyopadhyay, A., Valavala, P. K., Clancy, T. C., Wise, K. E. & Odegard, G. M. Molecular modeling of crosslinked epoxy polymers: The effect of crosslink density on thermomechanical properties. *Polymer* **52**, 2445–2452 (2011).

82. Hoti, G. *et al.* Effect of the Cross-Linking Density on the Swelling and Rheological Behavior of Ester-Bridged β-Cyclodextrin Nanosponges. *Materials* **14**, 478 (2021).
83. Putz, K. W., Palmeri, M. J., Cohn, R. B., Andrews, R. & Brinson, L. C. Effect of Cross-Link Density on Interphase Creation in Polymer Nanocomposites. *Macromolecules* **41**, 6752–6756 (2008).
84. Varley, R. J., Hodgkin, J. H. & Simon, G. P. Toughening of trifunctional epoxy system. V. Structure-property relationships of neat resin. *J. Appl. Polym. Sci.* **77**, 237–248 (2000).
85. Introduction to Molecular Dynamics. in *Computational Many-Particle Physics* (eds. Fehske, H., Schneider, R. & Weiße, A.) vol. 739 (Springer Berlin Heidelberg, Berlin, Heidelberg, 2008).
86. Shokuhfar, A. & Arab, B. The effect of cross linking density on the mechanical properties and structure of the epoxy polymers: molecular dynamics simulation. *J Mol Model* **19**, 3719–3731 (2013).
87. Nakamae, K., Nishino, T., AiRu, X. & Takatsuka, K. Pressure Dependence of the Curing Behavior of Epoxy Resin. *Polym J* **23**, 1157–1162 (1991).
88. Chang, T., Zhan, L., Tan, W. & Li, S. Void content and interfacial properties of composite laminates under different autoclave cure pressure. *Composite Interfaces* **24**, 529–540 (2017).
89. Skyflex K51 Epoxy Resin Prepreg Datasheet.pdf.
90. Loos, A. & Springer, G. Curing of Epoxy Matrix Composites.pdf. *Journal of Composite Materials* **17**, (1983).
91. Liang, Q. *et al.* Effect of curing pressure on the curing behavior of an epoxy system: Curing kinetics and simulation verification. *Polymer* **256**, 125162 (2022).
92. Slough, G. What is Differential Scanning Calorimetry? *TA Instruments* https://www.tainstruments.com/what-is-differential-scanning-calorimetry/ (2022).
93. Fernández Zapico, G., Ohtake, N., Akasaka, H. & Munoz-Guijosa, J. M. Epoxy toughening through high pressure and shear rate preprocessing. *Sci Rep* **9**, 17343 (2019).
94. Gushurst, N., Frerich, T. & Herrmann, A. Investigations on the Influence of High Pressures on the Curing Behaviour and Material Properties of Composite Structures for the Development of a Material Model. *Advances in Polymer Processing* (2020) doi:10.1007/978-3-662-60809-8_26.
95. Cruz, J. C. & Osswald, T. A. Monitoring epoxy and unsaturated polyester reactions under pressure—Reaction rates and mechanical properties. *Polymer Engineering & Sci* **49**, 2099–2108 (2009).
96. Dong, C. Effects of Process-Induced Voids on the Properties of Fibre Reinforced Composites. *Journal of Materials Science & Technology* **32**, 597–604 (2016).

97. Liu, H. *et al.* The effect of voids on the quasi-static tensile properties of carbon fiber/polymer-laminated composites. *Journal of Composite Materials* **52**, 1997–2015 (2018).
98. Chu, Y., Sun, L., Yang, X., Wang, J. & Huang, W. Multiscale simulation and theoretical prediction for the elastic properties of unidirectional fiber-reinforced polymer containing random void defects. *Polymer Composites* **42**, 2958–2972 (2021).
99. Varna, J., Joffe, R., Berglund, L. A. & Lundström, T. S. Effect of voids on failure mechanisms in RTM laminates. *Composites Science and Technology* **53**, 241–249 (1995).
100. Stamopoulos, A., Tserpes, K., Prucha, P. & Vavrik, D. Evaluation of porosity effects on the mechanical properties of carbon fiber-reinforced plastic unidirectional laminates by X-ray computed tomography and mechanical testing. *Journal of Composite Materials* **50**, 2087–2098 (2016).
101. Li, Y., Li, Q. & Ma, H. The voids formation mechanisms and their effects on the mechanical properties of flax fiber reinforced epoxy composites. *Composites Part A: Applied Science and Manufacturing* **72**, 40–48 (2015).
102. Zhu, H., Wu, B., Li, D., Zhang, D. & Chen, Y. Influence of Voids on the Tensile Performance of Carbon/epoxy Fabric Laminates. *Journal of Materials Science & Technology* **27**, 69–73 (2011).
103. Naganuma, T., Naito, K., Kyono, J. & Kagawa, Y. Influence of prepreg conditions on the void occurrence and tensile properties of woven glass fiber-reinforced polyimide composites. *Composites Science and Technology* **69**, 2428–2433 (2009).
104. Choudhry, R., Khan, K. A., Khan, S. Z., Khan, M. A. & Hassan, A. Micromechanical modeling of 8-harness satin weave glass fiber-reinforced composites. *Journal of Composite Materials* **51**, 705–720 (2017).
105. Lomov, S. *et al.* Meso-FE modelling of textile composites: Road map, data flow and algorithms. *Composites Science and Technology* **67**, 1870–1891 (2007).
106. Main Page - TexGen. https://texgen.sourceforge.net/index.php/Main_Page.
107. Van Den Broucke, B. *et al.* Modelling of textile reinforced composites using finite element tools.pdf. in (St-Petersburg).
108. Brown, L. P. TexGen. *Advanced Weaving Technology* https://link.springer.com/10.1007/978-3-030-91515-5_6 (2022) doi:10.1007/978-3-030-91515-5_6.
109. Tserpes, K. I., Stamopoulos, A. G. & Pantelakis, Sp. G. A numerical methodology for simulating the mechanical behavior of CFRP laminates containing pores using X-ray computed tomography data. *Composites Part B: Engineering* **102**, 122–133 (2016).

110. Zhang, A., Lu, H. & Zhang, D. Effects of voids on residual tensile strength after impact of hygrothermal conditioned CFRP laminates. *Composite Structures* **95**, 322–327 (2013).
111. Pineda, E. J., Bednarcyk, B. A., Ricks, T. M., Farrokh, B. & Jackson, W. Multiscale failure analysis of a 3D woven composite containing manufacturing induced voids and disbonds. *Composites Part A: Applied Science and Manufacturing* **156**, 106844 (2022).
112. Hernández, S., Sket, F., González, C. & LLorca, J. Optimization of curing cycle in carbon fiber-reinforced laminates: Void distribution and mechanical properties. *Composites Science and Technology* **85**, 73–82 (2013).
113. Springer, G., Tang, J.-M. & Lee, W. Effects of cure pressure on resin flow, voids, and mechanical properties.pdf. (1987).
114. Ashouri Vajari, D., González, C., Llorca, J. & Legarth, B. N. A numerical study of the influence of microvoids in the transverse mechanical response of unidirectional composites. *Composites Science and Technology* **97**, 46–54 (2014).
115. Sisodia, S., Gamstedt, E. K., Edgren, F. & Varna, J. Effects of voids on quasi-static and tension fatigue behaviour of carbon-fibre composite laminates. *Journal of Composite Materials* **49**, 2137–2148 (2015).
116. Li, B., Zhao, M. & Wan, X. The influence of void distribution on transverse mechanical properties of unidirectional composites. in *2017 8th International Conference on Mechanical and Aerospace Engineering (ICMAE)* 209–214 (IEEE, Prague, Czech Republic, 2017). doi:10.1109/ICMAE.2017.8038644.
117. D20 Committee. ASTM D790 Flexural Properties of Unreinforced and Reinforced Plastics and Electrical Insulating Materials.pdf. (2017).
118. Hagstrand, P.-O., Bonjour, F. & Månson, J.-A. E. The influence of void content on the structural flexural performance of unidirectional glass fibre reinforced polypropylene composites. *Composites Part A: Applied Science and Manufacturing* **36**, 705–714 (2005).
119. Hayashi, T. & Takahashi, J. Influence of void content on the flexural fracture behaviour of carbon fiber reinforced polypropylene. *Journal of Composite Materials* **51**, 4067–4078 (2017).
120. Chambers, A., Earl, J., Squires, C. & Suhot, M. The effect of voids on the flexural fatigue performance of unidirectional carbon fibre composites developed for wind turbine applications. *International Journal of Fatigue* **28**, 1389–1398 (2006).
121. D20 Committee. ASTM D2344 Short-Beam Strength of Polymer Matrix Composite Materials and their Laminates.pdf. (2016).
122. Wiedmer, S. & Manolesos, M. An Experimental Study of the Pultrusion of Carbon Fiber-Polyamide 12 Yarn. *Journal of Thermoplastic Composite Materials* **19**, 97–112 (2006).

123. Kohn, E. J., Sands, A. G. & Clark, R. C. Quantitative Measurement of Void Content in Glass-Filament-Wound Composites and Correlation of Interlaminar Shear Strength with Void Content. *I&EC Product Research and Development* **7**, 179–183 (1968).
124. Wisnom, M. R., Reynolds, T. & Gwilliam, N. Reduction in interlaminar shear strength by discrete and distributed voids. *Composites Science and Technology* **56**, 93–101 (1996).
125. Nikishkov, Y., Seon, G. & Makeev, A. Structural analysis of composites with porosity defects based on X-ray computed tomography. *Journal of Composite Materials* **48**, 2131–2144 (2014).
126. Di Landro, L. *et al.* Detection of Voids in Carbon/Epoxy Laminates and Their Influence on Mechanical Properties. *Polymers and Polymer Composites* **25**, 371–380 (2017).
127. Bureau, M. N. & Denault, J. Fatigue resistance of continuous glass fiber/polypropylene composites: consolidation dependence. *Composites Science and Technology* **64**, 1785–1794 (2004).
128. Costa, M. L., Almeida, S. F. M. de & Rezende, M. C. The influence of porosity on the interlaminar shear strength of carbon/epoxy and carbon/bismaleimide fabric laminates. *Composites Science and Technology* **61**, 2101–2108 (2001).
129. Goodwin, A. A., Howe, C. A. & Paton, R. J. The role of voids in reducing the interlaminar shear strength in RTM laminates. in *Proceedings of ICCM–11* 9 (Gold Coast, Australia, 1997).
130. Protz, R. *et al.* Voids and their effect on the strain rate dependent material properties and fatigue behaviour of non-crimp fabric composites materials. *Composites Part B: Engineering* **83**, 346–351 (2015).
131. Maragoni, L., Carraro, P. A., Peron, M. & Quaresimin, M. Fatigue behaviour of glass/epoxy laminates in the presence of voids. *International Journal of Fatigue* **95**, 18–28 (2017).
132. Gehrig, F., Mannov, E. & Schulte, K. Degradation of NCF-Epoxy Composites containing Voids. in 10 (2009).
133. Schmidt, F., Rheinfurth, M., Horst, P. & Busse, G. Multiaxial fatigue behaviour of GFRP with evenly distributed or accumulated voids monitored by various NDT methodologies. *International Journal of Fatigue* **43**, 207–216 (2012).
134. Zhang, A., Lu, H. & Zhang, D. Research on the mechanical properties prediction of carbon/epoxy composite laminates with different void contents. *Polym. Compos.* **37**, 14–20 (2016).
135. Bodaghi, M., Lomov, S. V., Simacek, P., Correia, N. C. & Advani, S. G. On the variability of permeability induced by reinforcement distortions and dual scale flow in liquid composite moulding: A review. *Composites Part A: Applied Science and Manufacturing* **120**, 188–210 (2019).

136. de Parscau du Plessix, B., Le Corre, S., Jacquemin, F., Lefebure, P. & Sobotka, V. Improved simplified approach for the prediction of porosity growth during the curing of composites parts. *Composites Part A: Applied Science and Manufacturing* **90**, 549–558 (2016).
137. Barari, B., Simacek, P., Yarlagadda, S., Crane, R. M. & Advani, S. G. Prediction of process-induced void formation in anisotropic Fiber-reinforced autoclave composite parts. *Int J Mater Form* **13**, 143–158 (2020).
138. Ledru, Y., Bernhart, G., Piquet, R., Schmidt, F. & Michel, L. Coupled visco-mechanical and diffusion void growth modelling during composite curing. *Composites Science and Technology* **70**, 2139–2145 (2010).
139. Raju, B., Hiremath, S. R. & Roy Mahapatra, D. A review of micromechanics based models for effective elastic properties of reinforced polymer matrix composites. *Composite Structures* **204**, 607–619 (2018).
140. Huang, Z.-M. & Zhou, Y.-X. *Strength of Fibrous Composites*. (Springer, 2012).
141. Hashin, Z. & Rosen, B. W. The elastic moduli of fiber-reinforced materials. (1964).
142. Selmi, A. Void Effect on Carbon Fiber Epoxy Composites. in *2nd International Conference on Emerging Trends in Engineering and Technology (ICETET'2014), May 30-31, 2014 London (United Kingdom)* (International Institute of Engineers, 2014). doi:10.15242/IIE.E0514613.
143. Mori, T. & Tanaka, K. Average stress in matrix and average elastic energy of materials with misfitting inclusions. *Acta Metallurgica* **21**, 571–574 (1973).
144. Liu, T., Fan, W. & Wu, X. Comparisons of influence of random defects on the impact compressive behavior of three different textile structural composites. *Materials & Design* **181**, 108073 (2019).
145. Huang, T. & Gong, Y. A multiscale analysis for predicting the elastic properties of 3D woven composites containing void defects. *Composite Structures* **185**, 401–410 (2018).
146. Gong, Y. *et al.* Multiscale Analysis of Mechanical Properties of 3D Orthogonal Woven Composites with Randomly Distributed Voids. *Materials* **14**, 5247 (2021).
147. Wang, M. Computational evaluation of the effect of defects on the tensile properties of 2D woven composite considering thermal residual stress. *Composite Structures* **299**, 116042 (2022).
148. Xu, K. & Qian, X. An FEM Analysis with Consideration of Random Void Defects for Predicting the Mechanical Properties of 3D Braided Composites. *Advances in Materials Science and Engineering* **2014**, 1–12 (2014).
149. McMillan, A. J. Material strength knock-down resulting from multiple randomly positioned voids. *Journal of Reinforced Plastics and Composites* **31**, 13–28 (2012).

150. Chowdhury, K. A., Talreja, R. & Benzerga, A. A. Effects of Manufacturing-Induced Voids on Local Failure in Polymer-Based Composites. *Journal of Engineering Materials and Technology* **130**, 021010 (2008).
151. Wang, M., Zhang, P., Fei, Q. & Guo, F. Computational evaluation of the effects of void on the transverse tensile strengths of unidirectional composites considering thermal residual stress. *Composite Structures* **227**, 111287 (2019).
152. ABAQUS/CAE. 8.10 Example scripts that access data from an output database. *ABAQUS Scripting User Manual* https://classes.engineering.wustl.edu/2009/spring/mase5513/abaqus/docs/v6.5/books/cmd/default.htm?startat=pt04ch08s10.html.
153. Jiang, H., Ren, Y., Liu, Z. & Zhang, S. Microscale finite element analysis for predicting effects of air voids on mechanical properties of single fiber bundle in composites. *J Mater Sci* **54**, 1363–1381 (2019).
154. Lubliner, J., Oliver, J., Oller, S. & Onate, E. A plastic-damage model for concrete.pdf. *Int. Journal of Solids and Structures* **25**, 299–326 (1989).
155. Ge, L., Li, H., Zhong, J., Zhang, C. & Fang, D. Micro-CT based trans-scale damage analysis of 3D braided composites with pore defects. *Composites Science and Technology* **211**, 108830 (2021).
156. Wang, C. H. & Duong, C. N. Failure criteria. in *Bonded Joints and Repairs to Composite Airframe Structures* 21–45 (Elsevier, 2016). doi:10.1016/B978-0-12-417153-4.00002-5.
157. Materials, equipment and training for advanced composites with next-day shipping and expert technical advice. - Easy Composites. https://www.easycomposites.co.uk/.
158. D30 Committee. *Test Method for Tensile Properties of Polymer Matrix Composite Materials*. http://www.astm.org/cgi-bin/resolver.cgi?D3039D3039M-17 doi:10.1520/D3039_D3039M-17.
159. D30 Committee. *Test Method for Compressive Properties of Polymer Matrix Composite Materials Using a Combined Loading Compression (CLC) Test Fixture*. http://www.astm.org/cgi-bin/resolver.cgi?D6641D6641M-16E1 doi:10.1520/D6641_D6641M-16E01.
160. GitHub - smrg-uob/PeriodicBoundaryCondition: A plugin for Abaqus CAE 2018 to define periodic boundary conditions to 3D geometry. *GitHub* https://github.com/smrg-uob/PeriodicBoundaryCondition.
161. Chevalier, J. *et al.* Micro-mechanics based pressure dependent failure model for highly cross-linked epoxy resins. *Engineering Fracture Mechanics* **158**, 1–12 (2016).
162. Eqra, R., Moghim, M. H. & Eqra, N. A study on the mechanical properties of graphene oxide/epoxy nanocomposites. *Polymers and Polymer Composites* **29**, S556–S564 (2021).

163. Callister., W. D. *Materials Science and Engineering : An Introduction*. (Wiley, New York ; Chichester, 1999).
164. FR4 G10 Plain Expoxy Glass Fibre GRP Laminate Sheet Material – Fortex Engineering Ltd. http://www.fortex.co.uk/product/fr4-plain-laminate-base-material/.
165. Sangha, P. Investigating the effects of processing, morphology and functionalisation on the properties of epoxy nanocomposites. (Cardiff University, Cardiff University, 2021).
166. *Plastics — Determination of Tensile Properties*. (2012).
167. Almudaihesh, F., Holford, K., Pullin, R. & Eaton, M. The influence of water absorption on unidirectional and 2D woven CFRP composites and their mechanical performance. *Composites Part B: Engineering* **182**, 107626 (2020).
168. Fiji. Fiji ImageJ.
169. Kazmi, S., Govigon, Q. & Bickerton, S. Control of laminate quality for parts manufactured using the resin infusion process.pdf. *Journal of Composite Materials* 327–343 (2019) doi:10.1177/0021998318783308.
170. Willett, M. An Introduction to Image Processing using ImageJ.pdf.
171. Serif Ltd. Affinity Photo.
172. Olivier, P., Cottu, J. P. & Ferret, B. Effects of cure cycle pressure and voids on some mechanical properties of carbon/epoxy laminates. *Composites* **26**, 509–515 (1995).
173. Carbon Fibre Pyrofil Fibre Specifications.pdf.
174. Yang, L., Yan, Y., Ran, Z. & Liu, Y. A new method for generating random fibre distributions for fibre reinforced composites. *Composites Science and Technology* **76**, 14–20 (2013).
175. Marklund, E., Asp, L. E. & Olsson, R. Transverse strength of unidirectional non-crimp fabric composites: Multiscale modelling. *Composites Part B: Engineering* **65**, 47–56 (2014).
176. Hobbiebrunken, T., Fiedler, B., Hojo, M. & Tanaka, M. Experimental determination of the true epoxy resin strength using micro-scaled specimens. *Composites Part A: Applied Science and Manufacturing* **38**, 814–818 (2007).
177. Hexcel | Composite Materials and Structures. https://www.hexcel.com/.
178. Hexcel. HiMax FCIM312 [C12K, 200, 0, W] Datasheet.pdf.
179. Hexcel. Carbon Fiber DataSheet | Hexcel. https://www.hexcel.com/Resources/DataSheets/Carbon-Fiber.
180. IN2 Epoxy Infusion Resin - Easy Composites. https://www.easycomposites.co.uk/in2-epoxy-infusion-resin.
181. Ashouri Vajari, D. A micromechanical study of porous composites under longitudinal shear and transverse normal loading. *Composite Structures* **125**, 266–276 (2015).

182. Chowdhury, K. A., Talreja, R. & Benzerga, A. A. Effects of Manufacturing-Induced Voids on Local Failure in Polymer-Based Composites. *Journal of Engineering Materials and Technology* **130**, 021010 (2008).
183. Zhang, C., Li, A., Gu, Y., Mao, C. & Xu, X. Investigation on off-axial tensile properties of 3D braided composites considering void defects. *Journal of Industrial Textiles* **51**, 5389S-5408S (2022).
184. Abbey, T. NAFEMS Ply Calculator Handbook.
185. Sisodia, S. M. *et al.* High-resolution computed tomography in resin infused woven carbon fibre composites with voids. *Composites Science and Technology* **131**, 12–21 (2016).
186. Campo, A. E. *Mechanical Properties of Polymeric Materials*. (William Andrew Publishing, 2008).
187. Henshaw, J. M., Sorem, J. R. & Glaessgen, E. H. Finite element analysis of ply-by-ply and equivalent stress concentrations in composite plates with multiple holes under tensile and shear loading. *Composite Structures* **36**, 45–58 (1996).
188. Davis, T., Healy, D., Bubeck, A. & Walker, R. Stress concentrations around voids in three dimensions: The roots of failure. *Journal of Structural Geology* **102**, 193–207 (2017).

10. Appendices

10.1. Appendix A – Python Scripts

The two scripts that were developed in the process of this thesis are presented here.

10.1.1. Void content measurement script

```
"""
A Script that takes an image of a cross section of a CFRP composite and
calculates the void content.

The script takes an image, converts it to grayscale, applys a threshold
which either sets the pixels to complete black or white and plots histogram

Author: Ben Fisher, Cardiff University
Date created: 2020-March-05

Update log:
2020-March-06
    1. plots each of the images
2021-December-02
    2. Save the last plot
    3. Increase save figure dpi to 300
    4. Remove axis ticks of all figures whilst leaving black boarder
"""

import numpy as np
import matplotlib.pyplot as plt
from PIL import Image, ImageFilter

import skimage
from skimage.viewer import ImageViewer
import sys


print ("")
print ("~~~~~~~~~~~~~~~~~~~~~~~~~~~~~~~~~~~~~~~~~~~~~~~~~~~~~~~~~~~~~~~~~~~~")
print ("Start of script")
print ("~~~~~~~~~~~~~~~~~~~~~~~~~~~~~~~~~~~~~~~~~~~~~~~~~~~~~~~~~~~~~~~~~~~~")
print ("")

#Loads and shows the image to be analyised as found
print ("This image to be analysed is:")
img = Image.open('4000grit 5 minutes.jpg')
#Converts image to an array, allowing image to be analysed
arr = np.asarray(img)
plt.xticks([])
plt.yticks([])
plt.imshow(arr)
plt.show()

#Retuns a Grayscale image
imgGS = img.convert("L")
#Converts image to an array, allowing image to be analysed
arrGS = np.asarray(imgGS)
plt.xticks([])
plt.yticks([])
plt.imshow(arrGS)
#Converts image to an array, allowing image to be analysed
arrGS = np.asarray(imgGS)
plt.imshow(arrGS)

```

Figure 10A-1 *Void content script, lines 1-55.*

```
56  #Function apply the gaussian filter the image
57  filteredImg = Image.fromarray(arrGS).filter(ImageFilter.GaussianBlur(radius=2))
58  plt.imshow(filteredImg, cmap='Greys_r')
59  print ("Blured grayscale image:")
60  plt.show()
61
62  #Algorithm to set pixels to either 0 or 255 based on threshold
63  #Lower is more white pixels
64  imgBW_Blurred = filteredImg.point(lambda x: 0 if x<65 else 255, '1')
65  arrBW_Blurred = np.asarray(imgBW_Blurred) #Creates an array of BW image
66
67  #Prints black and white image
68  print ("Image of voids:")
69  plt.imshow(arrBW_Blurred, cmap='Greys_r')
70
71  #removes axis from plot
72  plt.xticks([])
73  plt.yticks([])
74  #Following line saves image to working directory if needed
75  #plt.savefig("converted_Pic0.5B.png", bbox_inches='tight', dpi=300)
76  plt.show()
77
78  #sets up variables to count totoal, black and white pixels
79  totalPixels = len(arrBW_Blurred)*len(arrBW_Blurred[0])
80  blackPixels = np.count_nonzero(arrBW_Blurred==0)
81  whitePixels = totalPixels-blackPixels
82
83  print ("The size of array is: ", len(arrBW_Blurred), "x ",
84         len(arrBW_Blurred[0]), "= ", totalPixels)
85  print ("number of white pixels is: ", whitePixels)
86  print ("number of black pixels is: ", blackPixels)
87
88  voidContent = ((totalPixels-whitePixels)/totalPixels)*100
89  print ("The void content of this sample is: ", voidContent)
```

Figure 10A-2 *Void content script, lines 56 - 89.*

10.1.2. Modelling analysis script

```
"""
This script iterates through each element of an element set specified and
extracts the stress components, which are then used in a failure Criterion to
determine if the element has failed.

Author: Ben Fisher, Cardiff University
Creation Date: Friday 17th April 2020
Latest Update: Wednesday 22th April 2020

Change log:
1.0 - script creation. Iterate through all elements in a set to extract stress
        components and store in an array.
1.1 - create variables which correspondes to stress components. Use the stress
        components to work out the Stassi Criterion.
1.2 - Creating 2 element set based on elements that have failed or not

Notes for use:
1.    Write name of model in model object at start of code and in the
      "runJob" Function (first line of function).
2.    Write name of part in part object at start of code.
3.    The following regions need to be defined as a set:
         - Total elements as "Tot_Elm" - in Assembly Sets as type elements.
         - Initial matrix region "Initial_Matrix_Region" in Parts Set as type
           geometry.
3.    The matrix and inclusion element numbers (which can be found from the
      input file) need to be added to the script below.
4.    Create a set for the surface where the strain is applied and name the
      set either: "X Strained Region" or "Y Strained Region.
5.    Create the loading step.
6.    Set the name for the .csv file to be saved.
"""

print ' '
print '----------- Starting Stript -----------'
print ' '

from odbAccess import *
from abaqus import *
from abaqusConstants import *
import visualization
import numpy
import csv


model = mdb.models['2%_Matrix_Trans_Strength']
part = model.parts['EllipsoidUC']
assembly = model.rootAssembly

#Assign the arrays for failed or non failed elements
failedElm = []
nonFailedElm = []
failedElmNums = []
nonFailedElmNums = []
totalVonMisesArray = []
averageVonMises = []
```

Figure 10A-3 *Modelling analysis script, lines 1-55.*

```
56
57  #Set initial matrix set
58  matrixElmNums = [\
59  ]
60
61  #Set initial matrix set
62  voidElmNums = [\
63  ]
64
65  #Create the element set for the initial element and void regions
66  matrixElements = part.elements.sequenceFromLabels(matrixElmNums)
67  part.Set(elements=matrixElements, name='Matrix Element Set')
68  voidElements = part.elements.sequenceFromLabels(voidElmNums)
69  part.Set(elements=voidElements, name='Void Element Set')
70
71  print "number of elements in the original matrix is: ", len(matrixElmNums)
72
73  matrixElementsAssembly = assembly.instances['EllipsoidUC-1'].elements
74  elements1 = matrixElementsAssembly.sequenceFromLabels(matrixElmNums)
75  assembly.Set(elements=elements1, name='Mat_Elm')
76
77  #Create the initial Material Properties
78  def applyInitialProps():
79      #Matrix properties
80      matrixMaterial = model.Material(name='Matrix')
81      matrixMaterial.Elastic(type=ISOTROPIC, table=((0.0035, 0.3),  ))
82      #Void properties
83      voidMaterial = model.Material(name='Void')
84      voidMaterial.Elastic(type=ISOTROPIC, table=((1E-12, 0.3),  ))
85      #
86      #Create matrix section
87      model.HomogeneousSolidSection(name='Matrix Section',
88          material='Matrix', thickness=None)
89      #Create void section
90      model.HomogeneousSolidSection(name='Void Section',
91          material='Void', thickness=None)
92      #
93      matrixRegion = part.sets['Matrix Element Set']
94      part.SectionAssignment(region=matrixRegion, sectionName='Matrix Section',
95          offset=0.0, offsetType=MIDDLE_SURFACE, offsetField='',
96          thicknessAssignment=FROM_SECTION)
97      matrixRegion = part.sets['Matrix Element Set']
98      voidRegion = part.sets['Void Element Set']
99      part.SectionAssignment(region=voidRegion,
100         sectionName='Void Section', offset=0.0,
101         offsetType=MIDDLE_SURFACE, offsetField='',
102         thicknessAssignment=FROM_SECTION)
103     return
104
```

Figure 10A-4 *Modelling analysis script, lines 56-104.*

```
105 def applyDegradedProps():
106     #Reapply the void region
107     voidRegion = part.sets['Void Element Set']
108     part.SectionAssignment(region=voidRegion,
109         sectionName='Void Section', offset=0.0,
110         offsetType=MIDDLE_SURFACE, offsetField='',
111         thicknessAssignment=FROM_SECTION)
112
113     #Apply matrix to remaining matrix elements
114     remainingMatrixRegion = part.sets['Matrix Element Set']
115     part.SectionAssignment(region=remainingMatrixRegion,
116         sectionName='Matrix Section', offset=0.0,
117         offsetType=MIDDLE_SURFACE, offsetField='',
118         thicknessAssignment=FROM_SECTION)
119
120     #Failed element properties
121     failedElmMaterial = model.Material(name='Failed Element Properties')
122     failedElmMaterial.Elastic(type=ISOTROPIC, table=((1E-12, 0.3),  ))
123
124     #Create matrix section
125     model.HomogeneousSolidSection(name='Failed Element Section',
126         material='Failed Element Properties', thickness=None)
127     #
128     failedElmRegion = part.sets['Failed Elements']
129     part.SectionAssignment(region=failedElmRegion,
130         sectionName='Failed Element Section', offset=0.0,
131         offsetType=MIDDLE_SURFACE, offsetField='',
132         thicknessAssignment=FROM_SECTION)
133     return
134
135 #Definition to run job
136 def runJob():
137     mdb.Job(name='Job-1', model='2%_Matrix_Trans_Strength', type=ANALYSIS,
138         explicitPrecision=SINGLE, nodalOutputPrecision=SINGLE,
139         description='RUC Analysis',
140         parallelizationMethodExplicit=DOMAIN, multiprocessingMode=DEFAULT,
141         numDomains=12, numCpus=12, memory=50,
142         memoryUnits=PERCENTAGE, echoPrint=OFF, modelPrint=OFF,
143         contactPrint=OFF, historyPrint=OFF)
144     mdb.jobs['Job-1'].submit(consistencyChecking=OFF)
145     mdb.jobs['Job-1'].waitForCompletion()
146     return
```

Figure 10A-5 *Modelling analysis script, lines 105-146.*

```
148 #Following definition sorts the elements into sets according to whether they
149 #have failed or not. - note: Function closes .odb file so job can be rerun.
150 def findFailedElements():
151     print "Finding Failed Elements"
152     odb = openOdb(path='Job-1.odb')
153     elements1 = odb.rootAssembly.elementSets['MAT_ELM']
154     field = odb.steps.values()[-1].frames[-1].fieldOutputs['S']
155     SubField = field.getSubset(region=elements1)
156     #Tensile & Compressive strengths of matrix (units are TPa):
157     Tm = 0.00005 #changed from 60.2MPa to 50MPa
158     Cm = 0.000107
159 
160     #Loop to iterate through elements, extract stress components and identify
161     #failed elements
162     for i in range(0, len(SubField.values)):
163         stressComps = []        #Initiate the array to store the stresses in
164         for j in range(0, 6):    #Iterates through directions within specific
165                                  #element
166             elmStresses = field.getSubset(region=elements1).values[i].data[j]
167             stressComps.append(elmStresses)
168         S11 = stressComps[0]
169         S22 = stressComps[1]
170         S33 = stressComps[2]
171         S12 = stressComps[3]
172         S13 = stressComps[4]
173         S23 = stressComps[5]
174         #Von Mises:
175         vM = (1/sqrt(2))*(sqrt(((S11-S22)**2)+((S11-S33)**2)+((S33-S22)**2)\
176             +(6*(S12**2+S23**2+S13**2)**2)))
177         totalVonMisesArray.append(vM)
178         #
179         if vM > 0.00005:#Check if any elements have failed in tension
180             failedElmNums.append(i+1)
181         elif vM < -0.000107: #Check if any elements have failed in Compression
182             failedElmNums.append(i+1)
183         else:
184             nonFailedElmNums.append(i+1)
185     print "The number of failed elements are: ", len(failedElmNums)
186     print "The number of non failed elements are: ", len(nonFailedElmNums)
187     print "the length of the von mises array is: ", len(totalVonMisesArray)
188     averageVonMises = numpy.average(totalVonMisesArray)
189     print "the average stress is:, ", averageVonMises
190     #
191     #Creating the element set
192     failedElements = part.elements.sequenceFromLabels(failedElmNums)
193     nonFailedElements = part.elements.sequenceFromLabels(nonFailedElmNums)
194     #
195     #print "failed Elements are: ", failedElmNums
196     #
197     #Assigns the element set
198     part.Set(elements=failedElements, name='Failed Elements')
199     part.Set(elements=nonFailedElements, name='non Failed Elements')
200     #
201     odb.close()
202     return failedElmNums, averageVonMises
```

Figure 10A-6 *Modelling analysis script, lines 147-202.*

```
203 applyInitialProps()
204 strainValue = 0.01
205
206 #xStrainedRegion = assembly.sets['X Strained Region']
207 yStrainedRegion = assembly.sets['Y Strained Region']
208
209 #Create a text file to write results to using append method.
210 with open("2%MatrixTransResultsFileMATRIXONLY.csv", "a+") as csvfile:
211     writer = csv.writer(csvfile)
212     writer.writerow(["Number of elements in the matrix is: ",
213                      len(matrixElmNums)])
214
215     writer.writerow(["Stress/TPa", "Applied Strain"])
216
217     while len(failedElmNums) == 0:
218
219         strainValue = strainValue + 0.0001
220         print " "
221         print "~~~~~~~~~~~~~~~~~~~~~~~~~~~~~~~~~~~~"
222         print " "
223         print "number of failed elements is: ", len(failedElmNums)
224         print "Next Iteration"
225         print "Strain being applied is: ", strainValue
226
227         model.DisplacementBC(name='Y Strain', createStepName='Loading',
228             region=yStrainedRegion, u1=UNSET, u2=strainValue, u3=UNSET,
229             ur1=UNSET, ur2=UNSET, ur3=UNSET, amplitude=UNSET, fixed=OFF,
230             distributionType=UNIFORM, fieldName='', localCsys=None)
231
232         #Run job, find the elements that have failed in that analysis
233         print "Job has been submitted"
234         runJob()
235         print " "
236         result = findFailedElements()
237         writer.writerow([result[1], strainValue])
238
239     writer.writerow(["Number of Failed elements is: ", len(failedElmNums)])
240
241 print " "
242 print "---------------Completed Sucessfully---------------"
```

Figure 10A-7 *Model analysis script, lines 203-242.*

10.2. Appendix B – Load response graphs

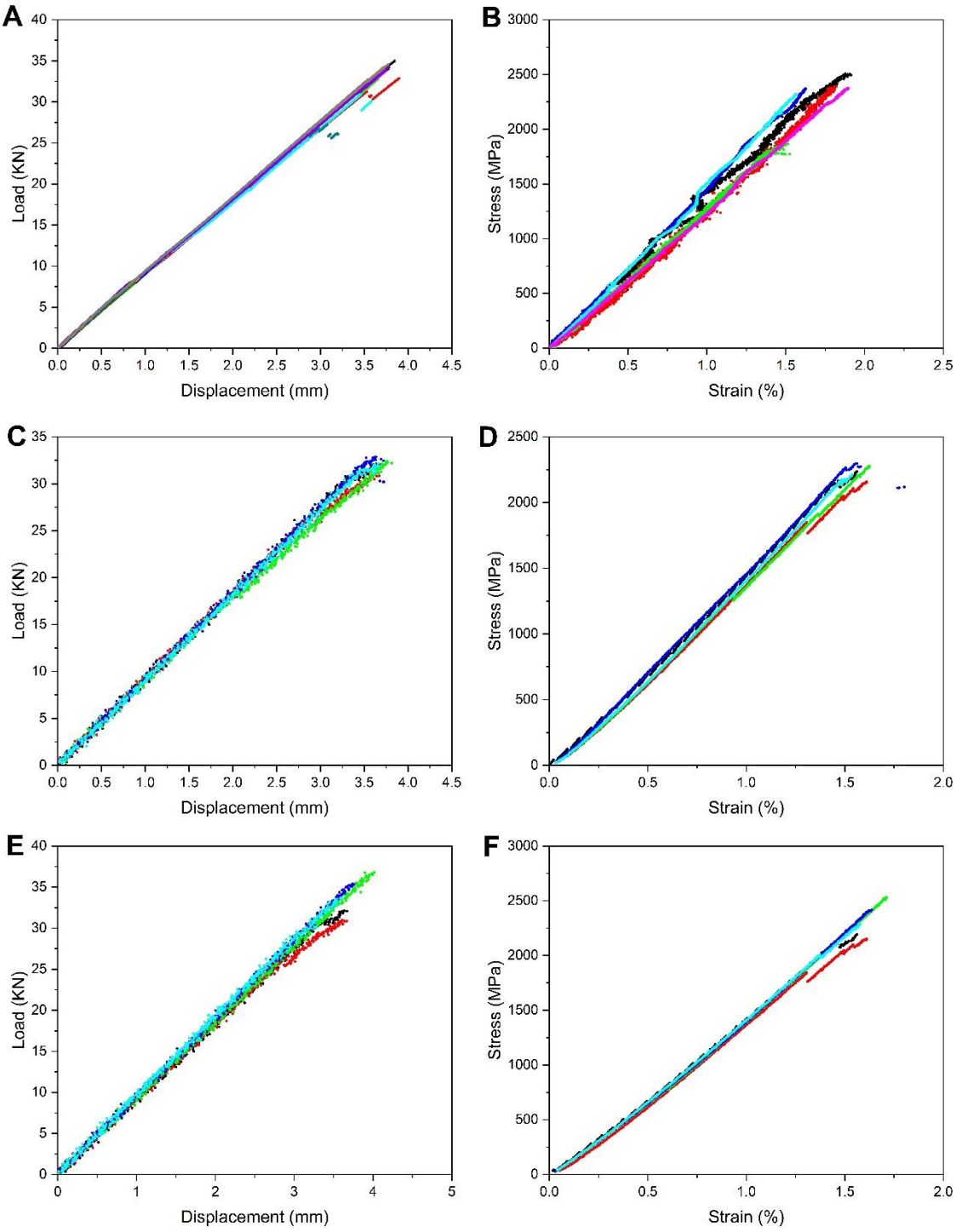

Figure 10B-8 *Load response for 0° tensile specimens. (**A**) & (**B**) 0.59 MPa, (**C**) & (**D**) 0.39 MP, (**E**) and (**F**) 0.05 MPa.*

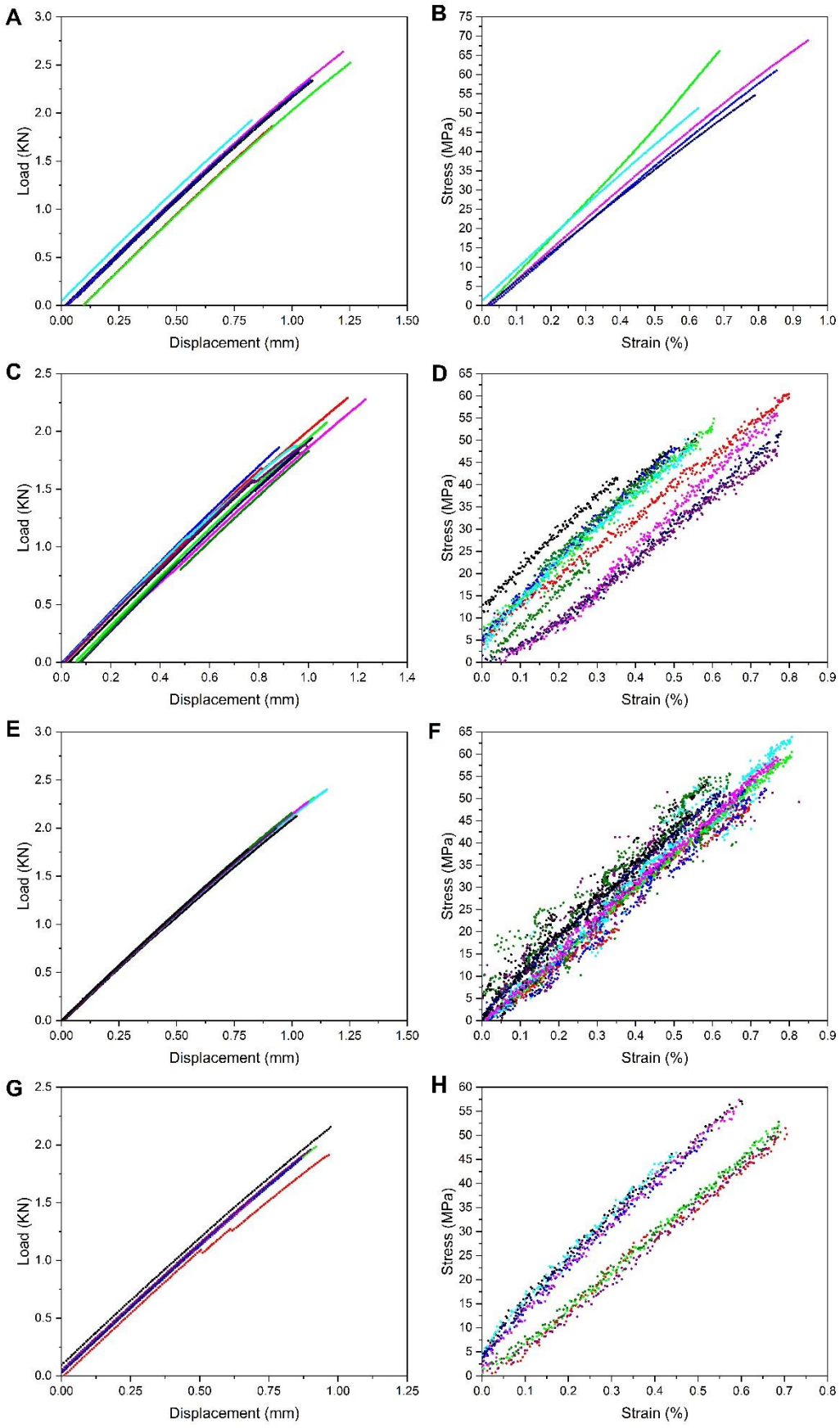

Figure 10B-9 *Load response for 90° compressive specimens. (**A**) & (**B**) 0.59 MPa, (**C**) and (**D**) 0.39 MPa, (**E**) and (**F**) 0.19 MPa and (**G**) and (**H**) 0.05 MPa.*

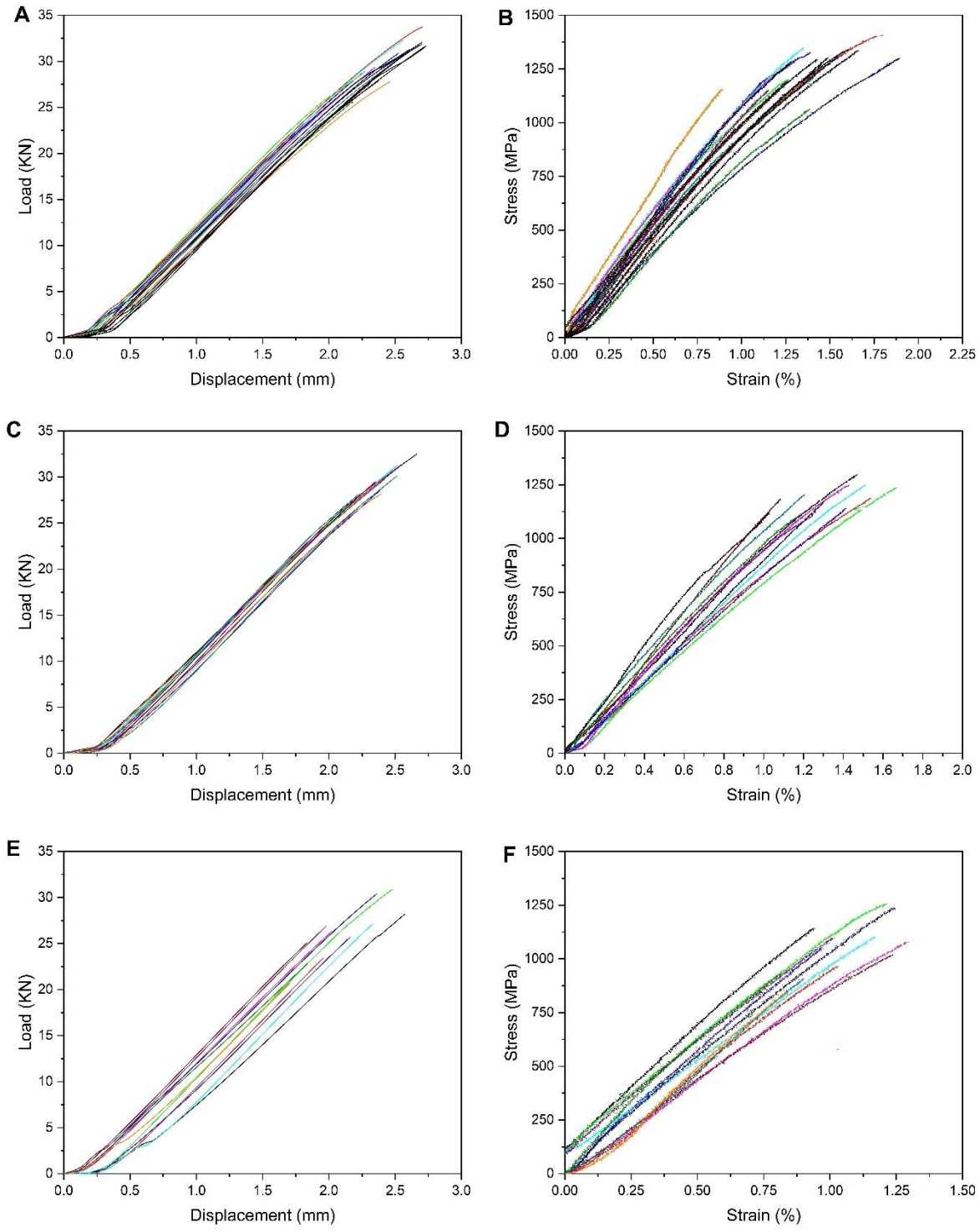

Figure 10B-10 *Load response for 0° compressive specimens. (**A**) & (**B**) 0.59 MPa, (**C**) & (**D**) 0.39 MP, (**E**) and (**F**) 0.05 MPa.*

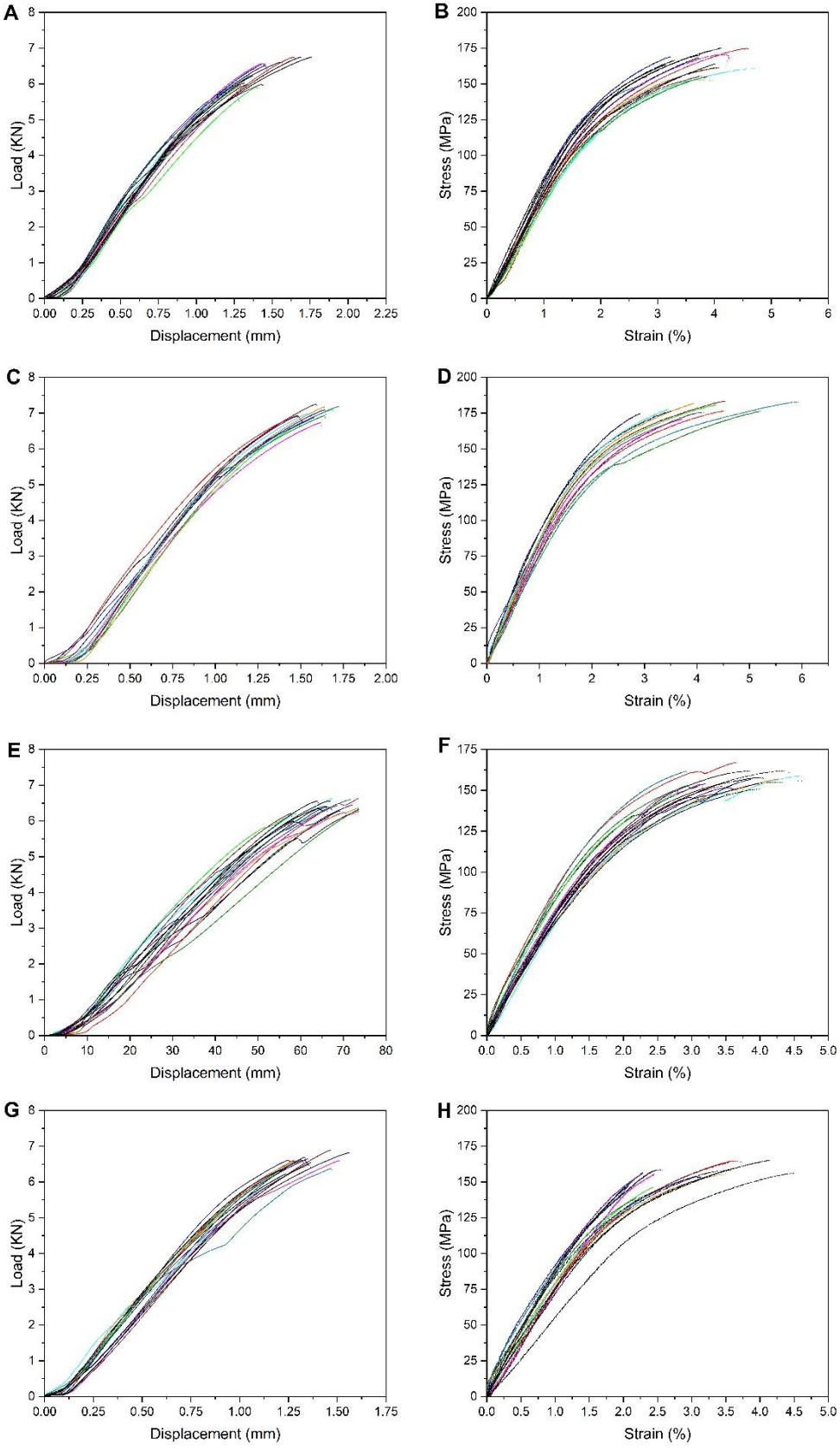

Figure 10B-11 *Load response for 90° compressive specimens. (**A**) & (**B**) 0.59 MPa, (**C**) and (**D**) 0.39 MPa, (**E**) and (**F**) 0.19 MPa and (**G**) and (**H**) 0.05 MP.*

10.3. Appendix C – Modelling Geometry

Table 10C-1 *Stage 1 Dimensions for Mean-All model*

Laminate Designation	Void Content	Long. Length/µm	Trans. Length/µm	Full Unit Cell Dimension / µm
90DT - 0.59 MPa	0.63%	7.86	7.01	34.30 x 30.59 x 30.59
90DT - 0.39 MPa	1.28%	7.45	6.95	25.67 x 23.95 x 23.95
90DT - 0.19 MPa	0.88%	21.54	18.84	84.09 x 73.55 x 73.55
90DT - 0.05 MPa	2.01%	57.58	28.48	170.69 x 84.43 x 84.43
90DC - 0.59 MPa	0.87%	11.97	8.83	46.91 x 34.60 x 34.60
90DC - 0.39 MPa	0.66%	10.14	6.11	43.57 x 26.25 x 26.25
90DC - 0.19 MPa	1.14%	13.33	8.68	47.74 x 31.09 x 31.09
90DC - 0.05 MPa	1.58%	25.72	18.86	82.61 x 60.58 x 60.58

Table 10C-2 *Stage 1 Dimensions for Mean-Std.Dev model.*

Laminate Designation	Void Content	Long. Length/µm	Trans. Length/µm	Full Unit Cell Dimension / µm
90DT - 0.59 MPa	0.63%	6.76	5.79	29.50 x 25.27 25.27
90DT - 0.39 MPa	1.28%	6.45	5.6	22.22 x 19.30 19.30
90DT - 0.19 MPa	0.88%	16.99	11.21	66.33 x 43.76 x 43.76
90DT - 0.05 MPa	2.01%	36.74	19.23	108.91 x 57.01 x 57.01
90DC - 0.59 MPa	0.87%	9.11	6.7	35.70 x 26.26 x 26.26
90DC - 0.39 MPa	0.66%	7.96	5.29	34.20 x 22.73 x 22.73
90DC - 0.19 MPa	1.14%	9.79	6.62	35.06 x 23.71 x 23.71
90DC - 0.05 MPa	1.58%	13.94	13.79	44.78 x 44.29 x 44.29

Table 10C-3 *Stage 1 Dimensions for Median model.*

Laminate Designation	Void Content	Long. Length/µm	Trans. Length/µm	Full Unit Cell Dimension / µm
90DT - 0.59 MPa	0.63%	6.98	5.55	30.46 x 24.22 x 24.22
90DT - 0.39 MPa	1.28%	6.82	5.33	23.49 x 18.36 x 18.36
90DT - 0.19 MPa	0.88%	19.08	12.29	75.49 x 47.98 x 47.98
90DT - 0.05 MPa	2.01%	41.39	23.08	122.70 x 68.42 x 68.42
90DC - 0.59 MPa	0.87%	9.59	6.51	37.58 x 25.51 x 25.51
90DC - 0.39 MPa	0.66%	8.64	5.56	37.12 x 23.89 x 23.89
90DC - 0.19 MPa	1.14%	10.94	6.5	39.18 x 23.78 x 23.78
90DC - 0.05 MPa	1.58%	19.66	16.23	63.15 x 52.13 x 52.13

Table 10C-4 *Stage 1 Dimensions for Mean-Lower Third model.*

Laminate Designation	Void Content	Long. Length/µm	Trans. Length/µm	Full Unit Cell Dimension / µm
90DT - 0.59 MPa	0.63%	4.78	3.71	20.86 x 16.19 x 16.19
90DT - 0.39 MPa	1.28%	5.08	4.24	17.50 x 14.61 x 14.61
90DT - 0.19 MPa	0.88%	8.08	7.04	31.54 x 27.48 x 27.48
90DT - 0.05 MPa	2.01%	16.4	10.81	48.62 x 32.04 x 32.04
90DC - 0.59 MPa	0.87%	6.84	4.68	26.81 x 18.34 x 18.34
90DC - 0.39 MPa	0.66%	5.86	3.64	25.18 x 15.64 x 15.64
90DC - 0.19 MPa	1.14%	6.87	5.25	24.6 x 18.8 x 18.8
90DC - 0.05 MPa	1.58%	8.43	6.71	27.08 x 21.55 x 21.55

10.4. Appendix D – Mesh convergency studies

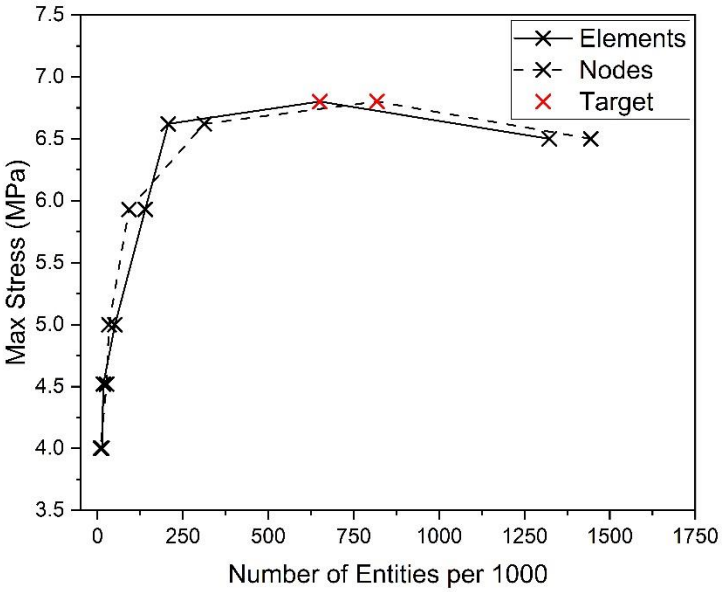

Figure 10C-12 *Mesh convergency study of defect length models.*

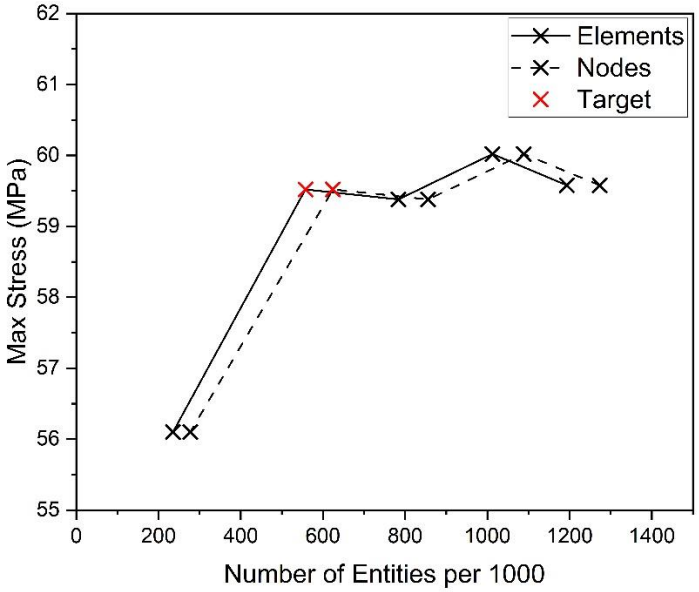

Figure 10C-13 *Mesh convergency study of defect radius models.*

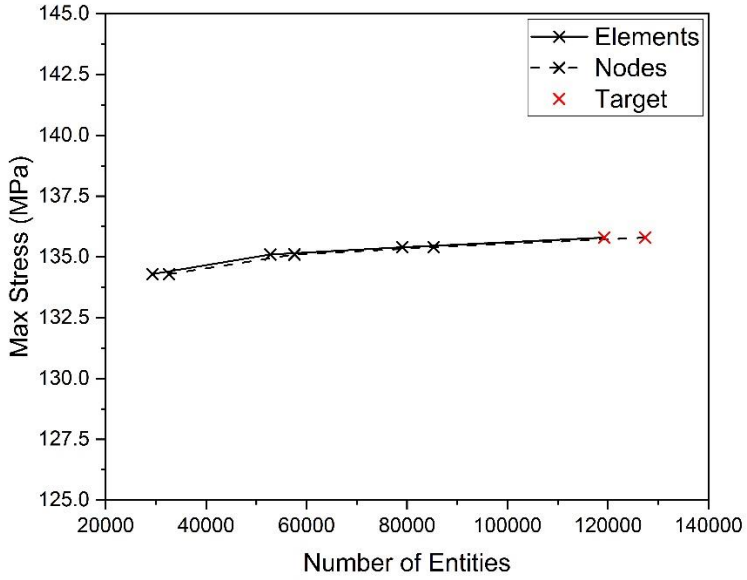

Figure 10C-14 *Mesh convergency study of the void module using the 90DT-4Bar model.*

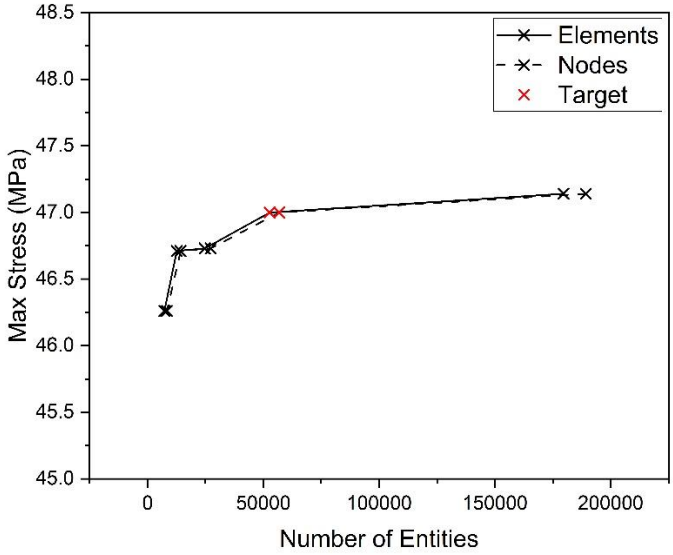

Figure 10C-15 *Mesh convergency study of the RUC using the 90DT-4Bar mode*